UNIVERSITAT DE BARCELONA

Assembly of colloidal nanocrystals into porous nanomaterials

Taisiia Berestok

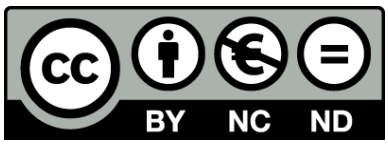

Tesi doctoral

Assembly of colloidal nanocrystals into porous nanomaterials

Autora: Taisiia Berestok

Directors: Prof. Francesca Peiró & Prof. Andreu Cabot

UNIVERSITAT DE BARCELONA

Assembly of colloidal nanocrystals into porous nanomaterials

Memòria presentada per optar al grau de doctor per la

Universitat de Barcelona

Programa de doctorat en Nanociències

Autora: Taisiia Berestok

Directors: Prof. Francesca Peiró i Prof. Andreu Cabot

Tutora: Prof. Francesca Peiró

Universitat de Barcelona

Institut de Recerca en Energia de Catalunya

UNIVERSITAT DE BARCELONA

Els doctors Francesca Peiró i Andreu Cabot, professors de la Universitat de Barcelona i de l'Institut de Recerca en Energia de Catalunya, CERTIFIQUEN:

Que la memòria titulada *Assembly of colloidal nanocrystals into porous nanomaterials*, presentada per Taisiia Berestok per optar al grau de Doctor en el programa de Nanociències que concedeix la Universitat de Barcelona, ha estat realitzada sota la seva direcció a la Universitat de Barcelona i el Institut de Recerca en Energia de Catalunya.

Barcelona, Maig de 2018

Prof. Francesca Peiró Prof. Andreu Cabot

Acknowledgements

Many of my favorite people have been involved in this work and every one of them gave me invaluable feedback, inspiration and encouragement. I sincerely thank to my supervisors Prof. Francesca Peiró and Prof. Andreu Cabot, for providing me with the opportunity to join their research teams and making this journey possible.

I owe my special debt of gratitude to Andreu Cabot for guidance during my research journey. Andreu has been helping me a lot to deal with the challenging tasks by constantly providing inestimable professional advices. I am very grateful to him for encouraging and criticizing my ideas, which helped me to improve myself, advance in my work and widen my research horizons, embracing different perspectives. Equally I am very thankful to Francesca Peiró for all the assistance and help offered during this long journey. Her advices, support and the collaboration of all her team at UB have been of inestimable value for me. Thank you both, Andreu and Francesca, for real.

Also, I would like to emphasize my special gratitude to Pablo Guardia for his patience; for providing with immense knowledge and sharing experience; for teaching me how to be creative, critical and sincere with myself. I thank him for continuous support in overcoming the numerous obstacles I have been facing through my research.

My truest thanks to Michaela Meyns and Raquel Nafria for constant support with valuable advices, sincere opinion, encouragement, motivation and positivism; for always being on my side, for willing to help anytime and for being perfect examples to follow.

I am also grateful to Prof. Stephanie L. Brock for a great chance of having experience to work with her and her research team.

I thank to the members of Functional Nanomaterials group for sharing with me lab work and space, experience and skills. I am happy that we could have been able to work and face the challenges together as a team, and that we could do it enjoying the experience.

I would like to thank my families, my friends and my loved one for supporting me spiritually throughout research and my life in general.

Scope of the thesis

The scope of the present thesis is to develop novel porous nanomaterials through the assembly of nanocrystal (NCs) building blocks and to study their properties. The main goals of the work are: i) developing of reliable strategies to produce NCs with controlled facets, size, crystal phase and composition, with optimized functional properties at the nanometer scale; ii) finding proper NC surface chemistries allowing their assembly into high surface area nanomaterials maintaining and even enhancing properties at the nanometer scale; iii) develop NC assembly strategies to produce porous nanomaterials with optimized properties at the macroscopic scale. Overall, this thesis aims at reducing the gap between NCs synthesis and their implementation into functional nanomaterials and devices.

The work is divided into two blocks. The first block is devoted to developing and optimizing the synthesis of NCs followed by the examination of their suitability for potential applications in catalysis and photocatalysis. The second block is dedicated to establish procedures to fabricate single-component or multicomponent porous nanomaterials from NC building blocks. To demonstrate the applicability of the developed strategies in different fields, several kind of materials were under research. Namely, metals (e.g. Au), metal oxides (e.g. CeO_2, TiO_2, Fe_2O_3), metal chalcogenides (e.g. In_2S_3, ZnS, PbS, $CuGaS_2$ and $Cu_2ZnSnSe_4$), and their composites. Additionally, a general overview on NCs synthesis, surface chemistries, NCs assemblies and the current state of research in these aspects is provided in the introduction of the present work.

The thesis is built around 8 chapters that comprise an introduction chapter, 6 chapters of experimental work, and a conclusion chapter. Each experimental chapter contains an introduction to the specific work described, a detailed experimental section, a presentation and discussion of the results, the obtained conclusions and the references.

The structure of the thesis is as follows:

- **Chapter 1. Introduction.** The goal of this chapter is to give insight into basics of the colloidal synthesis of NCs and the control of their properties, and to discuss the current state of the art in the strategies to control of NC surface chemistry and of NC assembly.

- **Chapter 2. Synthesis of metal oxide NCs: tuning branching in ceria NCs.** The main objective of this chapter is to present a synthetic protocol developed to produce colloidal metal oxide NCs which enables morphology and facet engineering. We particularly focused on the production of high surface area branched NCs that can conserve their capability to interact with the media upon assembly. The work aims at gaining insight into growth mechanism of NCs with complex shape for the paradigmatic case of ceria.

- **Chapter 3. Synthesis of metal chalcogenide NCs: phosphonic acids aid composition adjustment in $Cu_2ZnSnSe_4$ NCs.** In this chapter a synthetic route to produce metal chalcogenide NCs in scalable and reproducible manner is presented. As a paradigmatic example of chalcogenide NCs, the synthesis of $Cu_2ZnSnSe_4$ (CZTSe) NCs is considered here. The complex composition of such quaternary NCs makes the control over such a key parameter extremely challenging, but it is at the same time very rewarding as it provides

additional degrees of freedom to manipulate material properties. The main goal of the work is to achieve control over NCs composition, which enables manipulation of material electronic properties, and hence its functional properties.

- **Chapter 4. Assembly of metal oxide NCs into gels and aerogels.** The main objective of this chapter is to develop and optimize an approach to produce colloidal NC-based porous nanomaterials with large surface areas. The large surface area of NCs, together with their high crystallinity and possibility of size, facet and morphology engineering allows producing porous nanomaterials with excellent control over parameters at the nanometre scale. Cerium oxide NCs with their peculiar branched morphology that enables large surface areas are used as representative material to probe the advantages and determine the limitations of the new assembly strategy. To perform NC assembly, a proper surface chemistry adjustment needs to be applied, which is a main partial goal of this work. The versatility of the concept is proved by using the same approach for the production of iron oxide and titanium oxide porous nanomaterials.

- **Chapter 5. Assembly of metal chalcogenide NCs: the case of In_2S_3.** The main goal of the work reported in this chapter is to optimize a strategy to produce mesoporous architectures of metal chalcogenide NCs, and particularly In_2S_3 NCs. This chapter additionally targets to clarify the influence of surface ligands and microstructure over the photocatalytic activity of colloidal NCs and NC-based nanomaterials. The performance of colloidal NCs strongly depends on the way they are used for application, whether as colloid or when supported. Furthermore, the NC surface chemistry inevitably influences their properties. Thus, it is of great importance to perform a profound study on the influence of surface ligands that can be used for NCs assembly on the NCs performance.

- **Chapter 6. Assembly of multicomponent metal chalcogenide NCs: the case of $CuGaS_2$.** The main objective of this chapter is to extend the approach discussed in Chapter 5 for the production of porous multicomponent metal chalcogenide nanomaterials. The work aims to enhance the performance of $CuGaS_2$ NCs by combining them with ZnS NCs in the form of multicomponent layers or single component multilayers. Applied results of the NCs films and assembly of NCs into gel films are presented by testing their photoelectrochemical energy conversion capabilities.

- **Chapter 7. Multicomponent NC mesoporous structures with versatile composition through electrostatic assembly.** This chapter presents a new strategy to produce porous nanocomposites based on the electrostatic assembly of colloidal NCs. Combing different NCs into mesoporous architectures can lead to synergetic effect and enhanced efficiency. Thus the main objective of the research was to develop an approach to produce multicomponent porous nanocomposites through properly adjusting their surface chemistry. Applying of different ligands for NC surface functionalization endows their surface with different charges. Mixing of oppositely charged NCs with certain concentration enabled their assembly/gelation via electrostatic interaction. The proposed approach is suitable to produce multicomponent NC gels and aerogels. The detailed investigation of the gelation mechanism is shown for combination of metal-metal oxide and metal oxide-metal chalcogenide NCs (Au-CeO_2, CeO_2-PbS). By combining different

types of NCs we aim to achieve enhanced catalytic/photocatalytic activity, which is initially proven through the CO oxidation reaction.

- **Chapter 8. Conclusions.** This chapter summarizes the achievements of this work and their relevance.

Resumen

La presente tesis se centra en varios aspectos de la síntesis coloidal de nanocristales (NCs), la exploración de químicas de superficie relevantes que resultan en su organización y la implementación de estos NCs en nanomaterials porosos. Diferentes tipos de materiales fueron considerados, incluyendo metales, óxidos y calcogenuros.

La tesis se divide en 8 capítulos, incluyendo un capitulo introductorio, 6 capítulos de resultados y un capitulo con las conclusiones. Dentro de los 6 capítulos de resultados, los capítulos 2 y 3 presentan el estudio de la síntesis coloidal de NCs de óxidos y calcogenuros y los capítulos 4-7 se centran en la organización de los NCs en arquitecturas porosas. Los capítulos 4 y 5 recogen los resultados de la investigación de estructuras mesoporosas formadas por un solo componente. Los capítulos 6 y 7 incluyen los resultados de estructuras mesoporosas formadas a partir de diferentes tipos de NCs. Los capítulos están interconectados a través de la línea general de la obtención de nanomateriales de alta superficie y porosidad a partir de la organización de NCs con estructura, facetas, tamaño, composición y química superficial controlada.

El capítulo 2 incluye nuestros resultados en la síntesis de NCs de óxidos metálicos con propiedades controladas. Los métodos de síntesis coloidal nos permiten obtener NCs con un abanico amplio de formas y tamaños y con propiedades ajustadas para cada aplicación específica. Como ejemplo paradigmático, la síntesis de NCs de ceria (CeO_2, oxido de cerio) fue investigada al detalle con la intención de conseguir controlar la morfología, facetas expuestas, fase cristalográfica y composición para optimizar propiedades para aplicaciones específicas. Como punto de inicio, se escogió la síntesis de NCs de ceria con morfología esférica ya reportada. A partir de aquí, la variación de los parámetros de síntesis y los reactantes usados permitió influenciar en el mecanismo de síntesis de NCs de ceria. Así desarrollamos un protocolo de síntesis que nos permitió obtener NCs con cierta diversidad de formas, incluyendo NCs esféricos, NCs con forma de octapods, es decir con 8 ramas, estructuras altamente ramificadas más complejas y NCs en forma de cometa, con tamaños en el rango entre los 7 y los 45 nm. Vimos que la presencia de ácido oleico en la reacción permitió el crecimiento de ramificaciones, resultando en la formación de octapods. Incluyendo grupos alcohol resultó en el crecimiento adicional de ramificaciones laterales y eventualmente en NCs híper-ramificados. La modificación de la temperatura de reacción resultó en NCs en forma de cometa. El estudio sistemático del crecimiento de los NCs mediante HRTEM, TEM y SEM, espectroscopias de UV-vis, FTIR y NMR, y XRD permitió entender el mecanismo de crecimiento y permitió determinar la función de cada parámetro de la síntesis, facilitando la ingeniería de las propiedades de los NCs para mejorar funcionalidad. El estudio de la actividad catalítica de NCs con diferentes formas permitió demostrar la mejora de la eficiencia en NCs con forma de octapods debido a la gran superficie específica y actividad de las facetas expuestas al medio.

Si bien los óxidos metálicos juegan un papel fundamental en diversas aplicaciones catalíticas, cuando se pretende utilizar la energía solar para activar ciertos procesos catalíticos, materiales con una banda prohibida más estrecha son necesarios. Esto nos llevó al desarrollo de calcogenuros metálicos que puedan absorber la luz del sol en un rango más amplio del

espectro. En este contexto, el capítulo 3 está dedicado a la investigación de métodos de síntesis de NCs de calcogenuros metálicos y en particular de NCs de $Cu_2ZnSnSe_4$ (CZTSe). El CZTSe ha despertado un gran interés recientemente debito a sus excepcionales propiedades electrónicas y ópticas y a la abundancia, bajo coste y baja toxicidad de sus componentes. Así, diseñamos una ruta de síntesis para obtener NCs con una estrecha distribución de tamaños y con composición controlada. También demostramos que composiciones no estequiometrias daban lugar a altas concentraciones de portadores de carga y por lo tanto altas conductividades eléctricas.

En el capítulo 4 presentamos la continuación del estudio sobre los NCs de ceria, incluyendo el control de su química superficial y su organización en estructuras porosas, geles y aerogeles. Inspirados por los resultados obtenidos de la síntesis de NCs de ceria, es decir la diversidad de morfologías, altas superficies específica y alta capacidad de almacenamiento de oxígeno, decidimos usar este material para demostrar la organización de NCs en geles. El objetivo de la organización fue obtener materiales con alta superficie específica y a su vez mejor interconexión entre cristales para mejorar propiedades de transporte de carga. El primer paso necesario fue encontrar una química de superficie apropiada para llevar los NCs a solventes polares. En esta dirección, modificamos la superficie de los NCs mediante aminoácidos, lo que ofreció una aceptable estabilidad coloidal de los NCs en solventes polares y permitió a su vez eliminar los surfactantes nativos usados para la síntesis y que contenían largas cadenas de hidrocarbonos. El proceso de intercambio de ligando fue monitorizado mediante TEM, FTIR, DLS y medidas de potencial zeta. La inclusión de un epóxido en la solución de NCs estabilizados con glutamina resultó en la unión de los NCs en un gel de alta área superficial y cristalinidad. El mecanismo de gelificación fue investigado y los parámetros óptimos de formación fueron establecidos. La versatilidad de esta metodología fue probada mediante su uso para la producción de otros óxidos porosos, como el óxido de titanio y el óxido de hierro, a partir de NCs de estos materiales.

El capítulo 5 está focalizado al estudio de estrategias de organización de calcogenuros metálicos y en particular de NCs de In_2S_3. La química superficial y organización de NCs son parámetros cruciales que afectan su eficiencia en aplicaciones. Aun y así, un número limitado de investigaciones de la influencia de estos parámetros en las propiedades catalíticas se ha llevado a término. El principal objetivo de nuestro trabajo fue explorar químicas superficiales y organización de NCs de In_2S_3 y determinar el impacto de estos parámetros en sus propiedades y su eficiencia en aplicaciones catalíticas. Los NCs fueron producidos a partir de una ruta de síntesis coloidal. NCs con morfología de discos y tamaños de unos 18 nm fueron obtenidos después de ajustar los parámetros de reacción y el tipo de reactante. Para investigar la dependencia de las propiedades funcionales de los NCs, diferentes químicas superficiales fueron evaluadas, incluyendo los ligandos nativos, la funcionalización mediante ácido mercaptoundecanoico y el uso de moléculas inorgánicas. El proceso de intercambio de ligando fue analizado mediante TEM, DLS, FTIR, TGA y XPS. Para estudiar el efecto de la microestructura de nanomateriales obtenidos a partir de estos NCs, estos NCs fueron organizados en forma de geles y aerogeles de alta porosidad. El proceso de gelificación fue extendido a la producción de capas porosas de NCs con NCs interconectados, menor cantidad de orgánicos y altas superficies específicas para mejorar interacción del material con el medio. La influencia de ligandos superficiales en el comportamiento de los NCs fue evaluado a partir

de dos aproximaciones: i) NCs coloidales y geles usados para la degradación de un colorante; ii) Capas de NCs para reacciones fotoelectroquímicas. Los NCs terminados en ligandos inorgánicos demostraron las mejores eficiencias en la degradación de colorantes. La capa gelificada demostró mayores fotocorrientes, en un factor 5, comparado con las capas no gelificadas de NCs.

En el capítulo 6, la estrategia usada en el capítulo 5 fue extendida a NCs de $CuGaS_2$ (CGS) y en particular a la producción de geles multicomponente CGS/ZnS. Los NCs de CGS fueron usados para producir capas porosas mediante gelificación. La eficiencia de estas capas en reacciones fotoelectroquímicas fue evaluada. Las capas gelificadas demostraron mejoras en la actividad fotocatalítica comparado con las capas densas de NCs. Para mejorar aún más las propiedades fotoelectrocatalíticas, compuestos de más de un material fueron producidos para reducir la recombinación de portadores fotogenerados y facilitar la separación de carga. En particular, bicapas CGS/ZnS fueron producidas y expuestas a procesos de gelificación. Este proceso se trasladó en mejoras en la densidad de corriente y en la fotorespuesta comparado con capas producidas con un solo tipo de NCs o multicapas con NCs no tratados superficialmente.

El capítulo 7 se centra en la producción de nanomateriales porosos multicomponente a partir de la organización de diferentes tipos de NCs. Proponemos un nuevo método para producir nanocompuestos porosos que contienen diversos tipos de NCs preformados. El objetivo en la creación de nanocompuestos a partir de NCs es aprovechar no solo los efectos sinérgicos que nacen de la combinación de diferentes tipos de NCs, sino también de la gran superficie específica obtenida a partir de la organización de los NCs en estructuras porosas. La investigación detallada de la química superficial de los NCs desarrollada en los capítulos 3 y 4 propició una herramienta para producir nanomateriales multicomponente. El método desarrollado se basa en aprovechar las fuerzas electrostáticas entre NCs con cargas opuestas. Para producir NCs con diferente carga superficial, sus superficies fueron funcionalizadas bien con un aminoácido para obtener una carga positiva, o bien con un tiol para obtener carga negativa. Combinando los NCs con carga opuesta, estos se atrajeron unos a otros para formar un agregado poroso. La aproximación propuesta fue usada para producir compuestos porosos metal-oxido (Au-CeO_2) y oxido-semiconductor (CeO_2-PbS). Adicionalmente, los aerogeles de Au-CeO_2 fueron evaluados para la oxidación de CO.

Summary of results

This thesis focuses on different aspects of NCs colloidal synthesis, the exploration of the relevant surface chemistries that afford NC assembly and the NC implementation into porous nanomaterials. Different types of materials were considered, including metals, metal oxides and metal chalcogenides.

The thesis is divided in 8 chapters, including an introduction chapter, 6 chapters for results, and a chapter with the conclusions. Within the 6 experimental chapters, chapter 2 and 3 present the study on colloidal synthesis of metal oxide and metal chalcogenide NCs and chapters 4, 5, 6 and 7 deal with NCs assembly into porous architectures. Chapters 4 and 5 embrace the results of the investigation of single-component mesoporous assemblies. Chapters 6 and 7 provide results on multicomponent NCs mesoporous structures. Chapters are interconnected through the general line of obtaining NC-based nanomaterials with high surface area and a porous architecture through controlling NC synthesis, surface chemistry and assembly.

Chapter 2 provides our results on the synthesis of metal oxide NCs with desirable properties. Colloidal synthesis methods afford the possibility to obtain NCs with a myriad of different shapes in a wide range of sizes providing suitable properties necessary for specific application. As a paradigmatic example, ceria (CeO_2, cerium oxide) NCs synthesis was deeply investigated with the aim to achieve a proper control on the NCs morphology, facets exposed, crystal phase, composition, etc., required for application. As starting point, the reported synthesis of ceria NCs with spherical morphology was chosen. The variation of the synthesis parameters and reactants used enabled influencing on the formation mechanism of ceria NCs. Overall, ceria NCs with spherical, octapod-like branched, cubic hyperbranched, and kite-like morphology with sizes in the range 7 to 45 nm were produced by adjusting experimental conditions of the synthetic protocol. It was found out that the presence of oleic acid in the reaction enabled the growth of branches resulting in octapod geometry. Further evolving of the NC shapes arises from the addition of alcohol molecules leading to further side-branching and eventually to hyper-branched NCs. Modification of the reaction temperature resulted in kite-like NC shape. Systematic study of the NC growth using HRTEM, TEM, SEM imaging, along with UV-vis, FTIR spectroscopy and XRD and NMR analysis enabled understanding of the growth mechanism and allowed determination of the role of every parameter used, facilitating the NCs shape and size-design/engineering required for enhancing NC performance. Studying of the catalytic activity of the differently-shaped NCs demonstrated enhanced performance of the octapod-shaped NCs due to the high values of specific surface area and activity of facets exposed to the environment.

While metal oxides play important roles in several catalytic applications, when targeting the use of solar energy for a catalytic process, narrower band gap materials are required. This encouraged us to move to metal chalcogenides materials that can provide light conversion in a broad wavelength spectrum. Chapter 3 is devoted to the research on the colloidal synthesis of metal chalcogenides and particularly of $Cu_2ZnSnSe_4$ (CZTSe) NCs. CZTSe has created a great deal of interest due to its outstanding optical and electronic properties and the abundance,

low cost and low toxicity of its components. Thus, a synthetic route to obtain CZTSe NCs with narrow size distribution and controlled composition was designed. We also showed how off-stoichiometric CZTSe compositions were characterized by higher charge carrier concentrations and thus electrical conductivities.

Chapter 4 presents the continuation of the study of ceria NCs including the control of their surface chemistry and their assembly into porous architectures – gels and aerogels. Inspired by the results obtained for the synthesis of ceria NCs, namely diversity of the morphology, high specific surface area, and oxygen storage capacity, it was decided to use this same material to demonstrate NC assembly into gels. This organization offers high surface area required for catalysis, and at the same time implies NCs interconnection affording better charge transport. The first necessary step was finding a suitable surface functionalization procedure that enabled rendering NCs soluble in polar solvents. NCs surface modification through the ligand exchange with amino acids (glutamine, dopamine, glutamic acid) offered a fair NC solubility and resulted in removal of insulating native long-chain hydrocarbon ligands. The ligand exchange process was monitored with TEM, FTIR, DLS and Z-potential measurements. Addition of the epoxide molecules to the glutamine-capped NC sol led to their attachment into a gel with high surface area and crystallinity. The mechanism of gelation was investigated and the optimized synthesis parameters were established. The versatility of the approach was proven by applying it for gelation of titanium dioxide and iron oxide NCs.

Chapter 5 is focused on the study of assembly strategies for metal chalcogenides, and particularly for In_2S_3 NCs. Surface chemistry and organization of NCs are crucial parameters that affect their potential in application. Nonetheless, a limited number of investigations of the influence of these parameters on catalytic properties existed. The main objective was to explore the NCs surface chemistries and organization and their impact on the properties with the aim to find optimal strategies to maintain and enhance NCs efficiency. In_2S_3 NCs were produced using a colloidal synthetic procedure. NCs evolved in plate morphology with size of 18 nm that was tuned by adjustment of reaction time and the type of sulfur precursor. To investigate the NC efficiency, different surface chemistries were evaluated, including capping with native ligands, surface modification via ligand exchange with organic (mercaptoundecanoic acid) and inorganic molecules (phosphotungstic acid and In-Cl complex). The ligand exchange processes were analysed using TEM, DLS, FTIR, TGA and XPS techniques. To study the effect of NC organization, NCs were assembled into highly porous gels and aerogels. The gelation approach was extended to produce NC-based porous films, which were expected to have improved NC interconnection because of the less organic contents and higher surface area providing better contact between NCs and the surrounding media. The influence of surface ligands on the performance was evaluated using 2 approaches: i) unsupported NC sol and gels as catalysts for degradation of rhodamine B; ii) NCs films and NCs gel films as supported catalysts for photoelectrochemical reaction. The inorganic ligand capped NCs demonstrated the best efficiency for dye degradation. Gelated NC films yielded a five-fold photocurrent enhancement compared to non-gelated NC films.

In Chapter 6 the strategy used in chapter 5 was extended to $CuGaS_2$ (CGS) NCs and particularly to produce multicomponent CGS/ZnS gels. CGS NCs were used to produce NC films and porous NC gel films which efficiency against photoelectrochemical reactions was evaluated. CGS NC

gel films showed improvement in photocatalytic activity and demonstrated enhancement in photocurrent response compared to dense NC films. To further improve photoelectrocatalytic properties, composites were produced to reduce charge recombination and facilitate the charge transport. In particular, CGS/ZnS NC-based bilayers were produced and exposed to the sol-gel chemistry as in the case of CGS NC films. This yielded improved current densities and photoresponses compared to films produced from as-produced NCs.

Chapter 7 was focused on the production of NC-based porous nanocomposites. We proposed a new approach to produce porous nanocomposites containing several types of preformed NCs. The goal behind the production of nanocomposites using NCs was to take advantage not only of synergetic effect arising from the combination of different types of NCs, but also the high specific surface areas provided by their assembly into porous architectures. The detailed investigation of the NC' surface chemistries described in chapters 3 and 4 provided a tool for performing multicomponent (metal-metal oxide, metal oxide-metal chalcogenide, etc.) assemblies. The developed assembly approach was based on taking advantage of the electrostatic forces between oppositely charged NCs and did not require using any additives (assembler agents, oxidizers, etc.). To produce NCs with different charge, their surface was functionalized either with an amino-acid (for positive charge) or a thiol (for negative charge). Combining oppositely charged NCs, they attracted to each other and porous aggregate formed. The proposed approach was applied to produce metal-metal oxide (Au-CeO_2) and metal oxide-metal chalcogenide (CeO_2-PbS) nanocomposites porous gels. Additionally, the nanostructured aerogels of Au-CeO_2 were tested for CO oxidation.

List of Publications

This thesis contains 8 chapters including introduction and conclusions. The core of the thesis is formed around 6 articles, published or submitted to peer-review journals. The 6 publications included in the thesis are the following (as-published versions could be found in the Annex):

Ibáñez, M.; **Berestok, T.**; Dobrozhan, O.; Aaron LaLonde, O.A.; Izquierdo-Roca, V.; Shavel, A.; Pérez-Rodríguez, A.; Jeffrey Snyder, G.; Cabot, A. Phosphonic acids aid composition adjustment in the synthesis of $Cu_{2+x}Zn_{1-x}SnSe_{4-y}$ nanoparticles. *J. Nanopart. Res.* **2016**, *18,* 226.

Berestok, T.; Guardia, P.; Blanco, J.; Nafria, R.; Torruella, P.; López-Conesa, L.; Estradé, S.; Ibáñez, M.; de Roo, J.; Luo, Z.; Cadavid, D.; Martins, J. C.; Kovalenko, M. V.; Peiró, F.; Cabot, A., Tuning Branching in Ceria Nanocrystals. *Chemistry of Materials* **2017,** *29* (10), 4418-4424.

Berestok, T.; Guardia, P.; Blanco, J.; Estradé, S.; Llorca, J.; Peiró, F.; Cabot, A., Brock, S.L. Surface chemistry and nano/microstructure engineering on photocatalytic In_2S_3 nanocrystals. *Langmuir* **2018.** *Accepted.*

Berestok, T.; Guardia, P.; Estradé, S.; Llorca, J.; Peiró, F.; Cabot, A., Brock, S.L. $CuGaS_2$ and $CuGaS_2$-ZnS porous layers from solution-processed nanocrystals. *Nanomaterials* **2018,** *8, 220.*

Berestok, T.; Guardia, P.; Du, R.; Blanco, J.; Estradé, S.; Peiró, F.; Brock, S.L.; Cabot, A., Metal oxide aerogels with controlled crystallinity and faceting from the epoxide-driven cross-linking of colloidal nanocrystals. *ACS Applied Materials and Interfaces* **2018,** *Article ASAP DOI: 10.1021/acsami.8b03754.*

Berestok, T.; Guardia, P.; Ibáñez, M.; Meyns, M.; Colombo, M.; Kovalenko, M.; Peiró, F.; Cabot, A. Electrostatic-driven gelation of colloidal nanocrystals. *April* **2018.** *Submitted.*

Publications not included in the thesis:

Blanco-Portals, J.; **Berestok, T.**; Torruella, P.; Coll, C.; López-Conesa, L.; Guardia, P.; Coy, L. E.; Cabot, A.; Estradé, S.; Peiró, F., Atomistic modelling and high resolution electron microscopy simulations of CeO_2 nanoparticles. *Applied Physics Letters* **2017,** *111* (22), 223107.

Authors' Contribution

The research work presented in this thesis has been performed at the Department of Engineering: Section of Electronics of the University of Barcelona and at the Advanced Materials Department of the Catalonia Institute for Energy Research in the frame of the fellowship program Agaur FI-2015. The work described in the 6 articles discussed in the thesis has been carried out in collaboration with different institutions and authors. The results shown in the thesis have not been previously presented in any other PhD dissertation. All of the articles except one were published in first quartile journals according to the Science Citation Index which is according to the regulation of Nanoscience doctoral program of the University of Barcelona for a PhD dissertation presented by collection of publications. The impact factor of each journal is specified in the following list.

Overall, the PhD candidate, Taisiia Berestok contributed to all the experimental work, data analysis, discussion and manuscript writing. Francesca Peiró and Andreu Cabot were designing, planning and coordinating the work and contributed to writing the papers. The contribution of other co-authors for each paper was the following.

Chapter 2

Berestok, T.; Guardia, P.; Blanco, J.; Nafria, R.; Torruella, P.; López-Conesa, L.; Estradé, S.; Ibáñez, M.; de Roo, J.; Luo, Z.; Cadavid, D.; Martins, J. C.; Kovalenko, M. V.; Peiró, F.; Cabot, A., Tuning Branching in Ceria Nanocrystals. *Chemistry of Materials* **2017,** *29* (10), 4418-4424.

Impact factor 2017: 8.354

Pablo Guardia contributed to the design of the material synthesis and manuscript writing; Javier Blanco, Pau Torruella, Lluis Lopez-Conesa, Sonia Estradé contributed to HRTEM analysis; Raquel Nafria contributed to the catalytic measurements of the material and manuscript writing; Maria Ibáñez, Jonatan de Roo, J.C. Martins performed NMR measurements; Zhizhan Luo and Doris Cadavid contributed to the results discussion; Maksym Kovalenko contributed to the results discussion and NMR analysis.

Chapter 3

Ibáñez, M.; **Berestok, T.**; Dobrozhan, O.; Aaron LaLonde, O.A.; Izquierdo-Roca, V.; Shavel, A.; Pérez-Rodríguez, A.; Jeffrey Snyder, G.; Cabot, A. Phosphonic acids aid composition adjustment in the synthesis of $Cu_{2+x}Zn_{1-x}SnSe_{4-y}$ nanoparticles. *J. Nanopart. Res.* **2016**, *18,* 226.

Impact factor 2014: 2.088

Maria Ibáñez contributed to the material synthesis, results discussion and manuscript writing; Oleksandr Dobrozhan participated in the material synthesis and results discussion; O.A. Aaron LaLonde, and V. Izquierdo-Roca and A. Pérez-Rodríguez contributed to Raman

characterization; Alexey Shavel actively participated in the results discussion and work design; Jeffrey Snyder participated in the thermoelectric characterization and discussion.

Chapter 4

Berestok, T.; Guardia, P.; Du, R.; Blanco, J.; Estradé, S.; Peiró, F.; Brock, S.L.; Cabot, A., Metal oxide aerogels with controlled crystallinity and faceting from the epoxide-driven cross-linking of colloidal nanocrystals. *ACS Applied Materials and Interfaces* **2018,** *Article ASAP DOI: 10.1021/acsami.8b03754*

Impact factor 2016: 7.504

Pablo Guardia and Stephanie L. Brock contributed to the result discussion and work planning; Ruifeng Du contributed to the synthesis of titanium dioxide; Javier Blanco, Sonia Estradé contributed to HRTEM analysis; Massimo Colombo performed the surface area measurements of the material.

Chapter 5

Berestok, T.; Guardia, P.; Blanco, J.; Estradé, S.; Llorca, J.; Peiró, F.; Cabot, A., Brock, S.L. Surface chemistry and nano/microstructure engineering on photocatalytic In_2S_3 nanocrystals. *Langmuir* **2018.** *Accepted.*

Impact factor 2014: 3.833

Pablo Guardia participated in the design of the material synthesis; Javier Blanco and Sonia Estradé contributed to HRTEM analysis; Jordi Llorca performed the XPS measurements of the material; Stephanie L. Brock significantly contributed to the results discussion and writing of the manuscript.

Chapter 6

Berestok, T.; Guardia, P.; Estradé, S.; Llorca, J.; Peiró, F.; Cabot, A., Brock, S.L. $CuGaS_2$ and $CuGaS_2$-ZnS porous layers from solution-processed nanocrystals. *Nanomaterials* **2018,** *8, 220*

Impact factor 2016: 3.553

Pablo Guardia participated in the design of the material synthesis; Sonia Estradé contributed to results discussion; Jordi Llorca performed the XPS measurements of the material; Stephanie L. Brock actively contributed to the results discussion and writing of the manuscript.

Chapter 7

Berestok, T.; Guardia, P.; Ibáñez, M.; Meyns, M.; Colombo, M.; Kovalenko, M.; Peiró, F.; Cabot, A. Electrostatic-driven gelation of colloidal nanocrystals. *Langmuir* **2018.** *Submitted*

Impact factor 2017:

Pablo Guardia and Michaela Meyns contributed to the result discussion; Maria Ibáñez performed HRTEM analysis; Massimo Colombo performed the surface area measurements of the material; Maksym Kovalenko contributed to the results discussion and manuscript writing.

Contents

Abbreviations and symbols

Abbreviations

1,2-DDOL	1,2-decanediol
1,12-DDDOL	1,12-dodecanediol
1,2-HDDOL	1,2-hexadecanediol
1-DDOL	1-Dodecanol
Ar	Argon
Au	Gold
BET	Brunauer-Emmet-Teller
CeO_2	Ceria, cerium oxide
CGS	$CuGaS_2$, copper gallium sulfide
CO	Carbon dioxide
CZTS	CuZnSnSe, copper zinc tin selenide
DA	Dopamine
DDT	Dodecanethiol
DLS	Dynamic light scattering
DMF	N,N-dimethylformamide
EDX	Energy Dispersive X-ray Spectroscopy
Fe_2O_3	Iron oxide
FFT	Fast-fourier-transform
FTO	Fluorine doped tin oxide
FTIR	Fourier-transform infrared spectroscopy
Gln	L-Glutamine
Glu	Glutamic acid
HRTEM	High resolution transmission microscope
In_2S_3	Indium sulphide
IR	Infrared
IREC	Catalonia Institute for Energy Research
ITO	Indium tin oxide
MB	Methylene blue
MFA	N-methylformamide
MO	Methylene orange
MUA	11-mercaptoundecanoic acid
MQ-Water	Milli-Q water
NCs	Nanocrystals
NMR	Nuclear magnetic resonance
OAm	Oleylamine
OAc	Oleic acid

ODE	Octadecene
OSC	Oxygen storage capacities
PbS	Lead sulfide
PTA	Phosphotungstic acid hydrate
PO	Propylene oxide
RhB	Rhodamine B
S	Sulfur
SAED	Selected area electron diffraction
SEM	Scanning electron microscope
SSA	Specific surface area
t-DDT	Tert-dodecanethiol
TEM	Transmission electron microscope
TiO_2	Titanium dioxide
TG	Thermo-gravimetric-analysis
TGA	Thioglycolic acid
TMAOH	Tetramethylammonium hydroxide pentahydrate
TNM	Tetranitromethane
TOPO	Trioctylphosphine oxide
TPR	Temperature-programmed reduction
Z.A.	Zone axis
ZnS	Zinc sulfide
Ultraviolet–visible	UV-vis
XPS	X-ray photoelectron spectroscopy
XRD	X-ray diffractometer
(111),[111], <111>	Crystalline plane, crystalline direction and family of crystalline directions, respectively

Symbols and constants

ζ	Zeta potential	mV
λ	Wavelength	nm
h	Planck constant	eV·s
E_F	Fermi level	eV
FWHM	Full Width at Half Maximum	rad
V	Volume	m^3

1. Introduction

1.1. Motivation

The current fast growth of global population and the rapid industrialization of developing countries have accelerated consumption of fossil fuels such as coal, petroleum and natural gas, leading to environmental degradation and shortage of these resources. The continuous release of pollutants and industrial waste derived from fuel combustion or industrial activity results in diseases, global warming and related problems. These issues can be addressed via applying catalysts for environmental remediation, sensors for detection of pollutants and filters for prevention of pollution. In this sense, materials with large surface areas have been attracting a great deal of interest in the last decade to trap and decompose pollutants – for a short-term solution – and in emerging new generation photoconversion systems – for a longer term solution.

Heterogeneous catalysts are used for instance to enhance the decomposition rate of all kind of pollutants, including combustion-derived and organic dyes to name a few, into inert/non-toxic products. An archetypical case is that of three-way catalytic converters installed at exhaust pipes of combustion engines, which convert toxic/explosive CO, NO and/or other volatile organic compounds into inert CO_2, N_2 and H_2O. Another typical example is the environmental pollution by organic dyes that requires the use of heterogeneous catalysts that convert non-biodegradable and/or carcinogenic large dye molecules into smaller non-toxic compounds.

Another strategy to overcome the environmental issues seeks reduction of fuel consumption – rather than mitigation of combustion-derived adverse effects – by developing renewable energy technologies based on sources with sustainable supply for long-term application. Among the targeted sources, solar energy is the most interesting due to its abundance. Many different schemes have been investigated in order to convert solar energy into electricity – for immediate consumption – or into a clean fuel – for storage. In this direction, plenty of compounds for application as photocatalysts have been researched.

The methods commonly employed in industry for producing high surface area materials, including catalyst, are based on sol-gel chemistry and impregnation routes. While these techniques are scalable, they are limited in terms of control over constituent properties such as size, facets, composition and phase distribution, which affect performance parameters as conversion efficiency, selectivity and long-term stability.

Catalysts may benefit from the use of nanocrystals (NCs). NCs usage allows control of surface chemistry and hence enables facet and morphology engineering that in turns improves interaction with the media. High surface area provided by mesoporous architectures formed by interconnection of NCs – by means of gelation, sintering or template synthesis – allows increasing the kinetics of catalysts. A fine control of NCs size and concentration is needed in order to implement these structures in an optimized manner towards the desired application.

Colloidal synthesis of NCs is a versatile approach combing simplicity with an excellent ability to control shape, size and exposed facets. Colloidal synthesis routes allow producing a large variety of NCs including elemental metals, metal oxides, metal chalcogenides. Colloidal methods also allow producing more complex structures such as branched structures or heterostructures.

In most of the cases, the surface chemistry of the synthesized NCs has to be adjusted in order to meet the needs of specific applications. From one hand, the tailoring of the NCs surface composition can serve as a tool for engineering the NCs with desirable features starting from shape and size to colloidal stability, etc. From the other hand, if not properly applied, it can compromise the practical use affecting the capability to interact with the species from the media or with each other, or introducing surface defects and traps. Thus, proper NCs surface functionalization is an essential step to take advantage of their full potential.

The transition from nanoscale to macroscale is a crucial step that determines efficient performance. NC assemblies into gels and aerogels allow taking advantage of the NCs tuned properties. Nonetheless, it is still challenging to find the proper surface chemistry that maintains the peculiar properties of NCs and at the same time suitable for further NC assembly.

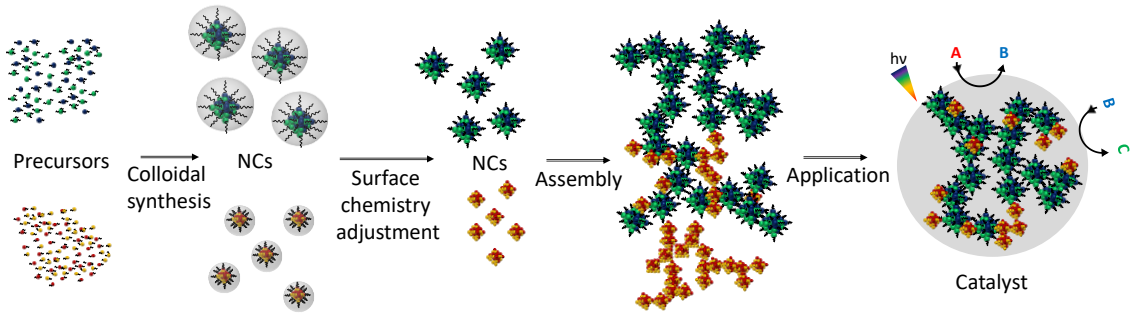

Fig. 1. Schematic representation of the progress of NCs implementation starting from synthesis of colloidal NCs, their surface modification followed by assembly and application.

All the above-mentioned only emphasized the necessity to develop the suitable strategy to produce single and multicomponent porous architectures made from NC building blocks in the manner that enables to maintain and boost their performance for potential application in the field of catalysis, including photocatalysis and electrocatalysis.

1.2. Colloidal NCs

NCs are particles with dimensions less than 100 nm in size. NC properties are strongly affected by their surface chemistry and also surrounding media. The most intriguing NCs peculiarity is their large surface area, which is a key parameter for a variety of applications involving interaction with the media. Another key feature is their size- and shape- depending properties. Electronic, optical and magnetic properties can be tailored by tuning the NCs size without changing the chemical composition or crystallographic structure. This opens a new avenue for their application.

All the above mentioned only underlines the importance of the precise control of NCs morphology. In this direction, we need strategies that offer ability to obtain homogeneous NC samples in terms of size, but also chemical composition, internal structure and surface chemistry. Synthetic methods can be divided into top-down and bottom-up approaches. Regarding to the top-down approach, e.g. ball-milling, obtaining of NCs requires fragmentation of a bulk material. This approach enables to obtain large quantities of NCs. However, its main disadvantage is limitation in NCs morphology and composition engineering.

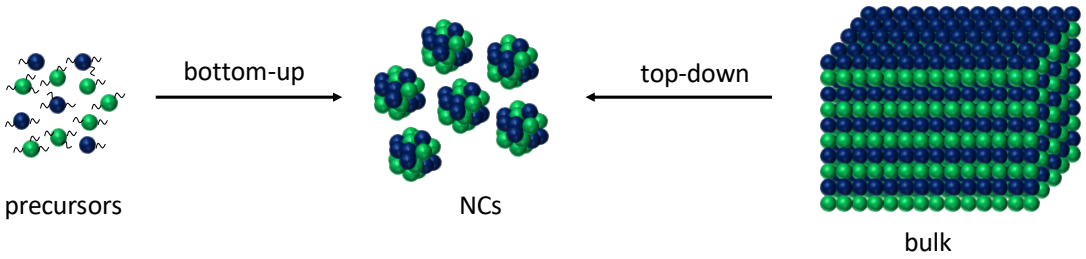

Fig. 2. Schematic drawing of the procedure to obtain NCs via bottom-up or top-down approaches

Contrary, bottom-up approaches, starting from precursor molecules, allow to control NCs growth at every stage and to obtain NCs with programmed tuneable morphology. Bottom-up approaches can be divided into gas-phase, vapour-liquid-solid and liquid-phase syntheses. Among them, a great deal of attention is devoted to liquid-phase methods due to possibilities of reducing the synthesis time and temperatures, but also there is no need to use ultra-pure chemical precursors; while obtaining high-quality NCs with immense diversity of morphologies in controlled and reproducible manner can be achieved.

Particular case of liquid-phase approaches is colloidal synthesis. The method implies maintaining of all particles in the solution, enabling simultaneous control of all the parameters to grow all the NCs with tailored morphology, homogeneity of sizes and composition while providing high throughput at the same time. High degree of morphology and size control, colloidal stability, etc. is offered by the usage of surface capping ligands.

Colloidal synthesis methods involve the reaction or decomposition of precursors in a proper solvent along with suitable capping ligands and potentially redox compounds. Involved in the reaction, surfactants bind to the NCs surface preventing their aggregation. Ligands endow NCs with repulsive forces with sufficient strength to avoid van der Waals attraction, thus agglomeration can be surpassed. The proper choice of the surfactant used also provides a versatile tool to direct NCs growth and engineer their morphology (see chapter 1.2.2.1). Surface ligands also endow NCs with preferred functionalities (see chapter 1.3), serving as a buffer between NC and its further implementation.

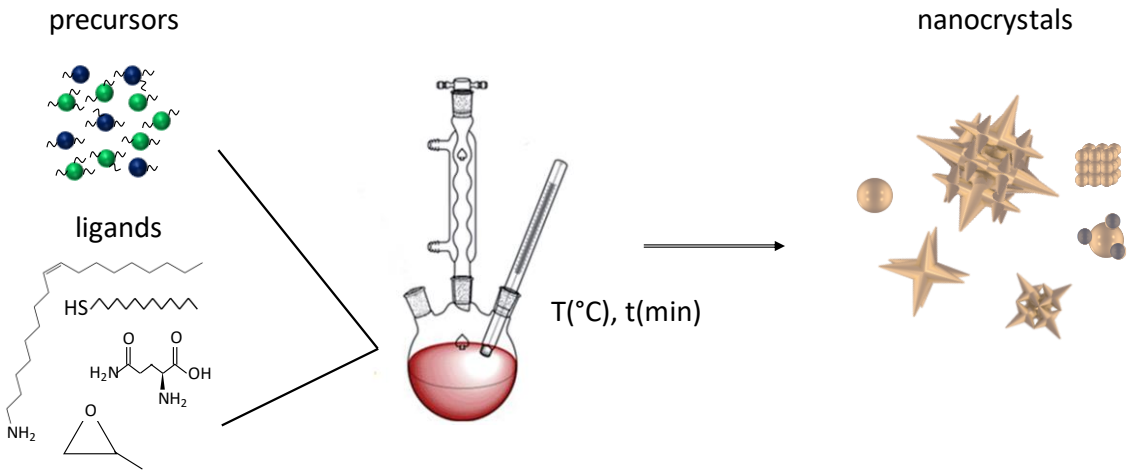

Fig. 3. Schematic drawing of the procedure to obtain NCs via colloidal approach.

The synthesis can be performed in aqueous or non-aqueous organic media. The main disadvantage of the aqueous approach is the limited synthesis temperature which generally translates in low NCs crystallinity and large density of defects. Furthermore, the concentration of colloidal NCs is reduced. These limitations can be overcome with the use of organic solvents. Additionally, non-aqueous syntheses offer a plethora of organic additives to facilitate control over all the reaction parameters in a precise manner resulting in variety of NCs shapes and sizes.

Once the synthesis is completed, NCs need to be purified by removing unreacted products and unbound free ligands. The use of repetitive precipitation-redispersion cycles is a common technique for NCs purification.

1.2.1. NCs formation mechanism

The NC production process is generally divided in two steps, nucleation and growth.[1-2] Nucleation takes place when the concentration of monomers reaches the super-saturation level (C_S) required to overcome the height of nucleation activation energy (ΔG). When the monomer concentration reaches C_{min}, self-nucleation takes place leading to increase of the nucleus radius to critical value r_c, resulting in particles growth. Nuclei with sizes below the critical one will be dissolved in the solution. Increasing the nuclei concentration leads to depletion of the monomer concentration below the nucleation level. At this point the nuclei formation stops and only the NCs growth process may remain.

The NC growth can be evolved in two ways, either “focusing” or “defocusing”.[3] The size focusing takes place when smaller NCs grow faster than the larger ones due to higher free energy which allows to easily surpass the nucleation activation barrier. This allows obtaining NCs with narrow-size distribution. The focusing mode can be achieved by temporal separation between nucleation and growth. In this scenario, the synthesis has to be designed in such way that a short burst of nucleation supplies a large amount of nuclei in a short period of time. This can be realized either by using hot-injection method where the reactants are supplied and the solution is saturated, or by a fast heat-up method.

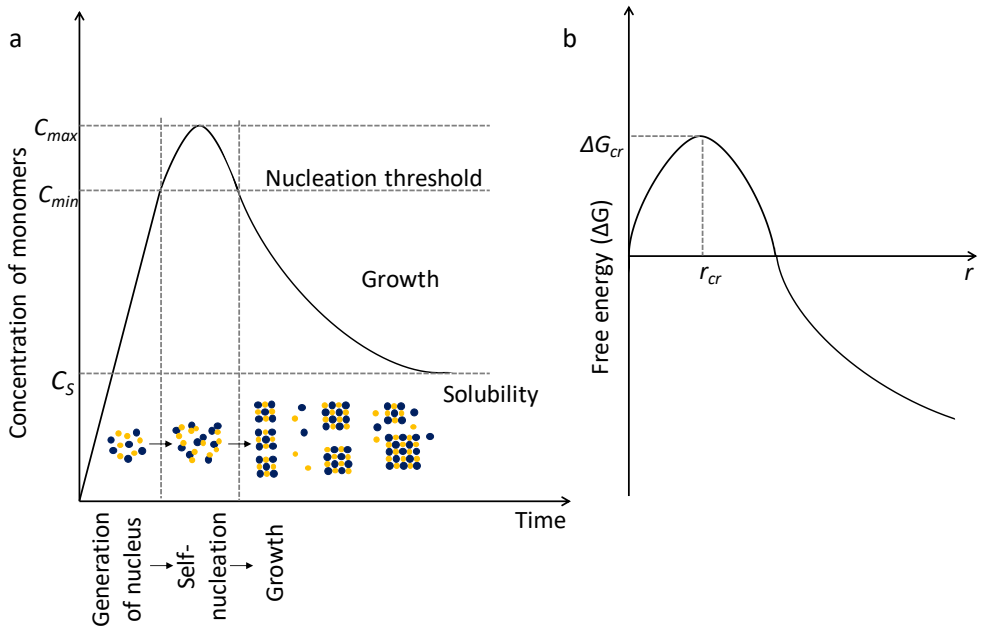

Fig. 4. Schematic representation of steps involved in the NCs formation (a). The curve represents the monomer concentration as a function of time. Overall free energy *ΔG* as a function of the growth of particle size *r* (b). The maximum of the curve at ΔG corresponds to the critical particle size at which they become stable (b).

In the defocusing mode, the depletion of monomer concentration resulting from NCs formation becomes significant. In this case the growth of large NCs occurs at the expense of smaller ones. The sizes of smaller NCs become below the critical one, eventually leading to their dissolution and recondensation of monomer on the surface of bigger, stable crystals. This growth process is known as Ostwald ripening. Also, collision of smaller NCs with larger ones leads to their fusion and hence to further reduction of the surface energy. Thus, a mass-transfer process mediated by diffusion and cluster coalescence takes place resulting in a broad size distribution with larger average NC size. Extending reaction time after a defocusing may lead to consumption of all small NCs by larger one and, “focusing mode” can be achieved with larger but uniform NCs.

1.2.2. Size and shape engineering

NCs size and shape control enables engineering of the facet exposed and tailoring the specific surface area. Understanding of the NCs formation mechanisms allows to design synthesis for NCs fabrication with predictable sizes and shapes, including zero-dimensional (spheres, polyhedrons, cubes), 1 dimensional (rods and wires), 2 dimensional (plates, discs), 3 dimensional (e.g. tetrapods) NCs. NC shape and size control can be achieved by adjusting the synthesis condition, through seeded growth, oriented attachment, selective adhesion of surfactants.

Growth regime conditions: In equilibrium conditions, at low monomer concentration or reaction rate, when the free surface energy tends to be minimized, the thermodynamic regime of growth occurs, resulting in NC shapes with minimized energy. The kinetic regime of growth takes place in non-equilibrium conditions when there is a high flux of monomers or reactivity. This regime generally induces formation of asymmetric NCs. The grow regime is thus mainly

controlled by monomer concentration and reactivity. The monomer concentration can be adjusted by the precursor concentration, the coordination of the solvent, and the chelation effect of pH, etc. Temperature contributes to the free energy in the reaction. High temperature leads to the energetic movement of molecules and ions resulting in high free energy of the reaction and NCs. The type of monomer and type and concentration of potential redox species also contribute to the reactivity.

Seeded growth: NCs can serve as seeds for further growth and shape control. This is efficient because the activation energy barrier for formation of new nuclei is larger than the one for attaching of the new precursor monomer to the surface of the seed, even in the case of formation of heterostructured NCs. The final shape of NCs is directed by the initial shape and crystal structure of the seed.[6] Typically, when the seed has a very symmetric phase, additional NC growth tend to be isotropic resulting in spherical or cubic shapes. On the other hand, lower symmetry seed structures may result in the growth of more asymmetric structures such as rods, disks or more complex shapes.

Ligand-mediated shape control: NCs are enclosed with facets that have different surface energies. Capping ligands bind selectively to the NCs crystallographic facets modifying their surface energy. At the same time, the ligand adhesion on a specific facet may block monomer addition to it. Hence depending on the ligand, the different rate of growth along different facets can be achieved and as a result, the same material can be produced with different geometries.[11-12]

Oriented attachment: The surface energy can be reduced by NC attachment and particularly by oriented attachment.[4-5] This process can foster more asymmetric morphology. In contrast to the Ostwald ripening where NCs formation occurs via dissolving of the smaller NCs and molecular recondensation leading to enlarge of larger NCs, the oriented attachment growth model refers as NCs fusing with each other along the same crystallographic facets.

1.2.3. Branched NCs

NCs with large surface area are of particular interest due to large amount of reactive sites involved in efficient interaction with the surrounding media. This facilitates adsorption of reactive species. High surface areas can be achieved by decreasing of NC sizes or by synthesis of NCs with complex morphologies, containing pores, voids or branches. Branching represents an elegant way to attain high surface area NCs. It provides enhanced transport properties upon assembly but also prevents NCs adherence with each other into compact clusters and hence from loss of surface area. Furthermore, branching enriches NC surface with controllable facets exposed, which is beneficial for catalysis. Branching can be induced by several mechanisms, including template-directed growth, selective etching, twinning, crystal splitting, polymorphic or heterogeneous seeded growth, kinetically controlled overgrowth and NC aggregation-based growth.[6-8]

The template-directed growth makes use of a scaffold to direct the growth of the targeted material, which grows within or around it.[9] The selective etching uses an etchant with the proper strength to sculpt the nanostructure geometry by selectively subtracting atoms from particular facets.[10] Crystal splitting takes advantages of the stresses created generally by the

presence of defects but also by a rapid volume expansion due to an additive reaction to split the crystal into multiple branches.[11] Twin plane describes as the plane that separates two identical crystal domain or twinned domains with equal plane stacking. Twinning uses the spontaneous formation of twin defects to change the growth orientation of a NC and results in branched structures in particular cases where an asymmetric growth of the crystal is also involved.[12] Twin boundaries can be formed because of the interfacial strain and unbalanced surface energy when the NCs growth takes place under kinetic non-equilibrium conditions. The seeded growth employs seeds with a different phase and/or composition to produce multiple branches by the asymmetric growth of a crystal at each different face of the seed.[13] This last is probably the most exploited and controlled method to produce high quality branched NCs, but it requires a very delicate adjustment of the growth conditions, and either a polymorphic material or a seed from another material which in most cases results in heterostructured NCs.

In the kinetically controlled overgrowth, reactants and reaction conditions are selected so ions add and react to the NC much faster than they can move through the surface.[8, 14] In these conditions, the overall growth rate is limited by the diffusion of ions in the reaction media. Compared with a thermodynamically controlled growth regime where large surface areas decisively penalize, a diffusion-limited growth scenario enables a richer family of shapes, potentially characterized by much higher surface areas. In the kinetically controlled growth, differential growth rates in each crystallographic direction are determined by the accessibility and reactivity of each facet. These parameters, and thus the NC geometry, can be manipulated through the use of surface-selective ligands. This is the most versatile and simplest strategy to produce branched nanostructures as already demonstrated for a number of systems.[6, 15-16]

On the other hand, aggregation-based growth takes place not by atomic addition but by the aggregation or attachment of NCs.[17,18] It generally results into randomly branched structures due to the difficult control of the rate of NC addition in each growth direction and the relatively low mobility of NCs, especially when compared with atoms in an atomic-addition growth scenario. The most studied case of aggregation-based growth is the dendrimers formation from supersaturated solutions, although aggregation can also take place in less concentrated solutions and it could involve oriented attachment and/or coalescence, and thus lattice continuity.[19] While it is not always straightforward to discern the mechanism involved in the formation of particular branched NCs, a main differential characteristic of aggregation growth when compared with atomic-addition is that aggregation growth takes place within a solution containing a population of small NCs which decreases as being added to larger structures. Eventually, when all small NCs have been consumed, growth stops.

1.3. NC' surface chemistry control

Despite all the beneficial effect that comes from ligands utilization during synthesis, their presence can also hamper the NCs properties. Ligands allow colloidal stabilization and NC growth control, but they can create an insulation barrier that hinders charge transfer for instance. Hence, being able to remove or replace the surface ligands is essential to exploit NCs potential. Removing of the capping ligands from the surface enables control of NCs aggregation; while replacing of the ligands allows NC surface chemistry adjustment required for preffered application.

1.3.1. Ligand removal

Heat treatment is one of the approaches to remove the excess of capping ligands. Exposure of the NCs to high temperature can foster the ligand decomposition, leaving the NCs surface clean. However, using of thermal method can lead to changes in morphology of NCs and their aggregation.[20] Another way to remove the ligand shell is light treatment. Furthermore, both light and heat treatment can be used at the same time. For instance, decomposition of long-chain hydrocarbon protecting ligands such as oleylamine (OAm) or oleic acid (OAc) requires applying of high-temperature and light treatment.[21] Depending on the type and the length of the molecule, amine ligands can be removed by heating and/or applying additional treatment with acid for instance. In the case of metal oxide NCs, Trizma ($(HOCH_2)_3CNH_2$) ligand are expected to bind to two metal centers resulting in strong binding affinity; while dopamine and glycine hydroxamate bind only to one metal atom representing low surface coverage. Strong affinity of amine-ligands can be weakened by applying of acetic acid along with mild heating. This implies protonation of amino-groups and their easy detachment from the NCs surface.[22] Furthermore, amine ligand removal can be induced by applying of a mild heating along with water addition. Present H_2O molecules adsorb and dissociate on the (101) and (001) NCs facets respectively. This provides the decreased amount of organic stabilizers on the surface; while heating leads to dissociation of water molecule inducing NC attachment with each other (see details in 1.4.2.1.2.). Similar effect was achieved via halides addition to the colloidal gold NCs.[23] Introducing of (I-) to the colloidal Au-tipped CdTe@CdSe NCs provokes displacement of the ligands from gold. This induced the NCs attachment with each other through gold domains and formation asymmetric morphologies.[24] Thiol ligands, that are often used in NC synthesis, can be displaced from the NCs surface by oxidation processes induced by light or oxidants. Exposure thiol-capped NCs to UV irradiation can induce disulfide bond formation that results into NCs aggregation. Introducing of an oxidant (H_2O_2, tetranitromethane) results in thiol ligand detachment followed by NC fusing with each other into porous network (see details in 1.4.2.1.1).

1.3.2. Ligand exchange

1.3.2.1. Ligand types

Thiols are compounds comprising of sulfhydryl (SH) group and aliphatic tail (alkyl, etc.). They are the most common capping ligands used to functionalize the surface of noble metal and chalcogenide NCs. They can bind to the NC surface in two ways: by adsorption of RSH molecule on the surface[25] or by cleavage of S-H bond that creates SR group on the surface. Thiols are used directly for synthesis of NCs or for posterior NCs surface modification depending on the application needs. In the second case, depending on the thiols, and the procedure applied for surface modification, NCs can be stabilized in polar or non-polar media. Furthermore, affinity of the ions to the surface determines whether thiol ligands bind through the sulfhydryl or aliphatic group. For instance, surface functionalization of FePt NCs with mercaptoalkanoic acid resulted in the binding of the carboxylate group to the iron atoms and the mercapto group to the platinum atoms. Modified NCs showed fair solubility in water.[26] Although, modification of the semiconductor NCs with thiols provides an easy and versatile way to shift between hydrophobic and hydrophilic NC surface, they can also poison the NCs by introducing the traps

affecting the properties. It was found, that in order to be beneficial on the NCs properties, the thiol redox energy level has to be lower than the top of the valence band of the target semiconductor. For instance, in case of the CdTe NCs, passivation with thiols such as ethanethiol, hexanethiol, etc., evolves in increased luminescent efficiency and provides solubility in water. However, in the case of the applying the same procedure to the CdSe or CdS NCs, the redox energy level lies above the top of the valence band which involves hole trapping and yields the quenching the luminescence. Moreover, the decrease of the quantum efficiency can arise from the photochemical instability of the thiol-capped NCs. It was found that upon UV-light illumination the photocatalytic oxidation of the thiol ligands took place resulting in its removing. The process was followed by photooxidation of the NCs and their further precipitation. To improve the NCs stability the excess of the thiols has to be used. However, the mentioned disadvantage can be beneficial for further processing of the NCs. The precipitation of the NCs initiated by thiols transformation into the disulfide bonds that can be easily detached from the NCs surface make it unprotected. The process can be followed by NCs attachment with each other and network formation (see details in chapter 1.4.2.1.1.).

Amino acids are another important class of compounds used for NCs surface functionalization. Variety of the amino acids offers the possibility of the synthesis and surface modification of metal, metal chalcogenide[27] and metal oxide[28] NCs. Amino acids are compounds comprised of amine (-NH_2) and carboxyl (-COOH) groups which makes them amphoteric. Free amino acids usually represent dipolar ions ("zwitterions"). However, upon changing the pH of the solution they can feature acid or base properties. Furthermore, tuning of the pH while ligand exchange can afford obtaining positively or negatively charged NC surface. Contrary to thiols, amino-acids demonstrate high stability against oxidation. Moreover, amino acids are often used for ligand exchange of metal-oxide NCs to make them water-soluble and biocompatible. Besides, the presence of the charge on the NCs surface can serve for improving of the colloidal stability of the NCs by means of the repulsive forces. Introducing of the acid during the ligand exchange with glutamine resulted in positively charged surface of NCs and provide stability in polar solvents.[29]

Inorganic ligands offer the possibility to improve NCs interaction between each other enhancing the charge transport, high charge carrier mobility and conductivity, for instance. Metal chalcogenides complexes (MCCs: SnS_4^{4-}, $Sn_2S_6^{4-}$, $In_2Se_4^{2-}$, $Ge_4S_{10}^{4-}$) are the class of the inorganic ligands that show high affinity to the NCs surface and provide complete removal of the original organic ligands.[30] The main limitation of this approach is in high toxicity of the hydrazine which is used for dissolving of the bulk main group or transition metal chalcogenides for MCCs preparation. Despite this, the proposed ligand exchange represents versatile tool to synthesize the hydrazine-stabilized MCCs for inorganic stabilization of Ga_2Se_3, Sb_2Se_3, Sb_2Te_3, $CuInSe_2$, $CuIn_xGa_{1-x}Se_2$, HgSe, CdSe, CdTe, Bi_2S_3, Au, Pd NCs with intact and even enhanced properties.

While the surface modification with the MCCs provides enhanced charge carrier transport, the presence of the foreign ions can change the properties of the original NCs. To circumvent this issue, it was proposed to use metal-free inorganic ligands such as S^{2-}, HS^{2-}, Se^{2-}, HSe^-, Te^{2-}, and HTe^-, OH^- and NH^{2-}. The adherence of the ligands on the NCs surface provides electrostatic stabilization in polar solvents and results in record high electron mobility. Another type of

inorganic metal-free ligands are halides, pseudohalide, and halometallate compounds (Cl^-, Br^-, I^-).

Chalcogenide- and halide-based ligands serve as versatile, cheap and robust strategy for NCs surface modification. However, typically the mentioned ligands are used for metals or metal chalcogenides NCs but not applicable for oxidatively stable NCs. Small inorganic oxoanions (PO_4^{3-}, MoO_4^{2-}) and polyoxometalate ligands developed by Talapin group are proved to allow stabilization not only metal chalcogenides but also metal oxide NCs. Fe_2O_3, ZnO, $CoFe_2O_4$, and TiO_2 NCs were successfully rendered stable in polar solvents using VO_4^{3-}, MoO_4^{2-}, WO_4^{2-}, PO_4^{3-}, AsO_4^{3-}, HPO_3^{2-}, H_2PO^{2-} ligands.

1.3.2.2. Ligand exchange approaches

Ligand modification involves exchange of the NCs native ligands acquired during the synthesis with another preferable one. Usually, ligand exchange entails the exposure of the NCs to the excess of the other type of ligands leading to their partial or complete exchange. Typically, ligand exchange procedure can be proceeded using solution one-phase transfer or phase separation transfer.

One phase ligand exchange involves the addition of the mixture with large amount of the competitive ligand to the NCs powder or precipitate, followed by their dissolving via prolonged mixing or sonication. In some cases, the native ligands can have higher degree of affinity to the NCs surface compare to incoming ones, making the ligand exchange process complicated. Prolonging of the procedure, multiple repeating or applying of temperature during the process can facilitate the ligand exchange. Furthermore, to remove particular native ligands, the acid treatment can be applied additionally. In this case, the solution contained acid can be injected into NCs sol which leads to ligand removal. Afterward, the obtained NCs dissolved in preferable ligand solution which ensures their attachment to the surface. However, mentioned approach implies NCs forcing to be redispersed or dissolved in the solvent contained new ligands which can lead to NCs aggregation. Furthermore, harsh acidic conditions can affect the NCs properties by introducing defects, charge carrier traps or oxidize the NCs surface.

Phase separation ligand exchange involves introducing of the solution with preferred ligands into the NCs solution. Depending on the solvents used, it usually leads to the two-phase mixture formation of polar and nonpolar solvents. Stirring or shaking of the obtained two-phase mixture results in NCs transfer from one phase to another, evidencing the attaching of new functionalities to the NCs surface. In some cases, the ligand exchange required prolonged mixing or shaking, or applying mild heating.

1.4. Aerogels

Surface area and porosity are two important features that determine the material performance.[31] A proper pore size and distribution can endow the material with enhanced accessibility of active sites, control transport phenomena, improve selectivity, etc, which is essential in variety of applications in the field of catalysis, sensors, adsorbents, etc.[32-34]

According to IUPAC definition, gels represent non-fluid colloidal or polymer network that expanded throughout its whole volume by a fluid. Aerogel are formed when the liquid inside of the gel pores is exchange with gas. They are characterized by low densities, large specific surface areas and open pores, and they can be made from almost any materials.[35]

The outstanding properties of aerogels such as low thermal conductivity, high sound absorbance, unique refractive indices, mechanical properties, etc. arise from their unique structural features such as huge surface area, low density, large open pores, etc. All the above mentioned make them promising candidates for a plethora of applications. Aerogel found usage in space technology, catalysis, for thermal insulation, adsorption and sensor applications, biotechnology and pharmaceutical applications.

The general strategy to produce an aerogel includes formation of a sol, applying of the appropriate gelation process to obtain a gel, and its super-critical (SC) drying (Fig. 6).

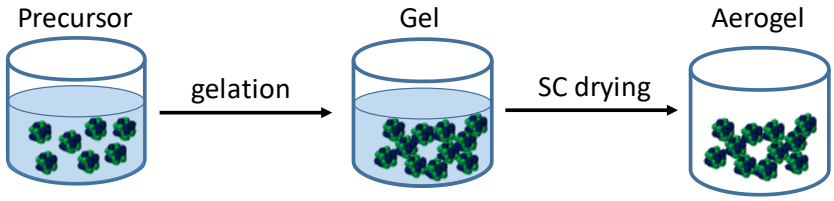

Fig. 5. Schematic representation of procedure for gel and aerogel obtaining

Conventionally, aerogels are producing by the gelation of an ionic or molecular sol. The advantage of the conventional precursor-based aerogel is in the ability of easy scale-up the synthesis, however in a variety of application, the high-temperature treatment is not avoidable which inevitably resulted in aerogel monolith shrinkage and collapsing of the porous structure.

Recently a new strategy to produce aerogels, based on the gelation of a colloidal solution of preformed NCs, has been described (Fig. 6). The peculiarity of NC-based aerogels is in combination of the structural features of aerogel with NCs properties which leads to synergetic effect and boost the final performance. Preserving the NCs properties while their assembly led to enlarging surface area exposed to the media, resulting in improved catalytic activity. Properly applied surface chemistries upon gelation allow to conserve optical properties of quantum dots. Furthermore, the gelation of NCs with 2D morphology can be used to prevent the NCs restacking with each other and afford their full potential usage.

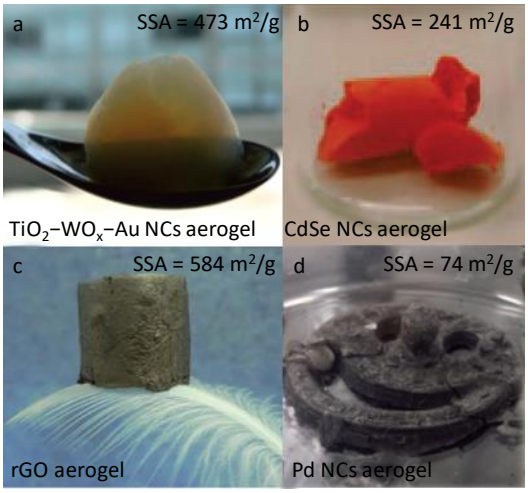

Fig. 6. Examples of aerogels made from different materials with corresponding specific surface area (SSA).[39,92,72,102]

Extension of the gelation approach to produce porous layers can afford possibility of their usage as porous electrodes in optoelectronic devices. CdSe/ZnS transparent porous xerogel films showed higher conductivity and enhanced of photocurrent compare to the CdSe/ZnS films obtained from non-functionalized NCs.[36-37] A great progress has been made in the field of environmental remediation where aerogels can be reused. ZnS xerogels showed promise for remediation of water from Pb^{2+} and Hg^{2+} via cation-exchange process where zinc ions undergo substitution with toxic metal from the aqueous media.[38] CdS NCs aerogels demonstrated high efficiency towards photoelectrocatalytic degradation of dyes.[39] Additionally PbTe and Bi_2Te_3 NCs aerogels demonstrated low thermal conductivity towards thermoelectric applications.[40-41]

1.4.1. Conventional aerogels

The first strategy is based on a sol-gel process using molecular precursor[42] and include hydrolysis and condensation reactions (Fig. 7). Simultaneous hydrolysis and condensation of the alkoxide precursor in an alcohol that is catalyzed by acid or base lead to formation of the gel 3D network comprised of pores with liquid inside. Hydrolysis reaction involves displacement of alkoxide (-OR) by hydroxyl (-OH) via nucleophilic interaction with water:

$$M - OR + H_2O \rightarrow M - OH + ROH$$

Interaction between two M-OH or M-OH and M-OR leads to oxolation or alkooxolation, correspondingly, which eventually resulted in condensation reaction and M-O-M bond formation:

$$M - OH + HO - M \rightarrow M - O - M + H_2O$$
$$M - OH + RO - M \rightarrow M - O - M + ROH$$

A great advance has been made in the field of synthesis of metal-oxide aerogels using the above-mentioned reaction mechanism.[43] The approach was extended for preparation of different binary oxides. [44-48] A great deal of attention was devoted to producing of titania gels and aerogels. Typically, the synthesis involved using of ethoxide,[49] isopropoxide,[50] butoxide[47]

and other titania precursors in an alcohol media resulting in amorphous monolythic gels and aerogels.[51,52,53] The traditional sol-gel technic for aerogel producing also was applied to obtain vanadium oxide aerogels for lithium ion batteries, storage.[54] Chromium oxide, magnesium oxide, aluminum oxide, zirconium oxide are another examples of aerogel producing via traditional precursor-based sol-gel procedure.[55-57]

Using the thiolysis (replacing of H_2O by H_2S) reaction instead of hydrolysis followed by condensation affords the possibility to produce chalcogenides amorphous gels and aerogels.[58] In this case the network formation occurred through S-S binding:

$$M - OR + H_2S \rightarrow M - SH + ROH$$
$$M - SH + HS - M \rightarrow M - S - M + H_2$$

Schematic procedure of precursor-based gel is represented in Fig. 7. To conclude, the main advantages of the conventional precursor-based aerogels is that they are relatively ease in fabrication. However, in order to achieve control and reproducibility, one must control a number of parameters during the synthesis to exploit the full potential.

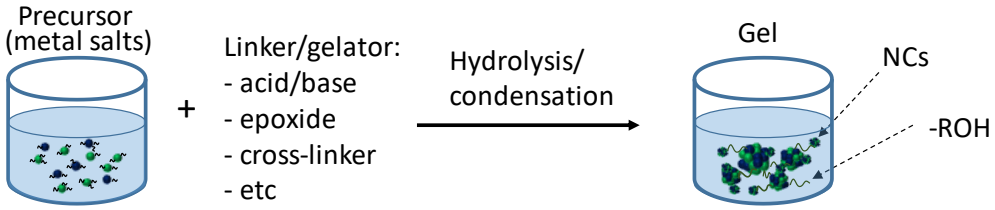

Fig. 7. Schematic representation of the strategy to produce conventional precursor-based gels.

Since the sol-gel process occurs spontaneously and in a continuous way, it became complicated to manipulate with the parameters of the obtained gels.[59] In this regards, the main criteria that plays a role is a precursor concentration. By playing with the precursor concentration, mixing different precursors, or applying additional precursor, the porosity of the gel can be tailored in a wide range. However, the precursor used is also one or the main limitation of the method. Conventional precursor-based sol-gel method linked to the producing of the relatively simple metal oxide gels, mainly due to the usage of metal alkoxides precursors that induce the polymerization process. Besides they are toxic and comparably expensive.

Another parameter that has to be controlled is the sol pH which regulates the hydrolysis/condensation reactions and, hence, the reaction speed and gel voluminousity. In order to induce the metal oxide network formation with further their interconnection into gel, the pH needs to be changes slowly. The fast pH change favors fast growth metal oxide particles and their fast condensation which results in a dense gel.

To change the pH in a controllable and continuous manner it has been proposed the epoxide-initiated gelation process. In this case the gelation is induced by hydrolysis of metal salt precursor with further epoxide ring-opening and slow particles condensation. The changing of pH occurs much slower than in the case of using base and resulted in extended metal oxide

network. Furthermore, opposite to the alkoxide-based, epoxide-driven gels allows usage of cheaper precursors. This approach was extended for preparation of SiO_2, Fe_2O_3, Fe_3C, CeO_2, Al_2O_3, more exotic - $NiCo_2O_4$, etc. aerogels.[60-64] Addition pf polyacrylic acid along with epoxide led to improving of mechanical properties of the aerogel and formation of more rigid monolith.[65]

One of the major issues of the conventional precursor-based sol-gel method is that typically produced aerogels are amorphous or have poor crystallinity which also limits the potential application.[66-68] Attempts to improve crystallinity by heat treatment usually resulted in phase segregation, high degree of shrinkage and loose of surface area. By the same token it is nearly impossible to control morphology of the particles in the gel, their sizes and distribution.

1.4.2. NCs-based aerogels

The 3D porous network of a gel can be built using preformed building blocks (Fig. 8). With all the variety of properties from metallic, semiconductor, magnetic, etc, colloidal NCs are suitable building blocks for the assembly. Besides precise control over the composition, morphology and phase offers the ability to tune the gel properties unlike in the case of conventional approach. Classification of the NCs-based aerogel with respect to the synthesis approach is represented in Table 1.

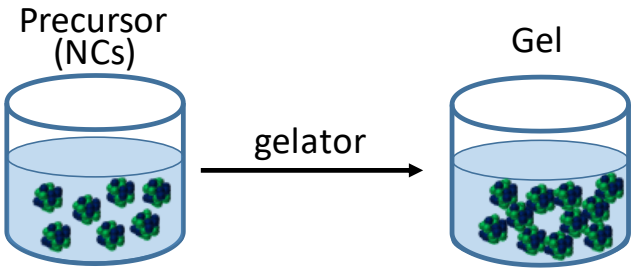

Fig. 8. Scheme of the general approach to produce NCs-based gels.

1.4.2.1.1. Oxidation induced ligand desorption gelation

First NCs-based aerogels were synthesized by Brock et al using controlled destabilization of the colloidal NCs.[69] The mechanism of gelation is based on thiol ligands detachment from the NC surface. Thiols are short-chain organic ligands which often used for ligand exchange.[70] MUA, TGA, MPA are the most common thiol capping stabilizers.[71] To provoke ligand removing, hydrogen peroxide was used. However, in some cases exposure of the NCs to such a strong oxidizer led to their inevitable oxidation and, hence, to deterioration of the properties, such as luminescence for instance.[72] To overcome this problem, the H_2O_2 was replaced with tetranitromethane (TNM) which is non-oxygen transferred gelation agent and considered as a mild oxidizer.[73] Ligand detachment leads to the NCs surface rich with metal ions that can be easily solvated by the solvent or present TNM resulted in sulfur shell on the NC surface. Sulfur ions in turns tend to form the disulfide bonds leading to NCs attaching with each other (Fig. 9). Thus the obtained aerogel are formed by native NC chalcogenide bonds and claimed to be organic-free.[74]

The peculiarity of the approach is in the ability to transform the approach for many different binary NCs including CdS,[75] CdSe,[76] ZnS,[38] PbS,[77] PbSe,[78] PbTe,[40] BiTe,[75] NiP,[79] InP[80]. Furthermore, it can be applied for NCs with different shapes and sizes.[81] The ligand desorption approach was also successfully implemented for metal NCs by Eychmuller team. However, in this case the destabilization process led to the oxide shell formation and obvious NCs performance decrease.

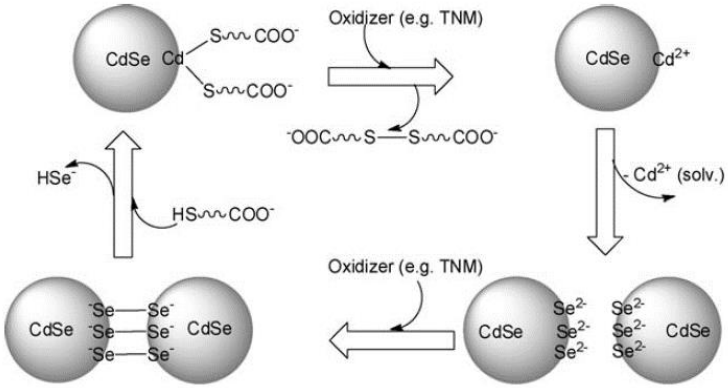

Fig. 9. CdSe NC gelation/dispersion using oxidative ligand desorption mechanism.[74]

1.4.2.1.2. Temperature induced ligand desorption gelation

The approach is based on the NC destabilization of the highly concentrated NC sol by heating which provoke ligands removal.[45] $BaTiO_3$ NC gels were produced via introducing of extra water to the [2-(2-methoxy)ethoxy]acetic acid capped NC sol followed by heating or ultrasonic treatment.[82] The destabilization does not involve any additional chemical or photochemical reaction, but occurs via ligands detachment. TiO_2-Au and TiO_2-SiO_2 NCs-based aerogels were obtained via NCs oriented attachment induced by destabilization of the trizma (2-amino-2-(hydroxymethyl)-1,3-propanediol) functionalized NCs via ligand desorption upon heat treatment.[81]

1.4.2.1.3. NC gelation through solvent removal or antisolvent addition

This approach is based on destabilization of the NCs via increasing of the NCs concentration by slow solvent removing or introducing 'poor' (antisolvent) solvent to the sol.[83] This led to decreasing of the interparticle steric hindrance, thus, the van-der-Waals forces of NCs attraction imposed their aggregation and subsequent fusing into continuous network. Analogously, the gelation of Y_2O_3 NCs was induced by simple centrifugation of organic-capped NCs. In this case, the van-der-Waals interaction between alkyl functionalities of the octylamine stabilizing ligands resulted in porous network formation. However, further implementation of the obtained gels and aerogels required clean NCs surface to remove organics, which imposed applying of thermal post-treatment.[84]

1.4.2.1.4. Metal ion assisted gelation

The strategy is based on the interaction of the coordination bond between NCs.[85] For the gelation the NC' surface firstly needs to be functionalized with chalcogenidometallate ligands.

The linkage of the NCs is induced by the introducing of the metal ions in the form of dehydrated salt that reacts with NCs ligands. The developed approach was applied for CdSe NCs with Pt^{2+} cations as linkers. However, the chalcogenidometallate ligands used for surface modification are toxic and air-sensitive which implies certain restrictions. Another way to produce hybrid aerogels was proposed by Eychmuller and co-workers. Prior gelation the NCs surface was functionalized with ligand contained of tetrazole functional group.[86] Adding of the metal salt to the NCs sol provoked the complexation of tetrazole group with metal ions resulting in the gel formation.[87] However, the main limitation of the former approach is in the necessity to synthesize the tetrazole compound. To address the above-mentioned issues, the same authors proposed to functionalize the ZnO, CdSe, PbSe NCs surface with inorganic ligands such as S^{2-}, I^-, Cl^-, F^- followed by introducing of the Cd^{2+}, Pb^{2+}, and Zn^{2+} ions, in the form of dehydrated acetate salts which induce gelation process (Fig. 10).[88]

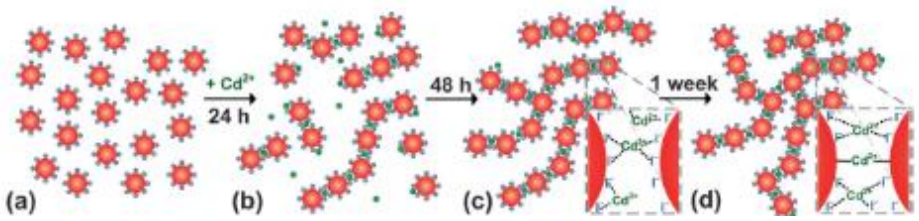

Fig. 10. Schematic representation of the gelation via metal-assisted process.[88]

1.4.2.1.5. Freeze gelation

The method implies NCs attachment during their freezing upon introducing them into liquid nitrogen. The NCs linkage can be attributed to the enhanced van der Waals forces between NCs squeezed between ice crystals. The freeze gelation approach can be applied for metal oxides (ZnO, Fe_2O_3, MnO_2) but also it was extended for numerous other materials, including noble metals (Au, Ag, Pd, Pt) and semiconductors (CdSe, CdS).[89-93] Furthermore, the cryogelation affords not only the possibility to assemble differently-shaped NCs but also to tailor the macroscopic shape of the final gel.

Table 1. Summary of the NCs-based aerogel produced via different gelation strategies

Gelation approach	NCs	SSA (SSA after heat treatment), m^2/g	Application	Ref.
Oxidation induced ligand desorption	CdS	240		75
	CdSe	79-241		94
	ZnS	182-202	Water-remediation	94
	PbSe	52		78
	PbS	119-141		69
	PbTe	74	Thermoelectrics	40

	Bi_2Te_3, $Bi_{2-x}Sb_xTe_3$	36-45	Thermoelectrics	41
	Ni_2P	177		79
	InP	200		80
	Au-CdTe	170		95
	Ag-Au, Pt-Ag	46		96
	ZnPd/ZnO	250	Catalytic methanol steam reforming	97
Temperature induced ligand desorption	TiO_2, Au-TiO_2	402, 305	Dye degradation: RhB	98
	Au-TiO_2-WO_x	473	Dye degradation: MB	99
	TiO_2-SiO_2	488		100
	BaTiO3	300		82
	$SbSnO_2$	340 (100, 400 °C) 100		101
NC gelation through solvent removal or antisolvent addition	Au, Ag, Au-Ag, Pt, Pd, PtPd	32-168		83
	Y_2O_3	445 (293, 400 °C) 293	Dye degradation: MB	84
Metal ion assisted	CdTe			102
	CdSe, ZnO, PbSe	173, 146		88
	Au, CdTe, Au-CdTe	50-130		103
	NiMoS, CoMoS, NiCoMoS, CoMoWS	340-528		104
	GeS, GeSe, SnS, SnSe	108-327		58
Freeze gelation	MnO_2		N_2H_4 sensing	93
	MnO_2	156	Li-O_2 batteries	92
	Pt, Pd, Au, Ag, Fe_2O_3, CdSe/CdS	33		89

*SSA: specific surface area; MB: methylene blue; RhB: rhodamine B

1.4.3. Gel processing

After gel is formed, typically the solvent inside the pores can be contaminated with gelation reaction traces. In order to get rid of the reaction products the solvent has to be exchanged with fresh one. During the solvent-exchange process especial care has to be paid in order not to destroy the porous structure.

Aerogels derive from the exchanging of the liquid inside of the gel pores with gas-phase. During this step preserving of the gel porous structure while the liquid phase evaporation is crucial. The collapse of the porous structure related with the increasing of the surface tension arises from the direct transition from the liquid to gas phase. The transition from liquid to gas phase results in increasing of the capillary forces, the pores network becomes rigid and finally induces the aerogel shrinkage.

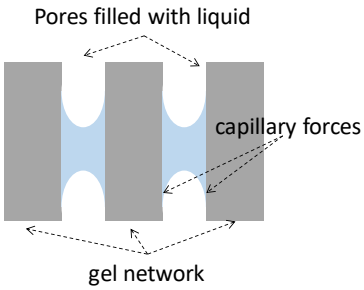

Fig. 11. Schematic representation of the process occurred upon direct phase transition from liquid to gas in the gel network

1.4.3.1. Polymer-assisted ambient gel drying

Modifying of the inner gel network surface with additional polymers can protect the aerogel walls from the capillary forces and minimize the shrinkage.[105] This method also can afford the aerogels with improved mechanical properties. However, the extra polymer can limit the accessibility of the surface of aerogel to the active media species from one side; and affect the conductivity of the produced material which can be not beneficial for some application.

1.4.3.2. Super-critical gel drying

To avoid the addition of extra reactants it has been developed another approach that based on the gel drying under solvent super-critical conditions. The main principle of the method is avoiding of the crossing liquid-gas phase during the extraction of the liquid inside of the pores.

As it is shown in the Fig. 12 to avoid direct liquid-gas transition the liquid inside of the gel pores has to be pressurized and heated above the solvent super-critical point. Depending on the solvent used there are two ways to perform super-critical drying process: high-temperature and low-temperature. In the first case liquid inside of the gel pores has to be replaced with an alcohol. In order to bring the chosen alcohol to the super-critical state, the high temperature and pressure needs to be applied which is one of the disadvantages of the method. The high temperatures can lead to undesirable reactions. Furthermore, the organic solvent can interact

with the gel surface. Moreover, in case of using this method for metal oxide based aerogel, the alcohol can act as a reducing agents leading to reduction of the metal oxide to metal.

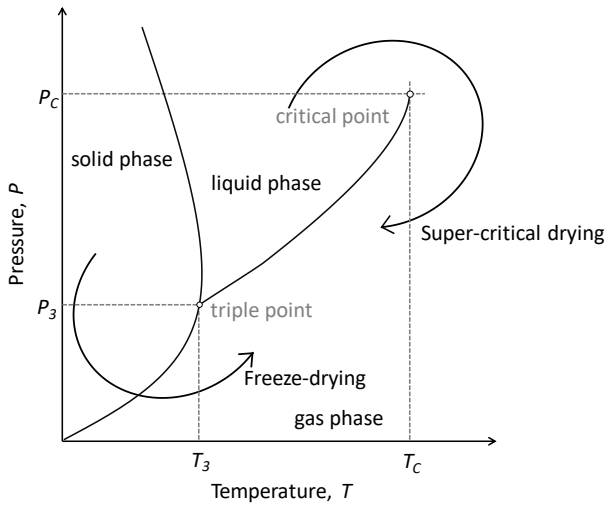

Fig. 12. CO_2 phase diagram represents the CO_2 behavior depending on the temperature and pressure. Drying under ambient condition occurred through the direct transition from liquid to gas phase. Super-critical drying takes place when the direct transition from liquid to gas overcome by increasing of the pressure and temperature until super-critical point reached. Oppositely, freeze-drying performed via sublimation while decreasing of the pressure and temperature via sublimation.

The low-temperature drying process is based on using of liquid CO_2 under super-critical condition achieved at pressure of 73 bars and temperature of 39 °C which is much lower than in the case of using alcohols. Furthermore, liquid CO_2 is inert and there is a low possibility to observe any unwanted reactions. However, it needs to be taken into account the miscibility of the chosen solvent with CO_2.[106-107]

1.4.3.3. Freeze-drying

Freeze-drying is another way to omit the direct phase transition from liquid to gas. The method is based on freezing of the gel solvent to convert it into solid, followed by the sublimation from solid to gaseous phase. In this case there is no need in high-pressure. However, high vacuum and low temperatures required for sublimation needs to be achieved.

1.5. References

1. Burda, C.; Chen, X.; Narayanan, R.; El-Sayed, M. A., Chemistry and Properties of Nanocrystals of Different Shapes. *Chemical Reviews* **2005,** *105* (4), 1025-1102.
2. Jun, Y.-w.; Choi, J.-s.; Cheon, J., Shape Control of Semiconductor and Metal Oxide Nanocrystals through Nonhydrolytic Colloidal Routes. *Angewandte Chemie International Edition* **2006,** *45* (21), 3414-3439.
3. Talapin, D. V.; Lee, J.-S.; Kovalenko, M. V.; Shevchenko, E. V., Prospects of Colloidal Nanocrystals for Electronic and Optoelectronic Applications. *Chemical Reviews* **2010,** *110* (1), 389-458.
4. Ribeiro, C.; Lee, E. J. H.; Longo, E.; Leite, E. R., Oriented Attachment Mechanism in Anisotropic Nanocrystals: A “Polymerization” Approach. *ChemPhysChem* **2006,** *7* (3), 664-670.
5. Zhang, J.; Huang, F.; Lin, Z., Progress of nanocrystalline growth kinetics based on oriented attachment. *Nanoscale* **2010,** *2* (1), 18-34.

6. Lim, B.; Lu, X.; Jiang, M.; Camargo, P. H. C.; Cho, E. C.; Lee, E. P.; Xia, Y., Facile Synthesis of Highly Faceted Multioctahedral Pt Nanocrystals through Controlled Overgrowth. *Nano Letters* **2008,** *8* (11), 4043-4047.
7. Manna, L.; Milliron, D. J.; Meisel, A.; Scher, E. C.; Alivisatos, A. P., Controlled growth of tetrapod-branched inorganic nanocrystals. *Nature Materials* **2003,** *2*, 382.
8. Weiner, R. G.; Skrabalak, S. E., Metal Dendrimers: Synthesis of Hierarchically Stellated Nanocrystals by Sequential Seed-Directed Overgrowth. *Angewandte Chemie* **2015,** *127* (4), 1197-1200.
9. Stearns, L. A.; Chhabra, R.; Sharma, J.; Liu, Y.; Petuskey, W. T.; Yan, H.; Chaput, J. C., Template-Directed Nucleation and Growth of Inorganic Nanoparticles on DNA Scaffolds. *Angewandte Chemie International Edition* **2009,** *48* (45), 8494-8496.
10. Ma, L.; Wang, C.; Gong, M.; Liao, L.; Long, R.; Wang, J.; Wu, D.; Zhong, W.; Kim, M. J.; Chen, Y.; Xie, Y.; Xiong, Y., Control Over the Branched Structures of Platinum Nanocrystals for Electrocatalytic Applications. *ACS Nano* **2012,** *6* (11), 9797-9806.
11. Tang, J.; Alivisatos, A. P., Crystal Splitting in the Growth of Bi2S3. *Nano Letters* **2006,** *6* (12), 2701-2706.
12. Jun, Y.-w.; Chung, H.-W.; Jang, J.-t.; Cheon, J., Multiple twinning drives nanoscale hyper-branching of titanium dioxide nanocrystals. *Journal of Materials Chemistry* **2011,** *21* (28), 10283-10286.
13. Fiore, A.; Mastria, R.; Lupo, M. G.; Lanzani, G.; Giannini, C.; Carlino, E.; Morello, G.; De Giorgi, M.; Li, Y.; Cingolani, R.; Manna, L., Tetrapod-Shaped Colloidal Nanocrystals of II–VI Semiconductors Prepared by Seeded Growth. *Journal of the American Chemical Society* **2009,** *131* (6), 2274-2282.
14. Cheong, S.; Watt, J.; Ingham, B.; Toney, M. F.; Tilley, R. D., In Situ and Ex Situ Studies of Platinum Nanocrystals: Growth and Evolution in Solution. *Journal of the American Chemical Society* **2009,** *131* (40), 14590-14595.
15. Zhao, R.; Fu, G.; Zhou, T.; Chen, Y.; Zhu, X.; Tang, Y.; Lu, T., Multi-generation overgrowth induced synthesis of three-dimensional highly branched palladium tetrapods and their electrocatalytic activity for formic acid oxidation. *Nanoscale* **2014,** *6* (5), 2776-2781.
16. Li, Y.; Luo, S.; Wei, Z.; Meng, D.; Ding, M.; Liu, C., Electrodeposition technique-dependent photoelectrochemical and photocatalytic properties of an In 2 S 3/TiO 2 nanotube array. *Physical Chemistry Chemical Physics* **2014,** *16* (9), 4361-4368.
17. Raju, M.; van Duin, A. C. T.; Fichthorn, K. A., Mechanisms of Oriented Attachment of TiO2 Nanocrystals in Vacuum and Humid Environments: Reactive Molecular Dynamics. *Nano Letters* **2014,** *14* (4), 1836-1842.
18. Boneschanscher, M. P.; Evers, W. H.; Geuchies, J. J.; Altantzis, T.; Goris, B.; Rabouw, F. T.; van Rossum, S. A. P.; van der Zant, H. S. J.; Siebbeles, L. D. A.; Van Tendeloo, G.; Swart, I.; Hilhorst, J.; Petukhov, A. V.; Bals, S.; Vanmaekelbergh, D., Long-range orientation and atomic attachment of nanocrystals in 2D honeycomb superlattices. *Science* **2014,** *344* (6190), 1377-1380.
19. Sans, V.; Glatzel, S.; Douglas, F. J.; Maclaren, D. A.; Lapkin, A.; Cronin, L., Non-equilibrium dynamic control of gold nanoparticle and hyper-branched nanogold assemblies. *Chemical Science* **2014,** *5* (3), 1153-1157.
20. Rioux, R. M.; Song, H.; Grass, M.; Habas, S.; Niesz, K.; Hoefelmeyer, J. D.; Yang, P.; Somorjai, G. A., Monodisperse platinum nanoparticles of well-defined shape: synthesis, characterization, catalytic properties and future prospects. *Topics in Catalysis* **2006,** *39* (3), 167-174.
21. Liu, Z.; Shamsuzzoha, M.; Ada, E. T.; Reichert, W. M.; Nikles, D. E., Synthesis and activation of Pt nanoparticles with controlled size for fuel cell electrocatalysts. *Journal of Power Sources* **2007,** *164* (2), 472-480.

22. Mazumder, V.; Sun, S., Oleylamine-Mediated Synthesis of Pd Nanoparticles for Catalytic Formic Acid Oxidation. *Journal of the American Chemical Society* **2009,** *131* (13), 4588-4589.
23. Cheng, W.; Dong, S.; Wang, E., Iodine-Induced Gold-Nanoparticle Fusion/Fragmentation/Aggregation and Iodine-Linked Nanostructured Assemblies on a Glass Substrate. *Angewandte Chemie International Edition* **2003,** *42* (4), 449-452.
24. Figuerola, A.; Franchini, I. R.; Fiore, A.; Mastria, R.; Falqui, A.; Bertoni, G.; Bals, S.; Van Tendeloo, G.; Kudera, S.; Cingolani, R., End-to-End Assembly of Shape-Controlled Nanocrystals via a Nanowelding Approach Mediated by Gold Domains. *Advanced Materials* **2009,** *21* (5), 550-554.
25. Templeton, A. C.; Wuelfing, W. P.; Murray, R. W., Monolayer-Protected Cluster Molecules. *Accounts of Chemical Research* **2000,** *33* (1), 27-36.
26. Bagaria, H. G.; Ada, E. T.; Shamsuzzoha, M.; Nikles, D. E.; Johnson, D. T., Understanding Mercapto Ligand Exchange on the Surface of FePt Nanoparticles. *Langmuir* **2006,** *22* (18), 7732-7737.
27. Simon, T.; Bouchonville, N.; Berr, M. J.; Vaneski, A.; Adrović, A.; Volbers, D.; Wyrwich, R.; Döblinger, M.; Susha, A. S.; Rogach, A. L.; Jäckel, F.; Stolarczyk, J. K.; Feldmann, J., Redox shuttle mechanism enhances photocatalytic H2 generation on Ni-decorated CdS nanorods. *Nature Materials* **2014,** *13*, 1013.
28. De Roo, J.; Van Driessche, I.; Martins, J. C.; Hens, Z., Colloidal metal oxide nanocrystal catalysis by sustained chemically driven ligand displacement. *Nature Materials* **2016,** *15*, 517.
29. Gaponik, N.; Talapin, D. V.; Rogach, A. L.; Hoppe, K.; Shevchenko, E. V.; Kornowski, A.; Eychmüller, A.; Weller, H., Thiol-Capping of CdTe Nanocrystals: An Alternative to Organometallic Synthetic Routes. *The Journal of Physical Chemistry B* **2002,** *106* (29), 7177-7185.
30. Kovalenko, M. V.; Scheele, M.; Talapin, D. V., Colloidal Nanocrystals with Molecular Metal Chalcogenide Surface Ligands. *Science* **2009,** *324* (5933), 1417-1420.
31. Storck, S.; Bretinger, H.; Maier, W. F., Characterization of micro- and mesoporous solids by physisorption methods and pore-size analysis. *Applied Catalysis A: General* **1998,** *174* (1), 137-146.
32. Wu, B.; Zheng, N., Surface and interface control of noble metal nanocrystals for catalytic and electrocatalytic applications. *Nano Today* **2013,** *8* (2), 168-197.
33. Adebajo, M. O.; Frost, R. L.; Kloprogge, J. T.; Carmody, O.; Kokot, S., Porous Materials for Oil Spill Cleanup: A Review of Synthesis and Absorbing Properties. *Journal of Porous Materials* **2003,** *10* (3), 159-170.
34. Wales, D. J.; Grand, J.; Ting, V. P.; Burke, R. D.; Edler, K. J.; Bowen, C. R.; Mintova, S.; Burrows, A. D., Gas sensing using porous materials for automotive applications. *Chemical Society Reviews* **2015,** *44* (13), 4290-4321.
35. Hüsing, N.; Schubert, U., Aerogels—Airy Materials: Chemistry, Structure, and Properties. *Angewandte Chemie International Edition* **1998,** *37* (1-2), 22-45.
36. Korala, L.; Wang, Z.; Liu, Y.; Maldonado, S.; Brock, S. L., Uniform Thin Films of CdSe and CdSe(ZnS) Core(Shell) Quantum Dots by Sol–Gel Assembly: Enabling Photoelectrochemical Characterization and Electronic Applications. *ACS Nano* **2013,** *7* (2), 1215-1223.
37. Korala, L.; Li, L.; Brock, S. L., Transparent conducting films of CdSe(ZnS) core(shell) quantum dot xerogels. *Chemical Communications* **2012,** *48* (68), 8523-8525.
38. Pala, I. R.; Brock, S. L., ZnS Nanoparticle Gels for Remediation of Pb2+ and Hg2+ Polluted Water. *ACS Applied Materials & Interfaces* **2012,** *4* (4), 2160-2167.
39. Korala, L.; Germain, J. R.; Chen, E.; Pala, I. R.; Li, D.; Brock, S. L., CdS aerogels as efficient photocatalysts for degradation of organic dyes under visible light irradiation. *Inorganic Chemistry Frontiers* **2017,** *4* (9), 1451-1457.

40. Ganguly, S.; Brock, S. L., Toward nanostructured thermoelectrics: synthesis and characterization of lead telluride gels and aerogels. *Journal of Materials Chemistry* **2011,** *21* (24), 8800-8806.
41. Ganguly, S.; Zhou, C.; Morelli, D.; Sakamoto, J.; Brock, S. L., Synthesis and Characterization of Telluride Aerogels: Effect of Gelation on Thermoelectric Performance of Bi2Te3 and Bi2–xSbxTe3 Nanostructures. *The Journal of Physical Chemistry C* **2012,** *116* (33), 17431-17439.
42. Kistler, S. S., Method of producing aerogels. Google Patents: 1937.
43. Akimov, Y. K., Fields of Application of Aerogels (Review). *Instruments and Experimental Techniques* **2003,** *46* (3), 287-299.
44. Venkateswara Rao, A.; Parvathy Rao, A.; Kulkarni, M. M., Influence of gel aging and Na2SiO3/H2O molar ratio on monolithicity and physical properties of water–glass-based aerogels dried at atmospheric pressure. *Journal of Non-Crystalline Solids* **2004,** *350* (Supplement C), 224-229.
45. Suh, D. J.; Park, T.-J., Sol−Gel Strategies for Pore Size Control of High-Surface-Area Transition-Metal Oxide Aerogels. *Chemistry of Materials* **1996,** *8* (2), 509-513.
46. Suh, D. J.; Park, T.-J.; Han, H.-Y.; Lim, J.-C., Synthesis of High-Surface-Area Zirconia Aerogels with a Well-Developed Mesoporous Texture Using CO2 Supercritical Drying. *Chemistry of Materials* **2002,** *14* (4), 1452-1454.
47. Campbell, L. K.; Na, B. K.; Ko, E. I., Synthesis and characterization of titania aerogels. *Chemistry of Materials* **1992,** *4* (6), 1329-1333.
48. Ji, L.; Lin, J.; Tan, K. L.; Zeng, H. C., Synthesis of High-Surface-Area Alumina Using Aluminum Tri-sec-butoxide−2,4-Pentanedione− 2-Propanol−Nitric Acid Precursors. *Chemistry of Materials* **2000,** *12* (4), 931-939.
49. Schneider, M.; Baiker, A., High-surface-area titania aerogels: preparation and structural properties. *Journal of Materials Chemistry* **1992,** *2* (6), 587-589.
50. Abramian, L.; El-Rassy, H., Adsorption kinetics and thermodynamics of azo-dye Orange II onto highly porous titania aerogel. *Chemical Engineering Journal* **2009,** *150* (2), 403-410.
51. Tai, Y.; Murakami, J.; Tajiri, K.; Ohashi, F.; Daté, M.; Tsubota, S., Oxidation of carbon monoxide on Au nanoparticles in titania and titania-coated silica aerogels. *Applied Catalysis A: General* **2004,** *268* (1), 183-187.
52. Qiu, B.; Xing, M.; Zhang, J., Mesoporous TiO2 Nanocrystals Grown in Situ on Graphene Aerogels for High Photocatalysis and Lithium-Ion Batteries. *Journal of the American Chemical Society* **2014,** *136* (16), 5852-5855.
53. Hamann, T. W.; Martinson, A. B. F.; Elam, J. W.; Pellin, M. J.; Hupp, J. T., Atomic Layer Deposition of TiO2 on Aerogel Templates: New Photoanodes for Dye-Sensitized Solar Cells. *The Journal of Physical Chemistry C* **2008,** *112* (27), 10303-10307.
54. Li, H.; He, P.; Wang, Y.; Hosono, E.; Zhou, H., High-surface vanadium oxides with large capacities for lithium-ion batteries: from hydrated aerogel to nanocrystalline VO2(B), V6O13 and V2O5. *Journal of Materials Chemistry* **2011,** *21* (29), 10999-11009.
55. Sui, R.; Rizkalla, A. S.; Charpentier, P. A., Direct Synthesis of Zirconia Aerogel Nanoarchitecture in Supercritical CO2. *Langmuir* **2006,** *22* (9), 4390-4396.
56. Skapin, T., Influence of the organic phase on the properties of CrO3-derived chromia aerogels. *Journal of Non-Crystalline Solids* **2001,** *285* (1), 128-134.
57. Jeevanandam, P.; Klabunde, K. J., A Study on Adsorption of Surfactant Molecules on Magnesium Oxide Nanocrystals Prepared by an Aerogel Route. *Langmuir* **2002,** *18* (13), 5309-5313.
58. Bag, S.; Trikalitis, P. N.; Chupas, P. J.; Armatas, G. S.; Kanatzidis, M. G., Porous Semiconducting Gels and Aerogels from Chalcogenide Clusters. *Science* **2007,** *317* (5837), 490-493.
59. Gesser, H. D.; Goswami, P. C., Aerogels and related porous materials. *Chemical Reviews* **1989,** *89* (4), 765-788.

60. Long, J. W.; Logan, M. S.; Rhodes, C. P.; Carpenter, E. E.; Stroud, R. M.; Rolison, D. R., Nanocrystalline Iron Oxide Aerogels as Mesoporous Magnetic Architectures. *Journal of the American Chemical Society* **2004,** *126* (51), 16879-16889.
61. Gash, A. E.; Tillotson, T. M.; Satcher, J. H.; Poco, J. F.; Hrubesh, L. W.; Simpson, R. L., Use of Epoxides in the Sol−Gel Synthesis of Porous Iron(III) Oxide Monoliths from Fe(III) Salts. *Chemistry of Materials* **2001,** *13* (3), 999-1007.
62. Meador, M. A. B.; Fabrizio, E. F.; Ilhan, F.; Dass, A.; Zhang, G.; Vassilaras, P.; Johnston, J. C.; Leventis, N., Cross-linking Amine-Modified Silica Aerogels with Epoxies: Mechanically Strong Lightweight Porous Materials. *Chemistry of Materials* **2005,** *17* (5), 1085-1098.
63. Wei, T.-Y.; Chen, C.-H.; Chien, H.-C.; Lu, S.-Y.; Hu, C.-C., A Cost-Effective Supercapacitor Material of Ultrahigh Specific Capacitances: Spinel Nickel Cobaltite Aerogels from an Epoxide-Driven Sol–Gel Process. *Advanced Materials* **2010,** *22* (3), 347-351.
64. Laberty-Robert, C.; Long, J. W.; Lucas, E. M.; Pettigrew, K. A.; Stroud, R. M.; Doescher, M. S.; Rolison, D. R., Sol−Gel-Derived Ceria Nanoarchitectures: Synthesis, Characterization, and Electrical Properties. *Chemistry of Materials* **2006,** *18* (1), 50-58.
65. Du, A.; Zhou, B.; Shen, J.; Xiao, S.; Zhang, Z.; Liu, C.; Zhang, M., Monolithic copper oxide aerogel via dispersed inorganic sol–gel method. *Journal of Non-Crystalline Solids* **2009,** *355* (3), 175-181.
66. Rolison, D. R., Catalytic Nanoarchitectures--the Importance of Nothing and the Unimportance of Periodicity. *Science* **2003,** *299* (5613), 1698-1701.
67. Morris, C. A.; Anderson, M. L.; Stroud, R. M.; Merzbacher, C. I.; Rolison, D. R., Silica Sol as a Nanoglue: Flexible Synthesis of Composite Aerogels. *Science* **1999,** *284* (5414), 622-624.
68. Tillotson, T. M.; Hrubesh, L. W., Transparent ultralow-density silica aerogels prepared by a two-step sol-gel process. *Journal of Non-Crystalline Solids* **1992,** *145* (Supplement C), 44-50.
69. Mohanan, J. L.; Arachchige, I. U.; Brock, S. L., Porous Semiconductor Chalcogenide Aerogels. *Science* **2005,** *307* (5708), 397-400.
70. Wuister, S. F.; de Mello Donegá, C.; Meijerink, A., Influence of Thiol Capping on the Exciton Luminescence and Decay Kinetics of CdTe and CdSe Quantum Dots. *The Journal of Physical Chemistry B* **2004,** *108* (45), 17393-17397.
71. Aldana, J.; Wang, Y. A.; Peng, X., Photochemical Instability of CdSe Nanocrystals Coated by Hydrophilic Thiols. *Journal of the American Chemical Society* **2001,** *123* (36), 8844-8850.
72. Muthuswamy, E.; Brock, S. L., Oxidation Does Not (Always) Kill Reactivity of Transition Metals: Solution-Phase Conversion of Nanoscale Transition Metal Oxides to Phosphides and Sulfides. *Journal of the American Chemical Society* **2010,** *132* (45), 15849-15851.
73. Evans, B. J.; Doi, J. T.; Musker, W. K., Fluorine-19 NMR study of the reaction of p-fluorobenzenethiol and disulfide with periodate and other selected oxidizing agents. *The Journal of Organic Chemistry* **1990,** *55* (8), 2337-2344.
74. Pala, I. R.; Arachchige, I. U.; Georgiev, D. G.; Brock, S. L., Reversible Gelation of II–VI Nanocrystals: The Nature of Interparticle Bonding and the Origin of Nanocrystal Photochemical Instability. *Angewandte Chemie International Edition* **2010,** *49* (21), 3661-3665.
75. Pawsey, S.; Kalebaila, K. K.; Moudrakovski, I.; Ripmeester, J. A.; Brock, S. L., Pore Structure and Interconnectivity of CdS Aerogels and Xerogels by Hyperpolarized Xenon NMR. *The Journal of Physical Chemistry C* **2010,** *114* (31), 13187-13195.
76. De Freitas, J. N.; Korala, L.; Reynolds, L. X.; Haque, S. A.; Brock, S. L.; Nogueira, A. F., Connecting the (quantum) dots: towards hybrid photovoltaic devices based on chalcogenide gels. *Physical Chemistry Chemical Physics* **2012,** *14* (43), 15180-15184.
77. Brock, S. L.; Arachchige, I. U.; Kalebaila, K. K., METAL CHALCOGENIDE GELS, XEROGELS AND AEROGELS. *Comments on Inorganic Chemistry* **2006,** *27* (5-6), 103-126.
78. Kalebaila, K. K.; Brock, S. L., Lead Selenide Nanostructured Aerogels and Xerogels. *Zeitschrift für anorganische und allgemeine Chemie* **2012,** *638* (15), 2598-2603.

79. Hitihami-Mudiyanselage, A.; Senevirathne, K.; Brock, S. L., Bottom-Up Assembly of Ni2P Nanoparticles into Three-Dimensional Architectures: An Alternative Mechanism for Phosphide Gelation. *Chemistry of Materials* **2014,** *26* (21), 6251-6256.
80. Hitihami-Mudiyanselage, A.; Senevirathne, K.; Brock, S. L., Assembly of Phosphide Nanocrystals into Porous Networks: Formation of InP Gels and Aerogels. *ACS Nano* **2013,** *7* (2), 1163-1170.
81. Yu, H.; Brock, S. L., Effects of Nanoparticle Shape on the Morphology and Properties of Porous CdSe Assemblies (Aerogels). *ACS Nano* **2008,** *2* (8), 1563-1570.
82. Rechberger, F.; Heiligtag, F. J.; Süess, M. J.; Niederberger, M., Assembly of BaTiO3 Nanocrystals into Macroscopic Aerogel Monoliths with High Surface Area. *Angewandte Chemie International Edition* **2014,** *53* (26), 6823-6826.
83. Liu, W.; Herrmann, A.-K.; Bigall, N. C.; Rodriguez, P.; Wen, D.; Oezaslan, M.; Schmidt, T. J.; Gaponik, N.; Eychmüller, A., Noble Metal Aerogels—Synthesis, Characterization, and Application as Electrocatalysts. *Accounts of Chemical Research* **2015,** *48* (2), 154-162.
84. Cheng, W.; Rechberger, F.; Niederberger, M., Three-Dimensional Assembly of Yttrium Oxide Nanosheets into Luminescent Aerogel Monoliths with Outstanding Adsorption Properties. *ACS Nano* **2016,** *10* (2), 2467-2475.
85. Singh, A.; Lindquist, B. A.; Ong, G. K.; Jadrich, R. B.; Singh, A.; Ha, H.; Ellison, C. J.; Truskett, T. M.; Milliron, D. J., Linking Semiconductor Nanocrystals into Gel Networks through All-Inorganic Bridges. *Angewandte Chemie International Edition* **2015,** *54* (49), 14840-14844.
86. Voitekhovich, S. V.; Lesnyak, V.; Gaponik, N.; Eychmüller, A., Tetrazoles: Unique Capping Ligands and Precursors for Nanostructured Materials. *Small* **2015,** *11* (43), 5728-5739.
87. Wolf, A.; Lesnyak, V.; Gaponik, N.; Eychmüller, A., Quantum-Dot-Based (Aero)gels: Control of the Optical Properties. *The Journal of Physical Chemistry Letters* **2012,** *3* (16), 2188-2193.
88. Sayevich, V.; Cai, B.; Benad, A.; Haubold, D.; Sonntag, L.; Gaponik, N.; Lesnyak, V.; Eychmüller, A., 3D Assembly of All-Inorganic Colloidal Nanocrystals into Gels and Aerogels. *Angewandte Chemie International Edition* **2016,** *55* (21), 6334-6338.
89. Freytag, A.; Sánchez-Paradinas, S.; Naskar, S.; Wendt, N.; Colombo, M.; Pugliese, G.; Poppe, J.; Demirci, C.; Kretschmer, I.; Bahnemann, D. W.; Behrens, P.; Bigall, N. C., Versatile Aerogel Fabrication by Freezing and Subsequent Freeze-Drying of Colloidal Nanoparticle Solutions. *Angewandte Chemie International Edition* **2016,** *55* (3), 1200-1203.
90. Jung, S. M.; Preston, D. J.; Jung, H. Y.; Deng, Z.; Wang, E. N.; Kong, J., Porous Cu Nanowire Aerosponges from One-Step Assembly and their Applications in Heat Dissipation. *Advanced Materials* **2016,** *28* (7), 1413-1419.
91. Gao, H.-L.; Xu, L.; Long, F.; Pan, Z.; Du, Y.-X.; Lu, Y.; Ge, J.; Yu, S.-H., Macroscopic Free-Standing Hierarchical 3D Architectures Assembled from Silver Nanowires by Ice Templating. *Angewandte Chemie International Edition* **2014,** *53* (18), 4561-4566.
92. Chen, S.; Liu, G.; Yadegari, H.; Wang, H.; Qiao, S. Z., Three-dimensional MnO2 ultrathin nanosheet aerogels for high-performance Li-O2 batteries. *Journal of Materials Chemistry A* **2015,** *3* (6), 2559-2563.
93. Liu, Z.; Xu, K.; She, P.; Yin, S.; Zhu, X.; Sun, H., Self-assembly of 2D MnO2 nanosheets into high-purity aerogels with ultralow density. *Chemical Science* **2016,** *7* (3), 1926-1932.
94. Arachchige, I. U.; Brock, S. L., Sol−Gel Assembly of CdSe Nanoparticles to Form Porous Aerogel Networks. *Journal of the American Chemical Society* **2006,** *128* (24), 7964-7971.
95. Hendel, T.; Lesnyak, V.; Kühn, L.; Herrmann, A.-K.; Bigall, N. C.; Borchardt, L.; Kaskel, S.; Gaponik, N.; Eychmüller, A., Mixed Aerogels from Au and CdTe Nanoparticles. *Advanced Functional Materials* **2013,** *23* (15), 1903-1911.
96. Bigall, N. C.; Herrmann, A.-K.; Vogel, M.; Rose, M.; Simon, P.; Carrillo-Cabrera, W.; Dorfs, D.; Kaskel, S.; Gaponik, N.; Eychmüller, A., Hydrogels and Aerogels from Noble Metal Nanoparticles. *Angewandte Chemie International Edition* **2009,** *48* (51), 9731-9734.

97. Ziegler, C.; Klosz, S.; Borchardt, L.; Oschatz, M.; Kaskel, S.; Friedrich, M.; Kriegel, R.; Keilhauer, T.; Armbrüster, M.; Eychmüller, A., ZnPd/ZnO Aerogels as Potential Catalytic Materials. *Advanced Functional Materials* **2016,** *26* (7), 1014-1020.
98. Heiligtag, F. J.; Rossell, M. D.; Suess, M. J.; Niederberger, M., Template-free co-assembly of preformed Au and TiO2 nanoparticles into multicomponent 3D aerogels. *Journal of Materials Chemistry* **2011,** *21* (42), 16893-16899.
99. Heiligtag, F. J.; Cheng, W.; de Mendonça, V. R.; Süess, M. J.; Hametner, K.; Günther, D.; Ribeiro, C.; Niederberger, M., Self-Assembly of Metal and Metal Oxide Nanoparticles and Nanowires into a Macroscopic Ternary Aerogel Monolith with Tailored Photocatalytic Properties. *Chemistry of Materials* **2014,** *26* (19), 5576-5584.
100. Heiligtag, F. J.; Kränzlin, N.; Süess, M. J.; Niederberger, M., Anatase–silica composite aerogels: a nanoparticle-based approach. *Journal of Sol-Gel Science and Technology* **2014,** *70* (2), 300-306.
101. Rechberger, F.; Ilari, G.; Niederberger, M., Assembly of antimony doped tin oxide nanocrystals into conducting macroscopic aerogel monoliths. *Chemical Communications* **2014,** *50* (86), 13138-13141.
102. Lesnyak, V.; Voitekhovich, S. V.; Gaponik, P. N.; Gaponik, N.; Eychmüller, A., CdTe Nanocrystals Capped with a Tetrazolyl Analogue of Thioglycolic Acid: Aqueous Synthesis, Characterization, and Metal-Assisted Assembly. *ACS Nano* **2010,** *4* (7), 4090-4096.
103. Lesnyak, V.; Wolf, A.; Dubavik, A.; Borchardt, L.; Voitekhovich, S. V.; Gaponik, N.; Kaskel, S.; Eychmüller, A., 3D Assembly of Semiconductor and Metal Nanocrystals: Hybrid CdTe/Au Structures with Controlled Content. *Journal of the American Chemical Society* **2011,** *133* (34), 13413-13420.
104. Bag, S.; Gaudette, A. F.; Bussell, M. E.; Kanatzidis, M. G., Spongy chalcogels of non-platinum metals act as effective hydrodesulfurization catalysts. *Nature Chemistry* **2009,** *1*, 217.
105. Tewari, P. H.; Hunt, A. J.; Lofftus, K. D., Ambient-temperature supercritical drying of transparent silica aerogels. *Materials Letters* **1985,** *3* (9), 363-367.
106. Day, C.-Y.; Chang, C. J.; Chen, C.-Y., Phase Equilibrium of Ethanol + CO2 and Acetone + CO2 at Elevated Pressures. *Journal of Chemical & Engineering Data* **1996,** *41* (4), 839-843.
107. Jennings, D. W.; Lee, R. J.; Teja, A. S., Vapor-liquid equilibria in the carbon dioxide + ethanol and carbon dioxide + 1-butanol systems. *Journal of Chemical & Engineering Data* **1991,** *36* (3), 303-307.

2. Synthesis of metal oxide NCs: tuning branching in ceria NCs

Abstract

Branched NCs are a particularly interesting type of material due to their high atomic surface exposure within a crystalline interconnected network providing optimized transport properties. In this chapter we investigate the colloidal synthesis of branched ceria NCs by means of a kinetically controlled overgrowth mechanism tuned by the use of ligands/reactants that display preferential adsorption/reaction on particular crystallographic facets. In particular, oleic acid promotes a preferential growth in the [111] direction, which results in the formation of ceria octapods. Alkanediols further promote the asymmetric growth through a faster alcoholysis, increasing the branch aspect ratio. The higher reaction rates also result in the formation of side branches, probably triggered by defect formation. Excess amounts of an alkanediol such as 1,2-hexadecanediol (1,2-HDDOL) results in dendritic growth and the formation of cubic hyper-branched structures. The addition of water results in a significant reduction of the growth rate, decreasing the reaction yield and eliminating side branching, which we associate to a reversible hydrolysis reaction. Overall, adjusting the amounts of each ligand, well-defined branched ceria NCs with tuned number, thickness and length of the branches and with overall size ranging from 7 to 45 nm are produced. We further demonstrate such branched ceria NCs to provide higher surface areas and related oxygen storage capacities (OSC) than quasi-spherical NCs.

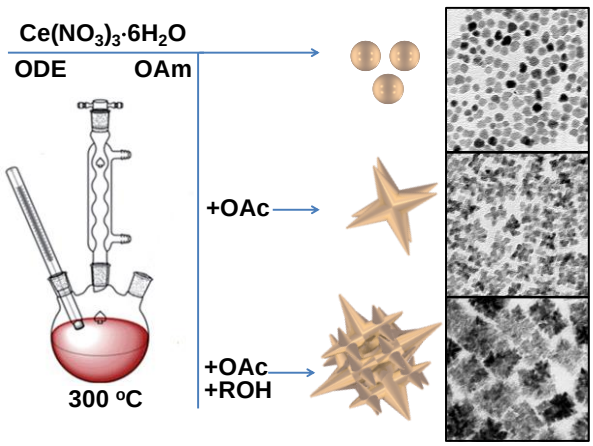

2.1. Introduction

Branching enables to significantly increase the surface-to-volume ratio of NCs.[1,2] At the same time, compared with NCs having spherical or regular polyhedral geometries, the use of branched NCs as building blocks to produce macroscopic nanomaterials improves transport properties and provides higher levels of porosity by preventing close-packed aggregation.[1,3,4] Branching therefore allows a higher extent of interaction with the media while simultaneously facilitating charge carrier injection and extraction, characteristics that are particularly valuable in the fields of catalysis, sensing and in some biomedical applications. Besides, branched nanostructures may show additional advantages such as higher magnetic anisotropy in magnetic NCs[5,6] and improved surface enhanced Raman spectroscopy enhancement factors in plasmonic NCs.[7] Branched NCs are also easier to manipulate, purify or recuperate than unbranched NCs with equivalent surface areas.

Branching is especially interesting in the field of catalysis, where it provides higher atomic surface exposure, potentially favourable facets and very large densities of edges and corners with highly reactive sites.[8-10] A particularly interesting material in this field is ceria, which is one of the most technologically important rare earth oxides, being widely used in three way catalysts, gas sensors and solid oxide fuel cells. Ceria is also used in biomedical applications to protect cells from radiation damages and oxidative stress.[11-13] As a result of its multi-valence and the highly positive Ce^{4+}/Ce^{3+} reduction potential, ceria contains a mixture of Ce^{3+} and Ce^{4+} oxidation states which confers outstanding capabilities to store, release and transport oxygen and oxygen vacancies, especially when nanostruc-tured.[12-14] In all applications that involve interaction with the media, ceria performance does not only depend on the crystal domain size but also on the facets exposed to the environ-ment.[15-17] For instance, it has been established that (100) and (110) facets have lower activation energy for the formation of oxygen vacancies than (111) facets.[18] This translates into higher catalytic activities for a set of oxidation reactions of nanorods displaying (100) and (110) when compared with polyhedral NCs with (111) facets.[19-24] Several protocols to produce ceria NCs with controlled morphologies, including nano-spheres, -cubes, -rods, -plates, -wires, sheets, tadpole, octahedral, and stars, are already available.[25-30] However, a strategy or mechanism to control branching in such a technologically important material is yet to be reported.

Branching can be induced by several mechanisms, including template-directed growth, selective etching, twinning, crystal splitting, polymorphic or heterogeneous seeded growth, ligand-mediated overgrowth and NC aggregation-based growth.[1,2,31-33] Among them, the overgrowth mechanism is the most versatile and simplest strategy to produce branched nanostructures as demonstrated for a number of systems.[1,9,34-35] Overgrowth mechanisms are generally considered as kinetically controlled. Thus, reactants and reaction conditions are selected so that ions add to the NC much faster than they can diffuse through the surface. In these conditions, the NC geometry is determined by the growth rate in each crystallographic direction, which depends on the accessibility and reactivity of each facet. These parameters, and thus the NC geometry, can be manipulated through the use of facet-selective surface ligands. Being the surface energy dependent not only on the intrinsic properties of the material, but also on the surface ligands, surfactants that display preferential adsorption on particular facets can be used to adjust the surface energy of each facet, controlling in this way

the overgrowth direction and thus the final NC geometry. This is the most versatile and simplest strategy to produce branched nanostructures as already demonstrated for a number of systems.

This chapter represents the strategy to produce ceria NCs with tuned branching by means of a kinetically controlled ligand-mediated overgrowth strategy. By carefully adjusting the synthetic parameters and particularly the amount and type of ligands, branched NCs with different arm thickness and hyper-branched structures originated from side-branching can be produced. While oleic acid induces the branching of the symmetric structures (octapods), small amounts of alkanediols provide higher asymmetric structures with more complex morphologies. We also measure the surface area and oxygen storage capacity of the ceria NCs with different geometries.

2.2. Experimental

Fig. 1 shows the schematic drawing of the syntheses procedures for producing CeO_2 NCs with quasi-spherical, octapod-like and hyper-branched morphology. The details of the syntheses are described in the sections 2.2.1-2.2.3.

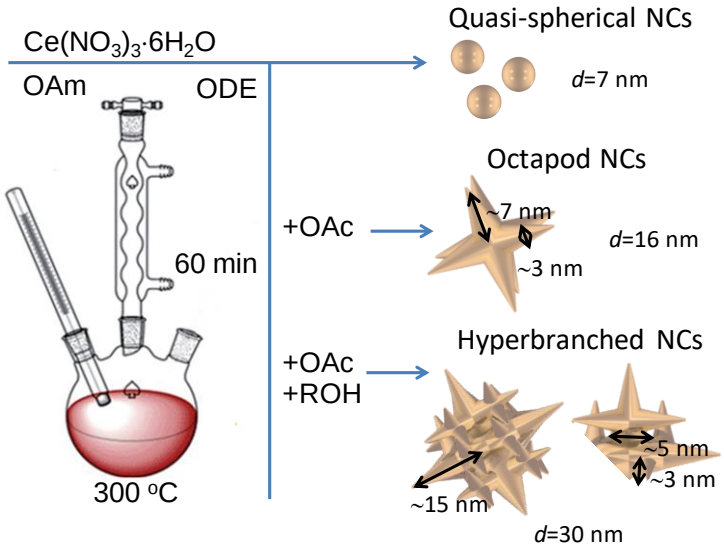

Fig. 1. Scheme of the synthesis procedures of ceria NCs with different shapes and sizes. The average dimensions of the branches were estimated from TEM images.

2.2.1. CeO_2 quasi-spherical NCs

0.434 g (1 mmol) of cerium (III) nitrate hexahydrate with 2 mL (6 mmol) of OAm were dissolved in 4 mL of ODE and kept under vacuum while stirring for 30 min at 80 °C until a light-brownish solution was formed (Fig. 2). The resulting solution was heated up to 300 °C (15 °C/min) under an Argon flow. After reaching 200 °C, the initial colour of the solution gradually changed from light-brownish to dark brown, suggesting the NCs formation. After 60 min of reaction, the solution was cooled down and 2 mL of toluene was injected at a temperature just below 160 °C. The NCs were precipitated by adding 25 mL of acetone and centrifuging the solution at 6500 rpm for 6 minutes. The supernatant was then discarded and the black precipitate was

dispersed in 5 mL of chloroform. This procedure was repeated at least four times to remove excess of surfactants. After 5 min of reaction, we observed the formation of quasi-spherical NCs with an average size of 4 nm. The average size increased to 6 nm and 7 nm when the reaction time was increased to 30 and 60 min, respectively. Relatively low yields were obtained after 5 and 15 min of reaction. 90 % material yields required longer reaction times of 60 min. The same trend, material yields increasing with the reaction time up to 60 min, was observed for branched ceria NCs.

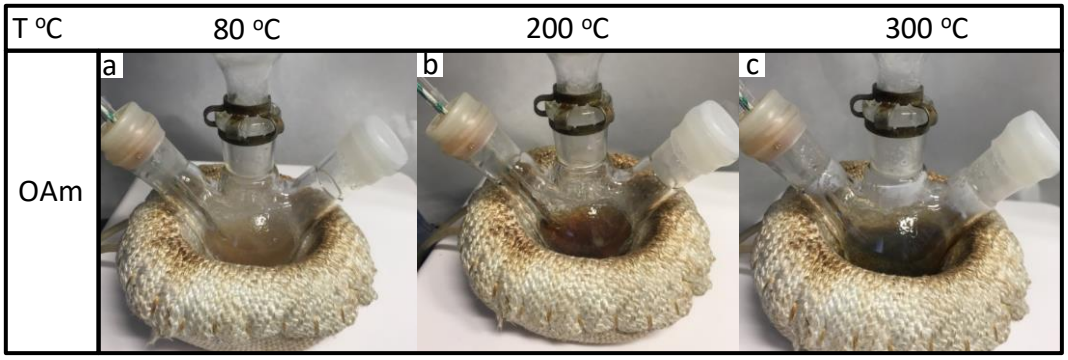

Fig. 2. Photographs showing colour change during the synthesis of quasi-spherical NCs while reaction temperature increases: a) 80 °C; b) 200 °C; c) 300 °C.

2.2.2. CeO_2 octapods

The synthesis protocol to produce CeO_2 NCs with octapod morphology was the same as for quasi-spherical NCs but adding 2 mL (6 mmol) of OAc to the initial mixture. The resulting solution was heated following the same procedure above reported. Note that when the reaction temperature reached 200 °C the solution colour already turned from light yellow to light brown (Fig. 3) and latter to dark brown when the temperature reached 250 °C. After cooling down and injecting 2 mL of toluene, the crude solution was cleaned following the same procedure above reported.

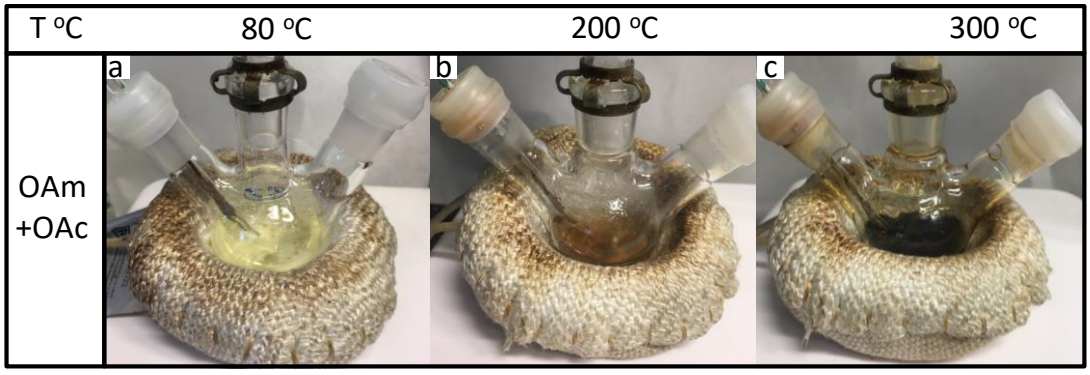

Fig. 3. Photographs showing colour change during the synthesis of octapod NCs while reaction temperature increases: a) 80 °C; b) 200 °C; c) 300 °C

2.2.3. CeO_2 hyperbranched NCs

Hyperbranched ceria NCs were obtained following the above procedure (including OAc) but adding alcohols (e.g. 1,2-HDDOL, 1,12-DDDOL, 1,2-DDOL, 1-DDOL) to the initial solution. In a

typical synthesis of hyperbranched ceria NCs, 1 mmol of cerium (III) nitrate hexahydrate, 2.5 mmol of alcohol molecule (1,2-HDDOL, 1,12- DDDOL, 1,2-DDOL or 1-DDOL), 2 mL of OAc, 2 mL of OAm and 4 mL of ODE were dissolved in a 25 mL three neck flask under magnetic stirring. In all cases a blurry white mixture was formed (Fig. 4**Fig.**). This solution was degassed under vacuum for 30 minutes at 80 °C to form a clear yellow solution. Then the temperature was raised up to 300 °C at a heating rate of 15 °C/min under an Argon flow. During the reaction the solution became turbid and small explosions started above 250 °C. The solution color changed to dark brown at this temperature evidencing the formation of NCs. After 60 minutes, the heating mantle was removed and the solution was allowed to cool down. At a temperature just below 160 °C, 2 mL of toluene were injected into the crude solution. The cleaning procedures were the same as for quasi-spherical NCs. The final precipitate was dispersed in 5 mL of chloroform. Note that the syntheses using 1,2-DDOL or 1-DDOL should be handle with especial safety measures to avoid the overpressure caused by decomposition of the reactants at the temperatures above 250 °C.

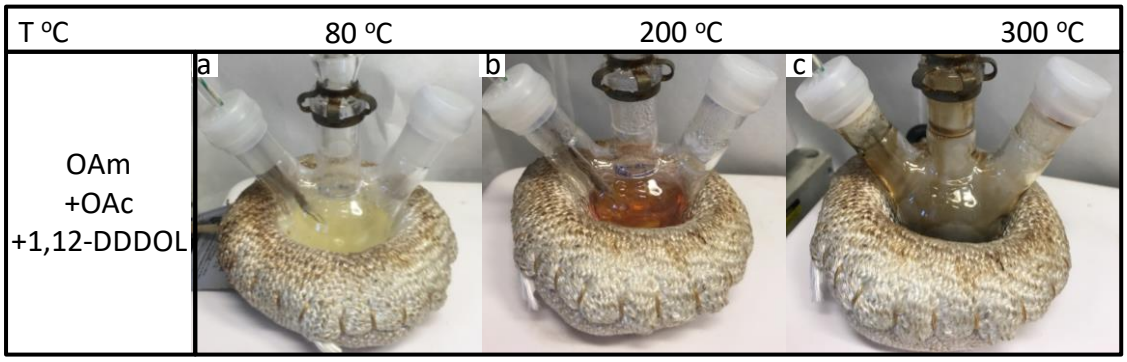

Fig. 4. Photographs showing colour change during the synthesis of hyperbranched NCs while reaction temperature increases: a) 80 °C; b) 200 °C; c) 300 °C

2.3. Results and discussion

CeO_2 NCs were produced by the decomposition of cerium nitrate in the presence of OAm at temperatures up to 300 °C (see experimental section 2.2.). Upon addition of the cerium salt to the ODE solution containing OAm and heating to 80 °C, a cerium-OAm complex was formed.[36] This complex started to decompose at around 200 °C to produce quasi-spherical CeO_2 NCs with sizes 7 nm and a ca. 90% material yield (Fig. 5). Note that in pure ODE, without OAm, cerium nitrate could not be dissolved and when attempting to react it at high temperature (300 °C), no CeO_2 NCs could be recovered.

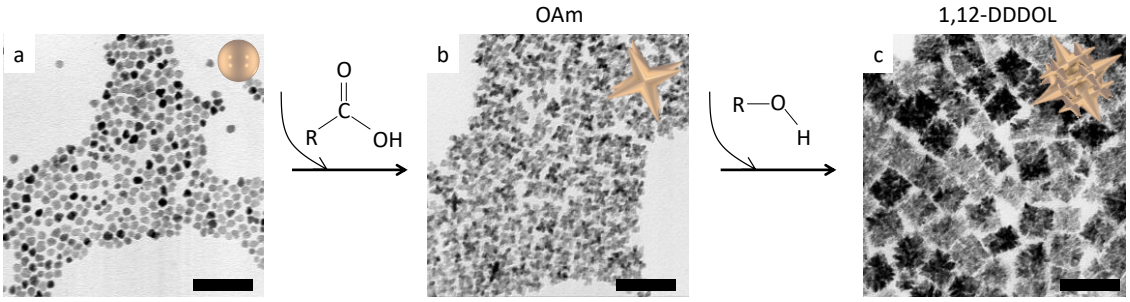

Fig. 5. Representative TEM micrograph of ceria NCs obtained in the presence of different ligands: a) Quasi-spherical NCs obtained in the presence of OAm; b) branched ceria NCs produced with the additional incorporation of OAc; c) side-branched ceria NCs obtained in the presence of alcohol molecule (1,12-Dodecanediol: 1,12-DDDOL). Scale bar of TEM images = 50 nm.

In the presence of OAc, cerium nitrate was soluble at moderate temperatures (100 °C), probably forming cerium oleate.[37] However, in the sole presence OAc (without OAm) no CeO_2 NCs were produced, probably due to the stability of the cerium oleate complex and the chemical dissolution of ceria by OAc. The incorporation of equivalent amounts of OAc and OAm prevented NC dissolution and resulted in the growth of ceria NCs with branched geometries (Fig. 5 b) and NCs size of 16 nm (Fig. 6). As calculated from the size of the obtained NCs and the total mass of material recovered, in the presence of OAc, a 3-fold decrease of the number of NCs and a 2-fold reduction of the final material yield of the reaction were obtained when compared with the growth in only OAm. Furthermore, addition of the alcohol molecule to along with OAc to the standard synthesis procedure resulted in formation of hyperbranched NCs with sizes in the range from 25 to 50 nm, depending on the alcohol molecule used (1,12-Dodecanediol, 1,2-Dodecanediol, or 1,12-Hexadecanediol).

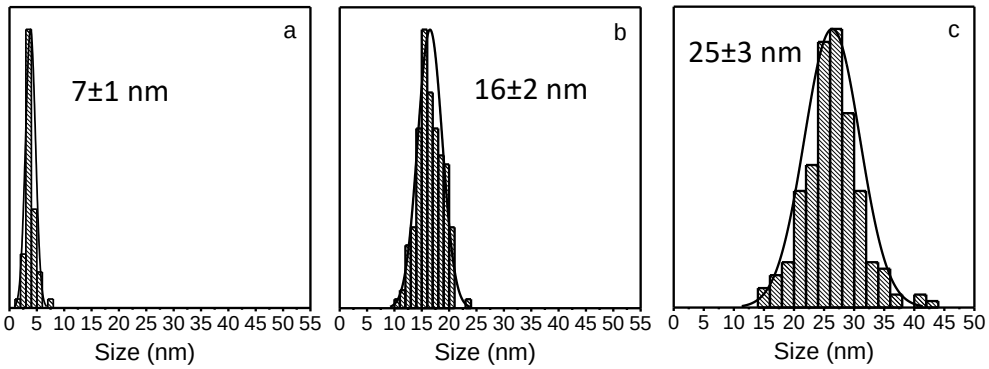

Fig. 6. Size distribution histograms obtained from the TEM images presented in **Fig.** 5: a) CeO_2 NCs with quasi-spherical shape and an average size of 7±1 nm. b) octapods with average sizes 16±2 nm. c) hyperbranched NCs with average sizes 25±3 nm.

HRTEM and electron diffraction analysis showed all branched NCs to be single crystal and branches to grow along the [111] crystallographic directions (Fig. 7 b, c). In contrast, aggregates of quasi-spherical NCs provided polycrystalline SAED pattern (Fig. 7 a)

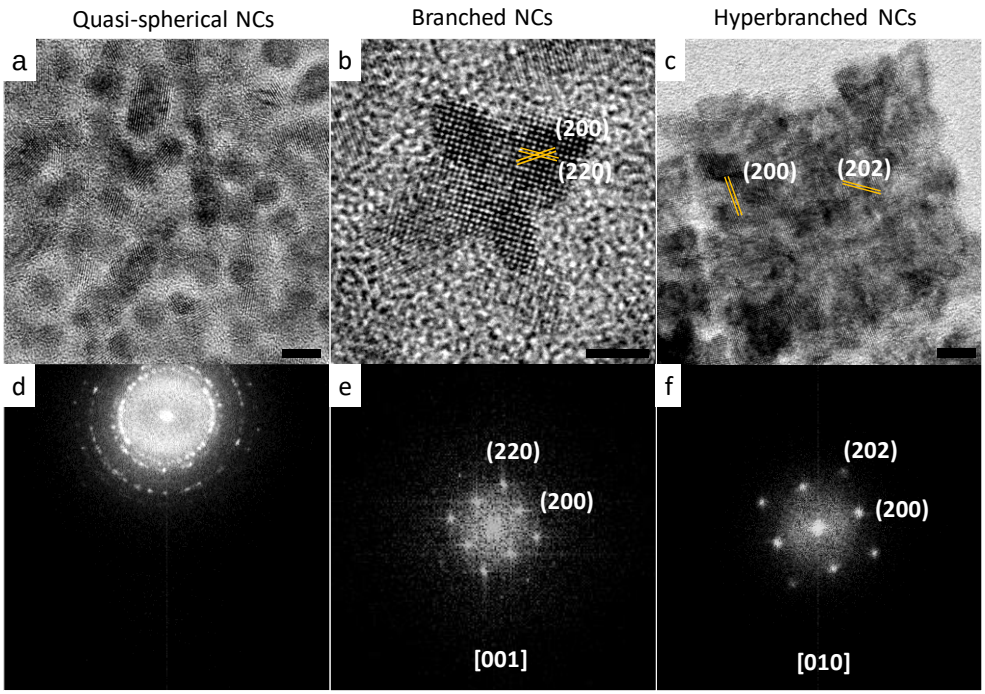

Fig. 7. High-resolution TEM images and corresponding fast Fourier transform of quasi-spherical (a, d), branched (b, e) and hyperbranched (c, f) NCs represented in Fig. 5. Scale bars = 5 nm.

Reconstruction of the crystal lattice of the CeO_2 octapod by inverse Fourier transformation represents the dominant 0.19 nm and 0.26 nm lattice fringes that corresponds to the (202) and (200) reflexes which indicated that octapods are enclosed with (220) and (202) facets (Fig. 8).

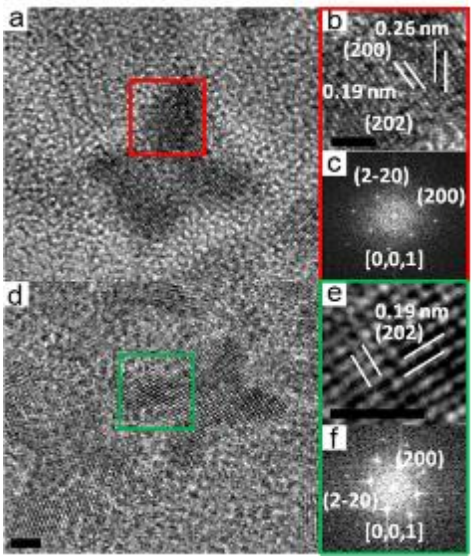

Fig. 8. HRTEM micrograph of CeO_2 octapod (a, d); Fast Fourier Transform (c, f) and reconstruction of the lattice by inverse (b,e). Scale bars = 2 nm.

HRTEM images of CeO_2 hyperbranched NCs show dominant (202) and (200) planes corresponding to interplanar distances of 0.2649 nm and 0.1875 nm respectively. This confirmed that NCs are enclosed with (202) and (200) facets exposed to the media. FFT images obtained from HRTEM images of hyperbrached NCs can be indexed to a [010] zone axis (Fig. 9).

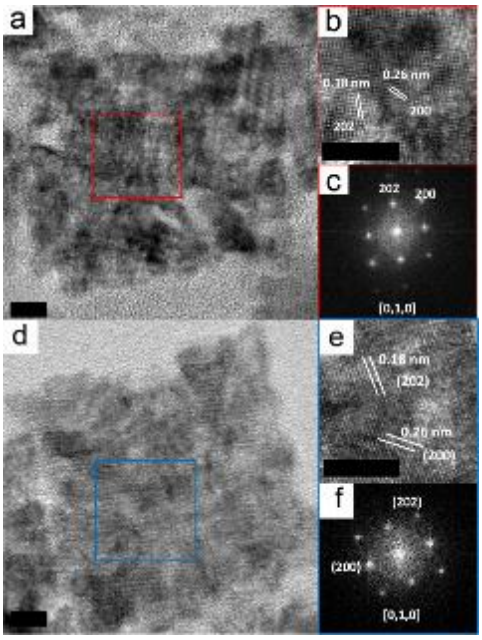

Fig. 9. HRTEM micrograph of hyperbranched CeO_2 NC (a, d); Reconstruction of the lattice by inverse Fourier transformation (b, e); Fast Fourier Transform obtained from the selected area (c, f). Scale bars = 5 nm.

In order to determine the exposed facets of ceria quasi-spherical NCs, we analysed the samples in different spots Fig. 10. Analysis of the FFT of the samples revealed that most of them oriented along [011] zone axis. In all cases we have observed a set of (200) and (111) reflexes that correspond to lattice fringes of 0.26 nm and 0.31 nm of CeO_2 with cubic fluorite structure.

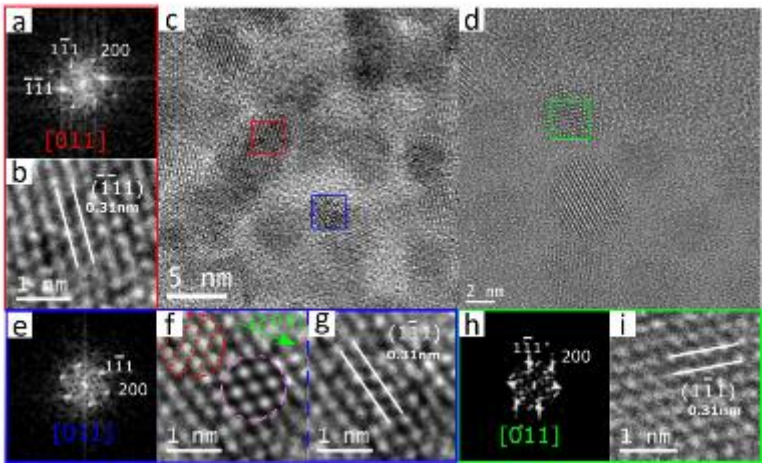

Fig. 10. HRTEM micrograph of 6 nm CeO_2 quasi-spherical NCs (c, d); Reconstruction of the lattice by inverse Fourier transformation (b, f, g, i); Fast Fourier Transform obtained from the selected area (a, e, h).

High-angle annular dark-field scanning transmission electron microscope (HAADF-STEM) tomography analysis revealed the NCs produced in the presence of OAc, but no alcohols, to have an octapod-like geometry (Fig.11). A more detailed view of the octapods morphology was obtained through atomic simulations (Fig.12). Modeling was conducted on NCs oriented along the [001] zone-axis, since HRTEM and FFT analyses showed this to be the most common for octapods. Simulations were carried out by dividing an octapod structure in a central body (spherical, zone-axis [001]) and a set of arms (hexagonal truncated pyramids) pointing in the

[111] directions corresponding to the corners of a cube centered in the origin of the supercell. Simulation results were in good agreement with experimental HRTEM images, where the distribution of the NC atomic planes was well reproduced.

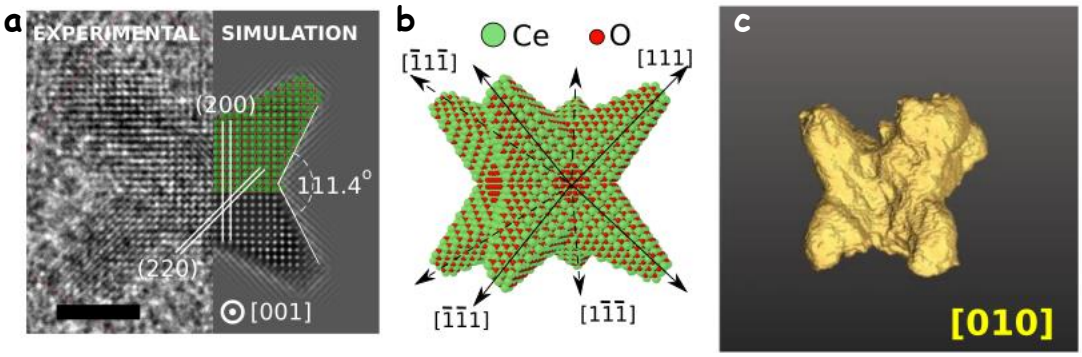

Fig. 11. Comparision between the HRTEM experimental (left) and simulated (right) images of a ceria octapod (Scale bar = 2 nm). b) 3D atomic model of a CeO_2 octapod. c) HAADF tomographic reconstruction of a ceria octapod seen along the [010] direction**.**

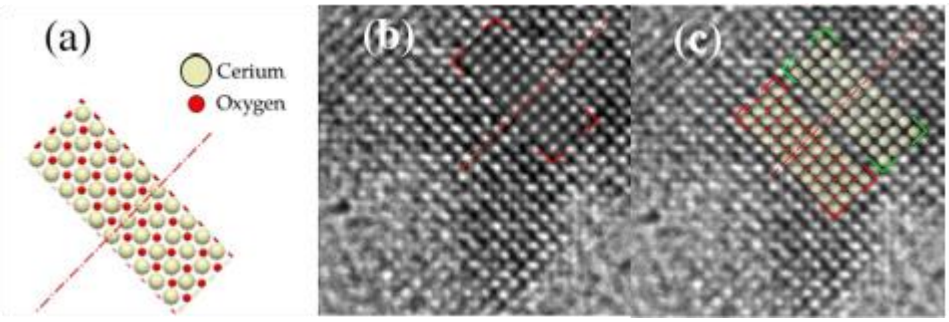

Fig. 12. Comparison between the atomic model, the simulation and the experimental HRTEM images. (a) Atomic model for the CeO_2 unit cell in zone axis [001]. The red line marks the [-220] direction. (b) Inside the red marks, simulated image. (c) Inside the green marks the atomic model containing only Ceria atoms, and inside the red ones containing both Ceria and Oxygen.

XRD patterns (Fig. 13) displayed the reflections of the CeO_2 fluorite structure (space group = Fm3m, JCPDS card No 34-0394) with lattice parameter a = 0.5412 nm. The crystal domain size calculated from the broadening of the XRD reflections using Scherrer equation matched well with the NC size obtained from TEM, including clear differences on the crystal domain size in different crystallographic directions (Table 1).

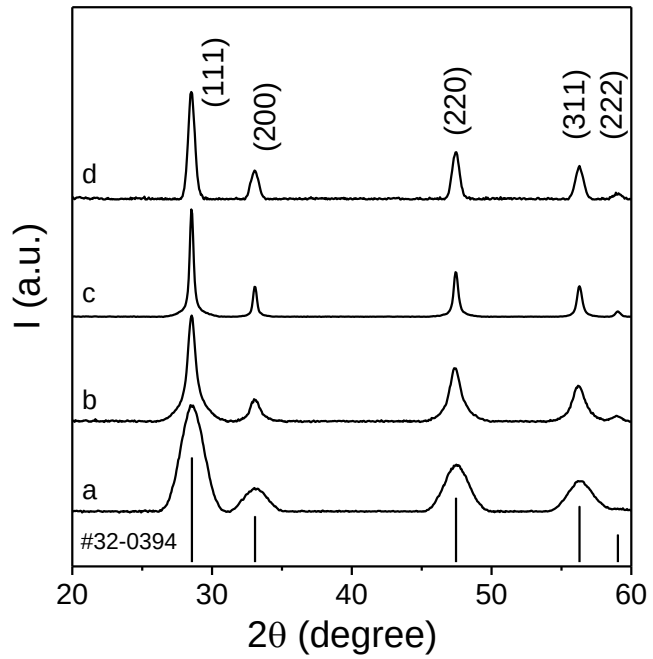

Fig. 13. XRD patterns for quasi-spherical NCs (a), octapods (b, d), hyperbranched NCs (c) are in agreement to a fluorite structure (JCPDS card 34-0394).

Table 1 - Summary of the crystal size domains for ceria NCs having different shapes calculated from TEM images and from XRD patterns using the Scherrer equation.

NC size / NC shape	L_{TEM} (nm)	L_{XRD} (nm)			
		(111)	(220)	(311)	(200)
Quasi-spherical	7±1	4.6	4.6	5.1	4.5
Octapods	16±2	17	10	15	13
Hyperbranched	33±4	25	22	21	26
Octapods made in the presence of H_2O	12±2	16	15	15	14

2.3.1. NCs growth mechanism

The formation of ceria octapods in the presence of OAc was consistent with previous reports demonstrating the synthesis of octapods of a range of metals and metal oxides.[5,6,36,38-40] Octapod formation has been associated either to a selective etching of [100] facets or the selective overgrowth in the [111] crystallographic direction. The latter case has been hypothesized to be triggered either by the preferential interaction of OAc with [100] facets blocking monomer delivery and thus hindering their growth, or quite the opposite by its preferential interaction with the [111] facets, providing monomer (oleate) and thus accelerating growth in this direction.[41,42] However, scarce evidences to support these hypotheses have been given.

Some previous works also reported the formation of complex CeO_2 nanostructures through the oriented attachment of cubic NCs mediated by the preferential binding of OAc at [100] facets.[43] While it is not always straightforward to discern the mechanism involved in the formation of particular branched NCs, a main differential characteristic of aggregation growth when compared with atomic-addition is that aggregation growth takes place within a solution containing a population of small NCs which decreases as being added to larger structures. Eventually, when all small NCs have been consumed, growth stops. To elucidate the growth mechanism of the ceria branched structures here described, aliquots at different reaction times were withdrew and analyzed (Fig. 14 - Fig. 15). Interesting, NCs produced at low reaction times already showed a branched geometry and no population of smaller NCs was observed. As reaction time increased, the size of all NCs in the ensemble simultaneously augmented while their geometry was preserved. This observation clearly pointed toward the formation of branched NCs through atomic addition and not through a selective etching or NC aggregation mechanism.

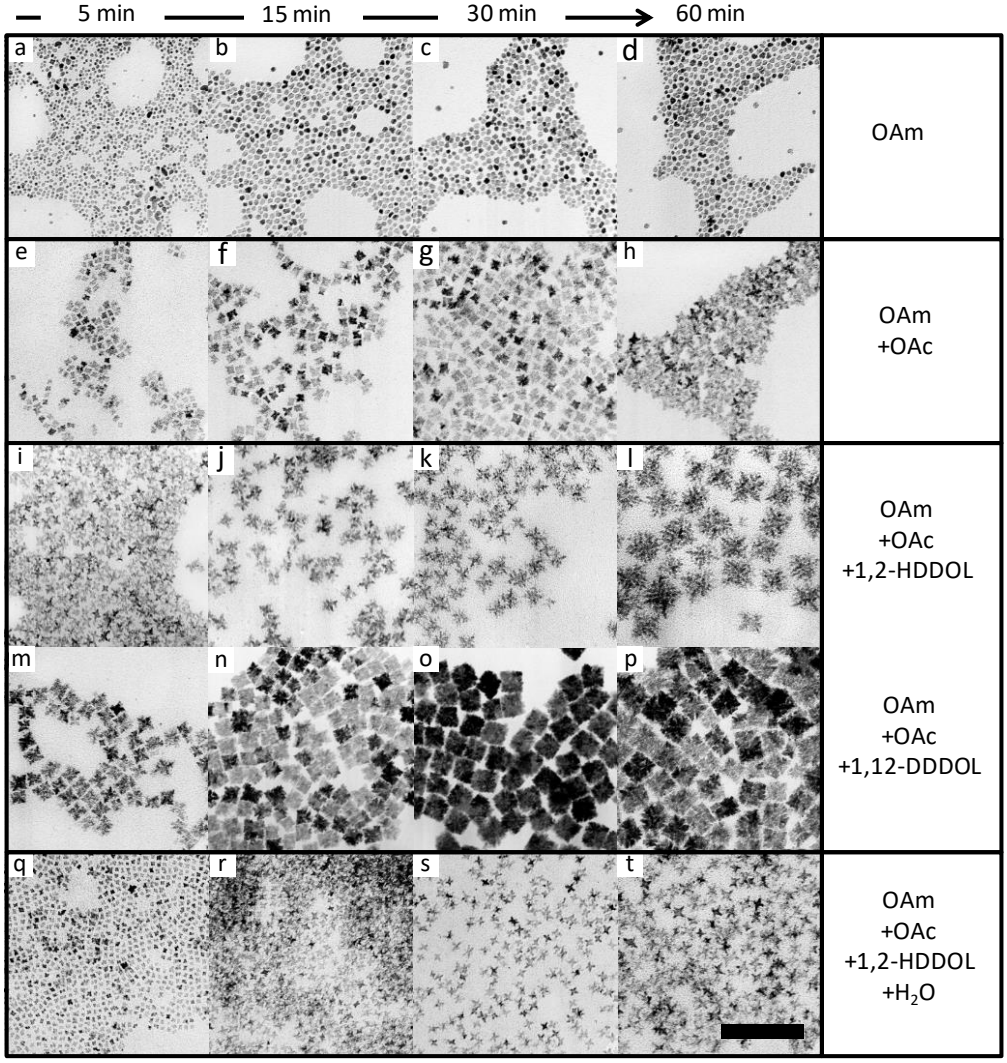

Fig. 14. Representative TEM micrographs of the ceria NCs obtained at different reaction times (5, 15, 30 and 60 min): a-d) in the presence of only OAm; e-h) adding OAc; i-l) adding OAc and 1,2-HDDOL; m-p) adding OAc and 1,12-DDDOL; q-t) adding OAc, 1,2-HDDOL and MQ-water. Experimental details for each image are summarized in Ошибка! Источник ссылки не найден.**Table 1**. All images were taken at the same magnification. Scale bar = 50 nm.

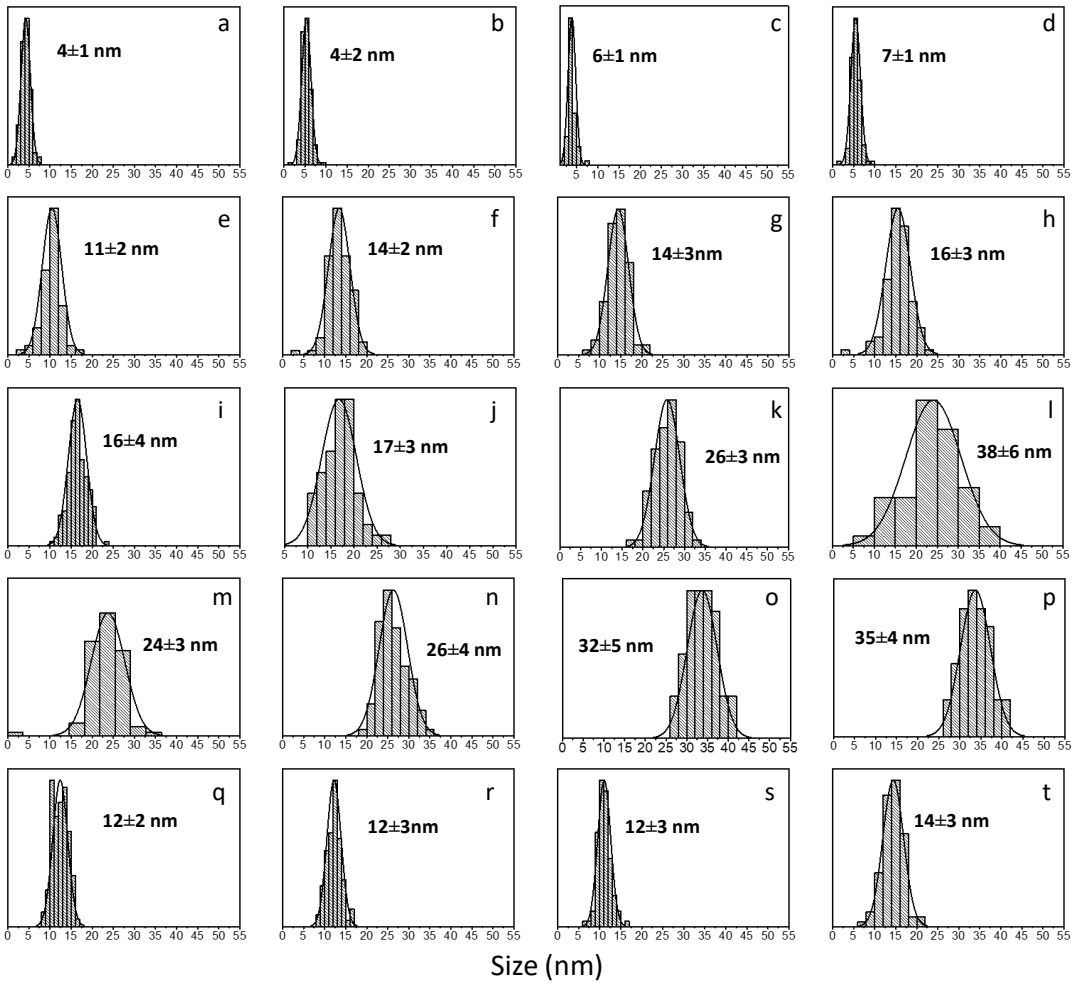

Fig. 15. Size histograms of CeO_2 NCs with different shapes represented in **Fig.14** synthesized by changing the reaction time from 5 to 60 min for quasi-spherical NCs (4 - 7 nm) (a-d); octapods (11 - 16 nm) (e-h) and (12 - 14 nm) (q-t); hyperbranched NCs (16 - 34 nm) (i-l) and (24 - 38 nm) (m-p).

2.3.2. Branching manipulation in CeO_2 NCs

2.3.2.1. Oleic acid as a branching agent

To determine the specific OAc effect, either to block monomer delivery to the (100) facets favoring in this way the preferential growth of the [111] direction or to preferentially deliver monomer to the (111) facets in an OAm-passivated crystal, the NC surface chemistry was examined. In the 1H NMR spectrum of purified hyperbranched NCs (obtained in the presence of OAm, OAc and an alcohol), the ligand resonances were broadened, which is in line with the large size and the many chemical environments of such nanostructures (Fig. 16). This broadening impeded the unequivocally direct determination of the ligand's identity.

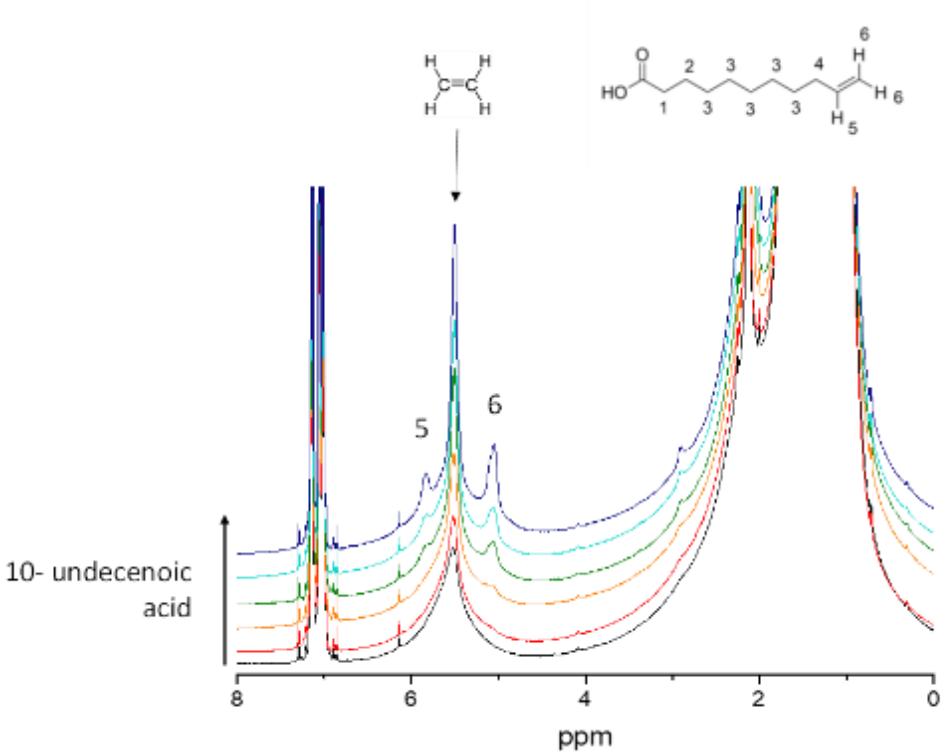

Fig. 16. 1H NMR spectra of the titration with 10-undecenoic acid of OAc-capped hyperbranched NCs.

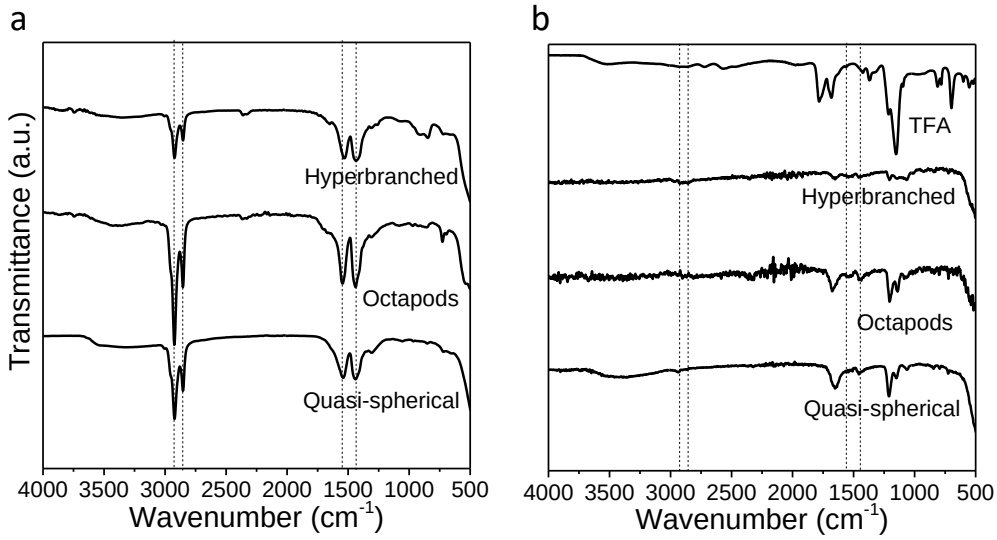

Fig. 17. FTIR spectra of as-synthesized CeO_2 NCs (a) and NCs treated with trifluoroacetic acid (b). The FTIR spectra of as-prepared samples show the absorption peaks in the region of 2820-2946 cm^{-1} attributed to C-H stretching vibration ascribed to oleic acid molecules. The absorption band at 1400-1600 cm^{-1} can be assigned to C-O vibrational stretch of the carboxilate group. The absence of the peaks in the range of 1400-1600 cm^{-1} on the FTIR spectra of TFA-treated CeO_2 NCs confirmed that the original organic ligands were stripped. The peaks at 1200 cm^{-1}, 1140 cm^{-1} and 1670 cm^{-1} could be ascribed to TFA absorbed on the NCs surface.

Therefore, we added TFA, which is known to be able to strip all kind of ligands from the NC surface.[44,45] Upon trifluoroacetic acid (TFA) addition, the NC precipitate was separated by centrifugation from the supernatant (containing the stripped ligands). Fig. 17 shows the FTIR spectra of NCs before and after ligand removal with TFA. As is clear from the absence of C-H stretching vibrations in the stripped samples, all the original ligands with aliphatic chains were removed. The only residual signals were attributed to bound TFA molecules, as is expected in an X-for-X type exchange and considering the charge neutrality conditions.

Fig. 18 shows the ^{1}H NMR spectrum of the cleaved ligands. A set of resonances that agrees with the fingerprint of OAc was clearly observed, while no sign of OAm and alcohols was visible. To further exclude the presence of OAm in the NC surface, we replaced OAc by decanoic acid in the synthesis, stripped the ligands from the NC surface and studied their composition (Fig. 18-Fig.). The 1H NMR spectrum of the ligands stripped from hyperbranched NCs produced in the presence of decanoic acid did not display the peak at around 5.33 ppm characteristic of the double bond present both in OAc and OAm, conclusively proving the absence of OAm at the NC surface.

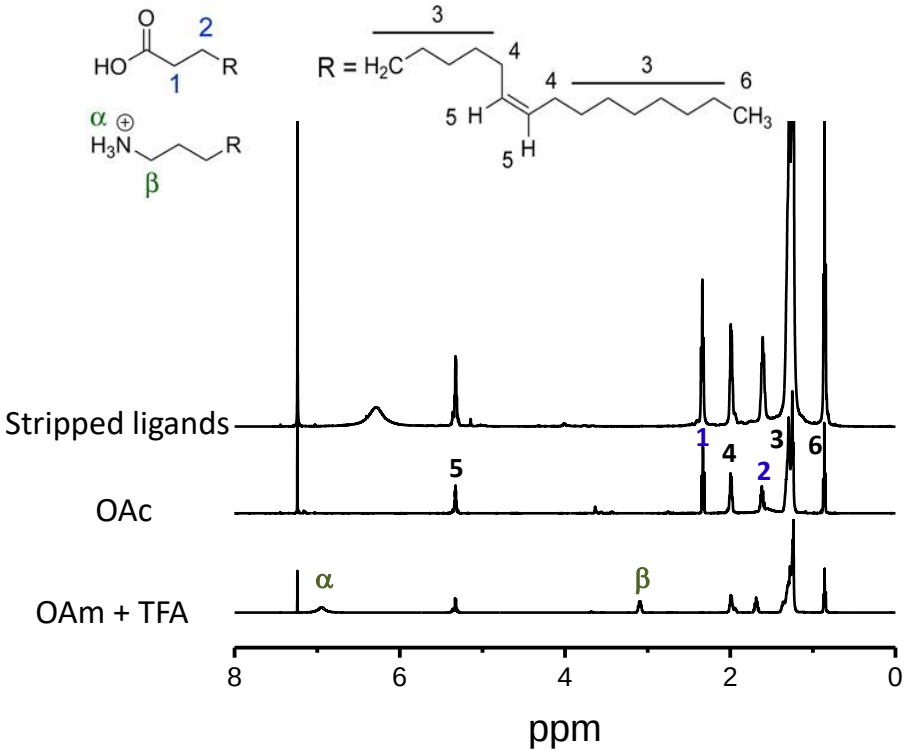

Fig. 18. 1H NMR spectrum of stripped ligands from hyperbranched ceria NCs and reference spectra of OAc and OAm.

To further determine the type of binding of OAc to the NC surface,[163] we added increasing amounts of 10-undecenoic acid to a dispersion of hyperbranched NCs and we measured the 1H NMR spectra of the NCs. When raising the amount of added 10-undecenoic acid, an increasing contribution of its broadened resonances and a concomitant sharpening of the OAc features were observed in the 1H NMR spectra (Fig. 20). These features indicated a progressive replacement of OAc by 10-undecenoic acid, i.e. an X-for-X ligand exchange, that proves OAc to bind as an X-type ligand at the CeO_2 surface.[47]

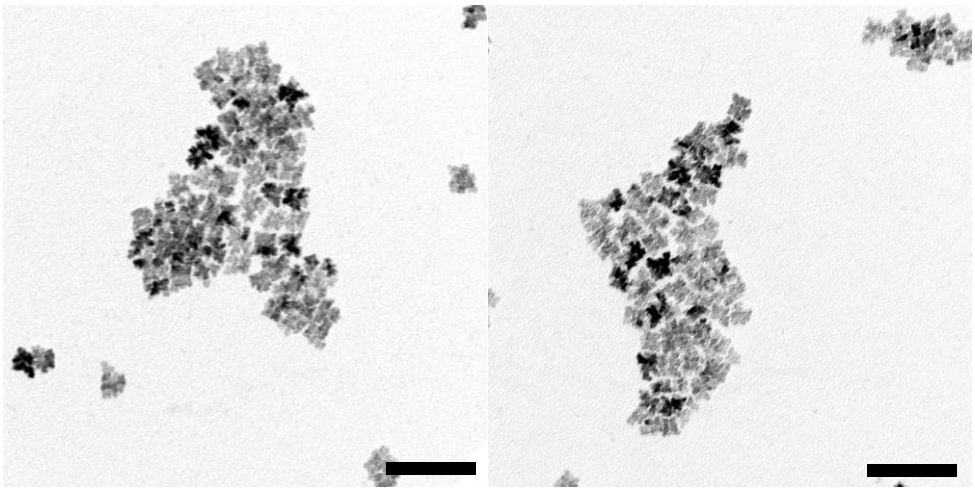

Fig. 19. TEM images of branched ceria NCs produced using decanoic acid instead of oleic acid. Scale bars = 50 nm.

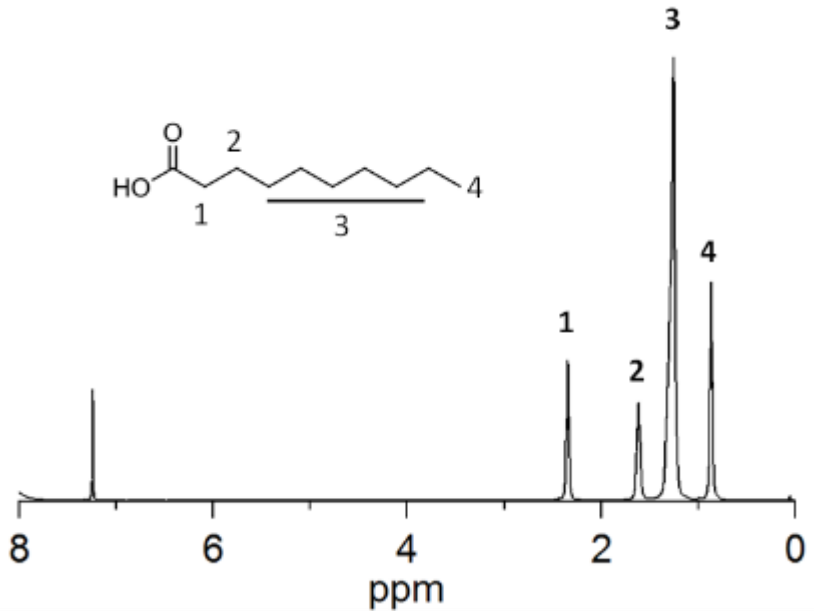

Fig. 20. 1H NMR spectrum of stripped ligands from ceria NCs when using decanoic acid instead of oleic acid.

Being OAc the surfactant covering the NC surface, stabilizing it in solution and controlling its growth, as deduced from 1H NMR analysis, the formation of branches triggered by its presence must be related to its differential coverage of particular facets, underprotecting them, instead of to its preferential decomposition in specific growth directions. Being branches grown in the [111] crystallographic directions, we conclude the (111) facets to have a lower coverage of OAc and thus are less protected from monomer delivery. Three intrinsic properties of the ceria crystal structure may explain the lower coverage of the (111) facets by OAc. First, the (111) is the most compact surface, which may prevent a close packed assembly of relatively bulky OAc. Additionally, (111) facets have surface atoms with the lowest coordination deficiency thus limited ligand bonding. Moreover, this facet is characterized by the highest oxygen vacancy formation energies and thus has the lowest density of such a defect which is required to compensate charge when OAc coordinates as an X-type ligand.

2.3.2.2. Influence of the alcohol molecule on the branching degree

With respect to the reaction mixture containing OAm and OAc, the incorporation of alcohols accelerated the NC growth and strongly increased the material yield, to ca. 80%. In the presence of alcohols, systematically larger ceria NCs containing additional branches were produced (Fig. 21 c). Increasing of the alcohol molecule concentration in the reaction led to side branching and eventually resulted in highly branched NCs (Fig. 21). Relatively large concentrations of alcohols (e.g. 2.5 mmol 1,2- HDDOL) resulted in hyperbranched NCs with an overall cubic shape.

Testing different alcohols (1-Decanediol: 1-DDOL; 1,2-Dodecanediol: 1,2-DDDOL; 1,2-Hexadecanediol: 1,2-HDDOL; and 1,12-Dodecanediol: 1,12-DDDOL) showed that the aliphatic chain length did not have evident influence on the NC growth, while the number of alcohol groups and their position just slightly modified the branch thickness and density (Fig. 22). For instance, 1,12-DDDOL promoted more densely packed branched structures when compared with 1-DDOL or 1,2- HDDOL.

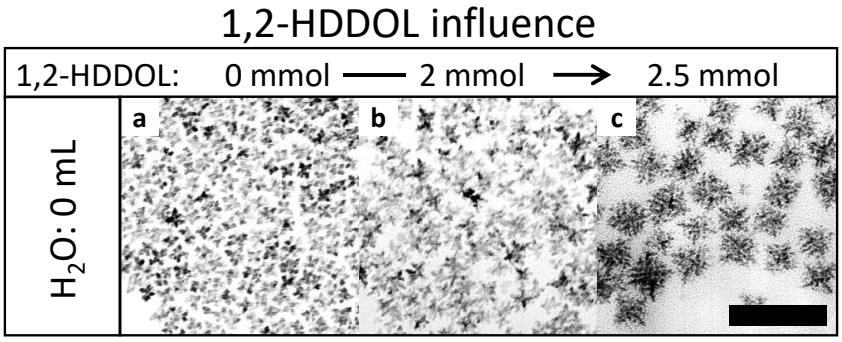

Fig. 21. TEM images of the morphological transformation of ceria NCs resulted from the addition of 0, 2 and 2.5 mmol of 1,2-HDDOL .Scale bars = 100 nm.

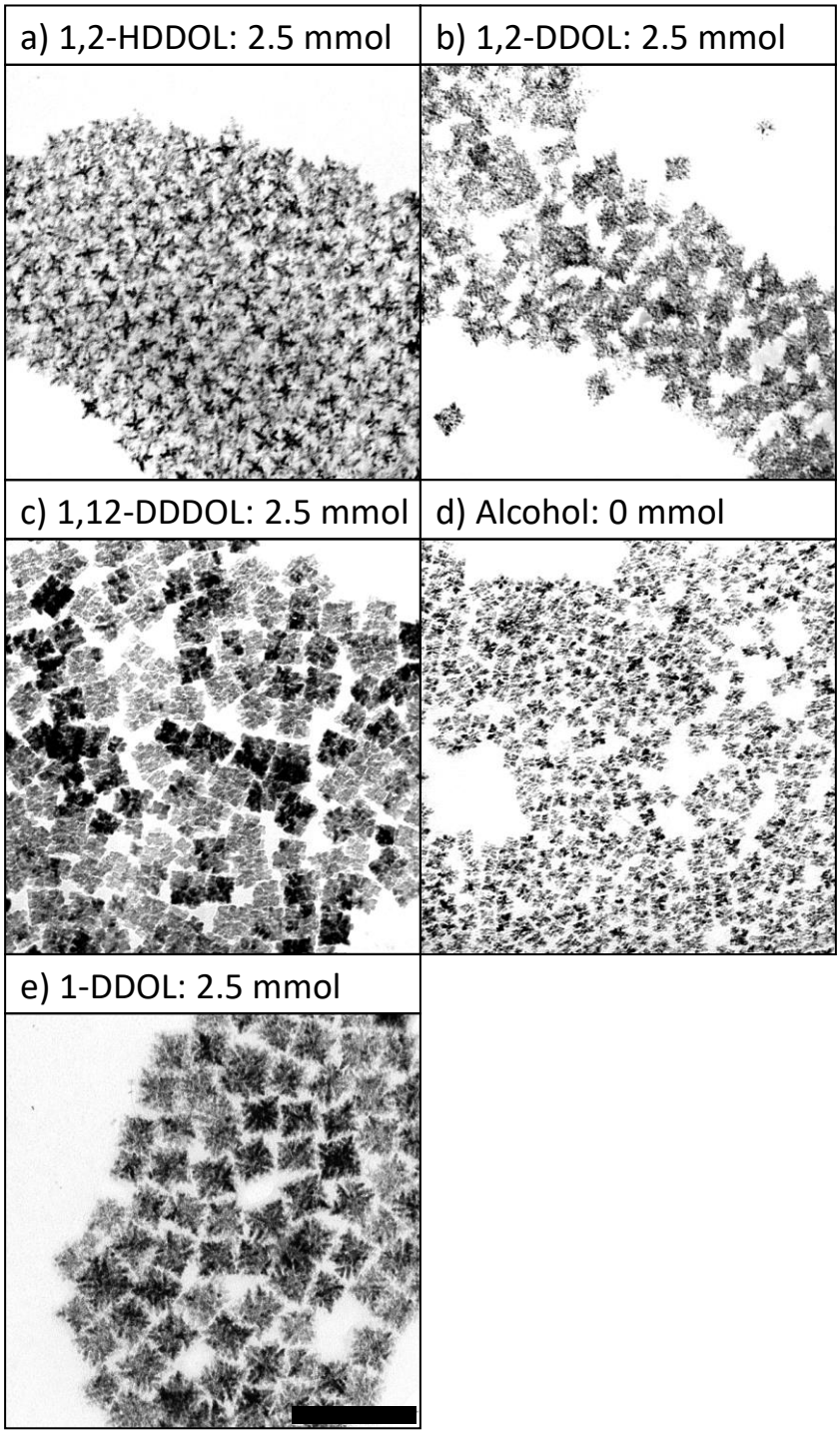

Fig. 22. TEM images of the morphological transformation of ceria NCs synthesized in the presence of 0 and 2.5 mmol of different alcohol molecules. Note that synthesis conditions (reaction temperature and time) and the amounts of cerium nitrate, OAm, OAc and ODE were standard for all the syntheses. Scale bars = 100 nm.

The absence of the alcohol fingerprint in the NMR spectrum and the increased growth rates observed with their presence in the reaction mixture indicated that alcohols take a role as reactant. We hypothesize alcohols accelerated the reaction by participating in an esterification alcoholysis reaction of the oleate monomer.[48-50] In parallel, alcohols may consume part of the free acid via the esterification reaction reducing the ceria dissolution rate. This overall modification of the growth kinetics directed the formation of sharper branches and triggered the creation of higher amounts of defects which acted as nucleation sites for new side

branches, thus resulting in hyper-branched structures. At high concentrations of alcohol groups, very fast growth rates and high side nucleation rates were obtained, resembling to a dendritic growth (Fig. 22). The UV-vis spectra of hyperbranched CeO_2 NCs (Fig. 23) shows a sign of their large density of defects in the form of a 20 nm shift of the wavelength of the absorption edge.

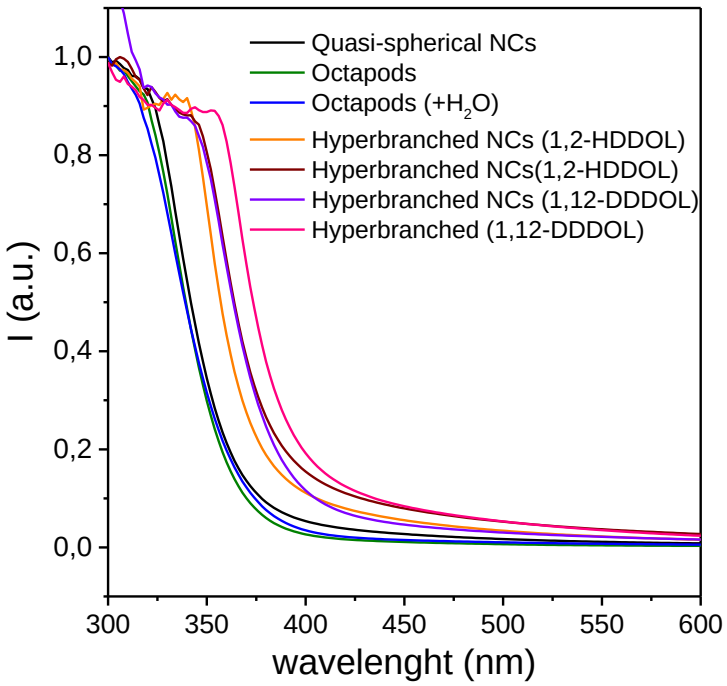

Fig. 23. UV-vis absorption spectra of as-synthesized CeO_2 NCs show the blue-shift from 363 nm for octapods to 376 nm for hyperbranched NCs.

2.3.2.3. H_2O effect on the reaction rate

The decision to investigate the influence of water came from two factors: i) The cerium nitrate used was already hydrated (6 molecules of H_2O per mol) and although a vacuum step was applied, we could not ensure the complete removal of water in solution. Additionally, cerium nitrate naturally absorbs water from the environment if not stored properly. Indeed, we observed a strong variability when using cerium nitrate of different batches or even from the same batch but stored under different conditions (under Ar atmosphere, inside a desiccator or under ambient conditions). Thus we performed all our syntheses using cerium nitrate hexahydrate stored under inert gas. ii) The esterification reaction results in the formation of water molecules.

To determine the water influence, we produced ceria NCs in the presence of different amounts of water introduced in the initial reaction mixture. Namely in a 25 mL three neck flask, 0.434 g (1 mmol) of cerium (III) nitrate hexahydrate, 0.645 g (2.5 mmol) of 1,2-HDDOL, 2 mL (6 mmol) of OAc, 2 mL (6 mmol) of OAm, and 1.5 ml (83 mmol) of MQ-Water (18.2 MΩ, filtered with filter pore size 0.22 µM, Millipore) were added to 4 mL of ODE under magnetic stirring. Degassing for 10 minutes at room temperature resulted in the formation of a milky yellow

solution (Fig. 24). Then the mixture was heated up to 300 °C at a heating rate 15 °C/min under an Argon atmosphere and kept at this value for 60 min. Above 200 °C, the initial solution became turbid and changed colour to orange. At 250 °C the mixture started suffering small explosions and its colour turned to dark brown. Note that explosions lasted for all the reaction process which led to a temperature oscillation. After the reaction was completed, the resulting mixture was cooled and 2 mL of toluene were injected just below 160 °C. The cleaning procedure was the same as above mentioned.

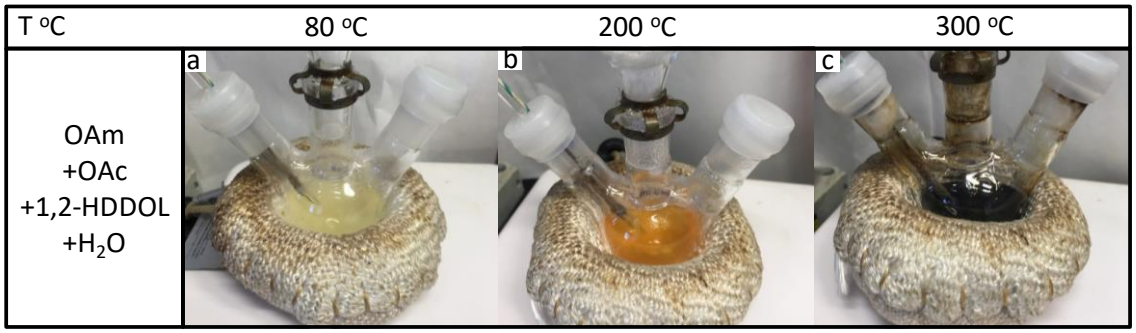

Fig. 24. Photographs showing color change during the synthesis of octapod NCs in the presence of water while reaction temperature increases: a) 80 °C; b) 200 °C; c) 300 °C.

Water is a byproduct of the esterification reaction that could influence the reaction kinetics. To elucidate this influence, controlled amounts of MQ-water were injected to the reaction mixture. The presence of MQ water had a contrary effect to that of alcohols, reducing the growth rate and yield and preventing side-branching. As shown in Fig.25 d-i, at a set amount of an alcohol (e.g. 2.5 mmols of 1,2 HDDOL), increasing the amount of added MQ-water (0, 1 and 1.5 mL) induced a morphology transformation from hyperbranched to octapod structures. However, the injection of constant amount of water independently of the aliphatic chain of the alcohol molecule and its concentration resulted in octapod morphology, suppressing side branching Fig. 25 a-c and Fig. 26. Additionally, NCs obtained in the presence of water were systematically smaller than those produced under the same conditions but in its absence. We believe that the presence of water slowed down the reaction of alcohols and fatty acids and thus the formation of an ester by a displacement of the esterification reaction. An alternative explanation is the more effective protection of NCs facets by filling the gaps between/left by OAc and increasing the overall ligand surface coverage.[51]

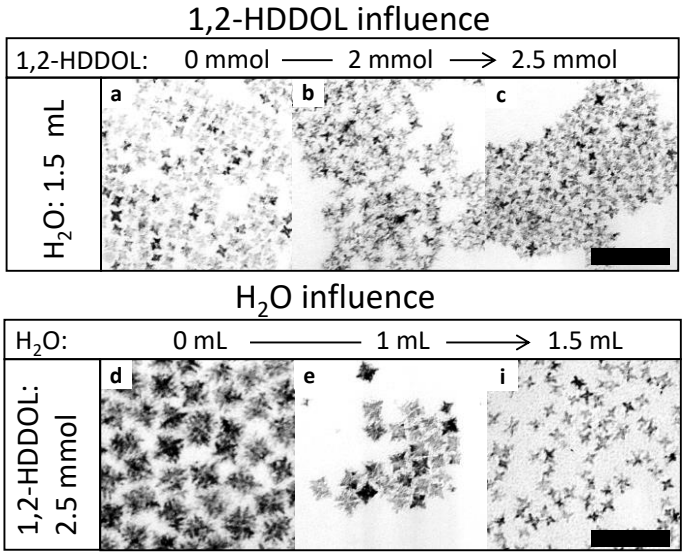

Fig. 25. Representative TEM micrograph of ceria NCs produced in the presence of different amounts of water while maintaining constant all other conditions. Notice with the increase of the water con-tent, NCs become smaller and side branching is prevented. Scale bar = 50 nm.

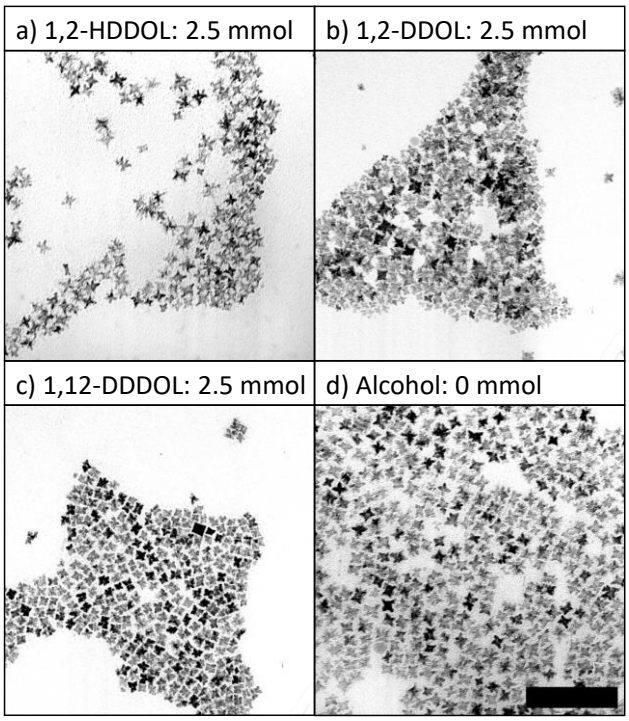

Fig. 26. TEM images of CeO_2 NCs synthesized using 1.5 mL (e - h) of MQ H_2O in the presence of different alcohols: 2.5 mmol of 1,2-HDDOL (a, e), 1,2-DDOL (b, f), 1,12-DDDOL (c, g); 0 mmol of alcohol (f, h). Note that in all cases synthesis parameters, namely reaction temperature and time, amount of Ce–precursor, OAm, OAc and ODE were constant and equal to the standard procedure. Scale bar = 100 nm.

2.3.2.4. NCs shape transformation with the reaction temperature

A temperature study of the system by doing synthesis at different temperatures while keeping the rest of parameters constant was performed. We observed that by mixing the same reactants (OAm, ODE, OAc and 1,12-DDDOL) but reducing the reaction temperature from 300 ^{o}C to 200 ^{o}C kite-like ceria NPs were synthesized (Fig. 27 g). These particles show a similar structure to that of nanoflowers but with the formation of a wire growing from one of the side of the NP. Samples were thoroughly imaged to exclude the formation of wires and flowers separately.

The formation of similar tadpole wire structures has been already reported by Hyeon and coworkers.[52] Nonetheless, our kite-like NPs show a larger head of about 9 nm with a wire tail size which ranges 10 to 20 nm. Noteworthy, Li et al. recently reported about the increasing performance of prism-anchored octahedronal ceria nanocrystals.[53] The resulting homo-junction between the prism and the face of the octahedral provided an efficient separation and fast transfer of photoinduced charge carriers thus boosting the photocatalytic performance compare with bare octahedral. The homo-junction there reported range the 4 to 6 nm size while in our case the junction is far below that value.

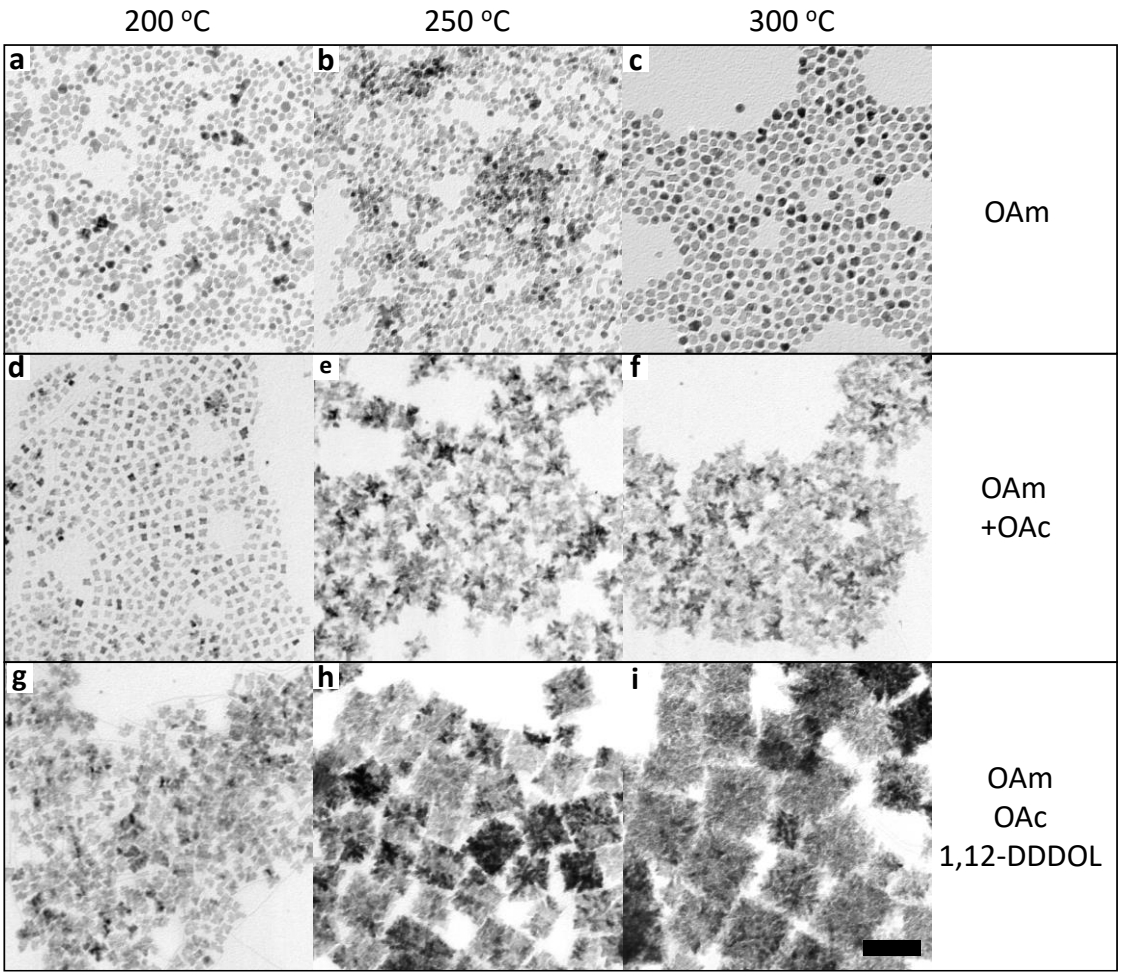

Fig. 27. TEM images of CeO_2 NCs synthesized at different reaction temperatures (200 °C, 250 °C, 300 °C): a-c) in the presence of only OAm; d-f) adding OAc; g-i) adding OAc and 1,12-DDDOL. Scale bar = 50 nm.

2.3.3. Effect of branching on the catalytic properties of the NCs (BET, OSC)

Before characterizing their functional properties, ceria NCs were annealed at 400 °C for 4 hours under oxygen atmosphere to completely remove surface ligands. This temperature was selected on the basis that it allowed to remove residual organics while conserving the NC morphologies (Fig. 28 - Fig. 30). Adsorption–desorption isotherm N_2 cycles were performed on the annealed samples showing physisorption isotherms characteristic of microporous materials for the quasi-spherical NCs and a distinctive IV type isotherm characteristic of mesoporous materials for all branched nanostructures (Fig.31).[54] The specific surface areas of the annealed samples were calculated using the Brunauer-Emmett-Teller (BET) model.

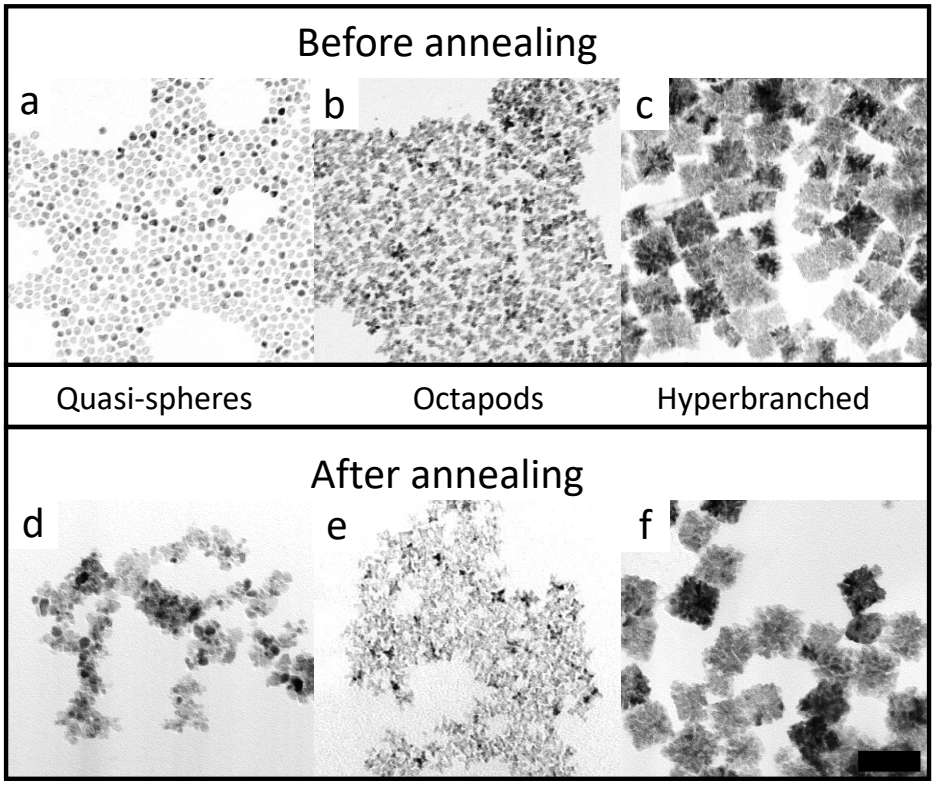

Fig. 28. TEM images of quasi-spherical NCs (a, d), octapods (b, e) and hyperbranched (c, f) NCs before and after annealing at 400 °C for 4 h, correspondingly. Scale bar = 50 nm.

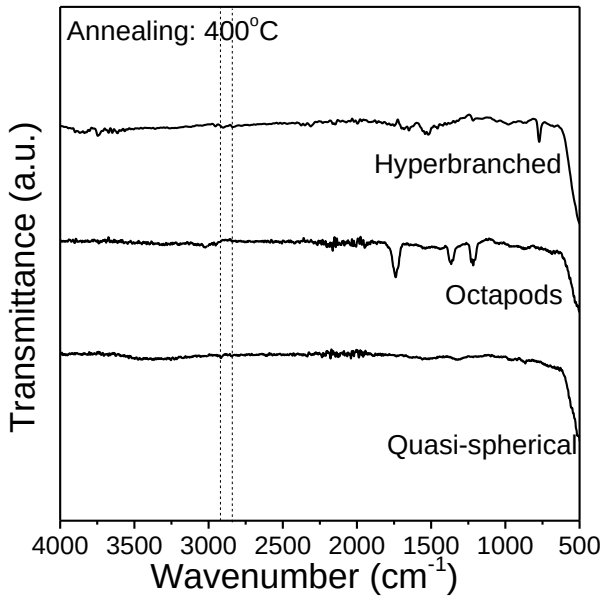

Fig. 29. TG analysis of Ceria NCs obtained after annealing at 400 °C for 4 h at a heating rate of 2 °/min

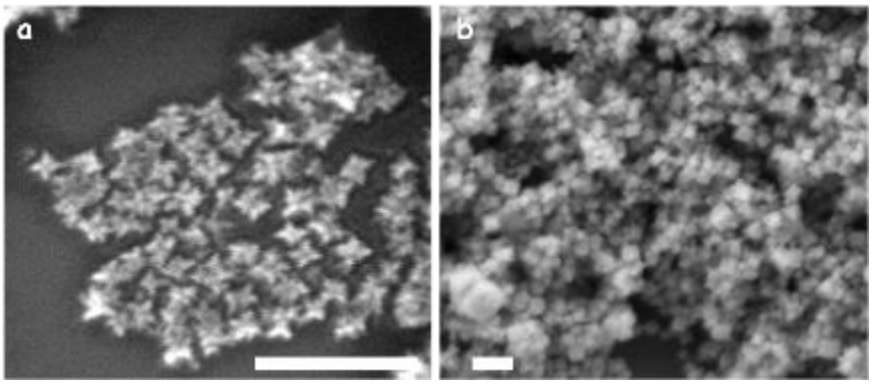

Fig. 30. SEM images of octapods (a) and hyperbranched (b) NCs after annealing. Scale-bars = 100 nm

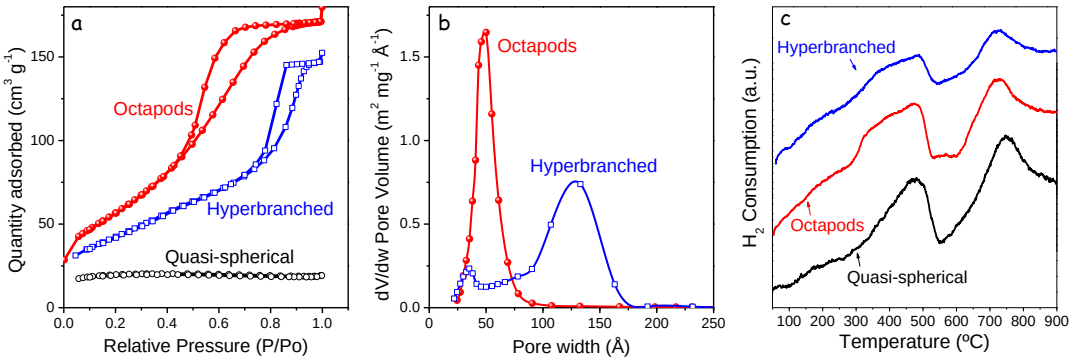

Fig. 31. a) Adsorption/desorption isotherm cycles performed on quasi-spherical, octapods and hyperbranched ceria NCs. b) BJH pore size distributions. c) H_2 temperature-programmed reduction profiles. Samples were preheated at 90 °C for 15 min under a He flow (50 mL/min) before reducing them in a 12% vol H2/Ar (50 mL/min) flow while increasing the temperature from room temperature up to 930 °C at a rate of 10 °C/min.

As expected, branched structures, particularly octapods, were characterized by much higher surface areas, up to 212 m^2/g against 63 m^2/g for quasi-spheres. We associated these differences mainly to the different packing of each type of NC. This packing difference was also manifested in the much higher porosity obtained from the branched structures. We believe octapods showed larger surface areas than hyper-branched NCs because of the smaller size and arm thickness of the former. Also, part of the surface (interface) area of the hyperbranched structures could be not accessible due to a too close NC packing within such highly branched nanostructures.

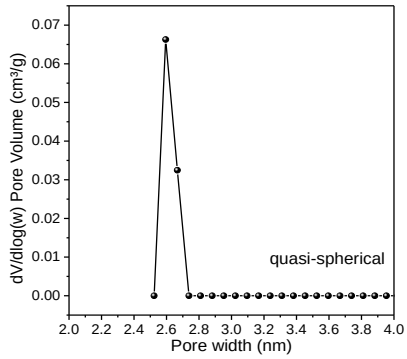

Fig. 32. Pore size distribution for quasi-spherical NCs performed using DFT model adjustment for cylindrical pores over oxide surface as a reference

TPR profiles of the annealed samples showed two major features (Fig. 31): In the range between 300-500 °C the reduction from Ce^{4+} to Ce^{3+} took place. This reduction occurred at lower temperatures at the NC surface compare with the bulk counterpart. The relative intensity between these two peaks in all the samples revealed a higher surface to volume ratio for the branched structures compared with the quasi-spherical, consistent with BET surface area results. In the same direction, higher OSC values were also obtained for branched materials, reaching values up to 720 mmol O_2/g (Table 3).

Table 3. Summary of the characterization performed on ceria spherical NCs, octapods and hyperbranched NCs. Description of experiments is summarized in the experimental section.

CeO_2 NCs	**BET Surface Area (m^2/g)**	**Pore Volume (cm^3/g)**	**Reduction at 823 K (x in CeO_x)[a]**	**OSC (µmol O/g)[b]**
Quasi-spherical	63	0.03	1.81	490
Octapods	212	0.28	1.56	720
Hyperbranched	157	0.24	1.53	630

[a] Value of x in CeO_x as measured at 823 K from hydrogen consumption. [b] Calculated from TGA in H_2 flow at 673 K

2.4. Conclusions

Branched ceria NCs were synthesized by reacting cerium nitrate in the presence of OAm, OAc and alcohols. OAc was found to bond to the NC surface as an X-type ligand hindering NC growth in all crystallographic directions but less efficiently in the [111]. This effect was attributed to the lower OAc coverage of the (111) facets due to their higher atomic compactness, lower coordination deficiency and reduced oxygen vacancy density. The preferential growth in the [111] direction resulted in the formation of ceria octapods. The presence of alcohols strongly accelerated the NC growth through an esterification alcoholysis reaction, which resulted in larger NCs with side branching. The concentration of water in the reaction mixture was found to play an import role in controlling this alcoholysis reaction and possibly in better protecting the NC surface. It was further demonstrated that branched NCs provided higher surface areas, porosities and OSC values when compared with quasi-spherical NCs.

2.5. References

1. Li, H.; Kanaras, A. G.; Manna, L. Colloidal Branched Semiconductor Nanocrystals: State of the Art and Perspectives. *Acc. Chem. Res.* **2013,** 46, 1387-1396.

2. Ye, E.; Regulacio, M. D.; Zhang, S.-Y.; Loh, X. J.; Han, M.-Y. Anisotropically branched metal nanostructures. *Chem. Soc. Rev.* **2015,** 44, 6001-6017.

3. Miszta, K.; de Graaf, J.; Bertoni, G.; Dorfs, D.; Brescia, R.; Marras, S.; Ceseracciu, L.; Cingolani, R.; van Roij, R.; Dijkstra, M.; Manna, L. Hierarchical self-assembly of suspended branched colloidal nanocrystals into superlattice structures. *Nat. Mater.* **2011,** 10, 872-876.

4. Arciniegas, M. P.; Kim, M. R.; De Graaf, J.; Brescia, R.; Marras, S.; Miszta, K.; Dijkstra, M.; van Roij, R.; Manna, L. Self-Assembly of Octapod-Shaped Colloidal Nanocrystals into a Hexagonal Ballerina Network Embedded in a Thin Polymer Film. *Nano Lett.* **2014,** 14, 1056-1063.

5. Zhao, Z.; Zhou, Z.; Bao, J.; Wang, Z.; Hu, J.; Chi, X.; Ni, K.; Wang, R.; Chen, X.; Chen, Z.; Gao, J. Octapod iron oxide nanoparticles as high-performance T2 contrast agents for magnetic resonance imaging. *Nat. Commun.* **2013,** 4, 2266

6. Douglas, F. J.; MacLaren, D. A.; Tuna, F.; Holmes, W. M.; Berry, C. C.; Murrie, M. Formation of octapod MnO nanoparticles with enhanced magnetic properties through kinetically-controlled thermal decomposition of polynuclear manganese complexes. *Nanoscale* **2014,** 6, 172-176.

7. Rodríguez-Lorenzo, L.; de la Rica, R.; Álvarez-Puebla, R. A.; Liz-Marzán, L. M.; Stevens, M. M. Plasmonic nanosensors with inverse sensitivity by means of enzyme-guided crystal growth. *Nat. Mater.* **2012,** 11, 604-607.

8. Yang, H.; Zhang, Y.; Hu, F.; Wang, Q. Urchin-like CoP Nanocrystals as Hydrogen Evolution Reaction and Oxygen Reduction Reaction Dual-Electrocatalyst with Superior Stability. *Nano Lett.* **2015,** 15, 7616-7620.

9. Zhao, R.; Fu, G.; Zhou, T.; Chen, Y.; Zhu, X.; Tang, Y.; Lu, T. Multi-generation overgrowth induced synthesis of three-dimensional highly branched palladium tetrapods and their electrocatalytic activity for formic acid oxidation. *Nanoscale* **2014,** 6, 2776-2781.

10. Tsai, Y.-H.; Chanda, K.; Chu, Y.-T.; Chiu, C.-Y.; Huang, M. H. Direct formation of small Cu_2O nanocubes, octahedra, and octapods for efficient synthesis of triazoles. *Nanoscale* **2014,** 6, 8704-8709.

11. Sun, C.; Li, H.; Chen, L., Nanostructured ceria-based materials: synthesis, properties, and applications. *Energy Environ. Sci.* **2012,** 5, 8475-8505.

12. Walkey, C.; Das, S.; Seal, S.; Erlichman, J.; Heckman, K.; Ghibelli, L.; Traversa, E.; McGinnis, J. F.; Self, W. T. Catalytic properties and biomedical applications of cerium oxide nanoparticles. *Environ. Sci.: Nano* **2015,** 2, 33-53.

13. Trovarelli, A. Catalytic Properties of Ceria and CeO_2-Containing Materials. *Catal. Rev.* **1996,** 38, 439-520.

14. Esch, F.; Fabris, S.; Zhou, L.; Montini, T.; Africh, C.; Fornasiero, P.; Comelli, G.; Rosei, R. Electron Localization Determines Defect Formation on Ceria Substrates. *Science* **2005,** 309, 752-755.

15. Sun, C.; Xue, D. Size-dependent oxygen storage ability of nano-sized ceria. *Phys. Chem. Chem. Phys* **2013,** 15, 14414-14419.

16. Aneggi, E.; Wiater, D.; de Leitenburg, C.; Llorca, J.; Trovarelli, A. Shape-Dependent Activity of Ceria in Soot Combustion. *ACS Catal.* **2014,** 4, 172-181.

17. Vilé, G.; Colussi, S.; Krumeich, F.; Trovarelli, A.; Pérez-Ramírez, J. Opposite Face Sensitivity of CeO_2 in Hydrogenation and Oxidation Catalysis. *Angew. Chem. Int. Ed.* **2014,** 53, 12069-12072.

18. Conesa, J., Computer modeling of surfaces and defects on cerium dioxide. *Surf. Sci.* **1995,** 339, 337-352.

19. Lei, W.; Zhang, T.; Gu, L.; Liu, P.; Rodriguez, J. A.; Liu, G.; Liu, M. Surface-Structure Sensitivity of CeO_2 Nanocrystals in Photocatalysis and Enhancing the Reactivity with Nanogold. *ACS Catal.* **2015,** 5, 4385-4393.

20. Jiang, D.; Wang, W.; Zhang, L.; Zheng, Y.; Wang, Z. Insights into the Surface-Defect Dependence of Photoreactivity over CeO_2 Nanocrystals with Well-Defined Crystal Facets. *ACS Catal.* **2015,** 5, 4851-4858.

21. Mann, A. K. P.; Wu, Z.; Calaza, F. C.; Overbury, S. H. Adsorption and Reaction of Acetaldehyde on Shape-Controlled CeO_2 Nanocrystals: Elucidation of Structure–Function Relationships. *ACS Catal.* **2014,** 4, 2437-2448.

22. Sayle, D. C.; Maicaneanu, S. A.; Watson, G. W. Atomistic Models for CeO_2(111), (110), and (100) Nanoparticles, Supported on Yttrium-Stabilized Zirconia. *J. Am. Chem. Soc.* **2002,** 124, 11429-11439.

23. Si, R.; Flytzani-Stephanopoulos, M. Shape and Crystal-Plane Effects of Nanoscale Ceria on the Activity of Au-CeO_2 Catalysts for the Water–Gas Shift Reaction. *Angew. Chem. Int. Ed.* **2008,** 47, 2884-2887.

24. Carrettin, S.; Concepción, P.; Corma, A.; López Nieto, J. M.; Puntes, V. F. Nanocrystalline CeO_2 Increases the Activity of Au for CO Oxidation by Two Orders of Magnitude. *Angew. Chem. Int. Ed.* **2004,** 43, 2538-2540.

25. Mai, H.-X.; Sun, L.-D.; Zhang, Y.-W.; Si, R.; Feng, W.; Zhang, H.-P.; Liu, H.-C.; Yan, C.-H. Shape-Selective Synthesis and Oxygen Storage Behavior of Ceria Nanopolyhedra, Nanorods, and Nanocubes. *J. Phys. Chem. B* **2005,** 109, 24380-24385.

26. Yang, S.; Gao, L. Controlled Synthesis and Self-Assembly of CeO_2 Nanocubes. *J. Am. Chem. Soc.* **2006,** 128, 9330-9331.

27. Wang, D.; Kang, Y.; Doan-Nguyen, V.; Chen, J.; Küngas, R.; Wieder, N. L.; Bakhmutsky, K.; Gorte, R. J.; Murray, C. B., Synthesis and Oxygen Storage Capacity of Two-Dimensional Ceria Nanocrystals. *Angew. Chem. Int. Ed.* **2011,** 50, 4378-4381.

28. Li, P.; Zhou, Y.; Zhao, Z.; Xu, Q.; Wang, X.; Xiao, M.; Zou, Z., Hexahedron Prism-Anchored Octahedronal CeO_2: Crystal Facet-Based Homojunction Promoting Efficient Solar Fuel Synthesis. *J. Am. Chem. Soc.* **2015,** 137, 9547-9550.

29. Lee, S. S.; Song, W.; Cho, M.; Puppala, H. L.; Nguyen, P.; Zhu, H.; Segatori, L.; Colvin, V. L. Antioxidant Properties of Cerium Oxide Nanocrystals as a Function of Nanocrystal Diameter and Surface Coating. *ACS Nano* **2013,** 7, 9693-9703.

30. Yu, T.; Joo, J.; Park, Y. I.; Hyeon, T. Large-Scale Nonhydrolytic Sol–Gel Synthesis of Uniform-Sized Ceria Nanocrystals with Spherical, Wire, and Tadpole Shapes. *Angew. Chem. Int. Ed.* **2005,** 44, 7411-7414.

31. Lim, B.; Xia, Y., Metal Nanocrystals with Highly Branched Morphologies. *Angew. Chem. Int. Ed.* **2011,** 50, 76-85.

32. Milliron, D. J.; Hughes, S. M.; Cui, Y.; Manna, L.; Li, J.; Wang, L.-W.; Paul Alivisatos, A.. Colloidal nanocrystal heterostructures with linear and branched topology. *Nature* **2004,** 430, 190-195.

33. Weiner, R. G.; Skrabalak, S. E. Metal Dendrimers: Synthesis of Hierarchically Stellated Nanocrystals by Sequential Seed-Directed Overgrowth. *Angew. Chem.* **2015,** 127, 1197-1200.

34. Li, Y.; Ding, W.; Li, M.; Xia, H.; Wang, D.; Tao, X. Synthesis of core-shell Au-Pt nanodendrites with high catalytic performance via overgrowth of platinum on in situ gold nanoparticles. *J. Mater. Chem. A* **2015,** 3, 368-376.

35. Lim, B.; Lu, X.; Jiang, M.; Camargo, P. H. C.; Cho, E. C.; Lee, E. P.; Xia, Y. Facile Synthesis of Highly Faceted Multioctahedral Pt Nanocrystals through Controlled Overgrowth. *Nano Lett.* **2008,** 8, 4043-4047.

36. Lee, S. S.; Zhu, H.; Contreras, E. Q.; Prakash, A.; Puppala, H. L.; Colvin, V. L. High Temperature Decomposition of Cerium Precursors To Form Ceria Nanocrystal Libraries for Biological Applications. *Chem. Mater.* **2012,** 24, 424-432.

37. Gu H.; Soucek M. D. Preparation and Characterization of Monodisperse Cerium Oxide Nanoparticles in Hydrocarbon Solvents. *Chem. Mater.* **2007**, 19, 1103–1110.

38. Cheong, S.; Watt, J.; Ingham, B.; Toney, M. F.; Tilley, R. D. In Situ and Ex Situ Studies of Platinum Nanocrystals: Growth and Evolution in Solution. *J. Am. Chem. Soc.* **2009,** 131, 14590-14595.

39. Yin, Z.; Zheng, H.; Ma, D.; Bao, X. Porous Palladium Nanoflowers that Have Enhanced Methanol Electro-Oxidation Activity. *J. Phys. Chem. C* **2009,** 113, 1001-1005.

40. Zhou, H.-P.; Zhang, Y.-W.; Mai, H.-X.; Sun, X.; Liu, Q.; Song, W.-G.; Yan, C.-H. Spontaneous Organization of Uniform CeO_2 Nanoflowers by 3D Oriented Attachment in Hot Surfactant Solutions Monitored with an In Situ Electrical Conductance Technique. *Chem. Eur. J.* **2008,** 14, 3380-3390.

41. Jun, Y.-w.; Choi, J.-s.; Cheon, J. Shape Control of Semiconductor and Metal Oxide Nanocrystals through Nonhydrolytic Colloidal Routes. *Angew. Chem. Int. Ed.* **2006,** 45, 3414-3439.

42. Zhang, J.; Ohara, S.; Umetsu, M.; Naka, T.; Hatakeyama, Y.; Adschiri, T. Colloidal Ceria Nanocrystals: A Tailor-Made Crystal Morphology in Supercritical Water. *Adv. Mater.* **2007,** 19, 203-206.

43. Deori, K.; Gupta, D.; Saha, B.; Deka, S. Design of 3-Dimensionally Self-Assembled CeO_2 Nanocube as a Breakthrough Catalyst for Efficient Alkylarene Oxidation in Water. *ACS Catal.* **2014,** 4, 3169-3179.

44. Mastria, R.; Rizzo, A.; Nobile, C; Kumar, S; Maruccio, G; Gigli, G. Improved photovoltaic performances by post-deposition acidic treatments on tetrapod shaped colloidal nanocrystal solids. *Nanotechnology*. **2012**, 23, 305403.

45. Liu, Y.; Cadavid, D.; Ibanez, M.; De Roo, J.; Ortega, S.; Dobrozhan, O.; V. Kovalenko, M.; Cabot, A., Colloidal $AgSbSe_2$ nanocrystals: surface analysis, electronic doping and processing into thermoelectric nanomaterials. *Journal of Materials Chemistry C* **2016**, 4, 4756-4762

46. Green, M. L. H.; Parkin, G. Application of the Covalent Bond Classification Method for the Teaching of Inorganic Chemistry. *J. Chem. Educ*. **2014**, 91, 807-816.

47. De Roo, J.; De Keukeleere, K.; Hens, Z.; Van Driessche, I. From ligands to binding motifs and beyond; the enhanced versatility of nanocrystal surfaces. *Dalton Trans.* **2016,** 45, 13277-13283.

48. Buonsanti, R.; Llordes, A.; Aloni, S.; Helms, B. A.; Milliron, D. J. Tunable Infrared Absorption and Visible Transparency of Colloidal Aluminum-Doped Zinc Oxide Nanocrystals. *Nano Lett.* **2011,** 11, 4706-4710.

49. Zhong, X.; Feng, Y.; Zhang, Y.; Lieberwirth, I.; Knoll, W. Nonhydrolytic Alcoholysis Route to Morphology-Controlled ZnO Nanocrystals. *Small* **2007,** 3, 1194-1199.

50. Chen, Y.; Kim, M.; Lian, G.; Johnson, M. B.; Peng, X. Side Reactions in Controlling the Quality, Yield, and Stability of High Quality Colloidal Nanocrystals. *J. Am. Chem. Soc.* **2005,** 127, 13331-13337.

51. Zherebetskyy, D.; Scheele, M.; Zhang, Y.; Bronstein, N.; Thompson, C.; Britt, D.; Salmeron, M.; Alivisatos, P.; Wang, L.-W. Hydroxylation of the surface of PbS nanocrystals passivated with oleic acid. *Science* **2014,** 344, 1380-1384.

52. Yu, T.; Joo, J.; Park, Y. I.; Hyeon, T., Large-Scale Nonhydrolytic Sol–Gel Synthesis of Uniform-Sized Ceria Nanocrystals with Spherical, Wire, and Tadpole Shapes. *Angewandte Chemie International Edition* **2005,** *44* (45), 7411-7414.

53. Li, P.; Zhou, Y.; Zhao, Z.; Xu, Q.; Wang, X.; Xiao, M.; Zou, Z., Hexahedron Prism-Anchored Octahedronal CeO2: Crystal Facet-Based Homojunction Promoting Efficient Solar Fuel Synthesis. *Journal of the American Chemical Society* **2015,** *137* (30), 9547-9550.

54. Sing, K. S. W.; Eerett, D. H.; Haul, R. A. W.; Moscou, L.; Pierotti, R. A.; Rouquerol, J.; Siemieniewska, T. Reporting physisorption data for gas/solid systems with special reference to the determination of surface area and porosity. *Pure Appl. Chem.* **1985,** 57, 603.

3. Synthesis of metal chalcogenide NCs: the case of $Cu_2ZnSnSe_4$ NCs

Abstract

The functional properties of quaternary I_2–II–IV–VI_4 nanomaterials, with potential interest in various technological fields, are highly sensitive to compositional variations, which is a challenging parameter to adjust. Here we demonstrate the presence of phosphonic acids to aid controlling the reactivity of the II element monomer to be incorporated in quaternary $Cu_2ZnSnSe_4$ (CZTSe) nanoparticles (NPs) and thus to provide a more reliable way to adjust the final NP metal ratios. Furthermore, we demonstrate the composition control in such multi-valence NPs to allow modifying charge carrier concentrations in nanomaterials produced from the assembly of these building blocks.

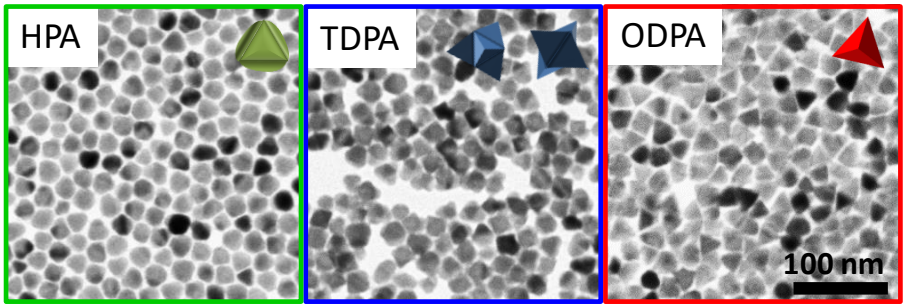

3.1. Introduction

Quaternary copper-based chalcogenides have been proposed as low-cost and non-toxic alternative materials in numerous applications.[1,2] In particular, I_2–II–IV–VI_4 compounds, such as Cu_2ZnSnS_4 (CZTS) and $Cu_2ZnSnSe_4$ (CZTSe) are highly suitable as photovoltaic[3-6] and photocatalytic[1,7-11] light absorbers. Besides, some of these I_2–II–IV–VI_4 compounds have been demonstrated excellent thermoelectric properties, showing a convenient band structure and a low thermal conductivity.[12-19] In most applications, adjusting the cation ratios is fundamental to optimize functional properties. CZTSe materials with [Cu]/([Sn]+[Zn])<1 and [Zn]/[Sn]>1 have provided solar cells with the highest efficiencies.[20-22] In contrast, higher photocatalytic activities have been obtained with Cu-rich materials.[9, 23] Besides, off-stoichiometric compositions allow to adjust charge carrier concentration, which is a critical parameter in the thermoelectric energy conversion field.[24]

While several protocols to produce quaternary chalcogenide NPs already exist,[13,14, 25-29] the control of the nanocrystal size, shape and composition of such complex materials still remains a challenge. Generally, relatively large size and shape dispersions have been obtained. While size and shape may play an irrelevant role in several applications, especially on those requiring a posterior crystallization treatment, broad distributions denote a poor control of the reaction mechanism and thus also of the composition. Indeed, broad size and shape distributions may be indicative of a large compositional dispersion within each sample, which may difficult the optimization of the compositional-dependent functional properties of the final nanomaterials.[25,30-32]

The formation of quaternary copper-based selenides is generally assumed not to proceed through the simultaneous reaction of the four elements in the stoichiometric amounts, but through the initial formation of Cu_xSe nuclei and the subsequent incorporation of the II and IV cations.[13, 14, 26, 33] Within this reaction mechanism, the reactivity of the II and IV precursors, or the related monomers formed, is essential. In this regard, conventional procedures based on the reaction of metal chlorides with trioctylphosphine selenide in the presence of amines have demonstrated the introduction of the II element to be particularly challenging.[33]

We demonstrate here the addition of phosphonic acids to aid introducing controlled amounts of Zn in CZTSe NPs. Furthermore, we also present here the compositional dependence of the electronic properties of CZTSe nanomaterials obtained from the consolidation of CZTSe NPs into pellets.

3.2. Experimental

3.2.1. Synthesis of $Cu_2ZnSnSe_4$ NCs

Copper (I) chloride (50 mg, 0.50 mmol), zinc oxide (41 mg, 0.50 mmol), zinc (IV) chloride pentahydrate (88 mg, 0.25 mmol), hexadecylamine (1234 mg, 5 mM) and n-phosphonic acid (0.1 mmol, hexylphosphonic acid, HPA, tetradecylphosphonic acid, TDPA or octadeclyphosphonic acid, ODPA) were dissolved in 10 mL ODE within a 50 ml three-neck flask connected to a Schlenk line through a Liebig condenser. The solution was heated under argon flow to 200 ºC and maintained at this temperature for 1h to get rid of low-boiling point impurities, including water. Then, the solution was heated to 295 °C. At this temperature, 4 mL of a 3 mM selenium solution prepared by dissolving selenium (IV) oxide in ODE (5h stirring at 190 ºC under argon atmosphere) and pre-heated to 180 °C to reduce the temperature drop, was injected through a septum. The mixture was allowed to react for 5 min before cooling down to ambient temperature. The formation of CZTSe NPs was qualitatively followed by the color change of the mixture from an initial light yellow to green and eventually black. 3 mL of oleic acid were added to the mixture during the cooling at ~70 °C to replace the weakly bound HDA. The final solution containing the CZTSe NPs was mixed with 10 mL of chloroform and sonicate for 5 minutes. Finally, CZTSe NPs were separated by centrifugation at 4000 rpm during 5 minutes.

3.2.2. Preparation of pellets

To characterize CZTSe transport properties, NPs were thoroughly purified by multiple redispersion (chloroform) and precipitation (isopropanol) cycles until they could not be re-disperse in organic solvents. Dried NPs were heated to 500 °C for 1 hour under an Ar flow inside a tube furnace. The obtained nanopowder was hot-pressed into 12 mm pellets at 40 MPa and 500 °C for 5 min using a Rapid Hot Press (RHP) system[34]. In this system, the heat is provided by an induction coil operated in the RF range applied directly to a graphite die acting as a susceptor. This set up configuration allows increasing temperature at a similar rate than spark plasma sintering (SPS). However, during RHP only the die body is heated inside the induction coil enabling faster cooling of the die and chamber. The density of the pressed pellets was in the range 92-96 % of theoretical value, measured by weight/volume.

3.2.3. Electrical conductivity and thermopower measurements

Seebeck coefficients were measured using a static DC method. Electrical resistivities were obtained by four-probe method. Both Seebeck coefficient and electrical resistivity were simultaneously measured on a Linseis LSR-3 system under helium atmosphere. Hall coefficients were measured using the Van der Pauw technique under a reversible magnetic field of 2 T.

3.3. Results and discussion

CZTSe NPs with narrow size distributions, having size dispersions below 10 %, were systematically obtained by the above detailed procedure as shown in the representative transmission electron microscopy (TEM) micrographs of Fig. 1. The average NP size could be controlled by the reaction time and temperature in the range from 10 to 25 nm. The particular reaction kinetics of the different elements with selenium impeded the preparation of stoichiometric CZTSe NPs with sizes below 10 nm as relatively long reaction times, few minutes, were needed for all the elements to be introduced in the appropriate amount. CZTSe NPs typically showed tetrahedral geometries, but the exact morphology after 5 min of reaction strongly depended on the phosphonic acid used. The length of the alkyl chain of the phosphonic acid ligands has been already demonstrated to be crucial in controlling the morphology of CdSe NPs.[35] However, in CZTSe NPs we could not identify a clear trend which we associated to the complexity of the system and the different reactivity of each element. Further explanation on the role of the phosphonic acid will be addressed further on.

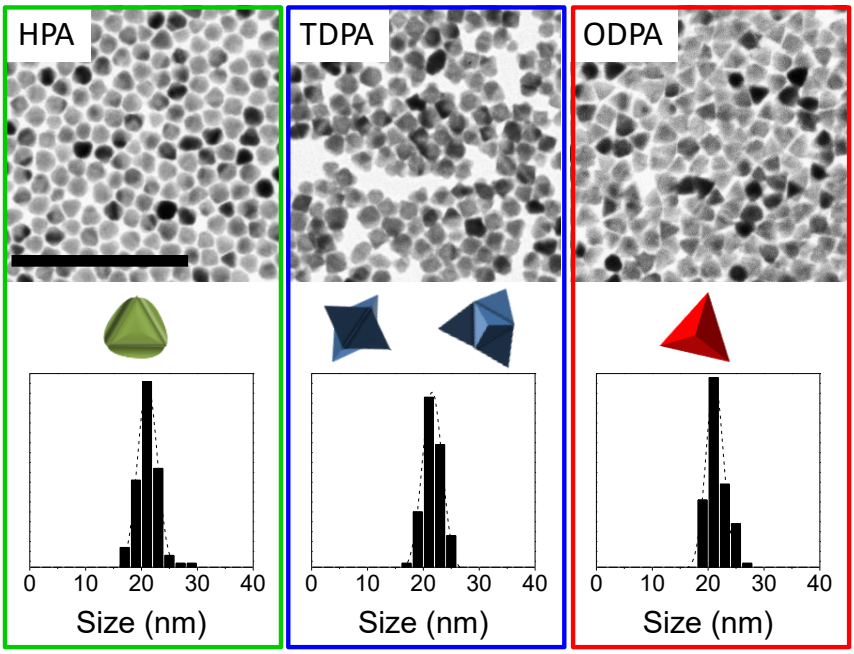

Fig. 1. TEM micrographs and size distribution histograms of the CZTSe particles obtained after 5 minutes of reaction using different phosphonic acids: HPA, TDPA and ODPA as indicated. Scale-bar = 200 nm.

The overall composition of the initially formed NPs was rich in Cu and Se thus poor in Zn and Sn as determined by energy dispersive EDX and verified by ICP analysis. With the reaction time, Sn first and Zn afterward were introduced within the NPs. In the absence of any phosphonic acid, zinc content introduced into the NPs was B10 % of the stoichiometric amount even with an excess of Zn precursor and after long reaction times. On the contrary, the addition of phosphonic acids allowed systematically obtaining >50 % of the stoichiometric Zn amount. However, just with TDPA acid, stoichiometric compositions could be properly obtained after 5 min reaction. Alkylphosphonic acids have been extensibly used to control nucleation and growth of II–VI semiconductors due to their stronger affinity with Cd^{2+} and Zn^{2+} ions to form complexes than fatty amines.[36-39] As previously reported, we believe phosphonic acids to complexate with Zn2? via dissolution of ZnO in the mixture of surfactants during

decomposition of the alkylphosphonic acid.[40] Such Znphosphonate complexes facilitate the introduction of Zn ions in preformed Cu–Se and Cu–Sn–Se NPs. This experimental evidence could be associated with the fact that usually a phosphonate group can coordinate with three or more cation centers, instead of one or two for the amine group.[41,42] This higher coordination could facilitate the incorporation of Zn^{2+} in the partially formed NPs and hence determine the NP shape as well.

Figure 2a shows a ternary diagram with the reaction time evolution of the NP composition when TDPA is used. After 10 s reaction $Cu_{2-x}Se$ NPs were obtained and the content of Zn and Sn slowly increased with reaction time until stoichiometric composition is obtained at 300 s. In view of these results, the different reaction kinetics of Cu, Zn, and Sn with Se offers a simple strategy to control the composition of such quaternary particles by just tuning the reaction time. Another obvious strategy to control composition is to adjust the ratio of the different elements in the precursor solution and give enough time for all the components to incorporate within the NP. In Fig. 2b, the average composition of CZTSe NP ensembles obtained from precursor solutions with tuned Zn composition is displayed. With this approach we could go from Cu_2SnSe_3 to $Cu_2ZnSnSe_4$, by simply adding increasing amounts of Zn. Stoichiometric composition was obtained for a [Cu]/[Zn] ratio of 1 (notice that we have a large nominal excess of Zn).

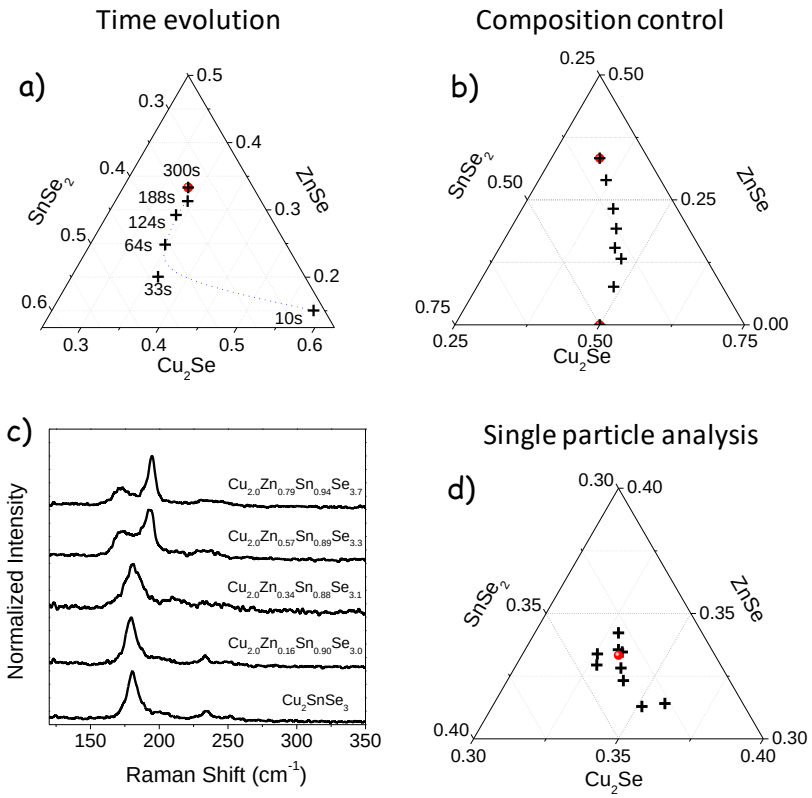

Fig. 2. a) Composition evolution of CZTSe nanoparticles obtained at 295 ºC in the presence of TDPA and using stoichiometric metal ratios in the precursor solution. b) Composition of nanoparticle ensembles obtained after 5 min reaction time at 295ºC in the presence of TDPA but using different initial precursor ratios. c) Raman spectra of the materials obtained after 5 min reaction time at 295 ºC in the presence of TDPA using different initial precursor ratios. d) Composition distribution as obtained by single particle HRTEM-EDX within a stoichiometric nanoparticle ensemble.

XRD patterns of the obtained NPs, resembled that of a tetragonal symmetry structure with the $I\overline{4}2m$ space group (JCPDS No. 01-070-7623). The similar crystal structures of compounds having different amounts of Zn did not allow us to follow the NP structural evolution with the reaction time by means of XRD. Conveniently, phonon resonance modes are much more sensitive to atomic dissimilarities within the structure. Figure 2c shows the Raman spectra of the CZTSe NPs having different amounts of Zn. A clear evolution of the spectra from Cu_2SnSe_3 to CZTSe could be observed when incorporating different amounts of Zn. No additional XRD or Raman peak was observed, pointing at the absence of secondary phases and to the possibility to produce NPs with a much broader compositional range than what can be obtained for bulk materials.[43-45] To confirm NP composition, single-particle analysis using HRTEM-EDX was also performed. On Fig. 2d a ternary diagram with the composition distribution of a stoichiometric CZTSe sample is displayed. Each cross corresponds to the composition of a single particle. In accordance with their narrow size and shape distribution, slim NP composition distributions also were measured. On the same graph, the average value of the single-particle analysis is also indicated (red point). This is in good agreement with the results of the SEM-EDX, HRTEM–EDX, and ICP analyses performed. The high yield of the detailed synthetic route (close to 90 % with respect to Cu precursor) allowed the production of grams of CZTSe NPs with narrow size distributions and controlled compositions and thus to measure their electronic properties as a function of composition. With this goal in mind, NPs were purified by multiple precipitation and re-dispersion treatments until they were not further soluble in chloroform. The final dried nanopowder was thermal treated at 500 °C for 1 h under argon atmosphere. Finally, 12 mm in diameter and 1 mm thick pellets with relative densities 92–95 % of the theoretical value were prepared by rapid hot pressing[34] (40 MPa and 500 °C for 5 min) 1 g of the annealed nanopowder. Figure 3a, b shows an SEM image and the XRD patterns of the final CZTSe nanomaterial produced. With the annealing and hot press treatments, the CZTSe crystal domain size increased by a factor 2, from an average size of 22 nm of the initial particles to an average size of 45 nm as estimated from the fitting of the XRD pattern of the final pellets. No measurable composition variations were observed with the thermal treatments.

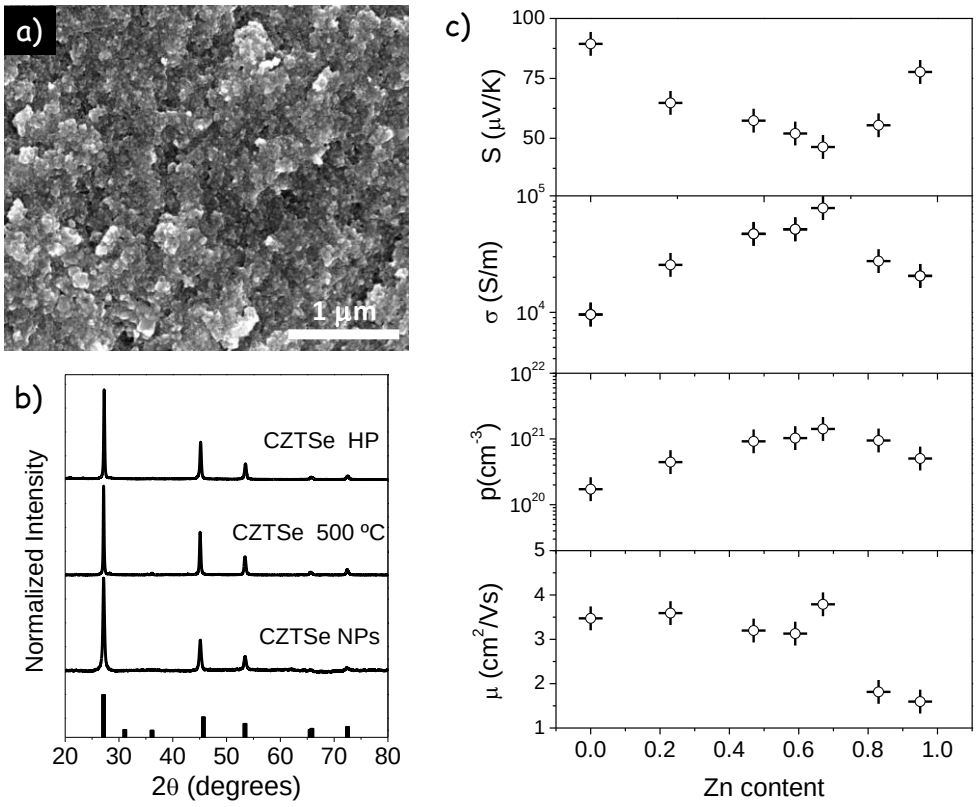

Fig. 3. a) SEM image of the hot pressed CZTSe material. b) XRD patterns of the initial nanoparticles and the nanomaterials annealed at 500 ºC and hot pressed at 500 ºC and 40 MPa. c) ambient temperature Seebeck coefficient (S), electrical conductivity (⍰), hole carrier concentration (p) and mobility (⍰) of the hot pressed nanomaterials with different Zn composition.

The Seebeck coefficient and electrical conductivity of the CZTSe nanomaterials with different Zn composition was measured at ambient temperature and are displayed in Fig. 3c. Notice how the electrical conductivity increased for the off-stoichiometric nanomaterials containing growing amounts of Zn, but decreases once approaching to the stoichiometric CZTSe composition. Hall measurements at ambient temperature showed very high carrier concentrations for all the nanomaterials, which we associate with a large interface area of the material which has associated with a large density of defects. Charge carrier concentrations increased with the initial introduction of Zn and decreased as the samples approximate the stoichiometric compositions. On the other hand, the mobility decrease with the Zn concentration in the whole composition range characterized.

3.4. Conclusions

A new synthetic strategy to produce CZTSe NPs with narrow size distribution and controlled composition involving the use of phosphonic acids was detailed. This procedure allowed controlling the composition of the final NPs in a wide range. We further demonstrated that, compositional control in these bottom-up processed multinary nanomaterials offered an accessible method to tune their charge carrier concentration within a relatively wide range.

3.5. References

1. Berger, L.; Prochukhan, V., Ternary Diamond-like Semiconductors. Consultants Bureau, New York, 1969, 55-63.
2. Aldakov, D.; Lefrançois, A.; Reiss, P., Ternary and quaternary metal chalcogenide nanocrystals: synthesis, properties and applications. *Journal of Materials Chemistry C* **2013,** *1* (24), 3756-3776.
3. Carrete, A.; Shavel, A.; Fontané, X.; Montserrat, J.; Fan, J.; Ibáñez, M.; Saucedo, E.; Pérez-Rodríguez, A.; Cabot, A., Antimony-based ligand exchange to promote crystallization in spray-deposited $Cu_2ZnSnSe_4$ solar cells. *Journal of the American Chemical Society* **2013,** *135* (43), 15982-15985.
4. Fella, C. M.; Romanyuk, Y. E.; Tiwari, A. N., Technological status of $Cu_2ZnSn(S, Se)_4$ thin film solar cells. *Solar Energy Materials and Solar Cells* **2013,** *119*, 276-277.
5. Mitzi, D. B.; Gunawan, O.; Todorov, T. K.; Wang, K.; Guha, S., The path towards a high-performance solution-processed kesterite solar cell. *Solar Energy Materials and Solar Cells* **2011,** *95* (6), 1421-1436.
6. Todorov, T. K.; Tang, J.; Bag, S.; Gunawan, O.; Gokmen, T.; Zhu, Y.; Mitzi, D. B., Beyond 11% efficiency: characteristics of state-of-the-art $Cu_2ZnSn(S, Se)_4$ solar cells. *Advanced Energy Materials* **2013,** *3* (1), 34-38.
7. Ikeda, S.; Nakamura, T.; Harada, T.; Matsumura, M., Multicomponent sulfides as narrow gap hydrogen evolution photocatalysts. *Physical Chemistry Chemical Physics* **2010,** *12* (42), 13943-13949.
8. Miyauchi, M.; Hanayama, T.; Atarashi, D.; Sakai, E., Photoenergy conversion in p-Type Cu_2ZnSnS_4 nanorods and n-Type metal oxide composites. *The Journal of Physical Chemistry C* **2012,** *116* (45), 23945-23950.
9. Yu, X.; Shavel, A.; An, X.; Luo, Z.; Ibáñez, M.; Cabot, A., Cu_2ZnSnS_4-Pt and Cu_2ZnSnS_4-Au heterostructured nanoparticles for photocatalytic water splitting and pollutant degradation. *Journal of the American Chemical Society* **2014,** *136* (26), 9236-9239.
10. Yu, X.; An, X.; Genç, A.; Ibáñez, M.; Arbiol, J.; Zhang, Y.; Cabot, A., Cu_2ZnSnS_4–Pt(M) (M= Co, Ni) nanoheterostructures for photocatalytic hydrogen evolution. *The Journal of Physical Chemistry C* **2015,** *119* (38), 21882-21888.
11. Yu, X.; Liu, J.; Genç, A.; Ibáñez, M.; Luo, Z.; Shavel, A.; Arbiol, J.; Zhang, G.; Zhang, Y.; Cabot, A., Cu_2ZnSnS_4–Ag_2S nanoscale p–n Heterostructures as sensitizers for photoelectrochemical water splitting. *Langmuir* **2015,** *31* (38), 10555-10561.
12. Heinrich, C. P.; Day, T. W.; Zeier, W. G.; Snyder, G. J.; Tremel, W., Effect of Isovalent Substitution on the Thermoelectric Properties of the $Cu_2ZnGeSe_{4-x}S_x$ Series of Solid Solutions. *Journal of the American Chemical Society* **2013,** *136* (1), 442-448.
13. Ibáñez, M.; Cadavid, D.; Zamani, R.; García-Castelló, N.; Izquierdo-Roca, V.; Li, W.; Fairbrother, A.; Prades, J. D.; Shavel, A.; Arbiol, J., Composition control and thermoelectric properties of quaternary chalcogenide nanocrystals: the case of stannite $Cu_2CdSnSe_4$. *Chemistry of Materials* **2012,** *24* (3), 562-570.
14. Ibáñez, M.; Zamani, R.; LaLonde, A.; Cadavid, D.; Li, W.; Shavel, A.; Arbiol, J.; Morante, J. R.; Gorsse, S.; Snyder, G. J., $Cu_2ZnGeSe_4$ nanocrystals: synthesis and thermoelectric properties. *Journal of the American Chemical Society* **2012,** *134* (9), 4060-4063.
15. Ibáñez, M.; Cadavid, D.; Anselmi-Tamburini, U.; Zamani, R.; Gorsse, S.; Li, W.; López, A. M.; Morante, J. R.; Arbiol, J.; Cabot, A., Colloidal synthesis and thermoelectric properties of Cu_2SnSe_3 nanocrystals. *Journal of Materials Chemistry A* **2013,** *1* (4), 1421-1426.
16. Li, W.; Ibáñez, M.; Zamani, R. R.; García-Castelló, N.; Gorsse, S.; Cadavid, D.; Prades, J. D.; Arbiol, J.; Cabot, A., Cu 2 $HgSnSe_4$ nanoparticles: synthesis and thermoelectric properties. *CrystEngComm* **2013,** *15* (44), 8966-8971.

17. Li, W.; Ibáñez, M.; Cadavid, D.; Zamani, R. R.; Rubio-Garcia, J.; Gorsse, S.; Morante, J. R.; Arbiol, J.; Cabot, A., Colloidal synthesis and functional properties of quaternary Cu-based semiconductors: $Cu_2HgGeSe_4$. *Journal of nanoparticle research* **2014,** *16* (3), 2297.
18. Liu, M. L.; Chen, I. W.; Huang, F. Q.; Chen, L. D., Improved Thermoelectric Properties of Cu-Doped Quaternary Chalcogenides of $Cu_2CdSnSe_4$. *Advanced Materials* **2009,** *21* (37), 3808-3812.
19. Zeier, W. G.; LaLonde, A.; Gibbs, Z. M.; Heinrich, C. P.; Panthöfer, M.; Snyder, G. J.; Tremel, W., Influence of a Nano Phase Segregation on the Thermoelectric Properties of the p-Type Doped Stannite Compound $Cu_{2+x}Zn_{1-x}GeSe_4$. *Journal of the American Chemical Society* **2012,** *134* (16), 7147-7154.
20. Chen, S.; Gong, X.; Walsh, A.; Wei, S.-H., Defect physics of the kesterite thin-film solar cell absorber Cu_2ZnSnS_4. *Applied Physics Letters* **2010,** *96* (2), 021902.
21. Tanaka, K.; Fukui, Y.; Moritake, N.; Uchiki, H., Chemical composition dependence of morphological and optical properties of Cu_2ZnSnS_4 thin films deposited by sol–gel sulfurization and Cu_2ZnSnS_4 thin film solar cell efficiency. *Solar Energy Materials and Solar Cells* **2011,** *95* (3), 838-842.
22. Xiao, W.; Wang, J.; Zhao, X.; Wang, J.; Huang, G.; Cheng, L.; Jiang, L.; Wang, L., Intrinsic defects and Na doping in Cu_2ZnSnS_4: A density-functional theory study. *Solar Energy* **2015,** *116*, 125-132.
23. Sevik, C.; Çağın, T., Assessment of thermoelectric performance of Cu_2ZnSnX_4, X= S, Se, and Te. *Applied Physics Letters* **2009,** *95* (11), 112105.
24. Liu, M.-L.; Huang, F.-Q.; Chen, L.-D.; Chen, I.-W., A wide-band-gap p-type thermoelectric material based on quaternary chalcogenides of Cu_2ZnSnQ_4 (Q= S, Se). *Applied Physics Letters* **2009,** *94* (20), 202103.
25. Fan, F. J.; Wang, Y. X.; Liu, X. J.; Wu, L.; Yu, S. H., Large-Scale Colloidal Synthesis of Non-Stoichiometric $Cu_2ZnSnSe_4$ Nanocrystals for Thermoelectric Applications. *Advanced Materials* **2012,** *24* (46), 6158-6163.
26. Ibáñez, M.; Zamani, R.; Li, W.; Shavel, A.; Arbiol, J.; Morante, J. R.; Cabot, A., Extending the nanocrystal synthesis control to quaternary compositions. *Crystal Growth & Design* **2012,** *12* (3), 1085-1090.
27. Khare, A.; Wills, A. W.; Ammerman, L. M.; Norris, D. J.; Aydil, E. S., Size control and quantum confinement in Cu_2ZnSnS_4 nanocrystals. *Chemical communications* **2011,** *47* (42), 11721-11723.
28. Singh, A.; Geaney, H.; Laffir, F.; Ryan, K. M., Colloidal synthesis of wurtzite Cu2ZnSnS4 nanorods and their perpendicular assembly. *Journal of the American Chemical Society* **2012,** *134* (6), 2910-2913.
29. Singh, A.; Singh, S.; Levcenko, S.; Unold, T.; Laffir, F.; Ryan, K. M., Compositionally tunable photoluminescence emission in $Cu_2ZnSn(S_{1-x}Se_x)_4$ nanocrystals. *Angewandte Chemie International Edition* **2013,** *52* (35), 9120-9124.
30. Guo, Q.; Hillhouse, H. W.; Agrawal, R., Synthesis of Cu_2ZnSnS_4 nanocrystal ink and its use for solar cells. *Journal of the American Chemical Society* **2009,** *131* (33), 11672-11673.
31. Haas, W.; Rath, T.; Pein, A.; Rattenberger, J.; Trimmel, G.; Hofer, F., The stoichiometry of single nanoparticles of copper zinc tin selenide. *Chemical communications* **2011,** *47* (7), 2050-2052.
32. Shavel, A.; Arbiol, J.; Cabot, A., Synthesis of Quaternary Chalcogenide Nanocrystals: Stannite $Cu_2Zn_xSn_ySe_{1+x+2y}$. *Journal of the American Chemical Society* **2010,** *132* (13), 4514-4515.
33. Riha, S. C.; Parkinson, B. A.; Prieto, A. L., Solution-based synthesis and characterization of Cu_2ZnSnS_4 nanocrystals. *Journal of the American Chemical Society* **2009,** *131* (34), 12054-12055.
34. LaLonde, A. D.; Ikeda, T.; Snyder, G. J., Rapid consolidation of powdered materials by induction hot pressing. *Review of Scientific Instruments* **2011,** *82* (2), 025104.

35. Wang, W.; Banerjee, S.; Jia, S.; Steigerwald, M. L.; Herman, I. P., Ligand control of growth, morphology, and capping structure of colloidal CdSe nanorods. *Chemistry of materials* **2007,** *19* (10), 2573-2580.
36. García-Rodríguez, R. l.; Hendricks, M. P.; Cossairt, B. M.; Liu, H.; Owen, J. S., Conversion reactions of cadmium chalcogenide nanocrystal precursors. *Chemistry of Materials* **2013,** *25* (8), 1233-1249.
37. Ji, X.; Copenhaver, D.; Sichmeller, C.; Peng, X., Ligand bonding and dynamics on colloidal nanocrystals at room temperature: the case of alkylamines on CdSe nanocrystals. *Journal of the American Chemical Society* **2008,** *130* (17), 5726-5735.
38. Peng, Z. A.; Peng, X., Nearly monodisperse and shape-controlled CdSe nanocrystals via alternative routes: nucleation and growth. *Journal of the American Chemical Society* **2002,** *124* (13), 3343-3353.
39. Pradhan, N.; Reifsnyder, D.; Xie, R.; Aldana, J.; Peng, X., Surface ligand dynamics in growth of nanocrystals. *Journal of the American Chemical Society* **2007,** *129* (30), 9500-9509.
40. Liu, H.; Owen, J. S.; Alivisatos, A. P., Mechanistic study of precursor evolution in colloidal group II− VI semiconductor nanocrystal synthesis. *Journal of the American Chemical Society* **2007,** *129* (2), 305-312.
41. Cao, G.; Lynch, V. M.; Yacullo, L. N., Synthesis, structural characterization, and intercalation chemistry of two layered cadmium organophosphonates. *Chemistry of materials* **1993,** *5* (7), 1000-1006.
42. Fredoueil, F.; Evain, M.; Massiot, D.; Bujoli-Doeuff, M.; Janvier, P.; Clearfield, A.; Bujoli, B., Synthesis and characterization of two new cadmium phosphonocarboxylates $Cd_2(OH)(O_3PC_2H_4CO_2)$ and $Cd_3(O_3PC_2H_4CO_2)_2{\cdot}2H_2O$. *Journal of the Chemical Society, Dalton Transactions* **2002,** (7), 1508-1512.
43. Dudchak, I.; Piskach, L., Phase equilibria in the Cu_2SnSe_3–$SnSe_2$–ZnSe system. *Journal of alloys and compounds* **2003,** *351* (1-2), 145-150.
44. Nakamura, S.; Maeda, T.; Wada, T., Phase stability and electronic structure of In-free photovoltaic materials: $Cu_2ZnSiSe_4$, $Cu_2ZnGeSe_4$, and $Cu_2ZnSnSe_4$. *Japanese Journal of Applied Physics* **2010,** *49* (12R), 121203.
45. Maeda, T.; Nakamura, S.; Wada, T., First principles calculations of defect formation in in-free photovoltaic semiconductors Cu_2ZnSnS_4 and $Cu_2ZnSnSe_4$. *Japanese Journal of Applied Physics* **2011,** *50* (4S), 04DP07

4. Assembly of metal-oxide NCs into gels and aerogels

Abstract

This chapter is devoted to establishing of the procedure to assemble of metal oxide NCs into gels and aerogels. We present a novel method to produce crystalline oxide aerogels which is based on the cross linking of preformed colloidal NCs triggered by propylene oxide (PO). Cerium oxide, titanium oxide and iron oxide were used to illustrate this new approach. Ceria, titania and iron oxide colloidal NCs with tuned geometry and crystal facets were produced in solution from the decomposition of a suitable salt in the presence of OAm. The native surface ligands were replaced by amino acids, rendering the NCs colloidally stable in polar solvents. The NC colloidal solution was then gelled by adding PO, which gradually stripped the ligands from the NC surface, triggering a slow NC aggregation. NC-based metal oxide aerogels displayed both high surface areas and excellent crystallinity associated with the crystalline nature of the constituent building blocks, even without any annealing step. Such NC-based metal oxide aerogels showed higher thermal stability compared with aerogels directly produced from ionic precursors using conventional sol-gel chemistry strategies.

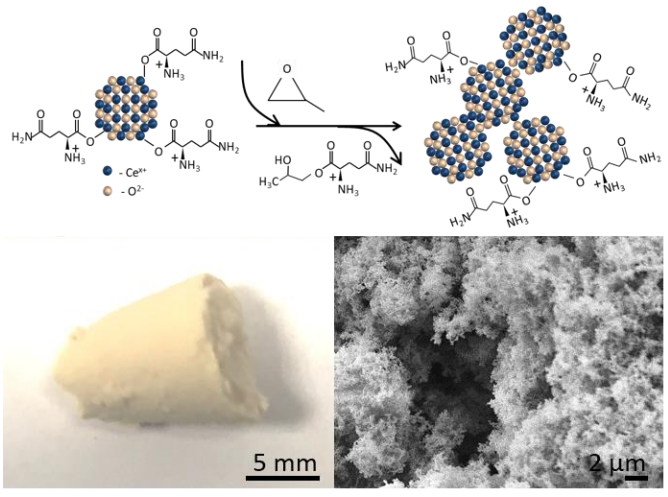

4.1. Introduction

Mesoporous materials with high surface to bulk ratios are essential components in applications involving interaction with the surrounding media, including catalysis, sensing, filtering and adsorption.[1-2] Among them, the highly porous disordered networks found in gels and aerogels are particularly appealing owing to the high accessibility they provide to fluids and reactants.

Such highly porous materials are commonly produced from ionic or molecular precursors following sol–gel chemistry approaches. Common protocols involve the use of metal alkoxide precursors that undergo hydrolysis and condensation.[3-4] Alternative metal salts are also used with the aid of an epoxide as gelation promoter.[5-8] Due to the moderate temperature of the gelation processes, the gels produced in this way are characterized by low crystallinities, thus generally requiring thermal annealing to achieve long range atomic order. This thermal process usually results in a reduction of the surface area and prevents accurate control over crystallographic domain size, facets and phase.

An alternative strategy to produce mesoporous materials with full versatility in terms of crystal domain parameters and composition is the cross-linking of pre-synthesized colloidal NCs.[9-12] This approach allows exploiting the huge palette of colloidal NCs with precisely controlled properties currently available. It thus offers evident advantages in terms of producing porous nanomaterials with improved crystallinity, controlled composition and structure and tuned surface facets, and porous nanocomposites with complex composition and phase distributions.

Colloidal NCs are generally produced using long chain surface organic ligands that control their growth and sterically stabilize them in non-polar solvents.[13-14] To optimize the NCs' performance, such ligands are generally replaced by smaller molecules that maximize or tune interaction with the surrounding media. In this vein, the use of short amino acids as surface ligands provides NCs with a high versatility and thus an ample range of potential applications, from biomedical, taking advantage of the biocompatibility of amino acids,[15] to technological, taking advantage for instance of the efficient CO_2 adsorption provided by the amino group.[16-19] Additionally, the presence of both a carboxyl and an amino group provides amino acids with a very appealing surface chemistry versatility, since depending on pH, the terminal amino or carboxyl group can bind to the surface.[20-22] Thus, the surface can be charged positively or negatively, which controls the capability of the NC to interact with different species in the media.

Among metal oxides, ceria is a particularly appealing material, especially in the form of a highly porous gel/aerogel. Cerium presents relatively stable Ce^{3+} and a Ce^{4+} oxidation states which can be exploited for redox chemistry.[23] This particularity and its high photo, thermal, and chemical stability makes ceria an excellent candidate material for a number of application fields that involve interaction with the surrounding media, e.g. heterogeneous catalysis,[24-28] solid oxide fuel cells,[29] gas sensors[30] and environmental remediation.[31] While having no biological role, its low toxicity and its particular characteristics also makes ceria an interesting material for biomedical applications, e.g. as scavenger of reactive oxidation species through shuttling between Ce^{3+} and Ce^{4+} oxidation states.[32]

Titanium dioxide is one of the most used metal oxides in the field of heterogeneous catalysis, and particularly in photocatalysis. Its advantages include the high abundance of its constituent elements, a low toxicity, being used in paints, sunscreen and even food coloring, an outstanding stability, a direct bandgap, a low density of recombination centers, a sufficiently positive valence band edge to oxidize water to oxygen, and overall a very suitable surface for a range of applications involving interaction with the media.[33,34]

Iron oxide NCs are another metal oxide material that is of great importance which mainly attributed to their magnetic behaviour under certain conditions. Nanostructuration and amplified surface area of NC-based aerogel can boost the performance of iron oxide NC building blocks and facilitate their usage for application where interaction with the media is crucial, including biomedical application, sensing, separation, decontamination, catalysis, etc. Thus, we employed developed NC-gelation approach to assemble of Fe_2O_3 NCs. Furthermore, assembled iron oxide NCs into aerogel being highly magnetic can demonstrate a great promise as reusable electrodes for application related with environmental remediation.

Recent advances in the synthesis of colloidal ceria and titania NCs with tuned size and shape make such building blocks particularly appropriate to produce NC-based mesoporous nanomaterials.[35,36] Here we use preformed ceria and titania NCs functionalized with amino acids to exemplify a novel strategy to produce metal oxide gels and aerogels. The process is based on the ligand displacement from the NCs surface by the introduction of an epoxide, which triggers the cross-linking of NCs into a porous network.

4.2. Experimental

4.2.1. Synthesis of metal oxide NCs

4.2.1.1. CeO2 NCs

Ceria NCs were synthesized according to the procedure described in section 2.2.1. In brief, ceria NCs were synthesized though the thermal decomposition of cerium(III) nitrate within ODE in the presence of OAm, according to a procedure we previously reported.[32] Briefly, 0.434 g (1 mmol) of cerium(III) nitrate hexahydrate were mixed with 2 mL (6 mmol) of OAm in 4 mL of ODE in a 25 mL three neck flask and under magnetic stirring. After degassing the mixture for 30 minutes at 80 °C, the obtained brown colour solution was heated under argon flow up to 300 °C at a rate of 15 °C/min. The mixture was allowed to react at this temperature for 60 minutes before cooling it down. NCs were washed with acetone at least four times and finally dispersed in a suitable solvent (hexane, chloroform or toluene) with a concentration of 10 mg/mL for later use

4.2.1.2. TiO_2 NCs

Titanium dioxide NCs with plate morphology were synthesized via seeded growth following the procedure reported by Gordon et al..[36] The synthesis started from the preparation of a 0.2 M Ti precursor stock solution by dissolving the proper amount of TiF_4 within a 1 M OAc solution in ODE. This solution was maintained at 80 °C for 30 min under stirring within an Ar-filled glovebox. Meanwhile, 30 mmol of OAm, 1.5 mmol of OAc and 10 mL of ODE were loaded into

a 100 mL flask and degassed under vacuum and magnetic stirring at 120 °C for 60 min. After degassing, the flask was cooled down to 60 °C, and 1.5 mL of the TiF_4 stock solution was injected. Then, temperature was increased up to 290 °C and maintained at this point for 10 min to allow seed formation. Subsequently, 8 mL of the TiF_4 stock solution were continuously added into the flask at a rate of 0.3 mL/min using a syringe pump. Afterward, the reaction was stopped by removing the heating mantle. Finally, NCs were isolated by adding a mixture of 2-propanol and methanol and followed by centrifuging at 6000 rpm. These NCs were labelled as TiO_2 OAm-NCs.

4.2.1.1. FeO_x NCs

Iron oxide NCs were produced using reported procedure.[37] In brief, 0.178 g (2 mmol) of FeO(OH) fine powder, 2.26 g (8 mmol) of OAc, and 5 g (8 mmol) of ODE were loaded in a three-neck flask under magnetic stirring. After degassing for 30 min at 80 °C, the vacuum was switched to the Ar and the mixture was heated up to 320 °C and kept at this temperature for 60 min. Obtained NCs were purified according to the reported procedure.[38]

4.2.2. NCs surface modification

4.2.2.1. Surface modification with amino acids

The procedure used to replace native organic ligands with amino acids was inspired by previous work by J. de Roo et al.[19] Ligand exchange processes were carried out in air atmosphere. In a typical procedure, 1 mL of NCs dispersed in hexane (typically, 10 mg/mL) was added to a solution (prepared using mild sonication) of 7 mg of Gln in 1 mL MFA, followed by the addition of TFA (0.2 mM). The two phase mixture obtained was stirred until NCs were transferred from the upper to the bottom phase. Then, the hexane phase was discarded and a hexane/acetone mixture was added to the remaining MFA solution containing the NCs. Then NCs were precipitated and subsequently washed at least two more times by addition of MFA as a solvent and a mixture of hexane/acetone and acetonitrile as an antisolvent. Finally, NCs were redispersed in a polar solvent such as water, methanol or MFA for later use. NCs obtained after surface modification with Gln were labelled as Gln-NCs.

4.2.3. MeO NCs assembly into gel and aerogels

4.2.3.1. Gel formation

4.2.3.1.1. Gelation using NCs as precursors

The gelation procedure was carried out in air. In a typical experiment, 2 mL of MQ-water were added to 2 mL of a MFA solution of amino acid functionalized NCs (20 mg/mL). The mixture was sonicated for approximately 15 min. Then gelation was induced by adding 4 mL of PO and leaving the solution undisturbed. Gelation started after 1 h of storing undisturbed the solution and it was completed within 24 h but gels were aged for several days. Then, MFA was carefully replaced by acetone using 5 mL of acetone each time. It must be noted that the solvent exchange should be conducted with special care to avoid destroying the NC network structure. The solvent exchange was repeated at least 6 times to ensure complete removal of MFA.

4.2.3.1.2. Preparation of ceria gel from a cerium salt

Gelation of a cerium chloride sol was performed under ambient conditions following a previously reported procedure.[8] Briefly, 1 mmol of $CeCl_3 \cdot 6H_2O$ was dissolved in 3 mL of methanol. To the obtained mixture, 10 mL of PO was added. The formed solution was shaken vigorously for approximately 10 seconds and left undisturbed. The gelation occurred in 30 min and was followed by changing the sol color from transparent to milky white and light brown when the gel was formed. The obtained gel was aged undisturbed for 12 h. Afterward the solvent was exchanged by fresh acetone and isopropanol in order to get rid of unreacted products.

4.2.3.2. Gel drying into aerogel

In order to prevent collapsing its porous structure, gels were dried from supercritical CO_2. Briefly, the gel in acetone was loaded into a super-critical point dryer (SCD) chamber. Then, the chamber was sealed and it was slowly filled with liquid CO_2 until the pressure reached 73 bar. To ensure that the CO_2 was in liquid state, the temperature of the system was maintained at 17-18 °C using a Peltier element. After overnight storage undisturbed, the liquid CO_2 inside of the chamber was half-drained and fresh CO_2 was introduced. This procedure was repeated at least 6 times in one-hour intervals in order to fully replace acetone with liquid CO_2. Then, the Peltier element was switched off and the chamber was heated up to 39 °C resulting in a pressure increase up to 80-90 bars and the transition of the CO_2 from liquid to a supercritical phase. The sample was kept under these conditions for 1 h followed by slowly releasing the pressure while keeping the temperature constant.

4.3. The case of ceria NCs assembly

4.3.1. Quasi-spherical NCs

Quasi-spherical ceria NCs with an average size of 7 $\pm$ 1 nm were produced following our previously reported procedure.[32] In brief, NCs were obtained through the decomposition at 300 °C of cerium nitrate hexahydrate in an ODE solution containing OAm (Fig. 1 a). The presence of OAm at the surface of the ceria NCs limited their growth and rendered them soluble in non-polar organic solvents.

OAm was replaced by amino acids using a two-phase procedure involving the mixing of the selected amino acid dissolved in MFA and TFA with a hexane solution containing the NCs. This mixture was mixed and sonicated for several minutes, resulting in the transfer of the NCs from hexane to MFA (see experimental section for details). The final NCs could be redispersed in polar solvents such as MFA, isopropanol, methanol or water. Fig. 1 displays TEM micrographs of ceria NCs before (OAm-NCs) and after ligand exchange with Gln (Gln-NCs). Similar hydrodynamic radii were measured by DLS from OAm-NCs dispersed in hexane and Gln-NCs in different polar solvents (Fig. 1 e). Additionally, positive zeta potentials (+26 mV) were measured for Gln-NCs, which was consistent with the passivation of these NCs with a ligand containing protonated amino group (Fig. 1 f).

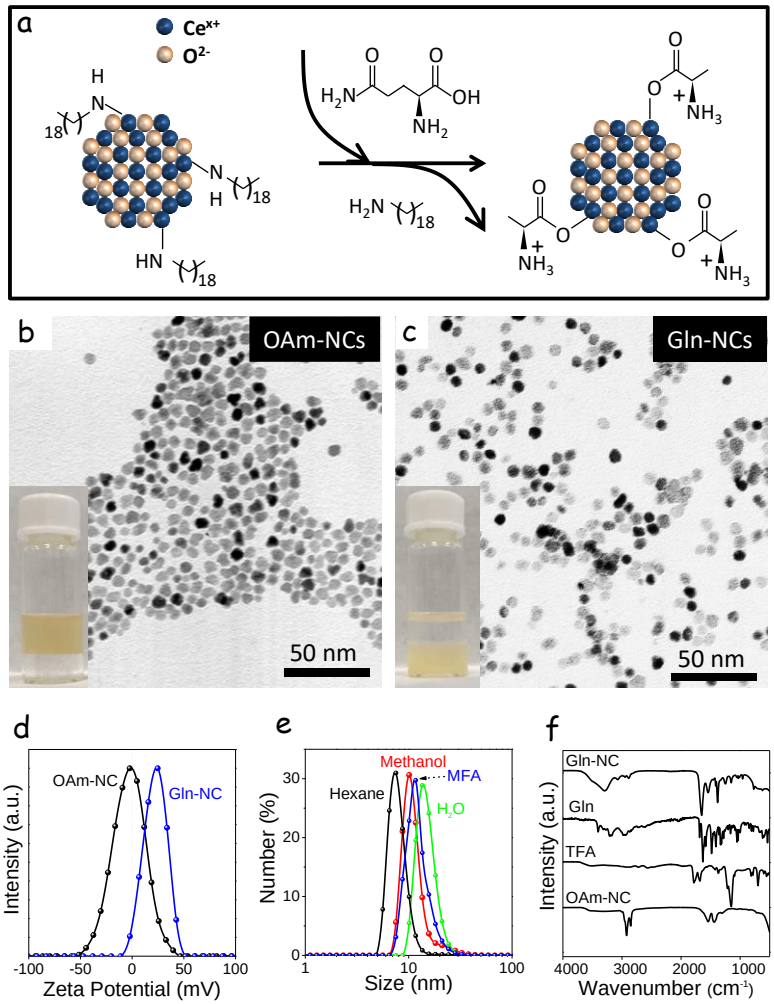

Fig. 1. a) Scheme of the OAm-to-Gln ligand exchange procedure. b) TEM micrograph of ceria NCs with native organic ligands (OAm-NC). Inset shows a photograph of the two-phase mixture used for ligand exchange purposes before mixing. The top phase corresponds to the nonpolar solvent (hexane) containing the NCs, and the bottom phase to the polar solvent (MFA) containing the amino acid and TFA. c) TEM micrograph of ceria NCs after ligand exchange with Gln (Gln-NC). Inset shows the two-phase mixture after ligand exchange, with the NCs in the polar phase. d) Zeta potential measurement of OAm-NCs and Gln-NCs. e) DLS curves of OAm-NCs in hexane and Gln-NC in H_2O, methanol and MFA.f) FTIR spectra of OAm-NCs, TFA, Gln and Gln-NCs.

FTIR analysis confirmed the displacement of OAm from the NCs surface upon ligand exchange with Gln (Fig. 1 f). The FTIR spectrum of the NCs after ligand exchange showed a strong suppression of the organic ligand fingerprint, i.e. the peaks in the region of 2820-2946 cm^{-1} attributed to the C-H stretching vibration. Besides, the similarity of the Gln and Gln-NC FTIR spectra, and in particular the peaks at around 1538 cm^{-1} and 1650 cm^{-1} ascribed to N-C=O and NH_2 stretching from the Gln molecule, confirmed the presence of this amino acid on the surface of ceria NCs after the ligand exchange process.

Amino acid-functionalized NCs were highly stable in solution, but they could be destabilized through addition of a base. We triggered the gelation of MFA solutions of ceria NCs by addition of PO. Gelation became visually evident 4 h after the addition of the epoxide and it evolved for the following 20 h. 24h after the addition of PO, the solvent was exchanged several times to eliminate residual reaction products and it was finally replaced by acetone. Then the gel was loaded into a SCD chamber where acetone was replaced by liquid CO_2. Finally, the gel was

dried from supercritical CO_2 to obtain a self-standing monolithic aerogel (see details in the experimental section, Fig. 2). Upon the supercritical drying process, the gel lost ca. 20% of its volume.

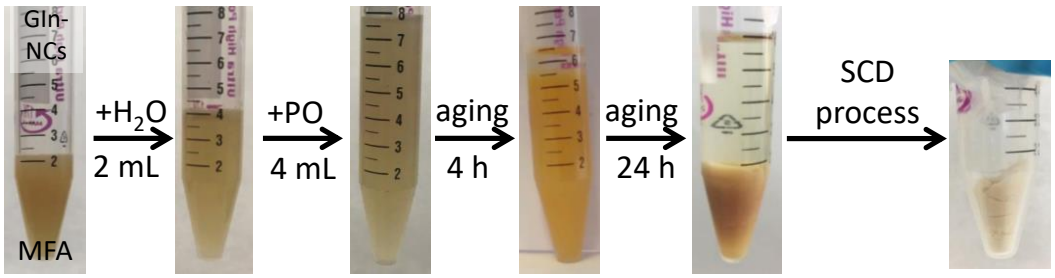

Fig. 2. Optical photographs of the different steps involved in the gelation process: 2 mL of a MFA solution containing GIn-NCs; addition of 2 mL of water and shaking to obtain homogeneous mixture; injection of 4 mL of PO; gelation became evident 4 h later; gelation visually evolved for 24 h; monolithic aerogel obtained after super-critical drying (SCD) process.

TEM and SEM micrographs (Fig. 3 a, b, respectively) displayed the ceria aerogels to have highly porous structures made of randomly interconnected ceria NCs.

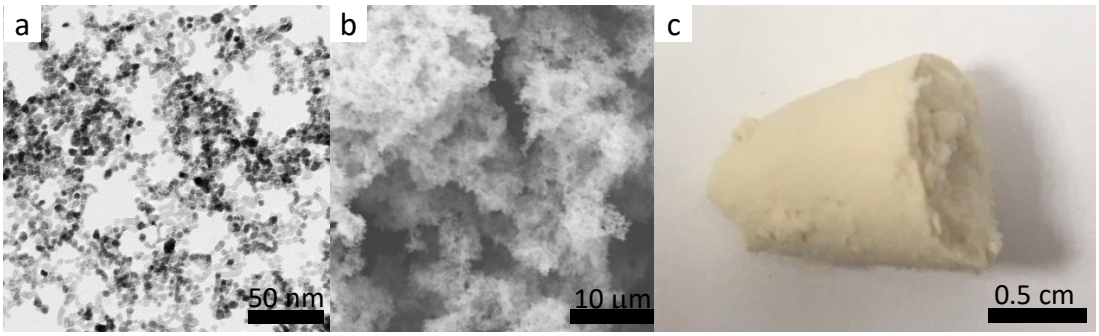

Fig. 3. a) TEM micrograph of the NC-based ceria gel obtained by the cross-linking of ceria NCs triggered by the addition of PO. b) SEM micrograph of the NC-based ceria aerogel obtained from drying the gel from supercritical CO_2 shown in (c) obtained by exposure them to propylene oxide followed by liquid CO_2 super-critical drying process.

Drying of the obtained gel using conventional method under room temperature and ambient pressure led to significant gel shrinkage and xerogel formation. However, SEM examination showed that the obtained xerogel consists of pores and voids (Fig. 4).

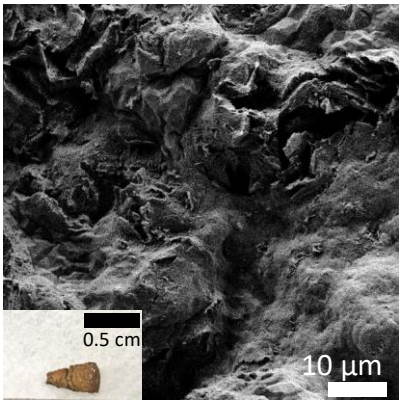

Fig. 4. SEM image of the ceria NCs xerogel and appropriate optical photograph in the inset.

Fig. 5**Fig.** represents HRTEM image and Fast Fourier Transform (FFT) of the elongated structures of CeO_2 highlighted in the images, revealing a [110] zone axis (ZA). It is confirmed that NCs aerogel is formed by the random attaching of several NCs conserving the crystalline orientation. The crystalline planes and the distance between them are indicated in black are in good agreement with the theoretical values for ceria. The FFT analysis revealed the cubic crystal lattice expected for the fluorite structure of the CeO_2 oriented in [111].

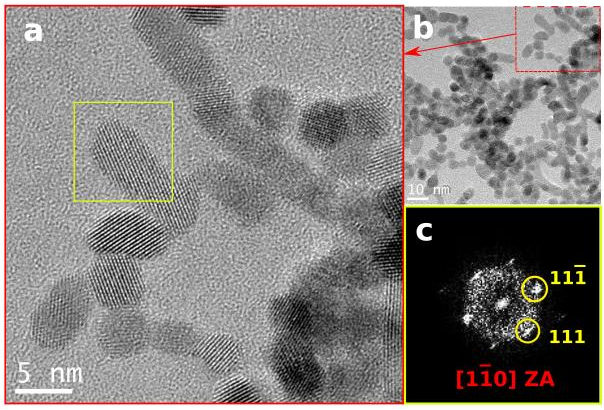

Fig. 5. CeO_2 aerogel HRTEM images. (a) Zoomed image of the highlighted area in red in (b). (c) FFT of the highlighted area in yellow in (a).

Introducing PO into a Gln-NC sol resulted in a slow cross-linking of the NCs into a disordered network, i.e. a gel. We hypothesize the NC cross-linking was triggered by a gradual stripping of Gln from the NC surface through interaction with PO. PO interacted with the acid group bond at the cerium sites, resulting in an opening of the PO ring and the stripping of the amino acid.[39] A scheme of the proposed gelation mechanism is shown in Fig. 6.

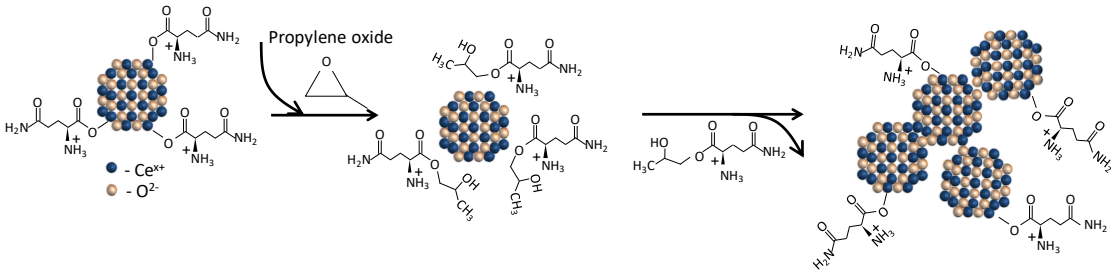

Fig. 6. Schematic representation of the gelation of the Gln-NC solution triggered by the introduction of PO.

FTIR spectra of the gel supernatant showed the presence of peaks at around 1538 cm^{-1} and 1650 cm^{-1} ascribed to N-C=O and NH_2 stretching, confirming stripping of Gln during the gelation process. FTIR spectra of the aerogel also displayed that part of the Gln remained on the NC surface as required to prevent the full collapse of the structure in solution. Additionally, TGA analysis confirmed the amount of organic in the final aerogel to be ca. 25% lower than in the precursor Gln-NCs, confirming a partial ligand removal (Fig. 7).

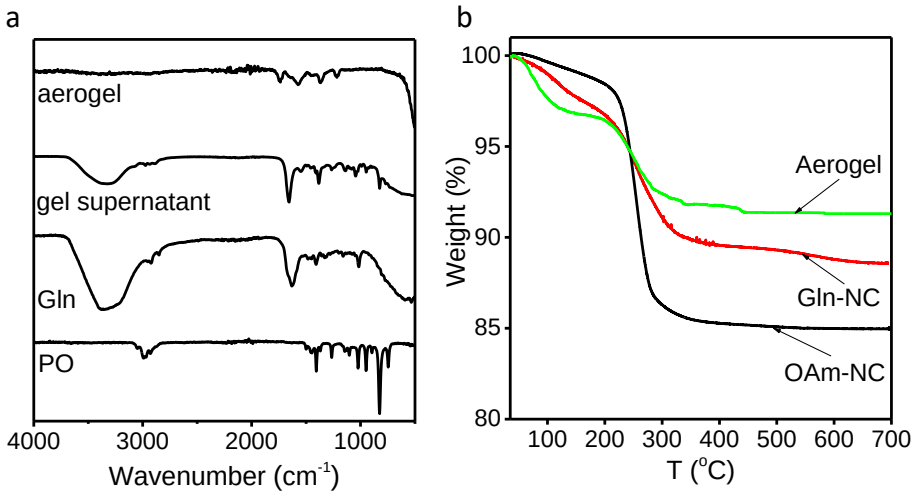

Fig. 7. a) FTIR spectra of PO, Gln, the gel supernatant and the aerogel. b) TGA profiles of the OAm-NCs, Gln-NCs and the Gln-NC-based aerogel.

PO, a soft base, triggers a slow cross-linking of the NCs, which favors the formation of a voluminous gel. On the contrary, when a strong base such as TMAOH was added, a rapid aggregation of the NCs occurred with no gel formation (Fig. 8 a). Actually, the amount of epoxide controlled the ligand stripping rate and thus the rate of NC cross-linking, which translated in gels with different voluminosity (Fig. 8). In this regard, an excessive amount of PO led to higher NC aggregation and gel shrinkage, while insufficient amounts were not able to cross-link all the particles resulting in none or partial gelation (Fig. 8 a).

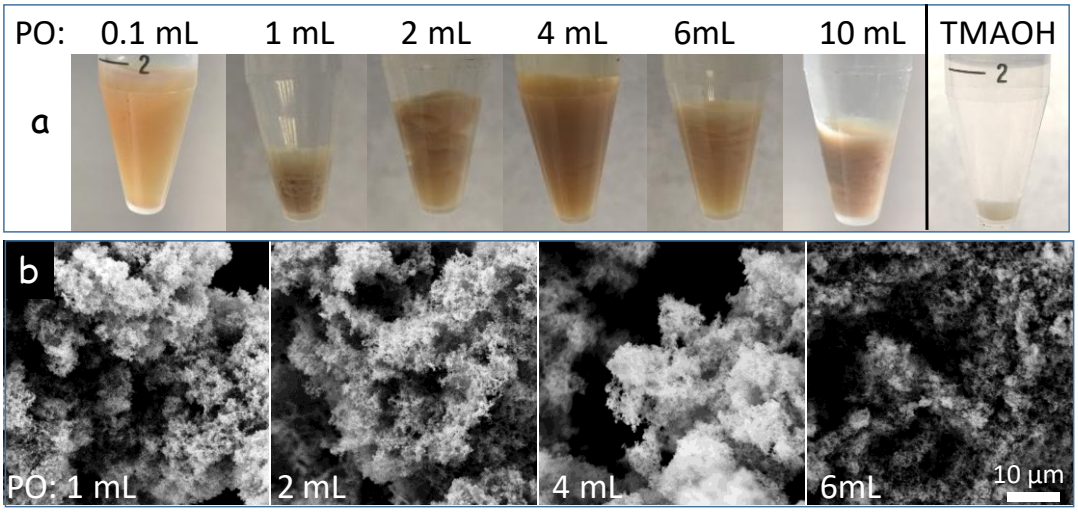

Fig. 8. a) Optical photographs of the ceria NC-based gels obtained 24 h after the introduction of different amounts of PO: 0.1 mL (no gel formed), 1 mL, 2 mL, 4 mL, 6 mL, 8 mL and 10 mL; or 500 µL of TMAOH (no gel formed, fast NC aggregation into powder), as indicated on top of each photograph. b) SEM images of the aerogels produced from the gels obtained from 1 mL, 2 mL, 4 mL and 6 mL of PO.

The use of molecules with multiple epoxy groups had a similar effect as PO. As an example, the addition of NGDE, with 2 epoxy groups instead of PO, also triggered the NC gelation, but with a lower voluminosity when added in the same amount as PO. Injection of 11 mL (0.057 mol) of NGDE, the molar equivalent to 4 mL of PO, resulted in gels with dense aggregates of NCs, which we associate to the double number of epoxy groups introduced (Fig. 9 a). When

reducing the amount of NGDE by half, thus introducing the same amount of epoxy groups, less dense aerogels, similar to those produced with PO were obtained (Fig. 9 b).

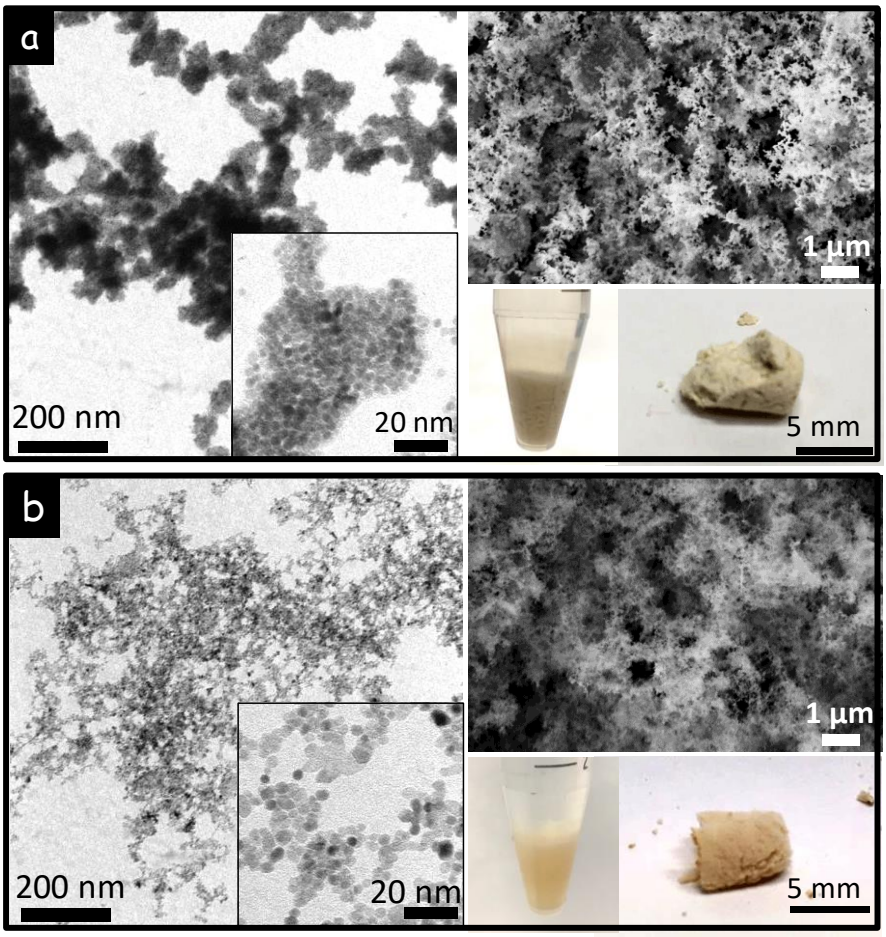

Fig. 9. a) TEM, SEM and optical photographs of the ceria NC-based gel and aerogel formed from the addition of 10 mL of NGDE. b) TEM, SEM and optical photographs of the ceria NC-based gel and aerogel formed from the addition of 5 mL of NGDE.

While the addition of H_2O to the MFA resulted in gels with higher voluminosity, the presence of H_2O was not essential for the NC gelation to occur. Attempts using MFA as the only solvent also led to NC gelation, but the obtained gels were significantly less voluminous (Fig. 10). When replacing MFA+H_2O with alcohols as the only solvent for NC gelation, no gel was formed. Upon PO addition to an alcohol solution of NCs, all NCs precipitated. Nevertheless, the addition of small amounts of water to the alcohol also allowed the NC gelation, although with a moderate voluminosity compared with MFA+H_2O (Fig. 10). Note that the poor miscibility of PO with H_2O barred the use of H_2O as the only solvent for NC gelation. Attempts to gelate NCs in the two-phase mixture created from the addition of PO to a NC solution in water, resulted in NC precipitation.

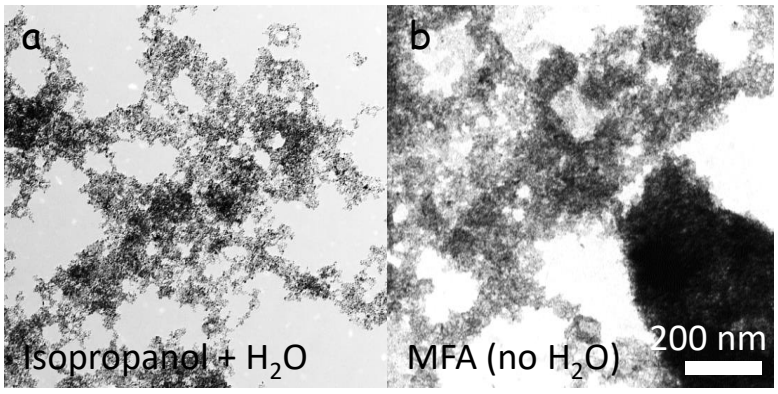

Fig. 10. Influence of the solvent used during the gelation process. TEM micrographs of the xerogels obtained from Gln-NCs dispersed in isopropanol with a small amount of water (2 mL, a) and MFA without water addition (b).

The same methodology allowed formation of NC-based ceria gels using ceria NCs functionalized with other amino acids, such as Glu and DA (Fig. 11). However, the gels produced from Glu-NCs and DA-NCs were slightly less voluminous than those produced from Gln-NCs (Fig. 12). We hypothesize the different gel voluminosity to be related to variations in the ligand displacement kinetics that would be in part associated to the fact that DA and Glu have just one amino group while Gln has two. Identical amounts of PO may result in a faster ligand displacement in DA- and Glu-NCs than in Gln-NCs and thus in less voluminous gels.

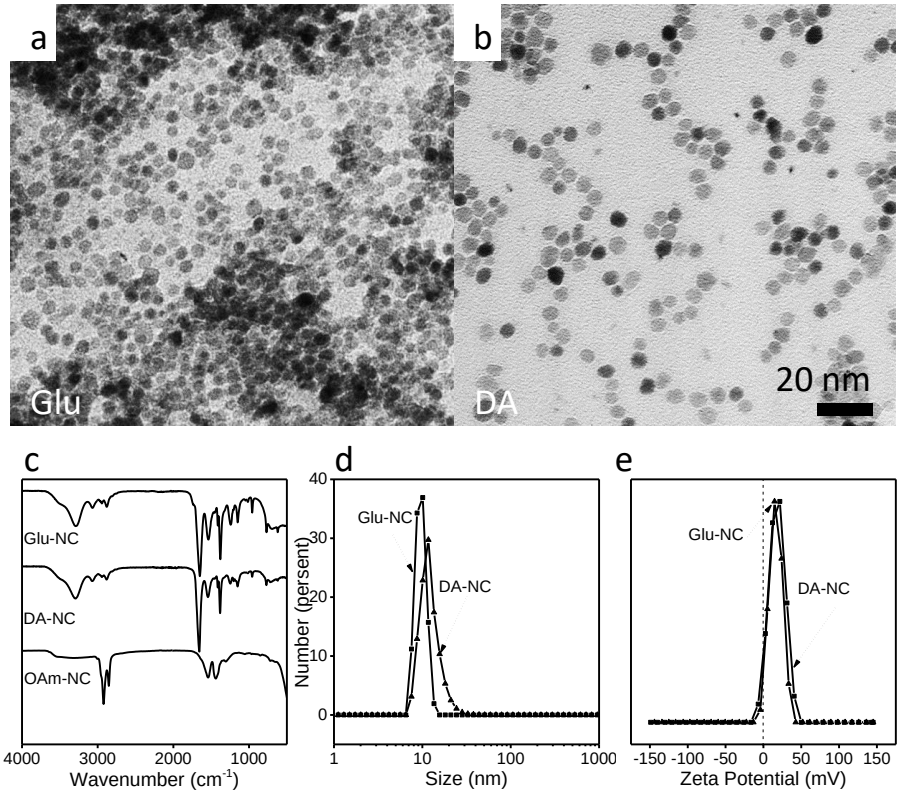

Fig. 11. TEM images of CeO_2 NCs capped with glutamic acid (a, Glu) and dopamine (b, DA). FTIR spectra of the as-synthesized NCs and treated with Glu and DA (c). DLS and Z-potential analysis of the produced samples.

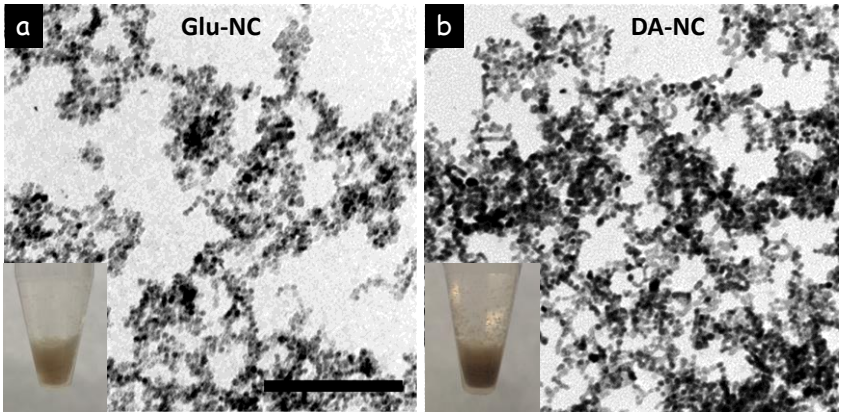

Fig. 12. a) TEM micrograph of an aerogel obtained from the cross-linking of Glu-NCs. b) TEM micrograph of an aerogel obtained from the cross-linking of DA-NCs. The scale bar is common for the two TEM micrographs and corresponds to 100 nm. Insets show optical photographs of the gels produced with each type of ceria NCs.

One of the essential parameter which differ aerogel from the NCs aggregate is high value of specific surface area. Thus, to evaluate the influence of each parameter on the aerogel porous structure we performed measurements of the specific surface area of the aerogels produced using different conditions.

Fig. 13 c shows adsorption–desorption isotherm obtained from a NC-based ceria aerogel annealed at 400 °C for 2 h. A specific surface areas determined using the Brunauer-Emmett-Teller (BET) model showed that the resulting ceria aerogels had remarkably large surface areas ranges from 73 to 225 m^2/g compare to the values obtained for nanopowder through the use of an antisolvent and centrifugation (63 m^2/g) which is over 3-fold lower. Low values of surface area of NCs sample are result from their compact aggregation which is bypassed in the case of aerogel. Aerogel synthesized using PO or NGDE showed the same values of surface area of 225 m^2/g confirming formation of the porous structure via NCs attachment. As it was expected, aerogel synthesized using PO and DA-NCs instead of Gln-NCs showed lower values of surface area (73 m^2/g) (Fig. 13 g, h) due to more compact monolith formation concluded from visual observation. NC-based ceria aerogels displayed a type IV adsorption–desorption isotherm with a hysteresis associated with capillary condensation. Barrett–Joynes–Halenda (BJH) plots of the pore-size distribution of the aerogel sample revealed broad pore size distributions, consistent with the porous but random nature of the aerogel.

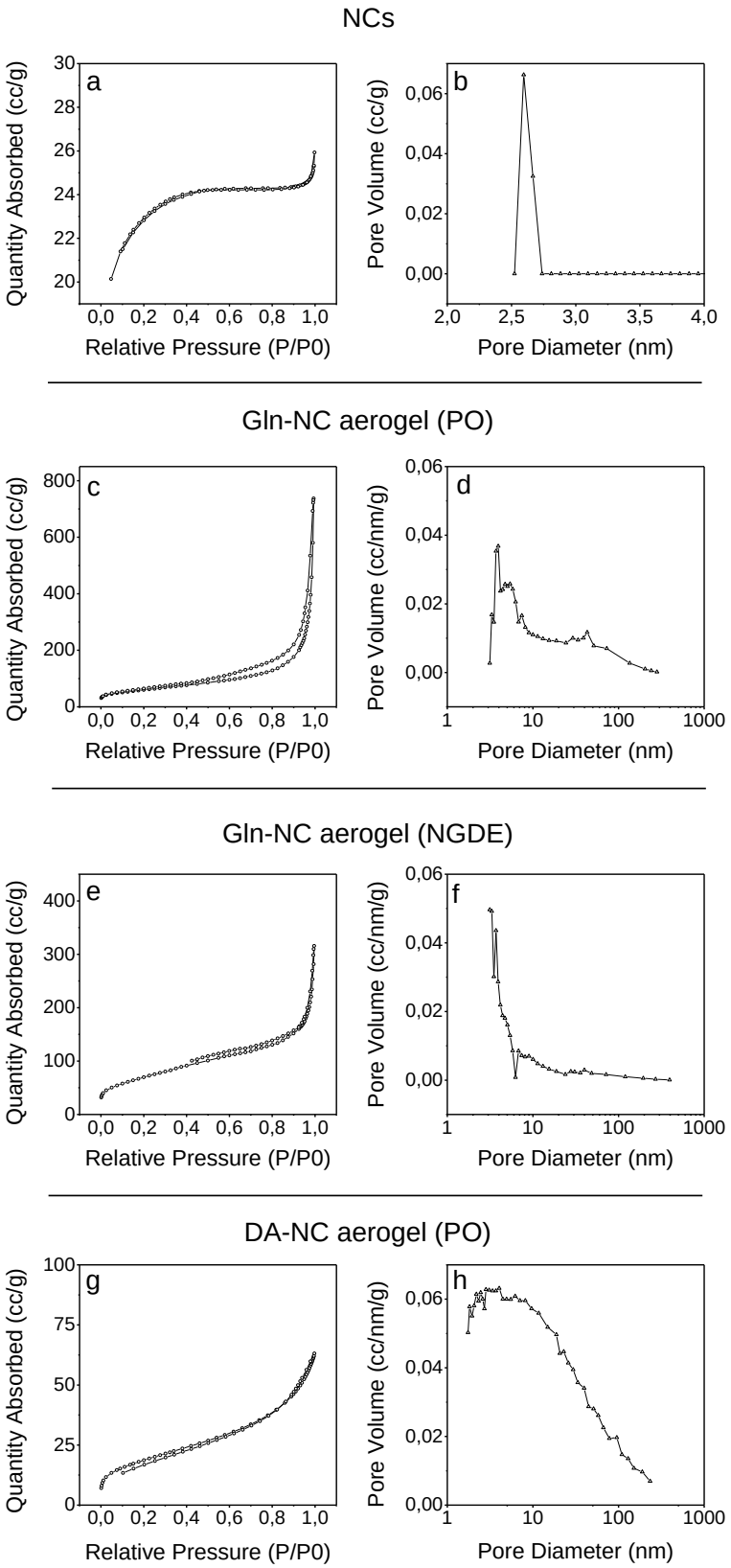

Fig. 13. Adsorption–desorption isotherm pore size distribution obtained from a NC powder obtained by precipitation of the colloidal NCs using an antisolvent and posterior centrifugation (a, b) and from a NC-based ceria aerogel produced via exposure Gln-NCs to PO (c, d) or NGDE (e, f), DA-CeO_2 NCs obtained via exposure them to PO (g, h). All materials were annealed at 400 °C for 2 h.

XRD analysis demonstrated that, unlike aerogels conventionally produced from sol-gel chemistry methods, as-prepared NC-based aerogels were highly crystalline as they retained the crystallinity of the precursor NCs (Fig. 15 c). XRD patterns displayed the reflections of the CeO_2 fluorite structure (space group = Fm3m, JCPDS card No 34-0394) with lattice parameter *a* = 0.5412 nm.

To further compare the two methodologies, we produced ceria aerogels from the gelation of a ceria chloride solution, also using PO as gelator promoter, as described by C. Laberty-Robert et al.[8] TEM inspection of the as-synthesized aerogel showed chain-like assembly which probably consisted of cerium hydroxide that was converted to cerium oxide upon heat treatment Fig. 14 a. Calcined aerogel samples demonstrated the transformation $Ce(OH)_x$ bundles into small NCs with average sizes of 5 nm attached into porous network Fig. 14 b.

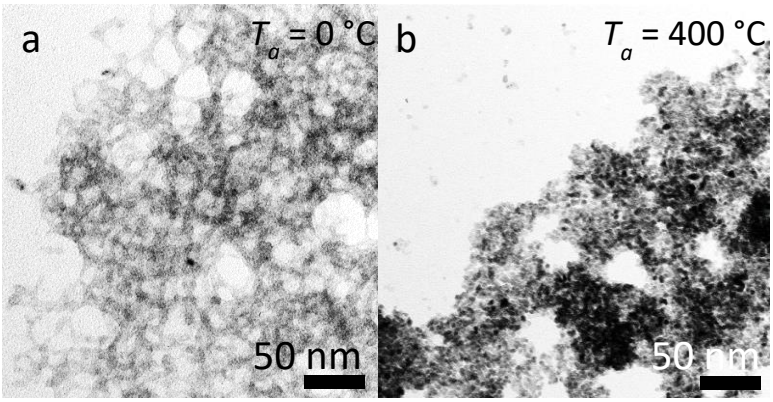

Fig. 14. TEM images of ceria aerogel obtained using precursor-based sol-gel method before (a) and after annealing (b) at T_a = 400 °C for 2 h.

Fig. 15 a displays optical photographs and SEM micrographs of the aerogel produced by this strategy before and after annealing at 400 °C. Using this approach, the BET specific surface areas of the as-produced aerogel were larger, up to 380 m^2/g, than that of the NC-based aerogel. However, this initial ceria aerogel was mostly amorphous and a thermal treatment at 400 °C was required to crystallize it (Fig. 15 c). During this thermal annealing process, notable shrinkage of the aerogel took place and the monolithic structure was lost (Fig. 15 a). Additionally, the specific surface area obtained decreased down to 180 m^2/g, below that obtained from the initial NC-based aerogel already displaying a proper crystallinity (Fig. 15 b). Additionally, NC-based aerogels did not collapse during the thermal treatment at 400 °C and their structure was mostly maintained.

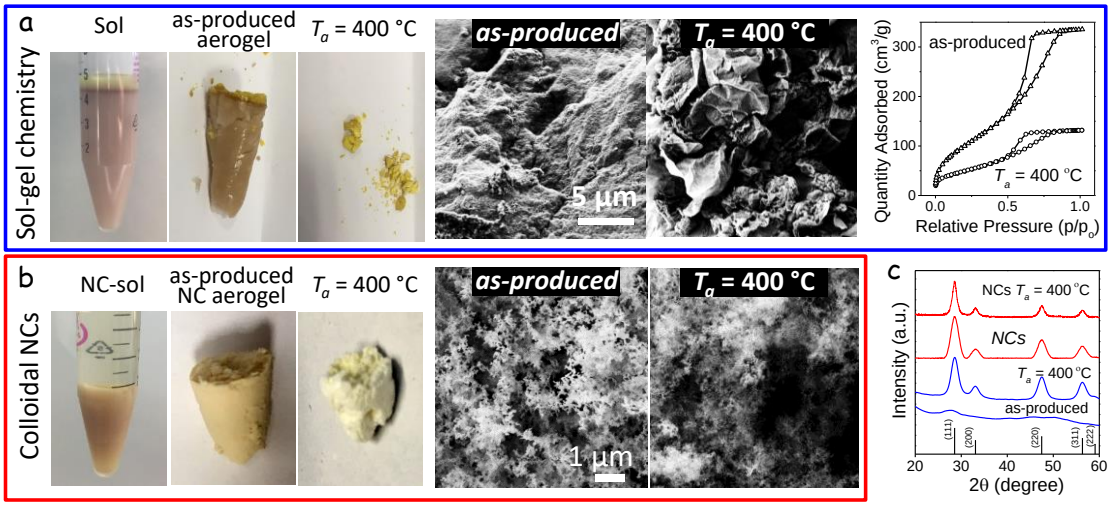

Fig. 15. a) Gel and aerogel produced following a sol-gel chemistry approach:[8] Optical photographs of the sol, the as-produced aerogel and the aerogel annealed at 400 °C; SEM micrographs of the as-produced aerogel and the aerogel annealed at 400 °C; and adsorption-desorption isotherms of the as-produced aerogel and the aerogel annealed at 400 °C. b) Gel and aerogel produced from the cross-linking of colloidal NCs: Optical photographs of the sol, the as-produced aerogel and the aerogel annealed at 400 °C; and SEM micrographs of the as-produced aerogel and the aerogel annealed at 400 °C. c) XRD patterns of (from bottom to top) the ceria aerogel produced following a sol-gel chemistry approach, as-produced and after annealing at 400 °C; the ceria NCs and the ceria NC-based aerogel annealed at 400 °C.

4.3.2. Branched NCs

The gelation approach here proposed was also used to produce NC-based ceria aerogels employing NCs with other sizes and geometries, and particularly hyperbranched ceria NCs (Figure 16).[35] Hyperbranched ceria NCs were characterized by an intrinsic porous structure that provides them with specific surface areas up to 157 m^2/g.[35] As for spherical ceria NCs, the surface of ceria hyperbranched NCs was in a first step functionalized with Gln to render the NCs soluble in polar solvents. In a second step, PO was added to trigger gelation. The gel obtained after 24h from the injection of PO was dried from supercritical CO_2. Figure 7 displays representative TEM and SEM micrographs of the aerogels produced following this procedure. N_2 adsorption/desorption isotherm curves of hyperbranched NCs aerogels displayed a type IV character with a H1 hysteresis loop that evidenced mesoporosity (Figure 16 c). BET calculations demonstrated large specific surface areas of 200 m^2/g, similar to those measured from aerogels produced from quasi-spherical NCs and above those of the precipitated hyperbranched NCs.

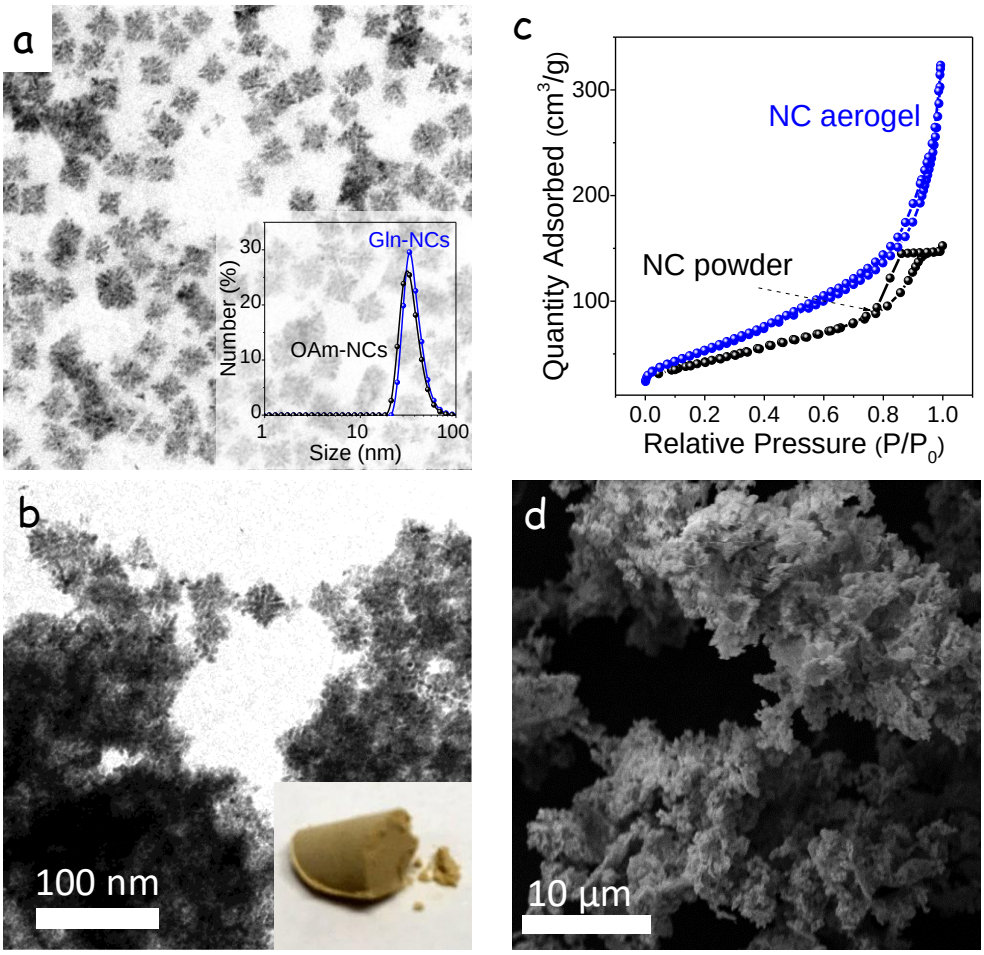

Fig. 16 a) TEM micrograph of hyperbranched ceria NCs.The inset displays DLS curves of hyperbranched OAm-NCs and Gln-NCs. b) Adsorption–desorption isotherm obtained from a hyperbranched NC-based ceria aerogel and from a NC powder obtained by precipitation of the colloidal NCs using an antisolvent and posterior centrifugation. Both materials were annealed at 400 °C for 2 h. c) TEM micrograph of the hyperbranched NC-based aerogel and optical photograph of the monolith aerogel (inset). d) SEM micrograph of the hyperbranched NC-based aerogel.

4.4. The case of titanium dioxide NCs assembly

The general approach to produce metal oxide aerogels detailed here was demonstrated for a second oxide besides ceria. As a second example, we targeted the production of NC-based aerogels of titanium dioxide, a key industrial nanomaterial in a range of applications. For this purpose, we produced TiO_2 NCs with controlled geometry and facets. In particular, for the present work, we produced anatase TiO_2 nanoplates with ample {001} facets following the procedure by Gordon et al. (Fig. 17).[36] Using the same procedure as for ceria NCs, we replaced the native organic ligands from the TiO_2 NC surface by Gln. Subsequently, the addition of PO to a solution containing TiO_2 Gln-NCs resulted in their random aggregation into a network, i.e. its gelation (Fig. 17). TiO_2 NCs gelation occurred slightly faster than for CeO_2 and it was completed after 60 min of reaction. Super-critical drying of the NC-based TiO_2 gels resulted in blue coloured monolithic aerogel (Fig. 17 d). The blue colour, characteristic of the initial TiO_2 NCs, evidenced the presence of a high concentration of oxygen vacancies and the overall

nonstoichiometric composition of the TiO_2 NCs obtained from the used colloidal synthesis protocol.[36]

Despite the fact that plate-like NCs were prone to stuck together to form compact aggregates, SEM imaging evidenced NC-based TiO_2 aerogels to be characterized by highly porous structures. NC-based TiO_2 aerogels displayed type IV adsorption/desorption isotherms (Fig. 8 b) and BET specific surface area up to 70 m^2/g.

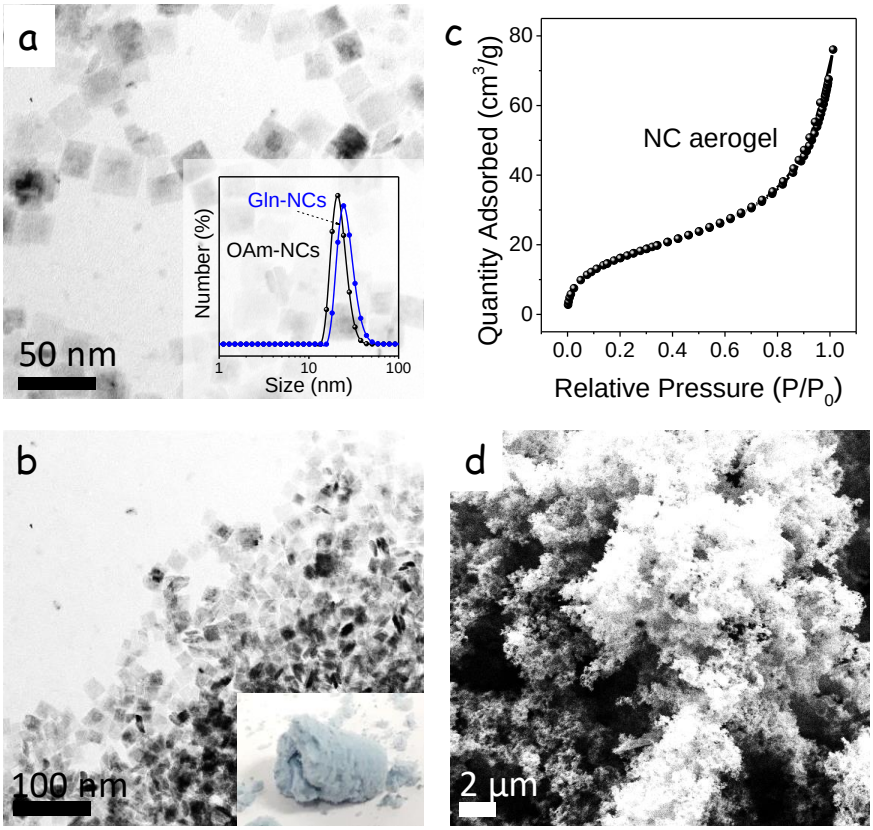

Fig. 17. a) TEM micrograph of TiO_2 NCs. Inset shows the DLS curves of TiO_2 OAm-NCs and Gln-NCs. b) Adsorption–desorption isotherms obtained from a NC-based TiO_2 aerogel. The material was measured after annealing at 400 °C for 2 h. c) TEM micrograph of the NC-based TiO_2 aerogel and optical photograph of the monolith aerogel (inset). d) SEM micrograph of the NC-based TiO_2 aerogel.

4.5. The case of iron oxide NCs assembly

Iron oxide NCs were producing using reported procedure through pyrolysis of FeO(OH) salt in the presence of oleic acid and 1-octadecene as a non-coordinating solvent.[37] Reaction for 30 min at 320 °C resulted in 30 nm Fe_2O_3 NCs with narrow size distribution.

Prior gelation, the surface of the as-synthesized iron oxide NCs were functionalized using the same approaches as for ceria NCs. Capping with Gln allows NCs stabilization in polar solvents. TEM inspection demonstrated that NCs preserves their morphology (Fig. 18 a). Measuring of the hydrodynamic radii of the treated NCs showed the similar NCs sizes for Gln-NCs confirming aggregation-free nature.

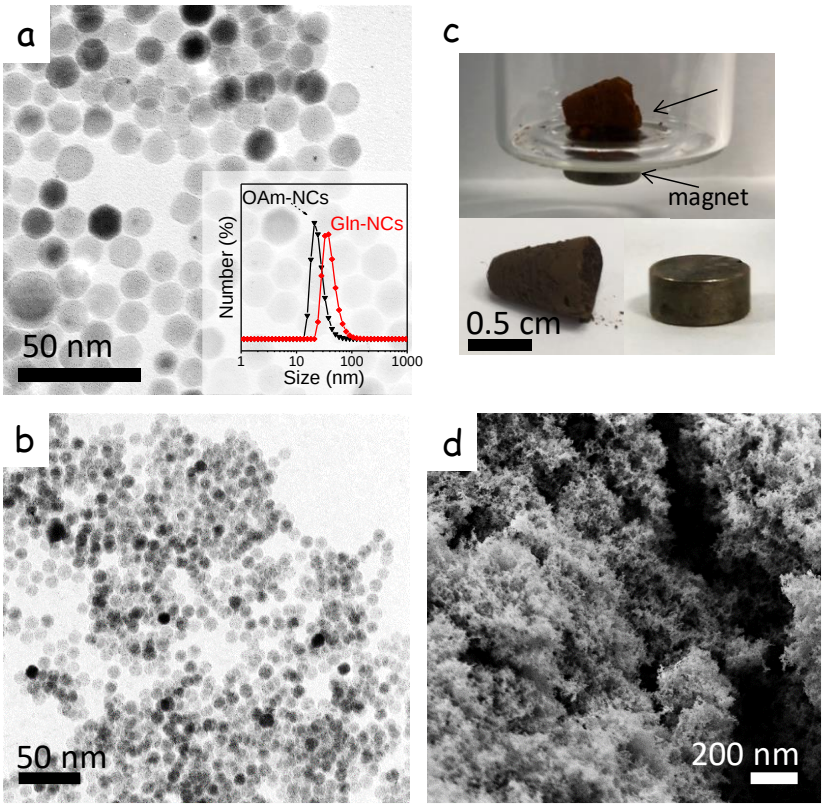

Fig. 18. a) TEM micrograph of iron oxide NCs. Inset shows the DLS curves of iron oxide OAm-NCs and Gln-NCs. b) TEM micrograph of the NC-based iron oxide aerogel. c) Optical photograph of the monolith aerogel evidenced its magnetic nature d) SEM micrograph of the NC-based TiO_2 aerogel.

To prove the versatility of the proposed approach, the same gelation procedure was applied to Fe_2O_3 NCs (Fig. 18). The exposure of the Gln-capped iron oxide NCs to the PO resulted in formation of the gel. TEM analysis evidenced that gel represents the interconnected NCs structure. The produced aerogel observed to be highly-porous. The annealing of the sample required for catalytic measurements, led to improved magnetic properties of the obtained aerogel, which can be clearly observed from the Fig. 18 c, where 20 mg weighted aerogel held the magnet with the weight of 3.2 g. This results are consistent with the results obtained for iron oxide NC powder after applying the same annealing process. Furthermore, the appeared magnetic properties improve the mechanical properties of the gel by increasing the NCs attraction to each other.

4.6. Conclusions

A novel strategy to produce crystalline oxide aerogels was detailed. The described approach was based on the cross linking of colloidal NCs by the addition of an epoxide to the colloidal NC dispersion. We hypothesize the epoxide gradually displaced amino acid ligands from the NC surface, thus triggering their slow cross linking into randomly interconnected networks, i.e. their gelation. NC-based ceria aerogels displayed both high surface areas and highly crystalline structures that were associated to the high crystallinity of the precursor NC building blocks. Additionally, the versatility of the proposed strategy was proved by using the same procedure to produce NC-based titanium dioxide aerogels using NC building blocks with controlled geometry and facets.

4.7. References

1. Zhang, J.; Li, C. M. Nanoporous metals: fabrication strategies and advanced electrochemical applications in catalysis, sensing and energy systems. Chem. Soc. Rev. 2012, 41 (21), 7016-7031.
2. Rolison, D. R. Catalytic Nanoarchitectures--the Importance of Nothing and the Unimportance of Periodicity. Science 2003, 299 (5613), 1698-1701.
3. Brinker, C. J.; Scherer, G. W. Hydrolysis and Condensation I: Nonsilicates. in sol-gel science, Academic Press: San Diego, 1990; pp 20-95.
4. Gash, A. E.; Tillotson, T. M.; Satcher Jr, J. H.; Hrubesh, L. W.; Simpson, R. L. New sol–gel synthetic route to transition and main-group metal oxide aerogels using inorganic salt precursors. J. Non-Cryst. Solids 2001, 285 (1), 22-28.
5. Ziegler, C.; Wolf, A.; Liu, W.; Herrmann, A.-K.; Gaponik, N.; Eychmüller, A. Modern Inorganic Aerogels. Angew. Chem. Int. Ed. 2017, 56 (43), 13200-13221.
6. Katti, A.; Shimpi, N.; Roy, S.; Lu, H.; Fabrizio, E. F.; Dass, A.; Capadona, L. A.; Leventis, N. Chemical, Physical, and Mechanical Characterization of Isocyanate Cross-linked Amine-Modified Silica Aerogels. Chem. Mater. 2006, 18 (2), 285-296.
7. Gash, A. E.; Tillotson, T. M.; Satcher, J. H.; Poco, J. F.; Hrubesh, L. W.; Simpson, R. L. Use of Epoxides in the Sol−Gel Synthesis of Porous Iron(III) Oxide Monoliths from Fe(III) Salts. Chem. Mater. 2001, 13 (3), 999-1007.
8. Laberty-Robert, C.; Long, J. W.; Lucas, E. M.; Pettigrew, K. A.; Stroud, R. M.; Doescher, M. S.; Rolison, D. R. Sol−Gel-Derived Ceria Nanoarchitectures: Synthesis, Characterization, and Electrical Properties. Chem. Mater. 2006, 18 (1), 50-58.
9. Rechberger, F.; Niederberger, M. Synthesis of aerogels: from molecular routes to 3-dimensional nanoparticle assembly. Nanoscale Horizons 2017, 2 (1), 6-30.
10. Rechberger, F.; Niederberger, M. Translucent nanoparticle-based aerogel monoliths as 3-dimensional photocatalysts for the selective photoreduction of CO2 to methanol in a continuous flow reactor. Mater. Horizons 2017, 4 (6), 1115-1121.
11. Heiligtag, F. J.; Rossell, M. D.; Suess, M. J.; Niederberger, M. Template-free co-assembly of preformed Au and TiO2 nanoparticles into multicomponent 3D aerogels. J. Mater. Chem. 2011, 21 (42), 16893-16899.
12. Heiligtag, F. J.; Kränzlin, N.; Süess, M. J.; Niederberger, M. Anatase–silica composite aerogels: a nanoparticle-based approach. J. Sol-Gel Sci. Technol. 2014, 70 (2), 300-306.
13. Kovalenko, M. V.; Manna, L.; Cabot, A.; Hens, Z.; Talapin, D. V.; Kagan, C. R.; Klimov, V. I.; Rogach, A. L.; Reiss, P.; Milliron, D. J.; Guyot-Sionnnest, P.; Konstantatos, G.; Parak, W. J.; Hyeon, T.; Korgel, B. A.; Murray, C. B.; Heiss, W. Prospects of Nanoscience with Nanocrystals. ACS Nano 2015, 9 (2), 1012-1057.
14. Coughlan, C.; Ibáñez, M.; Dobrozhan, O.; Singh, A.; Cabot, A.; Ryan, K. M. Compound Copper Chalcogenide Nanocrystals. Chem. Rev. 2017, 117 (9), 5865-6109.
15. Sapsford, K. E.; Algar, W. R.; Berti, L.; Gemmill, K. B.; Casey, B. J.; Oh, E.; Stewart, M. H.; Medintz, I. L., Functionalizing Nanoparticles with Biological Molecules: Developing Chemistries that Facilitate Nanotechnology. Chem. Rev. 2013, 113 (3), 1904-2074.
16. Zhang, C. Carbon dioxide capture: Multiple site absorption. Nat. Energy 2016, 1, 16084.
17. Ciftja, A. F.; Hartono, A.; Svendsen, H. F. Selection of Amine Amino Acids Salt Systems for CO2 Capture. Energy Procedia 2013, 37, 1597-1604.

18. Sanz, R.; Calleja, G.; Arencibia, A.; Sanz-Pérez, E. S. CO2 capture with pore-expanded MCM-41 silica modified with amino groups by double functionalization. Microporous and Mesoporous Materials 2015, 209, 165-171.
19. De Roo, J.; Coucke, S.; Rijckaert, H.; De Keukeleere, K.; Sinnaeve, D.; Hens, Z.; Martins, J. C.; Van Driessche, I. Amino Acid-Based Stabilization of Oxide Nanocrystals in Polar Media: From Insight in Ligand Exchange to Solution 1H NMR Probing of Short-Chained Adsorbates. Langmuir 2016, 32 (8), 1962-1970.
20. Sousa, M. H.; Rubim, J. C.; Sobrinho, P. G.; Tourinho, F. A. Biocompatible magnetic fluid precursors based on aspartic and glutamic acid modified maghemite nanostructures. J. Magn. Magn. Mater. 2001, 225 (1), 67-72.
21. Shultz, M. D.; Reveles, J. U.; Khanna, S. N.; Carpenter, E. E. Reactive Nature of Dopamine as a Surface Functionalization Agent in Iron Oxide Nanoparticles. J. Am. Chem. Soc. 2007, 129 (9), 2482-2487.
22. Stamplecoskie, K. G.; Kamat, P. V. Size-Dependent Excited State Behavior of Glutathione-Capped Gold Clusters and Their Light-Harvesting Capacity. J. Am. Chem. Soc. 2014, 136 (31), 11093-11099.
23. Alessandro, T. Catalysis by ceria and related materials. World Scientific: 2002, Vol. 2.
24. Bell, A. T., The Impact of Nanoscience on Heterogeneous Catalysis. Science 2003, 299 (5613), 1688-1691.
25. Xu, H.; Wang, A.-L.; Tong, Y.-X.; Li, G.-R., Enhanced catalytic activity and stability of Pt/CeO2/PANI hybrid hollow nanorod arrays for methanol electro-oxidation. ACS Catalysis 2016, 6 (8), 5198-5206.
26. Zhou, H.-P.; Wu, H.-S.; Shen, J.; Yin, A.-X.; Sun, L.-D.; Yan, C.-H., Thermally Stable Pt/CeO2 Hetero-Nanocomposites with High Catalytic Activity. J. Am. Chem. Soc. 2010, 132 (14), 4998-4999.
27. Wang, D.; Kang, Y.; Doan-Nguyen, V.; Chen, J.; Küngas, R.; Wieder, N. L.; Bakhmutsky, K.; Gorte, R. J.; Murray, C. B., Synthesis and Oxygen Storage Capacity of Two-Dimensional Ceria Nanocrystals. Angew. Chem. Int. Ed. 2011, 50 (19), 4378-4381.
28. Zhou, L.; Li, X.; Yao, Z.; Chen, Z.; Hong, M.; Zhu, R.; Liang, Y.; Zhao, J., Transition-Metal Doped Ceria Microspheres with Nanoporous Structures for CO Oxidation. Sci. Rep. 2016, 6, 23900.
29. Kharton, V. V.; Figueiredo, F. M.; Navarro, L.; Naumovich, E. N.; Kovalevsky, A. V.; Yaremchenko, A. A.; Viskup, A. P.; Carneiro, A.; Marques, F. M. B.; Frade, J. R., Ceria-based materials for solid oxide fuel cells. J. Mater. Sci. 2001, 36 (5), 1105-1117.
30. Liao, L.; Mai, H. X.; Yuan, Q.; Lu, H. B.; Li, J. C.; Liu, C.; Yan, C. H.; Shen, Z. X.; Yu, T., Single CeO2 Nanowire Gas Sensor Supported with Pt Nanocrystals: Gas Sensitivity, Surface Bond States, and Chemical Mechanism. J. Phys. Chem. C 2008, 112 (24), 9061-9065.
31. Channei, D.; Inceesungvorn, B.; Wetchakun, N.; Ukritnukun, S.; Nattestad, A.; Chen, J.; Phanichphant, S., Photocatalytic degradation of methyl orange by CeO2 and Fe–doped CeO2 films under visible light irradiation. Sci. rep. 2014, 4, 5757.
32. Kwon, H. J.; Cha, M.-Y.; Kim, D.; Kim, D. K.; Soh, M.; Shin, K.; Hyeon, T.; Mook-Jung, I., Mitochondria-Targeting Ceria Nanoparticles as Antioxidants for Alzheimer's Disease. ACS Nano 2016, 10 (2), 2860-2870.
33. Fujishima, A.; Rao, T. N.; Tryk, D. A., Titanium dioxide photocatalysis. J. Photochem. Photobiol C: Photochemistry Reviews 2000, 1 (1), 1-21.

34. Zhao, Z.; Tian, J.; Sang, Y.; Cabot, A.; Liu, H., Structure, synthesis, and applications of TiO2 nanobelts. Adv. Mater. 2015, 27 (16), 2557-2582.
35. Berestok, T.; Guardia, P.; Blanco, J.; Nafria, R.; Torruella, P.; López-Conesa, L.; Estradé, S.; Ibáñez, M.; de Roo, J.; Luo, Z.; Cadavid, D.; Martins, J. C.; Kovalenko, M. V.; Peiró, F.; Cabot, A., Tuning Branching in Ceria Nanocrystals. Chem. Mater. 2017, 29 (10), 4418-4424.
36. Gordon, T. R.; Cargnello, M.; Paik, T.; Mangolini, F.; Weber, R. T.; Fornasiero, P.; Murray, C. B., Nonaqueous Synthesis of TiO2 Nanocrystals Using TiF4 to Engineer Morphology, Oxygen Vacancy Concentration, and Photocatalytic Activity. J. Am. Chem. Soc. 2012, 134 (15), 6751-6761.
37. Yu, W. W.; Falkner, J. C.; Yavuz, C. T.; Colvin, V. L., Synthesis of monodisperse iron oxide nanocrystals by thermal decomposition of iron carboxylate salts. Chemical Communications 2004, (20), 2306-2307.
38. Yu, W. W.; Peng, X., Formation of High-Quality CdS and Other II–VI Semiconductor Nanocrystals in Noncoordinating Solvents: Tunable Reactivity of Monomers. Angewandte Chemie International Edition 2002, 41 (13), 2368-2371
39. Kakiuchi, H.; Iijima, T., The ring-opening reactions of propylene oxide with chloroacetic acids. Tetrahedron 1980, 36 (8), 1011-1016.

5. Assembly of metal chalcogenide NCs: the case of In_2S_3

Abstract

Colloidal NCs compete with molecular catalysts in the field of homogenous catalysis, offering an easier recyclability and a number of additional functionalities. Using high throughput printing technologies, colloidal NCs can be also supported onto substrates to produce cost-effective electronic, optoelectronic, electrocatalytic and sensing devices. In these two broad areas, NCs surface chemistry and supracrystal organization are key parameters determining final performance. In this chapter we performed complete study of the influence of the surface ligands and the NC organization on the catalytic properties of In_2S_3, both in colloidal form and as a supported layer. In solution, well dispersed NCs stabilized in solution by inorganic ligands show the highest photocatalytic activities. On the other hand, when NCs are supported on a substrate, their organization becomes an essential parameters determining performance, and NC-based films produced through a gelation process provided five-fold higher photocurrent densities than those obtained from dense films produced by the direct printing of NCs.

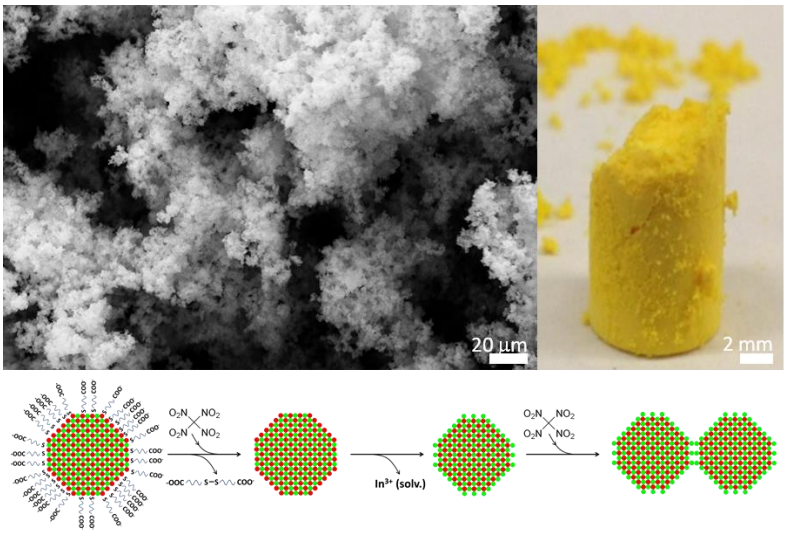

5.1. Introduction

Semiconductor nanocrystals (NCs) combine huge surface areas with a solid state platform for charge carrier photogeneration and transport.[1] This combination of properties makes them particularly appealing for applications involving interaction with the surrounding media, such as catalysis,[2,3,4] environmental remediation,[5,6] and sensing.[7] Colloidal NCs are especially suited for quasi-homogenous catalysis because relative to molecular catalysts they offer easier recyclability and added functionalities such as a magnetic moment for remote location or recovery, tunable band gaps for photocatalysis, and modulability to produce multisite systems by combining multiple co-catalysts.[8,9] However, the ability of colloidal NCs to interact with the surrounding media is controlled by their surface chemistry, which also determines several other fundamental properties, including colloidal and chemical stabilities and charge carrier and surface trap densities.[10] To find surface chemistries that simultaneously optimize all these parameters is extremely challenging and at the same time critical to exploit their full potential.

Colloidal NCs can be also assembled or supported within macroscopic structures and devices as required in electrocatalysis or sensing, for instance.[11-13] Beyond their huge surface area, solution processability, associated with high throughput and cost-effectiveness, is the main advantage of colloidal NCs in technological applications, especially when compared with thin films produced by vacuum-based technologies. When supported, a proper NC organization becomes essential to maintain their inherent large surface areas, while ensuring at the same time proper electrical conductivities for effective charge injection/extraction.[14-15] To face this key challenge, a plethora of approaches to engineer NC solids with controlled NC arrangement have been developed. A highly used approach involves slow NC assembly driven by an oversaturation of the NC concentration during solvent removal.[16,17] While yielding in some cases astonishing NC assemblies, this strategy does not generally provide materials with large surface areas and is strongly limited in terms of reproducibility, production throughput and scale up potential. To produce highly porous structures in a cost-effective manner, faster assembly strategies, based on destabilizing the NC dispersion in solution, are more suitable. This destabilization can be induced by externally triggering the ligand desorption or stimulating its binding.[11,18] The ultimate goal is to produce an interconnected NC network, i.e. a gel, with a proper surface chemistry to interact with the media.[19] In this direction, an effective approach to produce highly porous NC superstructures with good transport properties is the oxidative removal of thiolate ligands to link chalcogenide NCs through chalcogen-chalcogen bonds.20 Following this approach, gels of different metal chalcogenides have been produced.[21-23]

In_2S_3 is an n-type semiconductor (2.6 eV band gap) with large exciton Bohr radius of 33.8 nm[24] used in lithium-ion batteries,[25] in light emission devices,[26] as photodetector,[27] for solar energy conversion through photocatalysis,[28-30] and particularly as a host material for two-photon absorption processes through an intermediate band.[31-32] While its chemical stability, low defect density, simple synthesis, and proper band gap makes it an excellent candidate for photocatalytic applications, this material is yet underexplored in this area. A number of synthetic procedures to produce In_2S_3 NCs with different morphologies have been reported.[27,30,33,34] Ultrathin In_2S_3 nanobelts showed promise for phosphorous displays due to the blue emission in photoluminescence spectra.[27] Doping of In_2S_3 by Mn or Cu demonstrated tunable dual color emission at blue and orange depending on the excitation wavelength.[35]

Moreover, depending on the morphology of the NCs and facets enclosed, In2S3 can serve as an efficient catalysts for dye degradation under either UV, visible or NIR light irradiation.36 Several previous works have detailed the photocatalytic degradation of methylene blue,30 methylene orange[28] and rhodamine B[37] over In_2S_3 NCs. Furthermore, several works have demonstrated an improvement of photocatalytic performance in In_2S_3-based composites. In_2O_3/In_2S_3/Ag nanoheterostructures have demonstrated improved activity toward photoelectrochemical water splitting.[29] However, to the best of our knowledge, the study on the influence of the In2S3 NC surface chemistry and supracrystal organization has not been shown.

In this work, we evaluate the photocatalytic activity of colloidal In_2S_3 NCs both in solution and when supported. We analyze the effect of different surface chemistries and NC organizations to determine the conditions resulting in best performances for quasi-homogeneous catalysis and photoelectrocatalysis.

5.2. Experimental

5.2.1. Synthesis of In_2S_3 NCs

5.2.1.1. 20 nm-In_2S_3 plates:

Among the several established synthetic protocols to produce In_2S_3 NCs with different shapes and sizes, [23-24,27,29] we followed a slight variation of the procedure reported by Park et al.,[30] to obtain In_2S_3 NCs with a two-dimensional morphology. In a 25 mL flask three-neck flask, 1 mmol of $InCl_3$ and 10 mL of OAm were mixed and degassed (~100 mTors) for 60 minutes at 80 °C under magnetic stirring. During this time, a clear solution formed. Then, temperature was raised up to 220 °C (5 °C/min) and, at this temperature, a previously degassed (15 minutes) solution containing 1.5 mmol of sulphur powder in 5 mL of OAm was swiftly injected. Upon injection of the sulphur precursor, the color of the solution gradually changed from transparent to orange, indicating the NC formation. After 10 minutes, the reaction was quenched by removing the heating mantle and placing the flask in a water bath. During the cooling step, the color of the solution changed from orange to yellow. Once at room temperature, NCs were precipitated by adding 30 mL of acetone to the crude solution and centrifuging the mixture at 5700 rpm for 5 min. The supernatant was discarded and the precipitate was re-dispersed in 5 mL of hexane. A second purification step was performed following the same procedure. Finally, NCs dispersed in 5 mL of hexane were stored for posterior use. Attempts to prevent aggregation of the NCs by additionally using of OAc or DDT in the reaction did not lead to any improvement of the NCs stability but only led to a broader size distribution.

5.2.1.2. 90 nm-In_2S_3 plates

1 mmol of $InCl_3$ was dissolved in 10 mL of OAm in the 25 mL flask three neck flask. Degassing at 80 °C during 60 min under magnetic stirring resulted in transparent solution. The mixture was then heated under an Argon flow. At the temperature of 220 °C the previously degassed

mixture of 0.25 mL of DDT and 1.75 mL of tDDT was injected in the reaction solution and allowed to react for 10 min. The cleaning procedures were the same as in the synthesis.

5.2.2. Surface modification with phosphotungstic acid (PTA)

The procedure used to replace native organic ligands with PTA was based on previous work by J. Huang et al.[38] 1 mL of a 10 mg/mL dispersion of In_2S_3 NCs in hexane was mixed with 1 mL of a MFA solution that contained 20 mL of TFA and 50 mg of PTA ($(PW_{12}O_{40})^{3-}$), forming a biphasic solution. This solution was vigorously shacked for 10 seconds and stirred 30-60 minutes. After stirring, the mixture was allowed to separate in two phases. The migration of NCs from the upper hexane phase to the lower MFA phase indicated the success in the ligand exchange. The upper liquid phase was discarded and then 2 mL of a hexane: acetone (1:1) mixture was added to the vial. The solution was then shacked and centrifuged at 3000 rpm for 5 min. This step was repeated 3 times to remove the former un-bonded ligands. Finally, the precipitated NCs were redispersed in MQ-Water for dye degradation measurements and in methanol for film preparation.

5.2.3. Surface modification with InCl

The procedure used to replace native organic ligands with an In-Cl complex was based on previous work by V. Sayevich et al.[39] Basically, the same steps followed above to modify the In_2S_3 NCs surface with PTA were used to modify them with $InCl_3$, with two small differences: i) the 1 mL MFA solution contained 30 mg of $InCl_3$ (0.135 mmols); ii) to facilitate the phase transfer / ligand exchange, instead of TFA, 1 mL of acetone was additionally introduced in the initial biphasic solution before shaking. Finally, NCs were redispersed in MQ-Water or in methanol depending on whether they were to be used for dye degradation measurements or film preparation, respectively.

5.2.4. Surface modification with MUA

The procedure used to replace native organic ligands with MUA was based on a previous work by S. F Wuister et al.[40] Briefly, 5 mL of a 20 mg/mL dispersion of In_2S_3 NCs were mixed with 5 mL of a MUA solution (2 mM in methanol). The resulting biphasic solution was stirred under inert atmosphere for 30 min. During this time, NCs moved from the upper hexane phase to the bottom methanol phase. The upper part was removed and NCs were precipitated by addition of 30 mL of acetone and centrifuging at 4000 rpm for 5 min. The obtained precipitate was redispersed in methanol and precipitated one more time with acetone. NCs were finally dispersed in MQ-Water or methanol. It should be noted that repeating the washing procedure several more times led to NCs aggregation, but addition of few mL of the MUA solution (2 mM in methanol) permitted redispersion NCs back in solution.

5.2.5. Direct NC deposition

1 mL of the hexane or methanol solution containing In_2S_3 NCs (20 mg/mL) with the selected surface ligand (OAm, PTA^-, InCl, MUA) was spin-coated on previously washed ITO substrates at a rotation speed of 2000 rpm for 20 seconds. The obtained films were annealed at 250 °C for 60 min under argon flow.

5.2.6. NC deposition through xerogel formation

1 mL of MUA-caped In_2S_3 NCs (20 mg/mL) in methanol was spin-coated on ITO substrates at a rotation speed of 2000 rpm for 20 seconds. Immediately after preparation, the film was dipped in a TNM solution (50 µL of 3% TNM in 5 mL of acetone) for 1 min. Subsequently, the film was rinsed with fresh methanol to remove by-products and then annealed at 250 °C for 60 min under argon flow.

5.2.7. Gel and aerogel preparation:

The procedure used to produce In_2S_3 NC gels and aerogels was based on our previous work.[19] To produce In_2S_3 NC gels, 50 µL of a TNM solution (3% in acetone) were added into 2 mL of a methanol solution containing MUA-capped In_2S_3 NCs (10 mg/mL). The mixture was shaken vigorously for 30 seconds and then kept undisturbed for the whole gelation process. The gelation process visually evolved during 2 h, but the solution was left undisturbed for two days to ensure its completion. After two days, the solvent mixture (methanol and acetone) was exchanged to pure acetone, removing all the methanol and TNM residues. This process must be carried out with special care in order to not damage the porous network of the gel. At the same time, the solvent cannot be completely removed at any step. Thus, we partially replaced the solvent every 1-2 h for 2 days. While not optimized, relatively long time intervals between solvent replacements were used to ensure complete penetration of the fresh solvent into the porous structure of the gel. After the solvent exchange, the gel immersed in acetone was loaded into a supercritical point dryer chamber and soaked with liquid CO_2 overnight. After 12 h, the chamber was half drained and filled with fresh liquid CO_2. This procedure was repeated at least 6 times in one-hour intervals in order to replace acetone by liquid CO_2. Finally, the chamber was completely filled with liquid CO_2 and heated to 39 °C. Upon heating, the pressure increased up to 75-80 bars, thus surpassing the supercritical point of CO_2. The sample was kept under these conditions for 1 h. Afterward, the pressure was released while keeping the temperature constant.

5.2.8. Dye degradation experiments

The photocatalytic activity of In_2S_3 NCs was evaluated by photodegradation of RhB. In a typical experiment, 1 mL of an aqueous RhB solution (100 ppm) was added to 9 mL of an aqueous solution containing In_2S_3 NCs (1.1 mg/mL). Before reaction, the mixture was kept in the dark for 30 min under magnetic stirring. Then the glass reaction vessel was exposed through its open top to the light from a 300 W xenon lamp providing ca. 100 mW/cm^2 irradiance at the sample. Irradiation was maintained for 2 h.

5.2.9. Photoelectrochemical measurements

The photoelectrocatalytic activity of In_2S_3 NCs was evaluated through the photoelectrochemical oxidation of a polysulfide electrolyte:[70, 205]

$$S^{2-} + 2h^{+} \rightarrow S$$

$$S + S_{x-1}^{2-} \rightarrow S_x^{2-} \ (x = 2\text{-}5)$$

being the oxidized species, S_x^{2-}, converted back (reduced) to S^{2-} on the counter electrode:

$$S_x^{2-} + 2^{e-} \rightarrow S_{x-1}^{2-} + S^{2-}$$

Photocurrent measurements were performed using a three-electrode cell configuration with a Pt-coiled wire having a surface area of 2 cm^2 as a counter electrode and an Ag/AgCl reference electrode filled with 3M KCl solution. 1M aqueous solution of S, NaOH and Na_2S at pH=7 was used as an electrolyte. Bias voltage to the working electrode was applied through an electrical contact to the uncoated part of the ITO-glass substrate. A surface area of 1 cm^2 of the deposited film was in contact with the electrolyte. Illumination was provided by 8 xenon lamps (35 W each) radially distributed with a total power of 280 W and irradiance on the sample of ca. 100 mW/cm^2. Electrochemical impedance spectroscopy (EIS) was performed using versaSTAT3. Measurements were conducted in the frequency range from 100 kHz to 1 mHz with a 5 mV AC amplitude using the three-electrode cell configuration with the same conditions used for photocurrent measurements.

5.3. Results and discussion

5.3.1. Synthesis and characterization of In_2S_3 NCs

Figure 1 a displays a representative TEM micrograph of the 18 $\pm$ 2 nm In_2S_3 NCs produced through the injection of a OAm-sulfur solution into a hot (220 °C) OAm solution containing $InCl_3$, as described in the experimental section. Using this synthetic protocol, a slight variation of that reported by K. H. Park et al.,[34] β-In_2S_3 NCs with disk-like morphology were produced. The thickness of the In_2S_3 nanodisks was previously reported at 0.76 nm,[34] which corresponds to a single unit cell, and their diameter could be adjusted in the range from 18 nm to 90 nm by using different sulfur precursors and/or reaction times (Fig. 1-2).

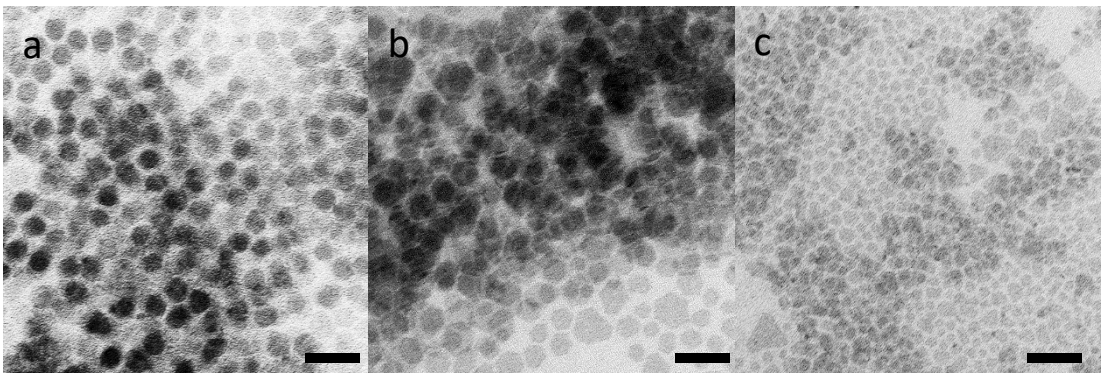

Fig. 1. TEM images of In_2S_3 NCs synthesised by injection of S:OAm into solution of $InCl_3$ along with OAm at 220 °C for 10 min (a), NCs prepared through the decomposition of $InCl_3$ in OAm in the presence of sulfur powder at 220 °C for 10 min (b). In_2S_3 NCs synthesised upon introducing of OAc (b) as co-surfactant into the solution of $InCl_3$ in OAm at 220 °C and keeping for 10 min. Scale-bars = 50 nm

The difference between the synthesis procedure reported by Park et al[30] is in injection step instead of one-pot synthesis which in our case led to broader size-distribution. The attempts to modify the synthesis by replacing elemental sulfur with tert-DDT which is commonly used sulfur precursor, but keeping the other parameters constant resulted in undesired increase of the NCs size (up to 90 nm).

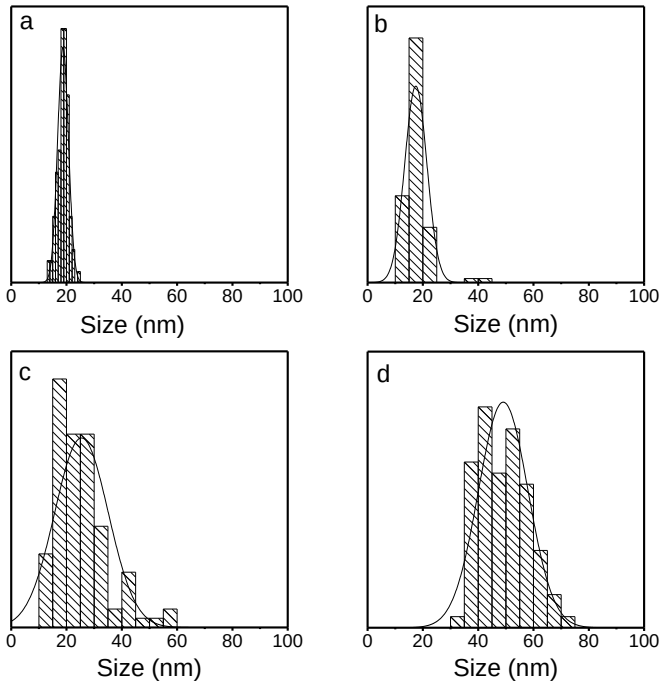

Fig. 2. Size distribution histograms of NCs (shown in **Fig. 1**) obtained using different synthetic procedures: In_2S_3 NCs synthesised by injection of S:OAm into solution of $InCl_3$ along with OAm at 220 °C for 10 min (a), NCs prepared through the decomposition of $InCl_3$ in OAm in the presence of sulfur powder at 220 °C for 10 min (b). In_2S_3 NCs synthesised upon introducing of OAc (b) as co-surfactant into the solution of $InCl_3$ in OAm at 220 °C and keeping for 10 min.

It should be noted that by changing the reaction time the size of NCs could be tuned. Already after 2 min of the reaction the size of NCs was 40 nm, extending reaction time to 5 min led to increasing in size to 50 nm and to assemble the NCs into rods. It should be noted thiols-precursors are considered as a highly reactive and aliquots taken at the reaction time of 1 min already showed the 40 nm In_2S_3 NCs. Increasing reaction time to 5 min resulted in 50 nm In_2S_3 plates that tend to assemble and form bundles. Further increasing of the reaction time led to significant size increase up to 90 nm. It should be noted that keeping the reaction mixture at 220 °C for a longer period of time resulted in increasing of the polydispersity of the samples in the case of using either S:OAm or tDDT+DDT as a source of sulphur. Furthermore, it is well-known that thiols could introduce mid-gap traps that serve as a non-radiative recombination centers. For sake of simplicity we explored 18 nm In_2S_3 plates for surface functionalization and further NCs assemble.

5.3.2. NCs surface chemistry investigation

The presence of OAm in the reaction mixture was fundamental to produce In_2S_3 crystals with sizes in the nanometer size regime and with narrow size and shape distributions. OAm binds indium ions at the NCs surface, limiting the access/reaction of additional monomer and thus confining the NC growth. At the same time, OAm molecules bound at the NC surface colloidally stabilized them during synthesis, enabling their homogeneous growth. The presence of OAm

was indicated by FTIR analysis (Fig. 4 c), and was expected to modulate the NC catalytic activity.

To determine the effect of surface ligands on the photocatalytic properties of In_2S_3 NCs and to direct their assembly, OAm was replaced from as-produced NCs (OAm-NCs) with three different ligands: a composition-matched inorganic ligand, In-Cl complex (InCl-NCs); a non-matching inorganic ligand, $(PW_{12}O_{40})^{3-}$ ($(PW_{12}O_{40})^{3}$-NCs); and a shorter organic ligand, MUA (MUA-NCs) (Fig. 7 c). In all cases, new ligands were introduced using previously reported two-phase methods adapted to our system.[38,39] In brief, OAm was replaced with MUA by mixing In_2S_3 NCs in hexane with a MUA solution in methanol.[18] On the other hand, MFA was used as a solvent to replace the native OAm with inorganic ligands. Briefly, a hexane solution containing the In_2S_3 NCs was mixed with a PTA/TFA solution in MFA or with an $InCl_3$ solution in MFA.

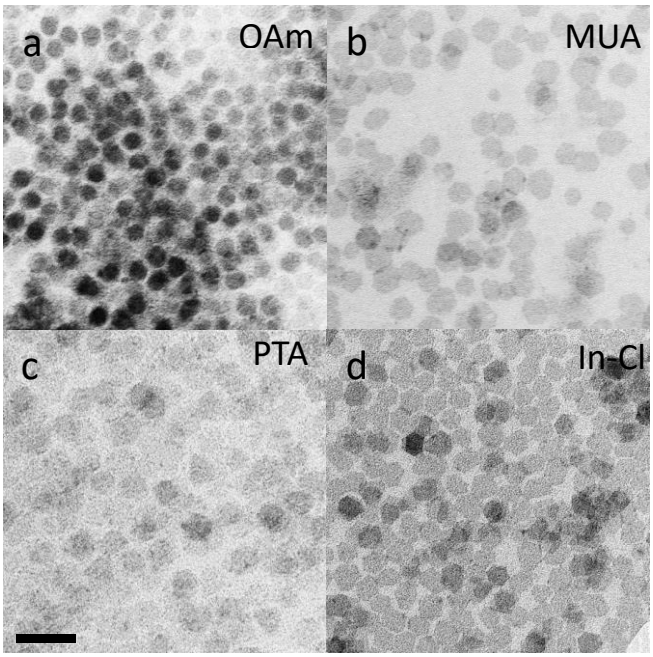

Fig. 3. a-d) Representative TEM micrographs of the initial In_2S_3 NCs (a) and of the In_2S_3 NCs capped with MUA (b), $(PW_{12}O_{40})^{3-}$ (c), and InCl (d). All micrographs have the same scale bar = 50 nm.

This process rendered the NCs soluble in polar media such as methanol or H_2O, as confirmed by TEM and DLS measurements (Fig. 4 b, c, d and Fig. 4). The surface of In_2S_3 NCs capped with MUA, InCl and $(PW_{12}O_{40})^{3-}$ ligands was characterized by the presence of negatively charged species, which resulted in negative ζ-potential values of -19 mV, -26 mV and -28 mV, respectively (Fig. 5).

FTIR spectra of In_2S_3 NCs stabilized with MUA (MUA-NCs) showed the presence of peaks at 2924 cm^{-1} and 2830 cm^{-1} that correspond to C-H stretching (Fig. 6). However, due to the shorter chain length of MUA compared with OAm, the intensity of these peaks was lower than in the initial OAm-stabilized In_2S_3 NCs (OAm-NCs). The disappearance of the weak peak at 2547 cm^{-1} present in the spectrum of pure MUA, and which was attributed to the S-H stretching, indicated the binding of the ligand to the metal atom through the thiolate group. Finally, the peaks at 1547 cm^{-1} and 1406 cm^{-1} observed in the FTIR spectrum of the MUA-NCs were

attributed to the asymmetric and symmetric vibrational bands of the carboxylate, again consistent with the presence of the MUA functional group.

FTIR spectra from the NCs stabilized with inorganic ligands demonstrated a strong but not total reduction of the peaks at 2800-2900 cm^{-1} assigned to the C-H vibration band from OAm. TGA analysis further confirmed OAm displacement. $(PW_{12}O_{40})^{3-}$-NCs showed 9% weight loss, much lower than the 50% loss measured for OAm-NCs, (Fig. 7). MUA-NCs contained a lower amount of organics than OAm-NCs, 18%, which was related to the lower molecular weight MUA compared with OAm.

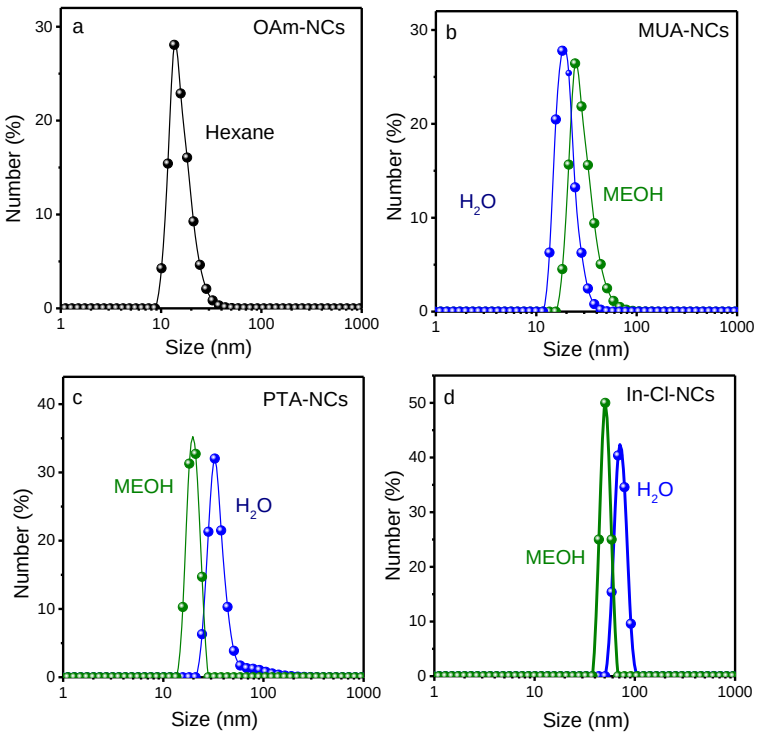

Fig. 4. DLS spectra of the initial In_2S_3 NCs (a) and of the In_2S_3 NCs capped with MUA (b), PTA (c), and InCl (d).

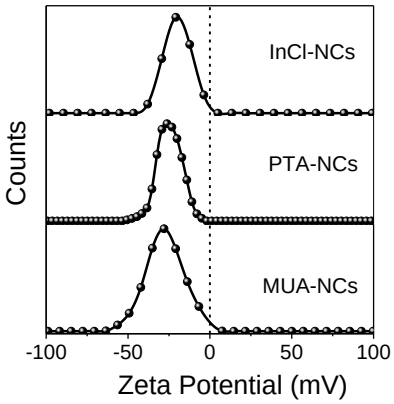

Fig. 5. Z-potential measurements of the In_2S_3 NCs capped with MUA, PTA-$(PW_{12}O_{40})^{3-}$, and InCl.

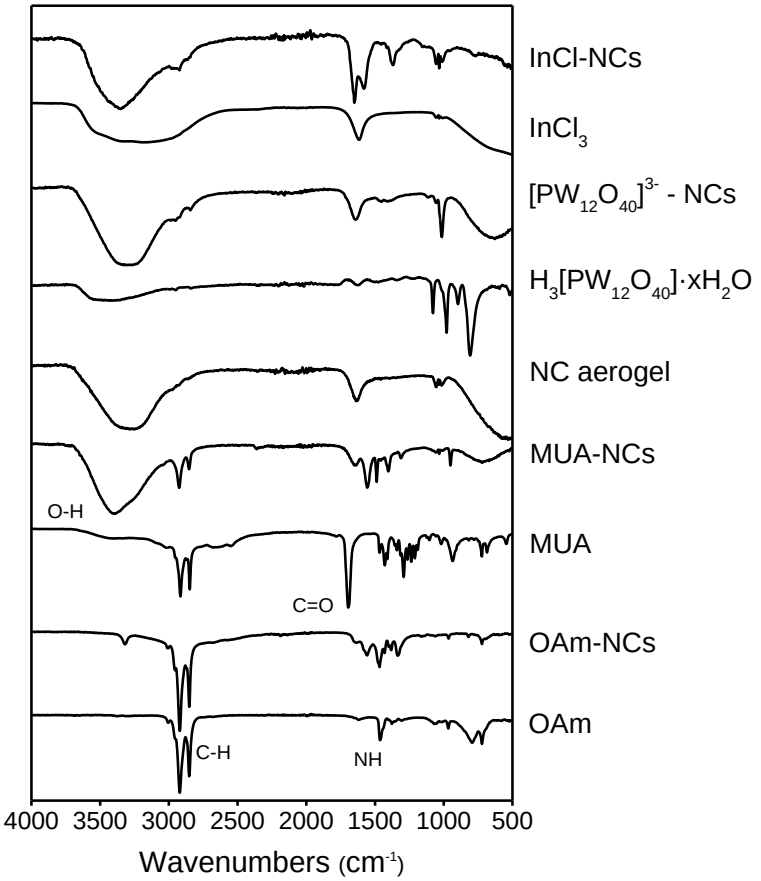

Fig. 6. FTIR spectra of MUA-NCs, PTA-NCs, InCl-NCs dispersed in methanol and OAm-NCs in hexane and corresponding ligands; and a NC aerogel.

XPS measurements corroborated the presence of $(PW_{12}O_{40})^{3-}$ and Cl on the surface of In_2S_3 NCs (Fig. 8). The XPS spectrum of $(PW_{12}O_{40})^{3-}$-NCs displayed the presence of tungsten at the In_2S_3 NC surface (~ 1 %), with a main oxidation state compatible with that of a tungstate (W 4f7/2 binding energy = 35.8 eV, Fig. 8 a).[35] The ratio In/S in $(PW_{12}O_{40})^{3-}$-NCs was slightly above that of stoichiometric In_2S_3: In/S = 0.87, and the main contribution to the In $3d_{5/2}$ electronic states (77 %) displayed a relatively high binding energy (In $3d_{5/2}$ binding energy =446.1 eV) compared to that of In_2S_3, which would be compatible with a higher electronegativity of $(PW_{12}O_{40})^{3-}$ anions. The second contribution to In $3d_{5/2}$ (In $3d_{5/2}$ binding energy =444.7 eV) was assigned to lattice In^{3+} in a In_2S_3 chemical environment. Two sulfur chemical states were also identified in this sample. Both components were found at lower binding energies than elemental sulfur, thus proving their less electronegative environment. The component at a higher binding energy (S $2p_{3/2}$ binding energy =162.9 eV) was assigned to surface sulfur exposed to the more electronegative $(PW_{12}O_{40})^{3-}$ anions, while the component at a lower binding energy (S $2p_{3/2}$ binding energy =161.6 eV) was assigned to S^{2-} within the In_2S_3 lattice.

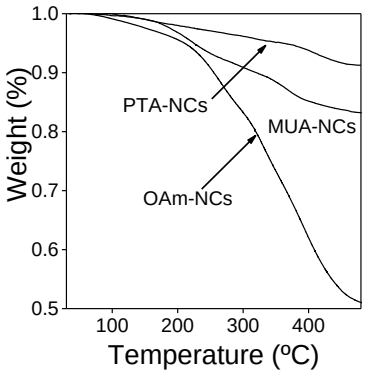

Fig. 7. TGA profiles of the initial In_2S_3 NCs (OAm-NCs) and of the In_2S_3 NCs capped with MUA and PTA-$(PW_{12}O_{40})^{3-}$.

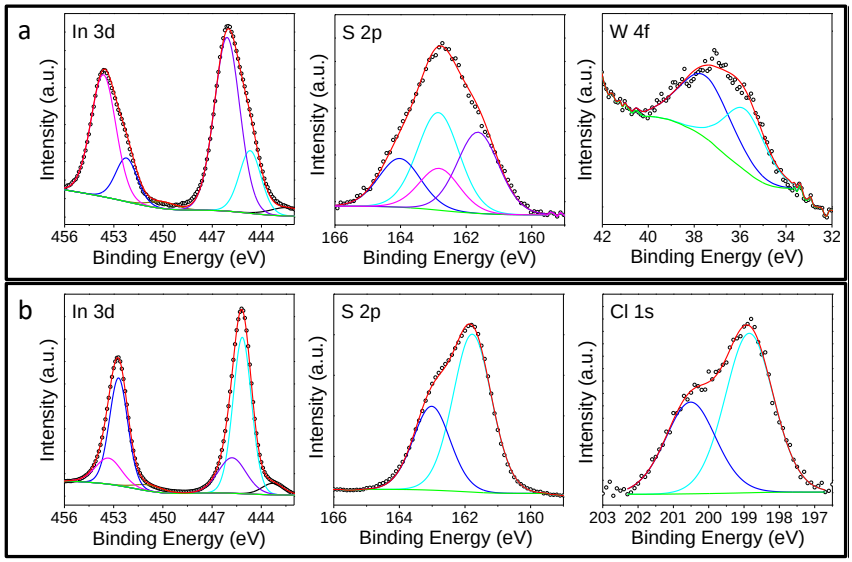

Fig. 8. a) XPS spectrum of the In 3d, S 2p and Cl 1s regions obtained from $(PW_{12}O_{40})^{3-}$-NCs. b) XPS spectrum of the In 3d, S 2p and Cl 1s regions obtained from InCl-NCs. c) FTIR spectra of OAm, MUA, MUA-NCs, OAm-NCs and a NC aerogel. Note that MUA-NCs and OAm-NCs were dispersed in methanol and hexane respectively.

The XPS spectrum of In_2S_3 NCs stabilized with $InCl_3$ (InCl-NCs) displayed the presence of Cl (~ 3%) in a metal chloride environment (Cl $2p_{3/2}$ binding energy = 198.9 eV, Figure 3 b). Additionally, the surface of InCl-NCs contained an even larger excess of In: In/S = 1.0. The main contribution to In electronic states (70 %) was compatible with both an In_2S_3 and an InCl chemical environment (In $3d_{5/2}$ binding energy = 445.2 eV, Figure 3 b), and a minor component at (In $3d_{5/2}$ binding energy =445.8 eV) could be assigned to $InCl_3$.[43] The S 2p region displayed a unique sulfur contribution (S $2p_{3/2}$ binding energy =161.7 eV) approximately coinciding with the lowest energy component in $(PW_{12}O_{40})^{3-}$-NCs and assigned to S^{2-} within the In_2S_3 chemical environment.

5.3.3. In_2S_3 NCs assembly into gels and aerogels

MUA-NCs were used as building blocks to produce In_2S_3 gels. The assembly of MUA-NCs was triggered by exposing them to a non-oxygen-transferring oxidant (Fig. 9), TNM (3% TNM

solution in methanol).[44] As previously described,[20] TNM oxidized the thiolate ligands bound to In^{3+} ions at the NC surface producing disulfides. Upon thiolate displacement from the NC surface, In^{3+} ions at the NC surface can be easily solvated by the carboxylate species or methanol, leaving a chalcogen-rich NC surface. In such chalcogen-rich NCs, and in the presence of sufficient oxidizer, chalcogen catenation takes place, resulting in the aggregation of the NCs into a network held together by interparticle chalcogen–chalcogen bonding.[19] This ligand-free gelation mechanism allows for direct connection of NCs without any intermediary ligand that could hinder, for instance, inter-particle charge transfer.

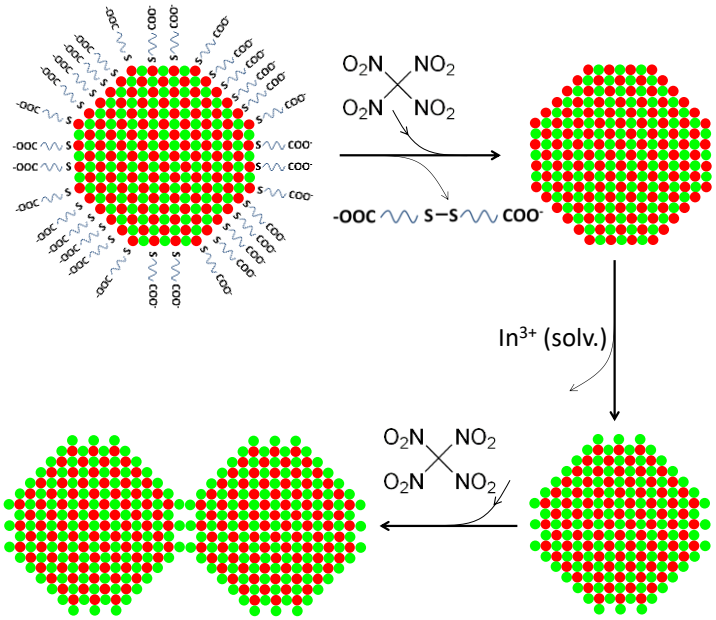

Fig. 9. Scheme of the gel formation by oxidation of MUA and sulphur ions at the NC surface.

The formed gel was subsequently dried under super-critical CO_2 to retain the porous structure. TEM characterization of the resulting aerogel (Fig. 10) revealed the random aggregation of the NCs. However, HRTEM micrographs showed some of the attached NCs to have coincident crystallographic orientations (Fig. 11). XRD patterns of the as-synthesized NCs displayed the reflections of the β-In_2S_3 crystallographic phase with a tetragonal crystal structure (Fig. 12). Two particularly intense peaks were observed on the diffraction patterns, suggesting a preferential growth of the material in these directions, which is consistent with the very asymmetric disk-shape of the NCs as observed by TEM. Similar patterns were reported by Park et al for In_2S_3 nanoplates.[34] The assembly of the In_2S_3 NCs into a gel did not substantially affect the material crystallinity as observed from the XRD pattern (Fig. 12), however additional peaks raised which could be related to the oriented attachment of the NCs and their growth in the direction normal to the disk plane.

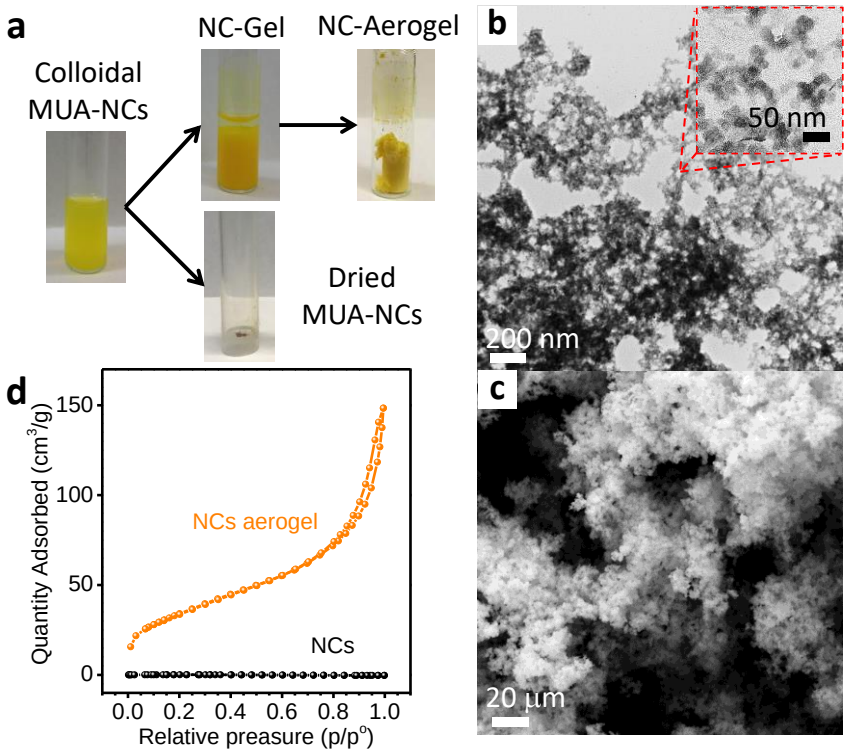

Fig. 10 a) Vials containing the MUA-NC solution in methanol, a NC wet gel, the super-critically dried NCs aerogel and the precipitated and dried MUA-NCs. b) TEM and c) SEM micrographs of an In_2S_3 NC aerogel. d) Nitrogen adsorption/desorption isotherms of an In_2S_3 NC aerogel and of dried MUA-NCs. e) Scheme of the gel formation by oxidation of MUA and sulphur ions at the NC surface.

SEM characterization of aerogels suggested a highly porous three dimensional structure with large voids (Fig. 10 d). FTIR analysis of the final aerogel evidenced that the gelation process was accompanied by the removal of MUA as proven by the suppression of the 2800-2900 cm^{-1} peak corresponding to the C-H vibration band (Fig. 6). The peak with low intensity at 2400 cm^{-1} could be ascribed to a residual amount of CO_2 in the measurement atmosphere or to the vibration of C=O ketone group originated from carboxylate group of MUA.

Type IV nitrogen adsorption/desorption isotherms, characteristic of mesoporous structures, were observed for the NC aerogels (Fig. 10 d). From the fitting of the data to a Brunauer-Emmett-Teller (BET) model,[46] the surface area of In_2S_3 NC aerogels was determined to be ca. 134 m^2/g, while that of precipitated MUA-NCs was just 40 m^2/g (Fig. 10 d). For comparison, the calculated surface area for colloidal In_2S_3 NCs with a disk-like geometry, a thickness of 1 nm and a diameter of 18 nm was 225 m^2/g

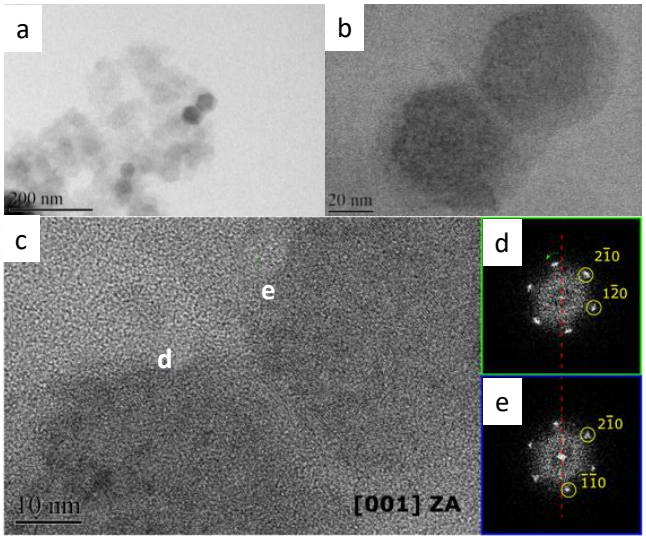

Fig. 11. TEM (a, b) and HRTEM (c) images of the In_2S_3 aerogel. (b) FFT of the NCs mark as b and c in the image (c).

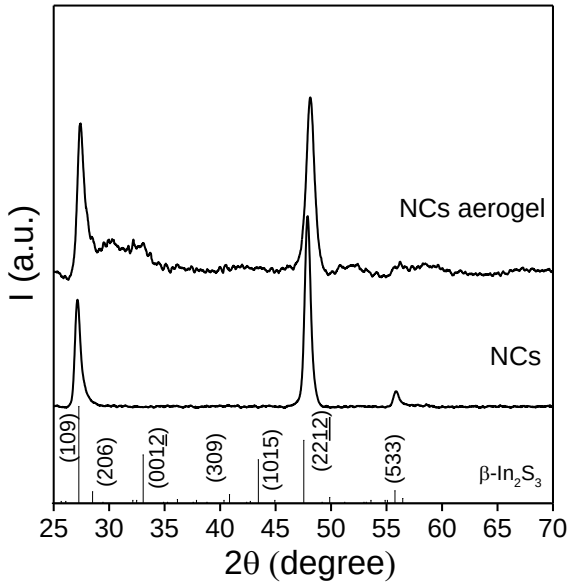

Fig. 12. XRD patterns of the In_2S_3 NCs and aerogel. The bars in the bottom correspond to the bulk β- In_2S_3 (JCPDS N 25-0390).

Fig. 13 displays the absorption spectra of the as-synthesized OAm-NCs and a NC-based aerogel. UV-vis measurements showed a slight blue shift of the absorption edge for the NC aerogel compared with OAm-NCs suggesting a change in the NCs sizes upon gelation. Indeed calculation of the NCs sizes using Scherrer equation demonstrated a slight decrease from $L_{(311)}$ = 18 nm for precursor NCs to $L_{(311)}$ = 15 nm for NC aerogel. These results are consistent with those obtained from CdSe NC aerogels and might be related to the etching of the NCs surface during the gelation process.[20] A shift of the absorption edge related to the aerogel interconnected structure was also observed for CdSe NC-based aerogels.[45] However, this effect had associated a red shift of the spectra, which was not observed here.

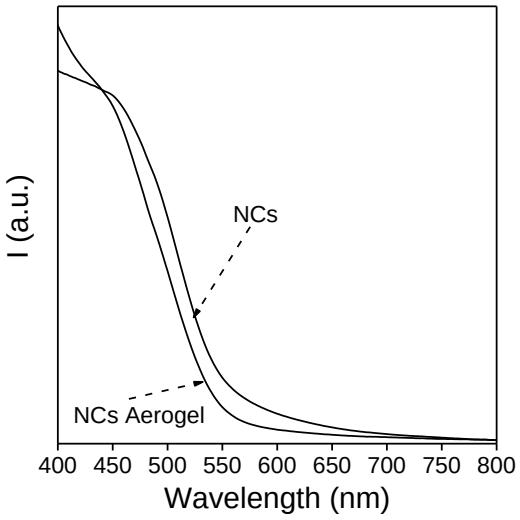

Fig. 13. Absorption spectra from OAm-NC and a NC aerogel**.**

The amount of oxidizing agent introduced was a key parameter controlling the gelation process. On one hand, low amounts of TNM resulted in partial NC aggregation and precipitation but without the formation of a proper NC network. On the other hand, an excess of the oxidizing agent resulted in much denser gels by strongly accelerated the NC aggregation through efficiently removing all the MUA molecules and leading to extensive chalcogen-chalcogen bond formation (Fig. 14).

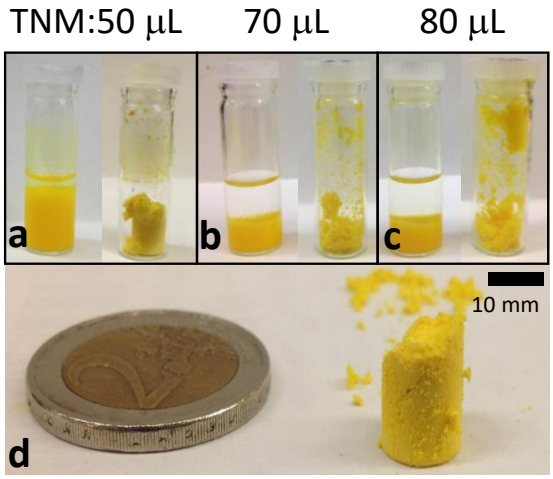

Fig. 14. Optical photographs of the In_2S_3 NCs-gel and corresponding aerogel synthesized by increasing of the amount of the gelator agent (3% TNM solution) from 50 μL (a, d) to 70 μL (b) and 80 μl (c) demonstrate that increasing the oxidizer concentration can lead to complete thiolate-ligand removing that offer more active sites for creation of disulfide native bonds and induce faster aggregation process resulting in denser and shrink gel (b, c). Scale bar is the same for all photographs.

5.3.4. Photocatalytic performance

The photocatalytic performance of In_2S_3 NCs in suspension was evaluated through the degradation of RhB under xenon lamp irradiation (300 W). In a typical measurement, 20 mg of NCs were suspended in 10 mL of MQ-water containing 10 ppm of RhB. Before irradiation, the solution was stirred in the dark for 30 min to achieve adsorption equilibrium. Note that OAm-

NCs were not stable in MQ-water and thus were not tested for RhB degradation. MUA-NCs showed a poor activity toward photodegradation of RhB, reaching just 50% of RhB degradation after 2 h illumination (Fig. 15). We associated this poor performance to the limited access of RhB to the MUA-covered NC surface. Under illumination, photogenerated electrons are transferred to adsorbed dye molecules to decompose them. If not properly extracted, photogenerated holes accumulate at the In_2S_3 NC and result in the oxidation of the NC surface.[11] In MUA-NCs, this photooxidation results in the detachment of MUA ligands as disulphides and, hence, induce irreversible NCs aggregation and consequent surface loss.[47-49]

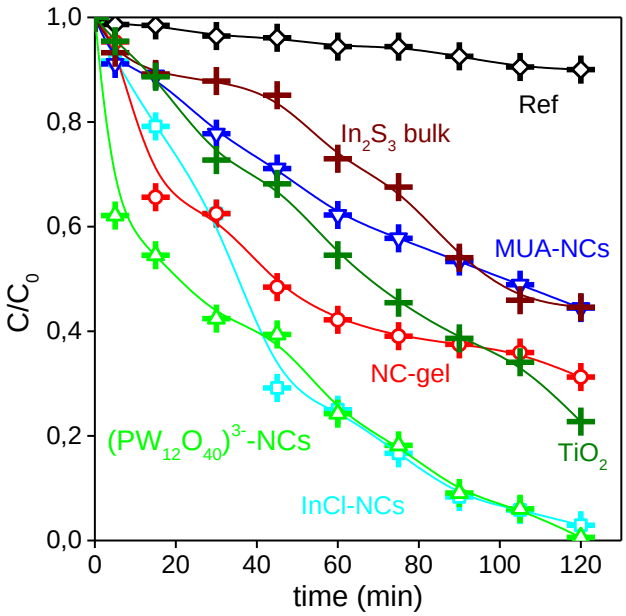

Fig. 15. Photocatalytic degradation curves of RhB on MUA-NCs, $(PW_{12}O_{40})^{3-}$-NCs, InCl-NCs and a NC-gel compare to commercial TiO_2 photocatalyst (Degussa P25) powder and In_2S_3 bulk. Experiments were carried out by irradiating a 10 ppm RhB mixture containing 20 mg of sample in MQ-water with a xenon lamp (300 W) for 2 hours**.**

$(PW_{12}O_{40})^{3-}$- and InCl-NCs provided the highest RhB degradation rates, which we attributed to the superior surface accessibility on these NCs due to the absence of organic ligands and their fair stability in solution during the whole experiment (Fig. 15). No photooxidation-induced aggregation was observed for $(PW_{12}O_{40})^{3-}$-NCs and InCl-NCs proving the presence of these ligands to provide a better stability. Noteworthy, the In_2S_3 NC-gel showed intermediate activity for RhB degradation (65 %) under the same experimental conditions. This intermediate efficiency of NC-gels corresponded to a partially organic-free surface compared to MUA-NCs but associated with a lower total active area if compared with colloidal $(PW_{12}O_{40})^{3-}$-NCs and InCl-NCs.

Additionally, we compared the catalytic performance of the In_2S_3 nanocrystalline material with that of bulk In_2S_3 and of a conventional TiO_2 catalyst. As expected, bulk In_2S_3 exhibited moderate catalytic activity compared to the nanocrystalline materials here analyzed. The TiO_2 nanopowder also showed a lower catalytic activity under the xenon light irradiation compared to In_2S_3 NCs stabilized with inorganic ligands. A comparison of the performance of the In_2S_3 NCs measured here with those obtained in previous works is given in the Table 1.

Table 1 – Comparison of the performance of In_2S_3 for dye degradation

Catalyst	Dye	Light	Irradiation time	Irradiation intensity, W/m^2	Catalyst amount, mg	Ref.
In_2S_3	MB	High-pressure mercury lamp	8 h		2.5	3
In_2S_3	MO	Halogen lamp	4.5 h	1134	40	4
In_2S_3	RhB	Xenon lamp	210 min	1000	30	5
In_2S_3–TiO_2	p-nitrophenol	Xenon lamp	250 min	700		6
In_2S_3	MO	Xenon lamp	180 min		20	7
In_2S_3	MB	Sodium vapor lamp	3 h		100	8
In_2S_3	RhB	Xenon lamp	120 min	1000	20	This work

To investigate their photoelectrocatalytic properties, In_2S_3 NCs were supported on ITO-covered glass substrates. NC layers were prepared by spin coating a methanol solution of the NCs (Fig. 16). To produce porous films, the MUA-NC layer was dipped into a TNM solution immediately after spin coating, interconnecting in this way the In_2S_3 NCs into a porous network.[20] The substrate was afterwards rinsed with methanol to remove excess of TNM and reaction by-products. All layers were annealed at 250 °C for 60 min under argon flow before photoelectrocatalytic characterization.

The photoelectrocatalytic performance of In_2S_3 NCs was evaluated using a three-electrode cell with a Pt-coiled counter electrode, an Ag/AgCl reference electrode and the NCs film as working electrode. A polysulfide solution, consisting of a 1 M aqueous solution of Na_2S, NaOH and S, was used as electrolyte. Figure 8 shows the results obtained from linear sweep voltammograms and time-dependent photocurrent measurements of the different samples analysed.

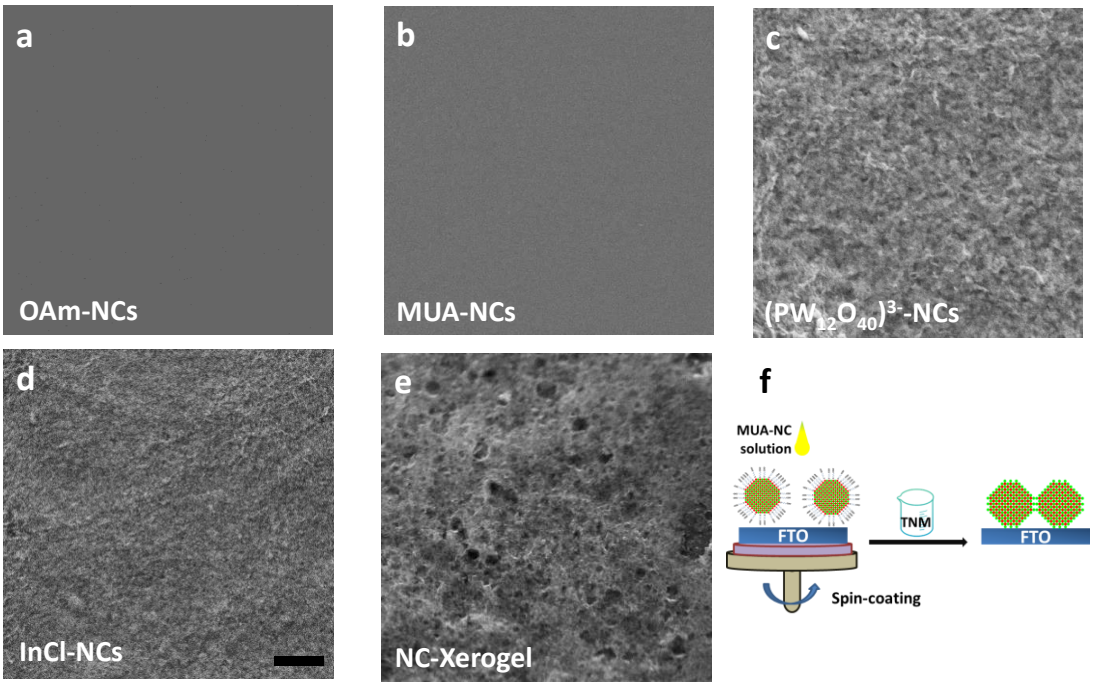

Fig. 16. a-e) SEM images of films obtained by spin-coating OAm-NCs (a), MUA-NCs (b), $(PW_{12}O_{40})^{3-}$-NCs (c), InCl-NCs (d), and MUA-NCs that were subsequently linked together by oxidation with TNM to produce a xerogel layer (e). Scale bar = 2 µm. f) Scheme of the process of formation of a gel layer**.**

Films obtained by spin coating OAm- and MUA-NCs showed the lowest performance. We attribute this poor performance to a limited access of the sulphide species to the NC's surface and to the low electrical conductivity of the film due to the presence of the insulating organic ligands. The lower performance of OAm-NCs if compared to MUA-NCs could result from the hydrophobic nature of OAm-NCs which may reduce the interaction with the reaction solution hence reducing the current density. The hydrophilic nature of MUA-NC films provided a better contact between the NCs and the electrolyte and hence slightly higher photocurrent densities. Layers produced from $(PW_{12}O_{40})^{3-}$-NCs and InCl-NCs showed improved photocurrents compared with OAm-NCs, which we attributed to a more efficient charge transfer with the media and a faster charge transport between the NCs. Surprisingly, gel layers provided the highest photocurrent densities, reaching 150 µA/cm^2 at 1.0 V vs Ag/AgCl which represent a five-fold increase compared to the $(PW_{12}O_{40})^{3-}$-NCs and InCl-NCs films (Fig. 17 a). We attributed such enhanced performance of the gel layers to: i) an organic-free NC interconnection, resulting in improved interaction and charge transfer, ii) a high degree of porosity offering large active surface areas for interaction with the media. EIS measurements confirmed the lower charge transfer resistance of the gel layers compared with $(PW_{12}O_{40})^{3-}$-NCs and InCl-NCs films, associated again to the higher surface area and the NC interconnection within the gel layers (Fig. 17 c).

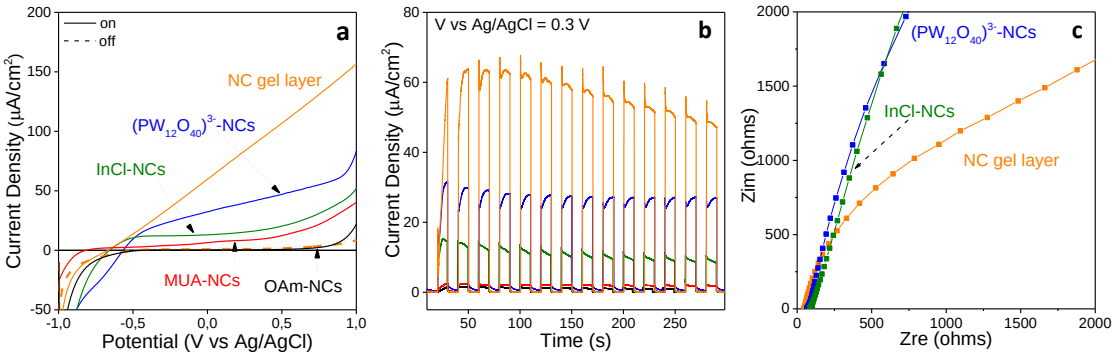

Fig. 17. Linear sweep voltammogram curves (a) and chronoamperometric characteristics normalized by the amount of photoactive material at 0.3 V vs. Ag/AgCl (b) of gel layers and layers produced from OAm-, MUA-, $(PW_{12}O_{40})^{3-}$- and InCl-NCs. Nyquist plots for $(PW_{12}O_{40})^{3-}$NCs, InCl-NCs and gel layer (c).

5.4. Conclusions

We compared the photocatalytic and photoelectrocatalytic performance of disk-shaped In_2S_3 NCs with different surface chemistries and supra-crystalline organization. Dispersions of In_2S_3 NCs, colloidally stabilized with inorganic ligands such as oxometallates or chlorides, showed the highest photocatalytic performance toward dye degradation in solution. We attributed this experimental fact to the higher accessibility of the NC surface provided by the inorganic ligands compared with the organic ones and to the colloidal stability of the materials, which provided maximized surface areas to interact with the media. On the other hand, organized NC assemblies provided higher photoelectrocatalytic performances than organic- and inorganic-capped NCs. The organization of the NCs into NC networks held together through chalcogen-chalcogen bonds simultaneously provided larger surface areas for interaction with the media compared with layers of precipitated NCs, and effective avenues for charge transport through the layer.

5.5. References

1. Talapin, D. V.; Lee, J.-S.; Kovalenko, M. V.; Shevchenko, E. V., Prospects of colloidal nanocrystals for electronic and optoelectronic applications. *Chem. Rev.* **2010,** *110*, 389-458.
2. Popczun, E. J.; McKone, J. R.; Read, C. G.; Biacchi, A. J.; Wiltrout, A. M.; Lewis, N. S.; Schaak, R. E., Nanostructured nickel phosphide as an electrocatalyst for the hydrogen evolution reaction. *J. Am. Chem. Soc.* **2013,** *135*, 9267-9270.
3. Li, D.; Baydoun, H.; Kulikowski, B.; Brock, S. L., Boosting the catalytic performance of iron phosphide nanorods for the oxygen evolution reaction by incorporation of manganese. *Chem. Mat.* **2017,** *29*, 3048-3054.
4. Lim, W. Y.; Hong, M.; Ho, G. W., In situ photo-assisted deposition and photocatalysis of $ZnIn_2S_4$/transition metal chalcogenides for enhanced degradation and hydrogen evolution under visible light. *Dalton Transactions* **2016,** *45* (2), 552-560.
5. Thatai, S.; Khurana, P.; Boken, J.; Prasad, S.; Kumar, D., Nanoparticles and core–shell nanocomposite based new generation water remediation materials and analytical techniques: A review. *Microchem. J.* **2014,** *116*, 62-76.
6. Yu, X.; Shavel, A.; An, X.; Luo, Z.; Ibáñez, M.; Cabot, A., Cu_2ZnSnS_4-Pt and Cu_2ZnSnS_4-Au heterostructured nanoparticles for photocatalytic water splitting and pollutant degradation. *J. Am. Chem. Soc.* **2014,** *136*, 9236-9239.
7. Mahmoud, M. A.; O'Neil, D.; El-Sayed, M. A., Hollow and solid metallic nanoparticles in sensing and in nanocatalysis. *Chem. Mat.* **2014,** *26* (1), 44-58.
8. Zhang, Q.; Su, H.; Luo, J.; Wei, Y., A magnetic nanoparticle supported dual acidic ionic liquid: a "quasi-homogeneous" catalyst for the one-pot synthesis of benzoxanthenes. *Green Chem.* **2012,** *14*, 201-208.
9. Xiang, Q.; Yu, J.; Jaroniec, M., Synergetic effect of MoS_2 and graphene as cocatalysts for enhanced photocatalytic h_2 production activity of TiO_2 nanoparticles. *J. Am. Chem. Soc.* **2012,** *134*, 6575-6578.
10. Talapin, D. V., Nanocrystal solids: A modular approach to materials design. *MRS Bull.* **2012,** *37*, 63-71.
11. Stolarczyk, J. K.; Deak, A.; Brougham, D. F., Nanoparticle clusters: assembly and control over internal order, current capabilities, and future potential. *Adv. Mater.* **2016,** *28*, 5400-5424.
12. Korala, L.; Germain, J. R.; Chen, E.; Pala, I. R.; Li, D.; Brock, S. L., CdS aerogels as efficient photocatalysts for degradation of organic dyes under visible light irradiation. *Inorg. Chem. Front.* **2017,** *4*, 1451-1457.
13. Wu, Z.-S.; Yang, S.; Sun, Y.; Parvez, K.; Feng, X.; Müllen, K., 3D nitrogen-doped graphene aerogel-supported Fe_3O_4 nanoparticles as efficient electrocatalysts for the oxygen reduction reaction. *J. Am. Chem. Soc.* **2012,** *134*, 9082-9085.
14. Kagan, C. R.; Lifshitz, E.; Sargent, E. H.; Talapin, D. V., Building devices from colloidal quantum dots. *Science* **2016,** *353,* 6302.
15. Yang, M.-Q.; Xu, Y.-J.; Lu, W.; Zeng, K.; Zhu, H.; Xu, Q.-H.; Ho, G. W., Self-surface charge exfoliation and electrostatically coordinated 2D hetero-layered hybrids. *Nature Communications* **2017,** *8*, 14224
16. Shevchenko, E. V.; Talapin, D. V.; Kotov, N. A.; O'Brien, S.; Murray, C. B., Structural diversity in binary nanoparticle superlattices. *Nature* **2006,** *439*, 55.

17. Redl, F. X.; Cho, K. S.; Murray, C. B.; O'Brien, S., Three-dimensional binary superlattices of magnetic nanocrystals and semiconductor quantum dots. *Nature* **2003,** *423*, 968.

18. Gaponic, N.; Herrmann, A.-K.; Eychmuller, A., Colloidal Nanocrystal-Based Gels and Aerogels: Material Aspects and Application Perspectives. *J. Phys. Chem. Lett.* **2012**, *3*, 8-17.

19. Mohanan, J. L.; Arachchige, I. U.; Brock, S. L., Porous semiconductor chalcogenide aerogels. *Science* **2005,** *307*, 397-400.

20. Pala, I. R.; Arachchige, I. U.; Georgiev, D. G.; Brock, S. L., Reversible gelation of II–VI nanocrystals: the nature of interparticle bonding and the origin of nanocrystal photochemical instability. *Angew. Chem. Int. Edit.* **2010,** *49*, 3661-3665.

21. Arachchige, I. U.; Brock, S. L., Sol–gel methods for the assembly of metal chalcogenide quantum dots. *Accounts Chem. Res.* **2007,** *40*, 801-809.

22. Korala, L.; Wang, Z.; Liu, Y.; Maldonado, S.; Brock, S. L., Uniform thin films of CdSe and CdSe(ZnS) Core(Shell) quantum dots by sol–gel assembly: enabling photoelectrochemical characterization and electronic applications. *ACS Nano* **2013,** *7*, 1215-1223.

23. Korala, L.; Li, L.; Brock, S. L., Transparent conducting films of CdSe(ZnS) core(shell) quantum dot xerogels. *Chem. Commun.* **2012,** *48*, 8523-8525.

24. Gschneidner, K.A.; Eyring, Jr. and L. *Handbook on the Physics and Chemistry of Rare Earths*; Gschneidner, K.A.; Eyring, Jr. and L., Eds.; Elsevier, 1999; Vol. 11, p.148.

25. Peng, S.; Li, L.; Wu, Y.; Jia, L.; Tian, L.; Srinivasan, M.; Ramakrishna, S.; Yan, Q.; Mhaisalkar, S. G., Size- and shape-controlled synthesis of $ZnIn_2S_4$ nanocrystals with high photocatalytic performance. *CrystEngComm* **2013,** *15*, 1922-1930.

26. Chen, W.; Bovin, J.-O.; Joly, A. G.; Wang, S.; Su, F.; Li, G., Full-color emission from In_2S_3 and In_2S_3: Eu^{3+} nanoparticles. *J. Phys. Chem. B* **2004,** *108* (32), 11927-11934.

27. Xie, X.; Shen, G., Single-crystalline In_2S_3 nanowire-based flexible visible-light photodetectors with an ultra-high photoresponse. *Nanoscale* **2015,** *7*, 5046-5052.

28. He, Y.; Li, D.; Xiao, G.; Chen, W.; Chen, Y.; Sun, M.; Huang, H.; Fu, X., A New application of nanocrystal In_2S_3 in efficient degradation of organic pollutants under visible light irradiation. *J. Phys. Chem. C* **2009,** *113*, 5254-5262.

29. Xu, R.; Li, H.; Zhang, W.; Yang, Z.; Liu, G.; Xu, Z.; Shao, H.; Qiao, G., The fabrication of In_2O_3/In_2S_3/Ag nanocubes for efficient photoelectrochemical water splitting. *Phys. Chem. Chem. Phys.* **2016,** *18*, 2710-2717.

30. Du, W.; Zhu, J.; Li, S.; Qian, X., Ultrathin β-In_2S_3 Nanobelts: Shape-Controlled Synthesis and Optical and Photocatalytic Properties. *Cryst. Growth Des.* **2008,** *8*, 2130-2136.

31. Lucena, R.; Aguilera, I.; Palacios, P.; Wahnón, P.; Conesa, J. C., Synthesis and spectral properties of nanocrystalline V-substituted In_2S_3, a novel material for more efficient use of solar radiation. *Chem. Mat.* **2008,** *20*, 5125-5127.

32. Tapia, C.; Berglund, S. P.; Friedrich, D.; Dittrich, T.; Bogdanoff, P.; Liu, Y.; Levcenko, S.; Unold, T.; Conesa, J. C.; De Lacey, A. L.; Pita, M.; Fiechter, S., Synthesis and characterization of V-doped β-In_2S_3 thin films on FTO substrates. *J. Phys. Chem. C* **2016,** *120*, 28753-28761.

33. Xue, B.; Xu, F.; Wang, B.; Dong, A., Shape-controlled synthesis of β-In_2S_3 nanocrystals and their lithium storage properties. *CrystEngComm* **2016,** *18* (2), 250-256.

34. Park, K. H.; Jang, K.; Son, S. U., Synthesis, Optical properties, and self-assembly of ultrathin hexagonal In_2S_3 nanoplates. *Angew. Chem. Int. Edit.* **2006,** *45*, 4608-4612.

35. Ghosh, S.; Saha, M.; Ashok, V. D.; Chatterjee, A.; De, S., Excitation dependent multicolor emission and photoconductivity of Mn, Cu doped In_2S_3 monodisperse quantum dots. *Nanotechnology* **2016,** *27* (15), 155708.
36. Chen, J.; Liu, W.; Gao, W., Tuning photocatalytic activity of In2S3 broadband spectrum photocatalyst based on morphology. *Appl. Surf. Sci.* **2016,** *368*, 288-297.
37. Liu, G.; Jiao, X.; Qin, Z.; Chen, D., Solvothermal preparation and visible photocatalytic activity of polycrystalline β-In_2S_3 nanotubes. *CrystEngComm* **2011,** *13* (1), 182-187.
38. Huang, J.; Liu, W.; Dolzhnikov, D. S.; Protesescu, L.; Kovalenko, M. V.; Koo, B.; Chattopadhyay, S.; Shenchenko, E. V.; Talapin, D. V., Surface functionalization of semiconductor and oxide nanocrystals with small inorganic oxoanions (PO_4^{3-}, MoO_4^{2-}) and polyoxometalate ligands. *ACS Nano* **2014,** *8*, 9388-9402.
39. Sayevich, V.; Guhrenz, C.; Sin, M.; Dzhagan, V. M.; Weiz, A.; Kasemann, D.; Brunner, E.; Ruck, M.; Zahn, D. R. T.; Leo, K.; Gaponik, N.; Eychmüller, A., Chloride and indium-chloride-complex inorganic ligands for efficient stabilization of nanocrystals in solution and doping of nanocrystal solids. *Adv. Funct. Mat.* **2016,** *26*, 2163-2175.
40. Wuister, S. F.; de Mello Donegá, C.; Meijerink, A., Influence of thiol capping on the exciton luminescence and decay kinetics of CdTe and CdSe quantum dots. *J. Phys. Chem. B* **2004,** *108*, 17393-17397.
41. Yang, Z.; Chen, C.-Y.; Roy, P.; Chang, H.-T., Quantum dot-sensitized solar cells incorporating nanomaterials. *Chem. Commun.* **2011,** *47*, 9561-9571.
42. Tauc, J.; Grigorovici, R.; Vancu, A., Optical properties and electronic structure of amorphous germanium. *Phys. Status Solidi B* **1966,** *15*, 627-637.
43. Moulder, J. F.; Stickle, W. F.; Sobol, P. E.; Bomben, K. D. Handbook of X-Ray Photoelectron Spectroscopy; Perkin-Elmer: Eden Prairie, MN, 1992.
44. Evans, B. J.; Takahashi Doi, J.; Kenneth Musker W., ^{19}F NMR study of the reaction of p-fluorobenzenethiol and disulfide with periodate and other selected oxidizing agents. *J. Org. Chem*. **1990**, *55*, 2337.
45. Yu, H.; Liu, Y.; Brock, S. L., Tuning the Optical Band Gap of Quantum Dot Assemblies by Varying Network Density. *ACS Nano* **2009,** *3* (7), 2000-2006.
46. Sing K. S. W., Reporting physisorption data for gas/solid systems with special reference to the determination of surface area and porosity*, Pure Appl. Chem.* **1982***,* 54, 2201.
47. Simon, T.; Bouchonville, N.; Berr, M. J.; Vaneski, A.; Adrović, A.; Volbers, D.; Wyrwich, R.; Döblinger, M.; Susha, A. S.; Rogach, A. L.; Jäckel, F.; Stolarczyk, J. K.; Feldmann, J., Redox shuttle mechanism enhances photocatalytic H_2 generation on Ni-decorated CdS nanorods. *Nat. Mater.* **2014,** *13*, 1013.
48. Aldana, J.; Wang, Y. A.; Peng, X., Photochemical Instability of CdSe Nanocrystals Coated by Hydrophilic Thiols. *J. Am. Chem. Soc.* **2001,** *123*, 8844-8850.
49. Rogach, A. L.; Kornowski, A.; Gao, M.; Eychmüller, A.; Weller, H., Synthesis and characterization of a size series of extremely small thiol-stabilized CdSe nanocrystals. *J. Phys. Chem. B* **1999,** *103*, 3065-3069.

6. Assembly of multicomponent metal chalcogenide NCs: the case of $CuGaS_2$

Abstract

The manufacturing of semiconducting layers using solution-based approaches is considered a low cost alternative to vacuum-based thin film deposition strategies. An additional advantage of solution processing methods is the possibility to control the layer nano/microstructure. This chapter is devoted to the investigation of the assembly of ternary sulfides into xerogel porous layers and study their photoelectrocatalytic activity. We formulate $CuGaS_2$ nanocrystal-based inks by replacing the native long-chain hydrocarbon ligands with shorter thiolate molecules. We produce layers using these inks and after deposition, we link the nanocrystals together by means of a non-oxygen transferring oxidant to form a porous structure. This oxidizing agent indirectly creates chalcogen-chalcogen bonds between the nanocrystals, which potentially reduce surface recombination sites and facilitates charge transport through the layer. We further produce $CuGaS_2$/ZnS nanocrystal-based bilayers and $CuGaS_2$–ZnS nanocrystal-based composite layers and demonstrate them to provide improved current densities and photoresponses than layers produced from as-produced nanocrystals.

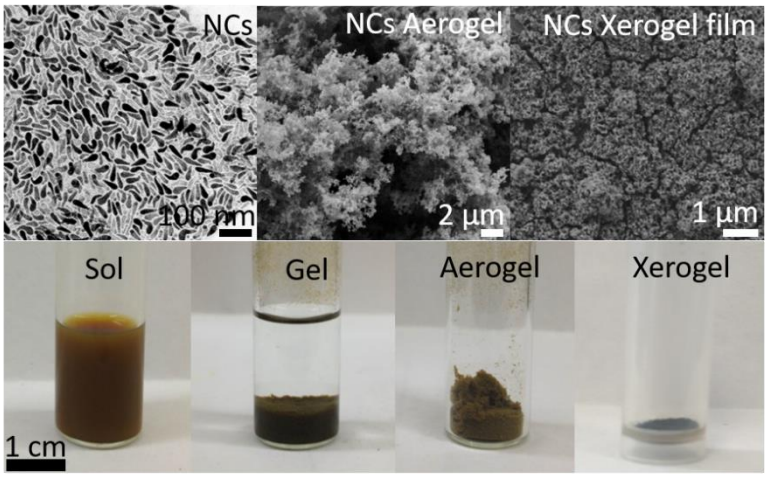

6.1. Introduction

The solution-based processing of semiconductor films has a number of advantages over the use of vacuum-based technologies. Solution-based processes require lower capital investments, have associated lower maintenance costs, and provide higher production throughput and material yields. These characteristics make them highly appropriate for large scale industrial production. Among the different solution-processing technologies, the deposition of inks formulated from nanocrystals (NCs) is particularly interesting as it allows unparalleled control over material properties and layer nano/microstructure, and it provides crystalline layers without mediating a thermal annealing step, thus reducing processing costs. However, in the absence of a sintering step, ink-based processes generally result in layers characterized by poor electrical conductivities, which is a drawback in most applications. While a thermal annealing is frequently used to improve performance, such treatment spoil main advantages of NC-based solution processes, such as the precise composition control and the cost reduction associated with the production of crystalline layers without the need of a sintering process. Additionally, even annealed NC-based layers contain significant amounts of carbon coming from added binders and from the surface ligands used to control NC growth and render NCs soluble in the ink media.[1] To fully remove carbon, heat treatments in an oxygen atmosphere are needed, but this is not compatible with materials that are susceptible to oxidation, such as chalcogenides. An alternative strategy to remove organics is the use of solution-based treatments, but these processes often involve toxic compounds such as hydrazine.[2,3] Besides toxicity, if not properly controlled, such solution-based ligand-stripping strategies can result in large concentrations of surface traps that may strongly limit the material performance.[4] An alternative strategy to remove organic ligands from NC-based layers and cross-link the NCs to facilitate charge transport involves using a non-oxygen-transferring oxidant.[5-7] This oxidizing agent produces chalcogen-chalcogen bonds between the NCs, potentially reducing surface recombination sites and facilitating charge transfer between NCs.[8,9] The concentration of this oxidizing agent also allows the porosity of the final material to be controlled. In this regard, in the particular case of photocatalysis and photoelectrocatalytic applications, the formation of porous layers may be advantageous since porous materials allow penetration of reactive species and expose huge surface areas for interaction with the media.[10]

Relative to metal oxides, metal sulfide NCs are of great importance because of their covalent bonding, which results in higher charge carrier mobilities, broader bands and narrower energy gaps.[1] Relative to other selenides and tellurides, sulfides present an obvious advantage in terms of abundance and cost. Among metal sulfides, $CuGaS_2$ (CGS), a p-type semiconductor, has gained special attention due to its relatively good stability, moderate cost and toxicity and its direct band gap in the visible (2.4 eV).[11] CGS is employed in green-light emitting LEDs as well as in visible-light-induced photocatalysis. Furthermore, its relatively large band gap makes it promising as host material for the introduction of intermediate band states to widen its absorption spectra.[12,13]

In this chapter, we use the oxidative assembly strategy[14] to produce porous CGS NC-based layers. We further extend this strategy to the production of porous multilayers of CGS and ZnS, and of porous composite layers combining CGS and ZnS NCs. We additionally characterize their

photoelectrochemical performance toward hydrogen evolution from a Na_2SO_4-containing water solution.

6.2. Experimental

6.2.1. Synthesis of $CuGaS_2$ NCs

1 mmol of $Cu(acac)_2$ and 1 mmol of $Ga(acac)_3$ together with 3.5 mmol of TOPO were mixed with 10 mL of OAm upon magnetic stirring. After degassing at 90 °C for 60 min under vacuum, an argon atmosphere was introduced and the reaction mixture was heated to 270 °C. At 150 °C, 1.12 mmol (0.25 mL) of DDT and 7.4 mmol (1.75 mL) of t-DDT were injected, which changed the color of the solution from dark blue to clear yellow. While increasing temperature, the solution color further changed to clear brown, indicating the NC nucleation, and dark-brown at 250 °C. The mixture was allowed to react at 270 °C for 30 min and afterward the heating mantle was removed to allow the solution to cool down naturally. NCs were isolated by adding 5 mL of acetone and centrifuging at 5700 rpm for 5 min. The supernatant was discarded and the precipitate was redispersed in 5 mL of hexane. Additional purification steps were performed following the same procedure. Finally, NCs were redispersed in 5 mL of hexane for later use.

6.2.2. Synthesis of ZnS NCs

2 mmol of $ZnCl_2$ and 6.5 mmol of TOPO were dissolved in 10 mL of OAm under Ar atmosphere at 170 ^oC for 60 min. After clear transparent solution was formed, the heating mantle was removed and the reaction was allowed to cool down to room temperature and the previously degassed mixture of 2.5 mmol of S in 5 mL of OAm was injected. Afterward the obtained mixture was heated to 320 ^oC and allowed to react for 60 min. The NCs were collected and washed by adding of 5 mL of ethanol followed by centrifugation. The washing procedure was repeated at least 2 more times and NCs were dispersed in 5 mL of hexane for further use.

6.2.3. NCs surface functionalization

6.2.3.1. TGA ligand exchange

For the ligand exchange on $CuGaS_2$ NCs, 4 mmol of TGA was added to 10 mL of methanol followed by increasing of pH level to 10 by introducing of TMAOH. The obtained solution was added to the precipitated $CuGaS_2$ NCs (approximately 20 mg) with subsequent sonication and continuous shaking for approximately 15 min. Afterward NCs were washed by adding 10 mL of acetone and centrifuging at 5700 rpm for 5 min. The purification step was repeated twice following by redispersion of NCs in 1 mL of methanol.

6.2.3.2. MUA ligand exchange

MUA ligands were used for surface functionalization of ZnS NCs. Ligand exchange was carried out by mixing 1 mL of ZnS NCs solution (20 mg/mL in hexane) with 1 mL of a MUA solution (4 mmol in 10 mL of methanol) at pH 10. The resulting bi-phase solution was shacked and sonicated for 15 min, afterward the upper part was removed and 5 mL of fresh acetone was

added followed by centrifuging for 5 min at 5000 rpm. The obtained precipitate was redispersed in 1 mL of methanol for further use.

6.2.4. NCs films

Typically, 1 mL of as-synthesized or thiol-capped (TGA for $CuGaS_2$ or MUA for ZnS) NCs (20 mg/mL) were spin-coated on previously washed FTO substrates at a rotation speed of 1500 rpm for 20 seconds. The obtained layers were annealed at 250 ^oC for 60 min under an Ar flow.

6.2.4.1. Porous xerogel films

1 mL of TGA capped $CuGaS_2$ NCs or MUA capped ZnS NCs with the concentration of 20 mg/mL were spin-coated on FTO substrates followed by procedure described above. Afterwards, the obtained layers were immediately dipped for 1 min in a solution contained of 3% of TNM in acetone. The films were rinsed with fresh methanol in order to remove byproducts and annealed at 250 ^oC for 60 min under Ar flow.

6.2.5. Photoelectrochemical measurements

Photocurrent measurements were performed using a three-electrode cell configuration with a Pt-mesh as a counter electrode (with the surface area of 2 cm^2) and a Ag/AgCl reference electrode filled with 3M KCl solution. 0.1M aqueous solution of Na_2SO_4 at pH7 was used as an electrolyte. Bias voltage to the working electrode was applied through an electrical contact to the uncoated part of the FTO glass substrate. A surface area of 1 cm^2 of the deposited film was in contact with the electrolyte. Illumination was provided by 8 xenon lamps (35 W each) radially distributed with a total power of 280 W and irradiance on the sample of ca. 100 mW/cm^2.

6.3. Results and discussion

CGS NCs were synthesized using a previously reported procedure with some modifications (see experimental section for details).[15] Briefly, NCs were produced through the reaction of DDT and t-DDT with $Cu(acac)_2$ and $Ga(acac)_3$ dissolved in OAm and in the presence of TOPO. The reaction mixture was heated up to 270 °C and maintained at this temperature for 30 min. From this procedure, CGS NCs with the wurtzite crystal phase, tadpole geometry and an average length of ca. 50 nm were produced (Fig. 1).

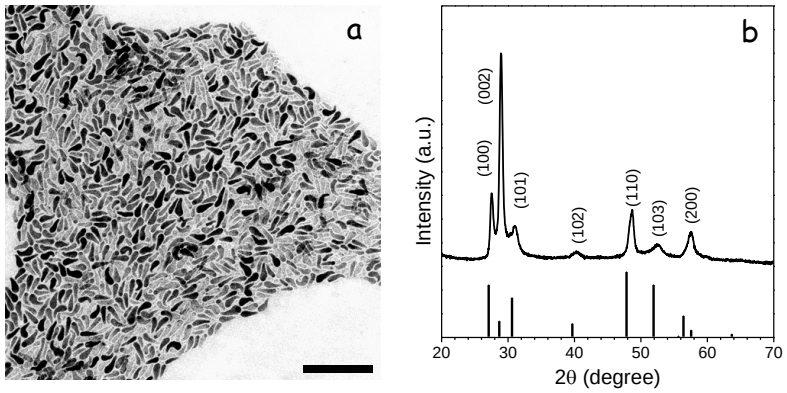

Fig. 1. Representative TEM micrograph (a) and XRD pattern (b) of CGS NCs with wurtzite crystal phase. TEM scale bar = 200 nm. The JCPDS 001-1280 pattern, corresponding to wurtzite CGS, is included as reference.

FTIR characterization showed the as-prepared CGS NCs to contain significant amounts of organic ligands, as revealed by the presence of peaks at 2924 cm^{-1} and 2830 cm^{-1} that correspond to C-H stretching (Fig. 2 a). This native surface organic ligand, most probably DDT according to previous reports,[16] was displaced using TGA. For this purpose, as-prepared CGS NCs (DDT-CGS) were dispersed through sonication and shaking in a methanol solution of TGA and the proper amount of TMAOH to adjust the pH to 10. After purification, FTIR spectra showed a drastic reduction of the C-H peak intensity consistent with the shorter organic chain of TGA. Thermogravimetric analysis also showed a significantly lower decrease of the weight loss from the TGA-CGS NCs compared with the DDT-CGS NCs, consistent with the lower organic content of the former (Fig. 2 b).

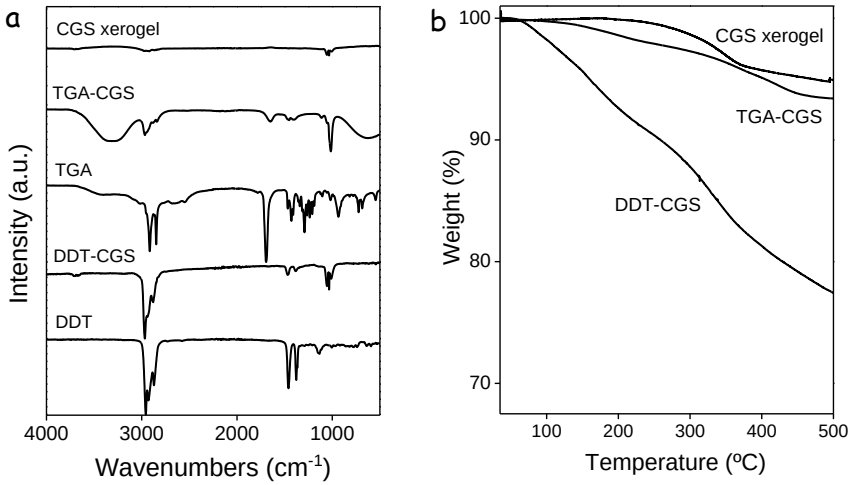

Fig. 2. a) From bottom to top: FTIR spectra of DDT; as-prepared CGS NCs (DDT-CGS); TGA; NCs functionalized with TGA (TGA-CGS); and the NC xerogel obtained by exposing TGA-NCs to the oxidant solution and naturally drying them. b) Thermogravimetric profile of the DDT-CGS NCs, TGA-CGS NCs and CGS xerogel.

After ligand exchange, TGA-CGS NCs in methanol were spin-coated onto FTO substrates to form CGS layers. Subsequently, TGA was removed using a TNM solution in acetone. For this purpose, immediately after spin coating, CGS layers were dipped into an acetone solution containing 3 vol% TNM for 1 min. Layers were washed afterward with methanol and allowed to dry naturally. Finally, they were annealed at 250 °C in Ar for 60 min. For comparison, we also produced CGS layers using DDT-CGS and TGA-CGS but with no ligand displacement

/oxidation step. Fig. 3 shows top-view SEM images of the different layers. The films produced after the displacement of TGA showed a much rougher surface than those obtained from DDT-CGS and from TGA-CGS (without TGA displacement/oxidation) suggesting greater porosity. As schematized in Figure 3d, exposure of TGA-CGS to the non-oxygen transferring oxidizer (TNM) resulted in partial removal of TGA. Unprotected surface metal ions were then solvated to result in a chalcogen rich NC surface that underwent NC-NC cross-linking through oxidation-induced chalcogen-chalcogen bonding. This mode of NCs cross-linking resulted in the formation of a porous network of interconnected NCs in solution; a NC-based gel.[17] The final material still contains TGA on the surface of particles. The ligand-oxidation process is competitive with ZnS sulfide oxidation; as portions of the particle are de-protected, they undergo assembly to form a linked network, but a portion of the particles still remains ligand-capped. To fully remove the ligand-related carbon from the final film, an additional chemical or thermal treatment of the layer is required.

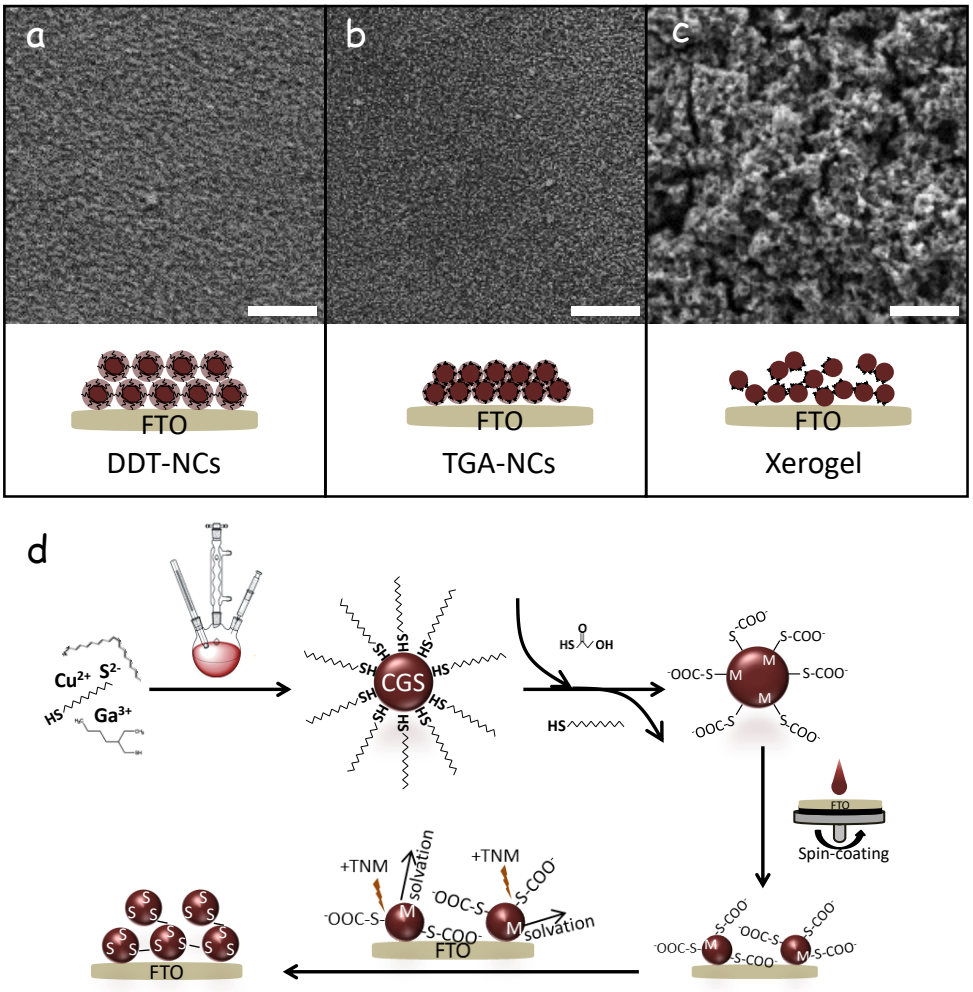

Fig. 3. a-c) Representative SEM micrographs and schematic representations of the CGS layers produced via spin-coating of DDT-CGS (a), TGA-CGS (b), and TGA-CGS after undergoing oxidative assembly with TNM to form a xerogel film (c). Scale bars = 1 μm. d) Schematic representation of the procedure to produce porous xerogel NCs films by removal of the thiol ligand through a non-oxygen transferring oxidant, TNM.

The layer thickness could be controlled through the NC concentration in solution and the number of spin coated layers. Fig. 4 a shows the UV-vis spectra of a TGA-CGS NC film and three

xerogel films with different thicknesses produced by the successive deposition of one, two or three CGS layers followed by their gelation. Notice how the transmittance of the layers decreases with the film thickness. Transmittance is slightly lower for the single xerogel film compared with the TGA-CGS film, which we associate with the higher scattering of the former. Fig. 4 b and 4 c display the thickness profiles of the films and their optical photographs

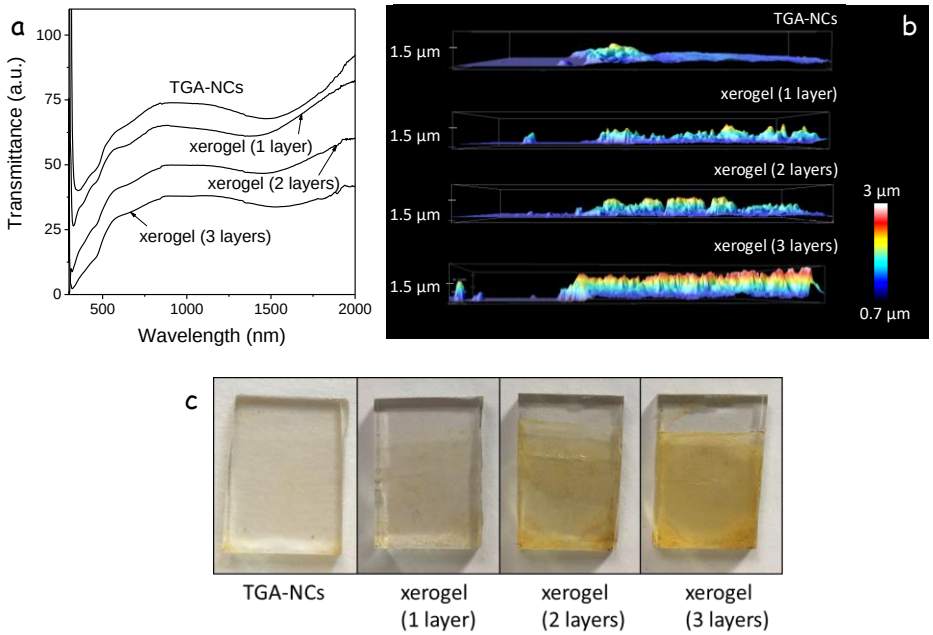

Fig. 4. a) Transmittance spectra of films produced from as-synthesized NCs, TGA-NCs, and xerogel films with different numbers of layers (1x – 1 layer, 2x – 2 layers; 3x – 3 layers). b) Thickness profiles of the produced films. c) Optical photographs of the films.

To gain insight into the mechanism of displacement of the TGA ligand in TGA-CGS NCs and the NC network formation, the same treatment was applied to unsupported NCs. In this case, the TNM solution in acetone was injected into a colloidal solution of TGA-CGS NCs in methanol. Upon injection, a gel started to form. Gelation visually evolved for 15 min, but was allowed to carry on for 48 hours. Afterward, the CGS NC gel was rinsed with fresh methanol and allowed to dry naturally into a xerogel (Fig. 4 d). FTIR characterization (Fig. 2 a) of the CGS xerogels revealed a significant decrease of the intensity of the C-H stretching peaks when compared with TGA-CGS NCs, evidencing a strong, but not complete, reduction of the amount of organics at the CGS NC surface. Thermogravimetric analysis (Fig. 2 b) further demonstrated the reduction of the organic content.

SEM micrographs of the obtained CGS xerogels displayed a porous structure of interconnected NCs (Fig. 5 b, c). When drying the CGS gel from supercritical CO_2 (see experimental section for details), highly porous aerogels, characterized with BET surface areas of 46 m^2g^{-1}, were obtained. Approximating the CGS NC geometry as cylindrical and considering an average cylinder length of 50 nm and an average diameter of 15 nm, their total surface area would be 64 m^2g^{-1}. Thus, within this approximation, the produced aerogels were able to keep over a 70% of the surface area of the colloidal NCs. CGS aerogels showed type IV adsorption-desorption isotherms with a combination of H1- and H3-type hysteresis loops, consistent with a

mesoporous structure (Fig. 5 d). Barrett–Joynes–Halenda (BJH) plots displayed a broad pore size distribution, characteristic of their aerogel nature (Fig. 5 e).

XPS analysis confirmed the formation of chalcogen-chalcogen bonds between the particles (Fig. 6). XPS spectra of TGA-NCs exposed to air displayed two contributions to the S 2p regions, one associated with the lattice S^{2-} (S $2p_{3/2}$ binding energy = 161.8 eV) and the second one associated with a sulphate (S $2p_{3/2}$ binding energy = 168.6 eV).[18] In the XPS spectra of the TNM-treated sample a third component became evident. This third chemical state (S $2p_{3/2}$ binding energy = 163.2 eV) had a slightly lower binding energy than elemental sulfur (S $2p_{3/2}$ binding energy = 163.7 eV).[18] Thus, we associated it to sulfur with a chemical environment compatible with that of disulphides which is consistent with formation of S_2^{2-} type linkages-Additionally, the sulphate component was strongly decreased in the gelated sample, the treatment with TNM eliminated both suface thiolates and surface oxidation layers

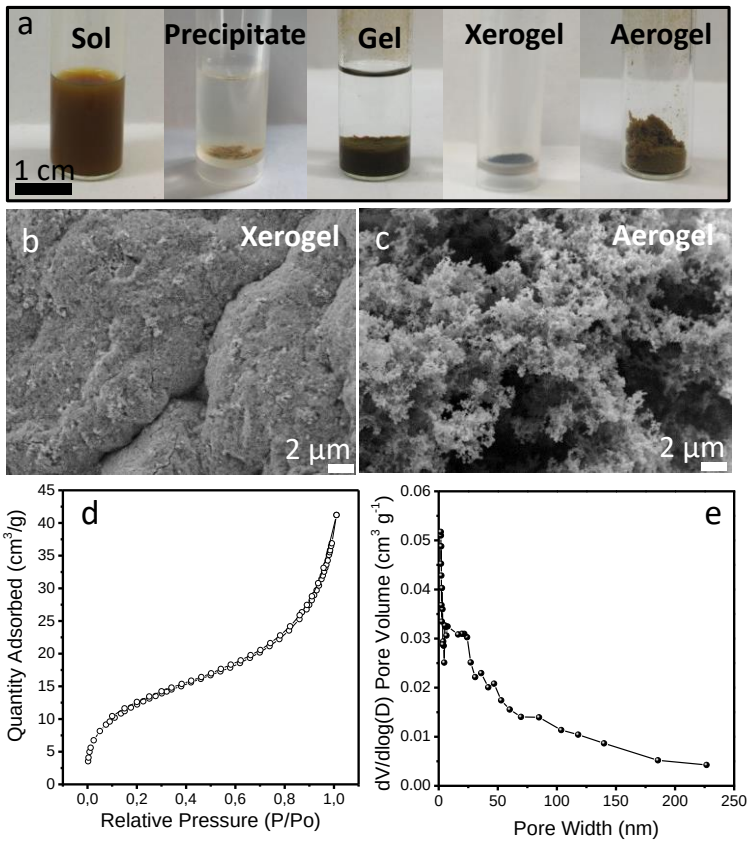

Fig. 5. a) Optical images of the CGS NC-based sol, precipitate, gel, aerogel and xerogel. b) SEM micrograph of a CGS xerogel. c) SEM micrograph of a CGS aerogel. d) Adsorption/desorption isotherm cycle from a CGS NC-aerogel, and e) its corresponding BJH pore size distribution.

ZnS NCs were produced following the procedure reported by T. Hyeon et al.,[19] reacting $ZnCl_2$ with elemental sulfur in OAm at 320 °C (see details in the experimental section). ZnS NCs produced following this procedure displayed the sphalerite crystal structure and quasi-spherical geometry with an average size of 10 nm (Fig. 7 a-b). The growth of ZnS NCs and their colloidal stability were controlled by the presence of OAm at their surface as observed by FTIR characterization (Fig. 7 c) and reported previously.[19] We replaced OAm with MUA by shaking and sonicating a bi-phase solution of OAm-ZnS NCs in hexane and MUA in methanol. Through

this process, ZnS NCs moved from the hexane to the methanol phase, where they were stabilized by MUA (MUA-ZnS). Then, the upper hexane solution containing the displaced OAm was discarded and the MUA-ZnS NCs in the methanol solution were collected and further purified as described in the experimental section.

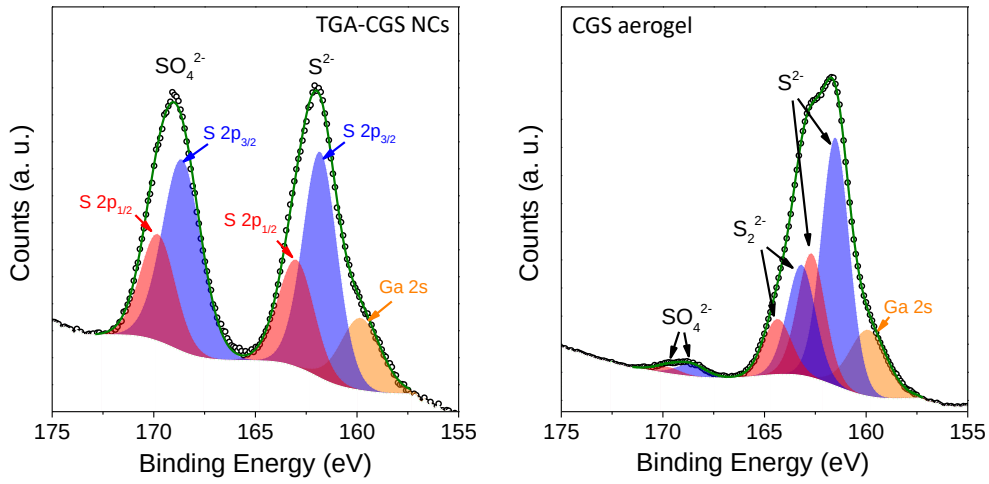

Fig. 6. S 2p region of the XPS spectra of the TGA-CGS NCs (left) and the CGS NC-based aerogel (right). S 2p3/2 states are plotted in blue and S 2p1/2 states in red. In the same region the Ga 2s state is observed.

Porous layers of interconnected ZnS NCs were produced following the same procedure as for CGS NCs, using TNM as non-oxygen transferring agent. Bulk ZnS gels and xerogels were also produced by adding TNM to a colloidal solution of MUA-ZnS NCs in methanol. Fig. 7 d shows a representative TEM micrographs and an optical image of the interconnected ZnS NC network produced upon addition of TNM to the colloidal solution of MUA-ZnS NCs. FTIR spectra from these gels showed a reduction of the intensity of the peaks at 2924 cm^{-1} and 2830 cm^{-1} attributed to organic ligands, consistent with their partial removal (Fig. 7 c). Notice that due to the larger size of MUA compared with TGA, the intensity of the peaks associated with C-H vibrations in the FTIR spectrum of the ZnS-based gel is stronger than in the CGS-based one.

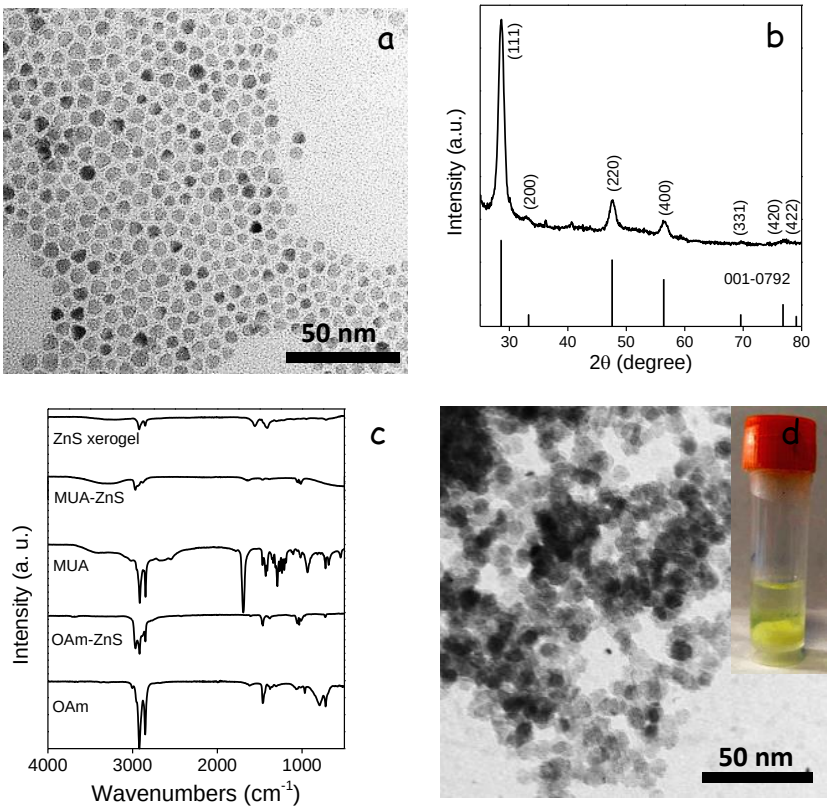

Fig. 7. a) TEM micrograph of ZnS NCs. b) XRD pattern of ZnS NCs including the JCPDS 001-0792 pattern corresponding to sphalerite ZnS as reference. c) From bottom to top, FTIR spectra of: OAm, as-produced ZnS NCs (OAm-ZnS), MUA, ZnS NCs obtained after ligand exchange with MUA (MUA-ZnS) and ZnS NC-based xerogel. d) TEM micrographs of the ZnS xerogel obtained from MUA-NCs treated with TNM. Inset shows an optical image of the formed ZnS gel.

Combining p-type CGS with n-type ZnS in bilayer structures or blended layers should allow a more effective separation of photogenerated charge carriers, reducing charge recombination and promoting photocatalytic performance. Additionally, a faster charge carrier separation should promote the material chemical stability, since metal sulfides suffer from significant photocorrosion during photocatalytic reactions associated with the surface accumulation of photogenerated holes that induce rapid oxidation of lattice S^{2-} ions to S^0 or soluble sulfates.[10,21] Therefore, beyond single component films, we produced CGS/ZnS bilayers and CGS-ZnS mixed layers. Fig. 8 a and 8 b show top-view SEM micrographs of CGS/ZnS bilayers produced from the sequential spin-coating of DDT-CGS and OAm-ZnS NCs (Fig. 8 a) and from the sequential spin coating and gelation of TGA-CGS and MUA-ZnS NCs (Fig. 8 b). Figure 8 c shows a top-view SEM micrograph of the layer produced from the spin coating and subsequent gelation of a solution containing a blend of TGA-CGS and MUA-ZnS NCs. Note that a thermal treatment (250 °C for 60 min under Ar atmosphere) was required to stabilize the DDT-CGS layer before deposition of the OAm-ZnS NCs layer, to prevent dissolution of the former. However, such thermal treatment was not necessary for layer deposition on top of gelated materials. This represents a clear advantage over multiple layer deposition procedures that require an annealing step in between each process.

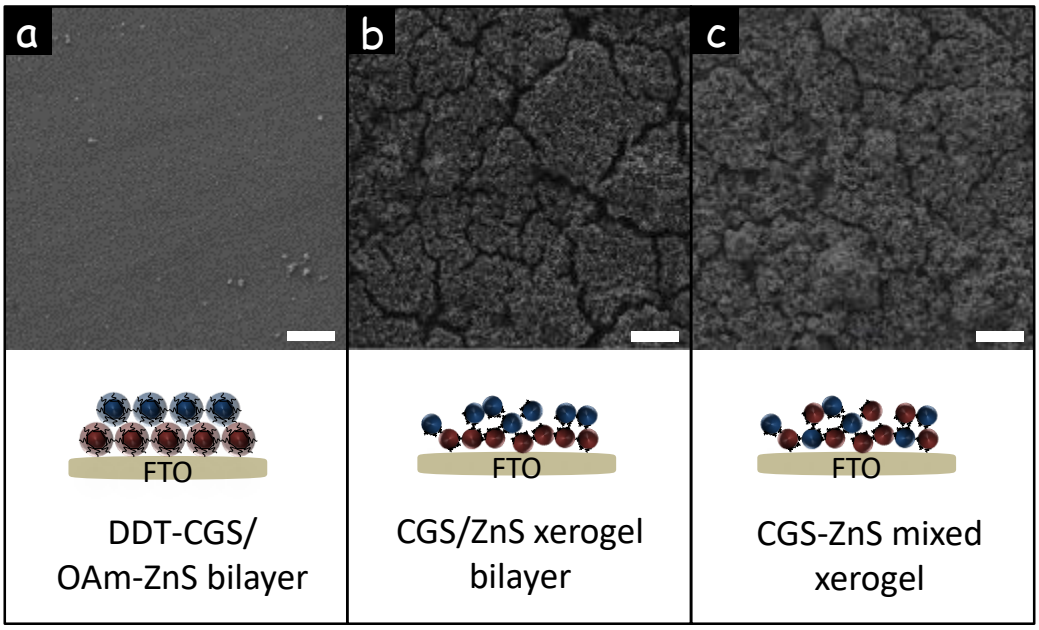

Fig. 8. SEM micrographs and schematic representations of the following structures: a) a bilayer obtained from the sequential spin coating of DDT-CGS NCs and OAm-ZnS NCs; b) a bilayer produced from the spin coating and gelation of TGA-CGS NCs and the subsequent deposition and gelation of MUA-ZnS NCs; c) a blended CGS-ZnS NC layer obtained from the spin coating of a solution containing both TGA-CGS NCs and MUA-ZnS NCs followed by treating it with TNM. Scale-bars = 1 μm.

The performance of CGS NC-based layers was evaluated against the photoelectrocatalytic hydrogen evolution reaction in a 0.1 M aqueous solution of Na_2SO_4 at neutral pH. Photoelectrocatalytic measurements were carried out with a 3-electrode electrochemical cell using the NC-based layers annealed at 250 °C for 60 min as working electrodes.

Note that no catalyst was used in these experiments, thus overall layer performances were relatively low, but still qualitatively significant to probe dissimilarities between the differently treated samples. Compared with the layers produced from DDT-CGS, higher current densities were obtained from the layers prepared with a shorter organic ligand (TGA-CGS) and particularly from the gelated layer (CGS xerogel) (Fig. 9 a). This experimental evidence is associated with two properties: i) the higher surface area of the CGS xerogel, which provided enhanced interaction with the media; and ii) the enhanced charge carrier transport within the TGA-CGS layer and particularly the CGS xerogel layer compared with DDT-CGS. EIS measurements confirmed the lower impedance of the gelated layers compared with DDT-CGS and TGA-CGS films, associated again with the lower organic content and the higher surface area of the xerogel films (Fig. 9 b). Similar results were obtained from ZnS layers, demonstrating significantly larger current densities for ZnS xerogels than for OAm-ZnS-based layers (Fig. 9 c).

Current densities were increased when combining CGS and ZnS xerogels into a bilayer structure, which we associated with a favorable surface energy band arrangement. On the other hand, blended xerogel layers were characterized by lower current densities probably associated to the reduced charge carrier mobility in a nanocrystalline network containing a large density of energy barriers introduced by the random distribution of the p-type and n-type semiconductors.

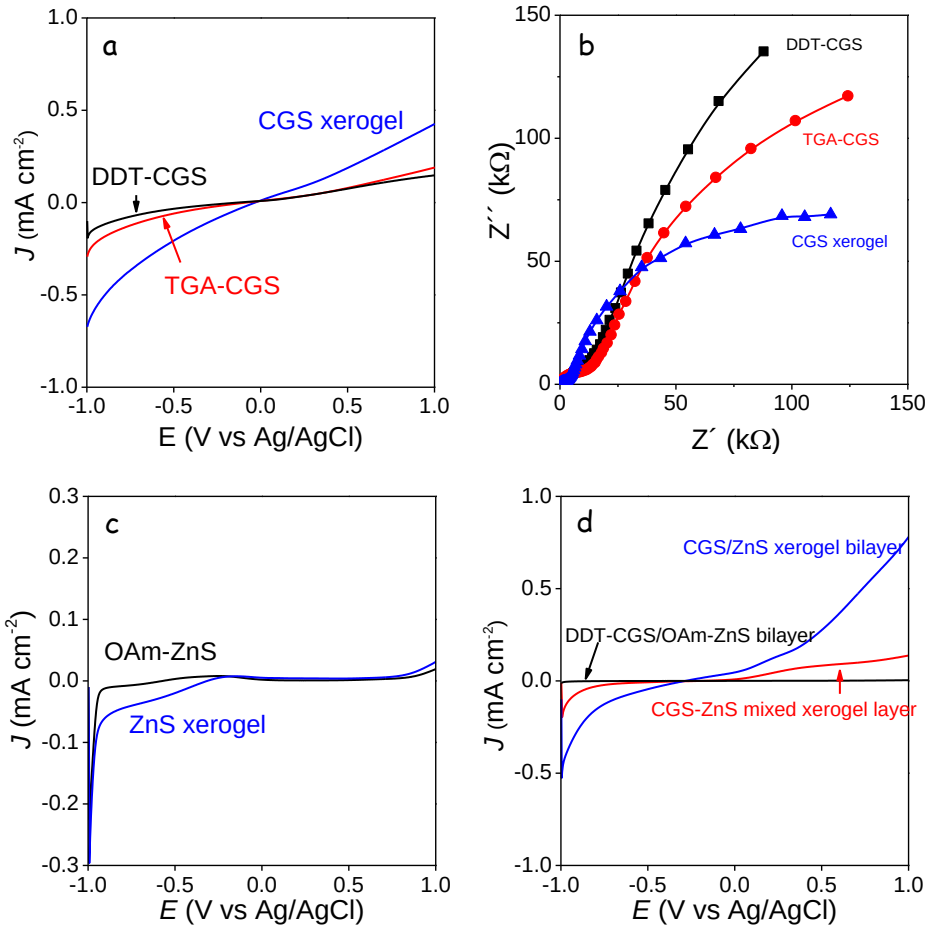

Fig. 9. a) Linear sweep voltammogram curves at a scan rate of 0.1 V s^{-1} ofDDT-CGS, TGA-CGS and gelated TGA-CGS NC-based layers. b) Nyquist plots for DDT-CGS, TGA-CGS and CGS xerogel films. c) Linear sweep voltammogram curves at a scan rate of 0.1 V s^{-1} of OAm-ZnS and gelated MUA-ZnS NC-based layers. d) Linear sweep voltammogram curves at a scan rate of 0.1 V s^{-1} of DDT-CGS/OAm-ZnS NC-based bilayer, a gelated TGA-CGS/MUA-ZnS NC-based bilayer and a gelated layer produced from a blend of TGA-CGS and MUA-NCs.

The highest photocurrents were obtained from CGS xerogel monolayers and CGS/ZnS xerogel bilayers (Fig. 10). Improved photocatalytic performance with respect to DDT-CGS, TGA-CGS and DDT-CGS/MUA-ZnS layers was related to the enhanced charge transport within the interconnected NC network and the larger surface area of the porous xerogel films. CGS/ZnS xerogel bilayers provided even higher photocurrents than CGS xerogel layers, which we attributed to the more efficient charge separation at the n-p junctions, reducing recombination, and possibly to a more efficient injection of charge to the solution species through a proper band adjustment.

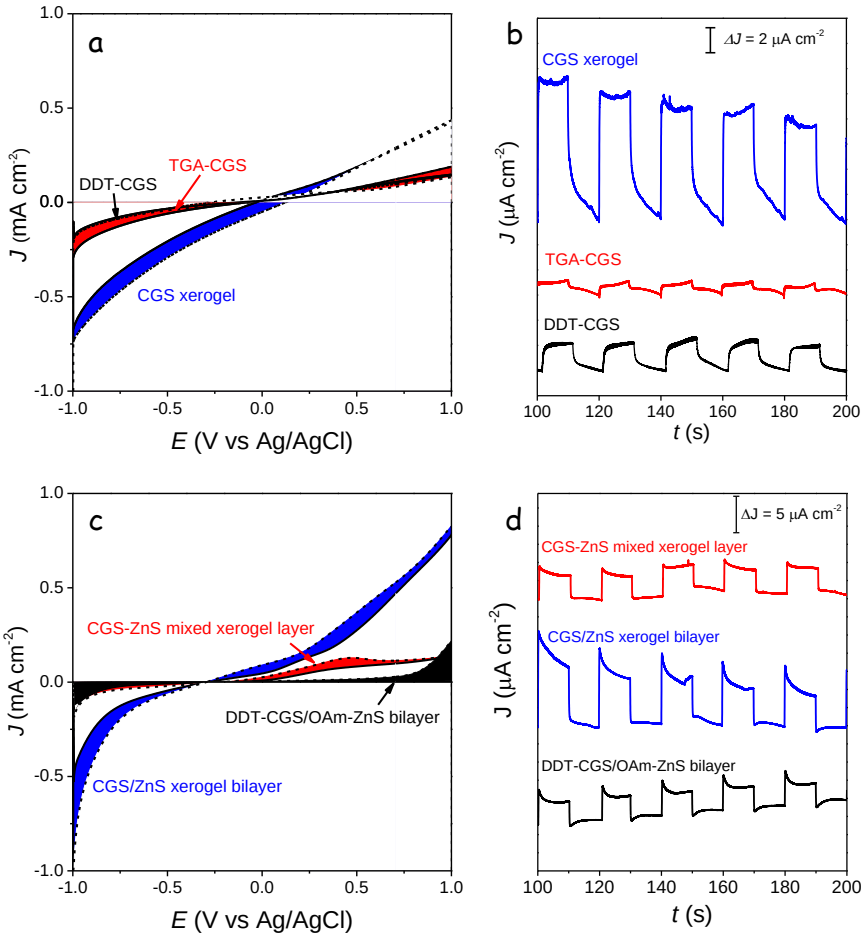

Fig. 10. a-b) Linear sweep voltammogram curves at a scan rate of 0.1 V s^{-1} (a) and time-dependent characteristics (b) of the photocurrent response of CGS layers having different surface chemistries. c-d) Linear sweep voltammogram curves at a scan rate of 0.1 V s^{-1} (c) and time-dependent characteristics (d) of the photocurrent response of CGS/ZnS bilayers and a CGS-ZnS mixed layer. Time-dependent characteristics were obtained by applying -0.6 V with respect to an Ag/AgCl reference electrode.

6.4. Conclusions

We demonstrated the formation of porous layers of CGS and ZnS from the treatment of TGA-capped CGS NCs and MUA-capped ZnS NCs with a non-oxygen transferring agent, TNM. This oxidizing agent indirectly creates chalcogen-chalcogen bonds between the nanocrystals, anchoring them together. We further produced $CuGaS_2$/ZnS nanocrystal-based bilayers and $CuGaS_2$–ZnS nanocrystal-based composite layers and probed them to be characterized with higher current densities and photoresponses than layers produced from as-produced nanocrystals.

6.5. References

1. Coughlan, C.; Ibáñez, M.; Dobrozhan, O.; Singh, A.; Cabot, A.; Ryan, K.M. Compound Copper Chalcogenide Nanocrystals. *Chem. Rev.* **2017**, *117,* 5865-6109, DOI: 10.1021/acs.chemrev.6b00376
2. Lee, J.-S.; Kovalenko, M. V.; Huang, J.; Chung, D. S.; Talapin, D. V. Band-like transport, high electron mobility and high photoconductivity in all-inorganic nanocrystal arrays. *Nat. Nanotech.* **2011**, *6*, 348–352, DOI:10.1038/nnano.2011.46.
3. Kovalenko, M. V.; Scheele, M.; Talapin, D. V. Colloidal Nanocrystals with Molecular Metal Chalcogenide Surface Ligands. *Science* **2009,** *324* (5933), 1417-1420, DOI: 10.1126/science.1170524
4. Engel, J. H.; Alivisatos, A. P. Postsynthetic Doping Control of Nanocrystal Thin Films: Balancing Space Charge to Improve Photovoltaic Efficiency. *Chem. Mater.* **2014,** *26* (1), 153-162, DOI: 10.1021/cm402383r
5. Brock, S. L.; Arachchige, I. U.; Kalebaila, K. K. Metal chalcogenide gels, xerogels and aerogels. *Comments Inorg. Chem.* **2006,** *27* (5-6), 103-126, DOI:10.1080/02603590601084434
6. Muthuswamy, E.; Brock, S. L. Oxidation Does Not (Always) Kill Reactivity of Transition Metals: Solution-Phase Conversion of Nanoscale Transition Metal Oxides to Phosphides and Sulfides. *J. Am. Chem. Soc.* **2010,** *132* (45), 15849-15851, DOI: 10.1021/ja106397b
7. Davis, J. L.; Chalifoux, A. M.; Brock, S. L. Role of Crystal Structure and Chalcogenide Redox Properties on the Oxidative Assembly of Cadmium Chalcogenide Nanocrystals. *Langmuir* **2017,** *33* (37), 9434-9443, DOI: 10.1021/acs.langmuir.7b01118.
8. Pala, I. R.; Arachchige, I. U.; Georgiev, D. G.; Brock, S. L. Reversible Gelation of II–VI Nanocrystals: The Nature of Interparticle Bonding and the Origin of Nanocrystal Photochemical Instability. *Angew. Chem. Int. Ed.* **2010,** *49* (21), 3661-3665, DOI: 10.1002/anie.201000034.
9. Evans, B. J.; Doi, J. T.; Musker, W. K. Fluorine-19 NMR study of the reaction of p-fluorobenzenethiol and disulfide with periodate and other selected oxidizing agents. *J. Org. Chem.* **1990,** *55* (8), 2337-2344, DOI: 10.1021/jo00295a020.
10. Hagfeldt, A.; Grätzel, M. Molecular Photovoltaics. *Acc. Chem. Res.* **2000,** *33* (5), 269-277, DOI: 10.1021/ar980112j.
11. Ghosh, A.; Thangavel, R.; Rajagopalan, M. Electronic and optical modeling of solar cell compound Cu_XY_2 (X = In, Ga, Al; Y = S, Se, Te): first-principles study via Tran–Blaha-modified Becke–Johnson exchange potential approach. *J. Mater. Sci.* **2015,** *50* (4), 1710-1717, DOI: 10.1007/s10853-014-8732-z.
12. Hashemi, J.; Akbari, A.; Huotari, S.; and Hakala, M. Multi-intermediate-band character of Ti-substituted $CuGaS_2$: Implications for photovoltaic applications. *Phys. Rev. B* **2014**, *90*, 075154, DOI: 10.1103/PhysRevB.90.075154.
13. Han, M.; Zhang, X.; Zeng, Z. The investigation of transition metal doped $CuGaS_2$ for promising intermediate band materials. *RSC Advances* **2014,** *4* (107), 62380-62386, DOI: 10.1039/C4RA10007G.
14. Korala, L.; Wang, Z.; Liu, Y.; Maldonado, S.; Brock, S. L., Uniform Thin Films of CdSe and CdSe(ZnS) Core(Shell) Quantum Dots by Sol–Gel Assembly: Enabling Photoelectrochemical Characterization and Electronic Applications. *ACS Nano* **2013,** *7* (2), 1215-1223, DOI: 10.1021/nn304563j.

15. Yu, X.; An, X.; Shavel, A.; Ibanez, M.; Cabot, A. The effect of the Ga content on the photocatalytic hydrogen evolution of $CuIn_{1-x}Ga_xS_2$ nanocrystals. *J. Mater. Chem. A* **2014,** *2* (31), 12317-12322, DOI: 10.1039/C4TA01315H.

16. Xia, C.; Cao, L.; Liu, W.; Su, G.; Gao, R.; Qu, H.; Shi, L.; He, G. One-step synthesis of near-infrared emitting and size tunable $CuInS_2$ semiconductor nanocrystals by adjusting kinetic variables. *CrystEngComm* **2014,** *16* (32), 7469-747, DOI: 10.1039/C4CE00889H.

17. Mohanan, J. L.; Arachchige, I. U.; Brock, S. L. Porous Semiconductor Chalcogenide Aerogels. *Science* **2005,** *307* (5708), 397-400, DOI: 10.1126/science.1104226.

18. Moulder, J. F.; Stickle, W. F.; Sobol, P. E.; Bomben, K. D. Handbook of X-Ray Photoelectron Spectroscopy; Perkin-Elmer: Eden Prairie, MN, 1992, DOI: 10.1002/sia.740030412.

19. Joo, J.; Na, H. B.; Yu, T.; Yu, J. H.; Kim, Y. W.; Wu, F.; Zhang, J. Z.; Hyeon, T. Generalized and Facile Synthesis of Semiconducting Metal Sulfide Nanocrystals. *J. Am. Chem. Soc.* **2003,** *125* (36), 11100-11105, DOI: 10.1021/ja0357902.

20. Iwase, A.; Ng, Y. H.; Amal, R.; Kudo, A. Solar hydrogen evolution using a $CuGaS_2$ photocathode improved by incorporating reduced graphene oxide. *J. Mater. Chem. A* **2015,** *3* (16), 8566-8570, DOI: 10.1039/C5TA01237F.

Shen, Q.; Kobayashi, J.; Diguna, L. J.; Toyoda, T. Effect of ZnS coating on the photovoltaic properties of CdSe quantum dot-sensitized solar cells. *J. Appl. Phys.* **2008,** *103* (8), 084304, DOI: 10.1063/1.2903059

7. Multicomponent NC mesoporous structures with versatile composition through electrostatic assembly

Abstract

The assembly of colloidal nanocrystals (NCs) is a unique strategy to produce porous materials with high crystallinity and unmatched control over structural and chemical parameters. This strategy has been demonstrated mostly for single component nanomaterials. In the present work, we report the gelation of colloidal NC solutions driven by the electrostatic interaction of oppositely charged NCs. A key step for leading this strategy to success is to produce a stable colloidal solution of the positively charged component. We achieved this by means of functionalizing NCs with inexpensive and non-toxic amino acids such as glutamine. We demonstrate the combination of positively and negatively charged NCs in the proper concentrations to result in gels with a homogeneous distribution of the two compounds. In this way, porous nanocomposites with virtually any combination can be produced. We illustrate this approach by combining positively charged ceria NCs with negatively charged gold NCs to form Au-CeO_2 gels. These gels were dried from supercritical CO_2 to produce highly porous Au-CeO_2 aerogels with specific surface areas of 120 $m^2 g^{-1}$. We further demonstrate the versatility of this strategy to produce porous metal chalcogenide-metal oxide nanocomposites by the example of PbS-CeO_2.

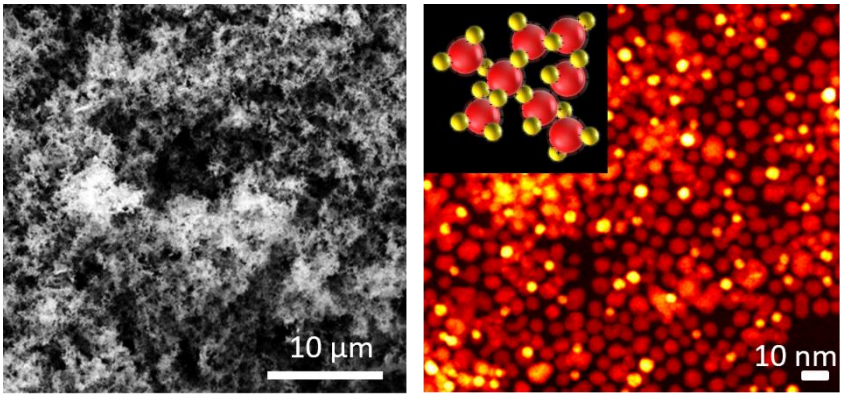

7.1. Introduction

Porous nanocomposites are critical components in the fields of catalysis, chemical sensing and filtering, to mention just a few. Such nanomaterials are generally produced in two steps; first a porous matrix is obtained using sol-gel chemistry methods and later this base material is impregnated with the second component which adds the required complementary functionality, e.g. a co-catalyst or a light sensitizer.[1-3] This approach presents important limitations. Sol-gel chemistry routes generally result in amorphous materials that require a thermal sintering to attain proper crystallinity.[4-8] This sintering step strongly reduces the material surface area and prevents tuning grain size, crystal facets and in some cases crystallographic phase. Additionally, widely used impregnation methods offer a very limited control over the distribution and structural/chemical parameters of the impregnated gel.

An alternative strategy to produce porous nanomaterials is through the cross-linking of colloidal NCs.[5,9,10] Colloidal NCs with a plethora of compositions can be currently produced with full control over size, facets and crystal phase.[11-20] Its assembly into gels and aerogels allows to produce highly porous structures with full control over structural and chemical parameters at the nanometer scale. This strategy has so far been developed mostly to produce single component gels and aerogels, mainly of metals and metal chalcogenides.[5,9,10,21,22] While few examples exist on the gelation of a colloidal dispersion of different types of NCs into a porous nanocomposite,[5,10,23-26] most current approaches to colloidal NC gelation are not well suited for the production of composite gels because they do not include any assembly director that provides the gel with a proper compositional distribution.

In the present work, we demonstrate the electrostatic interaction between NCs of opposite surface charge to be a very convenient strategy to produce high surface area nanocomposites with virtually any composition. We illustrate this approach using different types of NCs (Au, CeO_2 and PbS) having positive and negative surface charge

7.2. Experimental

7.2.1. Synthesis of CeO_2 NCs

Ceria NCs were synthesized though the thermal decomposition of cerium precursors in the presence of OAm and ODE as detailed in our previous work.[20] Briefly in a 25 mL three neck flask, 0.434 g (1 mmol) of cerium(III) nitrate hexahydrate were mixed with 2 mL (6 mmol) of OAm within 4 mL of ODE under magnetic stirring. After degassing the mixture for 30 minutes at 80 °C, a brown colour solution was formed. The mixture was then heated up under argon flow to 300 °C at a rate of 15 °C/min. The mixture was allowed to react at 300 °C for 60 minutes before cooling down to room temperature. NCs were precipitated and washed with acetone at least four times before suspending them in different organic solvents (hexane, chloroform or toluene) producing stable colloidal dispersions (c.a. 10 mg/mL). This sample was labelled OAm-CeO_2.

7.2.2. Synthesis of Au NCs

Au NCs were synthesized following the procedure reported by S. Peng et al. with slight modifications.[27] In brief, 0.25 mmol (0.1 g) of gold(III) chloride trihydrate, 10 mL of tetraline and 10 mL of OAm were loaded into a 50 mL three neck round bottom flask. The mixture was magnetically stirred under argon flow at room temperature for 30 min. Afterward, a previously prepared solution of 0.5 mmol of TBAB, 1 mL of tetraline and 1 mL of OAm was injected in the reaction flask. Upon this injection, the colour of the solution turned purple. The mixture was allowed to react for 2 h. NCs were isolated by adding 5 mL of isopropanol and centrifuged for 5 min at 7000 rpm. The collected precipitate was redispersed in 10 mL of hexane for later use. This sample was labelled OAm-Au.

7.2.3. Synthesis of PbS NCs

PbS NCs were synthesized using a previously reported procedure.[28] 0.45 g (2 mmol) of lead(II) oxide, 1.57 mL (4 mmol) of OAc and 7.5 mL of ODE were mixed in a 25 mL three neck round bottom flask under magnetic stirring. After 30 min of degassing at 120 °C, vacuum was switched to Ar atmosphere and the temperature was set to 190 °C. Separately, in a vial, 2 mmol of sulfur powder were dissolved in 3 mL of OAm by sonication for 10 minutes. This solution was swiftly injected to the reaction flask as soon as this reached 190 °C. The mixture was allowed to react for 5 min before the heating mantle was removed and the solution cooled down naturally. After washing with acetone at least 3 times, NCs were redissolved in hexane for later use. The samples were labelled OAc-PbS.

7.2.4. Surface modification with Gln

This procedure was inspired by the work of J. De Roo et al.[29] Ligand exchange processes were held under ambient atmosphere. In a typical procedure, 7 mg of Gln (0.047 mM) was dissolved using mild sonication in 1 mL MFA followed by the addition of 20 µL TFA (0.2 mM). To the obtained mixture, 1 mL of a CeO_2 NC dispersion in hexane (5 mg/mL) was added, resulting in the formation of a two-phase mixture. The mixture was shaken and sonicated until NCs moved from the upper hexane to the bottom MFA phase, leaving a clear hexane solution on the top. Then the supernatant was removed and a fresh hexane:acetone mixture (1:1) was added. The solution was shaken and the NCs were precipitated by centrifugation at 7000 rpm for 10 minutes. This purification procedure was repeated for three times, using MFA to redisperse the NCs at each step. Finally, NCs could be redispersed in polar solvents such as methanol, MFA and water, although colloidal stability in water was moderate. This sample was labeled Gln-CeO_2.

7.2.5. Surface modification with MUA

5 mL of a 5 mg/mL dispersion of Au NCs were mixed with 5 mL of a 0.02 mM solution of MUA in MFA at pH=9. Level of pH was adjusted by the addition of TMAOH. The resulting biphasic solution was stirred under inert atmosphere for 30 min. During this process, NCs moved from the upper hexane phase to the bottom MFA phase. Then, the clear upper part was removed and NCs were precipitated by addition of 5 mL of acetonitrile and centrifugation at 4000 rpm

for 5 min. The obtained precipitate was redispersed in 5 mL of MFA and precipitated one more time with acetonitrile. It should be noted that repeating the washing procedure led to the aggregation of the NCs, but addition of MUA redispersed them back to solution. The sample was labelled MUA-Au. The same process was used with PbS NCs (MUA-PbS).

7.2.6. NCs assembly

2.5 mL of a 5 mg/mL MUA-Au NC solution in MFA was injected into 2.5 mL of a 5 mg/mL Gln-CeO_2 NCs solution in MFA. Immediately after mixing, NCs started to aggregate to form a gel. The solution was left undisturbed for 30 min, until the supernatant became transparent, which indicated the completion of the gelation by the consumption of all the NCs. MFA was then carefully replaced with acetone (approximately 5 mL). Solvent exchange with fresh acetone was repeated at least 6 times to ensure complete removal of MFA. The same procedure was followed to prepare PbS-CeO_2 NCs gels mixing MUA-PbS and Gln-CeO_2.

7.2.7. Aerogel formation

The gel soaked in acetone was loaded into a custom designed supercritical point drier (SPD). The chamber was sealed and it was slowly filled with liquid CO_2 until the pressure reached 73 bars. To ensure that CO_2 was in liquid phase, temperature was maintained at 17-18 °C by using a Peltier element and the pressure level was set higher than 73 bars. After storing the sample undisturbed overnight, the liquid CO_2 inside of the chamber was half-drained and flushed with fresh one. This exchange was repeated at least 6 times in one hour intervals in order to completely replace acetone with liquid CO_2. After the solvent exchange was completed, the chamber at 73 bars was heated up to 39 °C using a heating mantle which drove the transition of the CO_2 from the liquid to the supercritical phase. The sample was kept under these conditions (39 °C and 90 bars) for 1 h, followed by a slow release of the pressure while keeping the temperature constant.

7.2.8. Catalytic test

The CO oxidation catalytic activity of the CeO_2 and Au-CeO_2 aerogels was measured using a micro reactor system coupled with a NDIR analyzer that allowed the continuous detection of CO and CO_2 concentrations at the reactor outlet. Typically, 15 mg of the gel was loaded into a quartz reactor (internal diameter = 6 mm). The feed gas was a mixture of 1 % v/v CO and 10 % v/v O_2 balanced with He. The flow rate was set to 40 Ncc/min. The catalysts were tested directly after synthesis, without any pretreatment. For one test cycle, the reactor was heated from room temperature to 400 °C with a heating rate of 5 °C/min and kept at 400 °C for 30 min, then cooled down to RT. To ensure that the obtained activity results were reliable, the test cycle for each catalyst was repeated 4 times. Transient activity data were collected during the test, and the CO conversion was defined as the percentage of CO feed that had reacted.

7.3. Results and discussion

Quasi-spherical CeO_2 NCs with an average diameter of 7$\pm$1 nm were produced following our previously reported procedure.[20] CeO_2 NCs were colloidally stable in non-polar organic

solvents due to the presence of OAm on their surface. Gold NCs of 4±1 nm were produced following the procedure reported by Peng et al. also using OAm as surface ligand.[27] Figure 1 shows representative TEM micrographs of the OAm-CeO_2 and OAm-Au NCs used in the present work and their hydrodynamic size distribution obtained from DLS measurements in hexane.

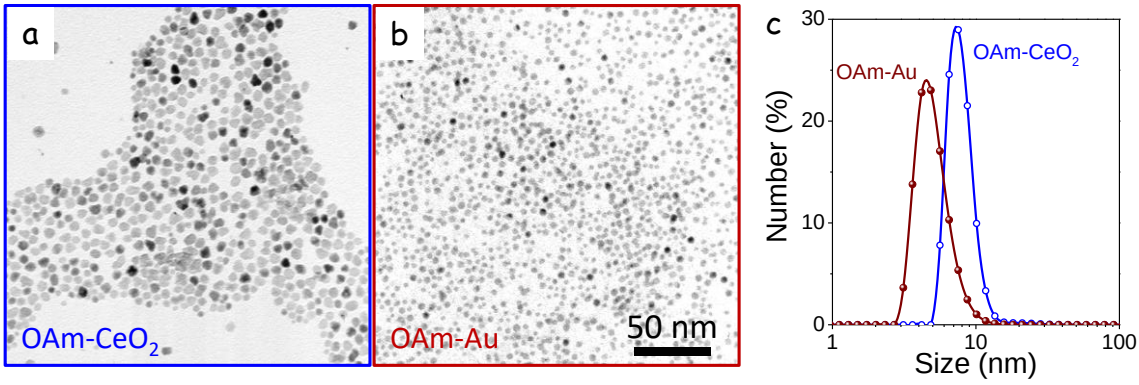

Fig. 1. a) TEM image of OAm-CeO_2 NCs. b) TEM image of OAm-Au NCs. c) DLS spectra of OAm-CeO_2 and OAm-Au NCs.

A first key step toward electrostatic assembly is the introduction of opposite charges at the surface of the different NCs to be assembled. While a variety of methods is available to create a negatively charged ligand surface, very few are reported for positive electrostatic stabilization.[30] Additionally, in most reported procedures the reagents used to introduce a positive surface charge can be harmful and need to be handled with care and/or they are excessively expensive for real application.[31,32] To introduce a positive charge at the surface of CeO_2 NCs, we replaced OAm with safe and inexpensive amino acids (Fig. 2).[29,33] Briefly, an MFA solution of Gln and TFA was mixed with a hexane solution of CeO_2 NCs. Through moderate stirring, CeO_2 NCs moved from the hexane phase to the MFA. Then, the hexane phase was discarded and NCs were purified by multiple precipitation and redispersion steps (see details in the experimental section). In the presence of TFA, the amino acid was bond to the metal atoms on the NCs surface through the carboxylate group, leaving a protonated amino group exposed to the medium, thus providing a positive charge to the NC. A positive zeta potential peak at +26 mV confirmed the positive surface charge of the Gln-CeO_2 NCs (Figure 2f). The presence of Gln at the CeO_2 NC surface was further proved by peaks at around 1538 cm^{-1} and 1650 cm^{-1} in the FTIR spectrum, which were ascribed to N-C=O and NH_2 vibration modes of the second amine group of the Gln molecules (Fig. 2d).[34-35]

To introduce a negative charge at the surface of Au NCs, OAm was replaced by MUA. The exchange from OAm to MUA was performed via a two-phase ligand exchange procedure by mixing OAm-Au NCs in hexane with a MUA solution in MFA. After agitation, MUA-Au NCs moved to the MFA phase (see experimental section for details). In the presence of a strong base, TMAOH, the thiol (-SH) and carboxyl (-COOH) groups of MUA were deprotonated, which facilitated the bonding of MUA to the NCs surface. For the particular case of Au, the thiol group was bond to the surface due to the strong affinity between thiol groups and Au surfaces, thus leaving the acid group exposed to the media. In these conditions, the acid group provided the NC with a negative surface charge.[36,37] The FTIR spectrum of MUA-Au NCs showed absorption bands in the 2820-2946 cm^{-1} region, which were attributed to C-H stretching

vibration from the carboxylic acid of MUA ligands.[38] Additionally, the disappearance of the broad peak at around 2600 cm^{-1} associated to S-H stretching confirmed the ligands attachment to the NCs surface through deprotonated thiol head groups.[38,39] The peaks at 1571 cm^{-1} and 1401 cm^{-1} associated to carboxylate vibrations suggested the presence of the carboxyl salt on the NCs surface.[39] A negative zeta potential peak at -50 mV further demonstrated the attachment of MUA to Au NCs and the negative surface charge (Fig. 2f).

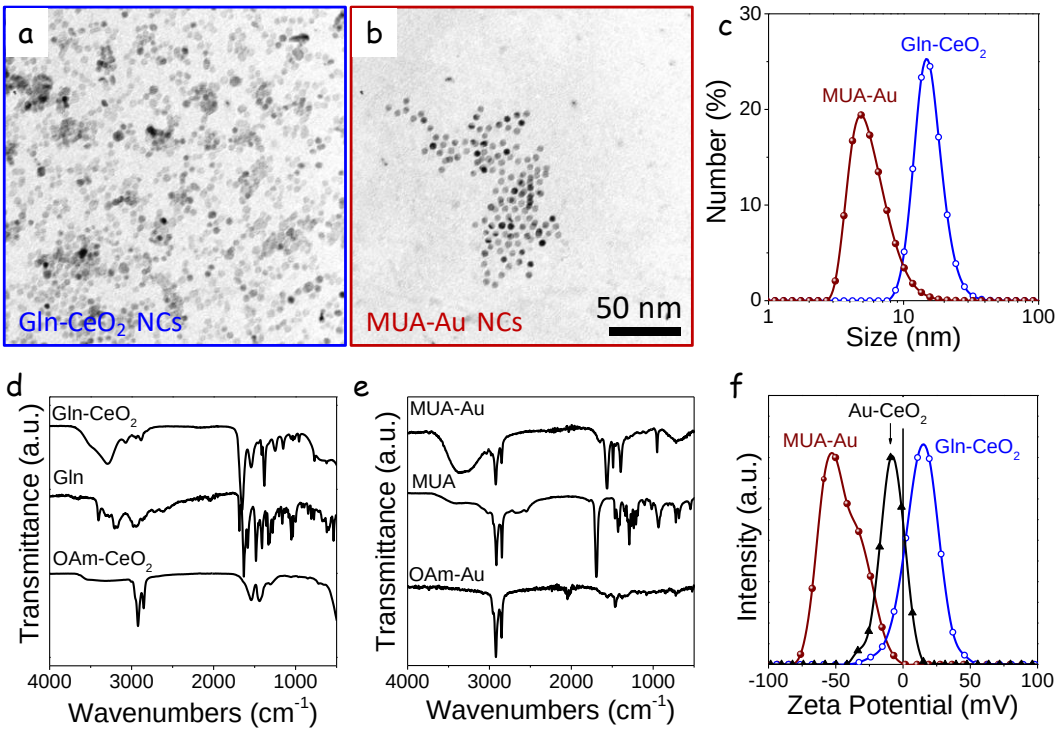

Fig. 2. a) TEM image of Gln-CeO_2 NCs. b) TEM image of MUA-Au NCs. c) DLS size distribution of Gln-CeO_2 and MUA-Au NCs. d) FTIR spectra of OAm-CeO_2 NCs, Gln and Gln-CeO_2 NCs. e) FTIR spectra of OAm-Au NCs, MUA and MUA-Au NCs. f) Zeta potential curves of Gln-CeO_2 NCs, MUA-Au NCs and the gel formed after mixing Gln-CeO_2 NCs and MUA-Au NCs.

Both, Gln-CeO_2 and MUA-Au NCs were colloidally stable in MFA. However, when combining MFA solutions of Gln-CeO_2 NCs and MUA-Au NCs, a random aggregation of the NCs into a gel took place. The gelation was moderately fast, reaching completion after about 30 min. For this process to be successful, the high dielectric constant of MFA (ε = 171) was very convenient, both to properly stabilize each type of charged colloidal NC in solution and to allow gel formation upon their mixing. The NC-based gel was dried from super-critical CO_2 to maintain the porous structure (see experimental section for details). After drying, a very low density material with a dark garnet color was obtained. Figure 3 shows representative TEM, SEM and optical images of the gel and aerogel produced following this process, using a 4:1 mass ratio of Gln-CeO_2 to MUA-Au NCs, which corresponds to a CeO_2:Au NC ratio of ca. 2:1. A highly porous structure with large open pores and voids consistent with the nature of an aerogel was evident from the SEM image of the dried gel (Figure 3b). Figure 3c shows the adsorption-desorption isotherm of the same Au-CeO_2 aerogel. From these curves, a BET surface area of 120±10 m^2/g was calculated, which is a very high value taking into account the high density of the two compounds, especially Au. Figure 4 displays bright field and dark field TEM micrographs and

HRTEM micrographs of the Au-CeO_2 gel formed, showing the homogeneous distribution of the two materials.

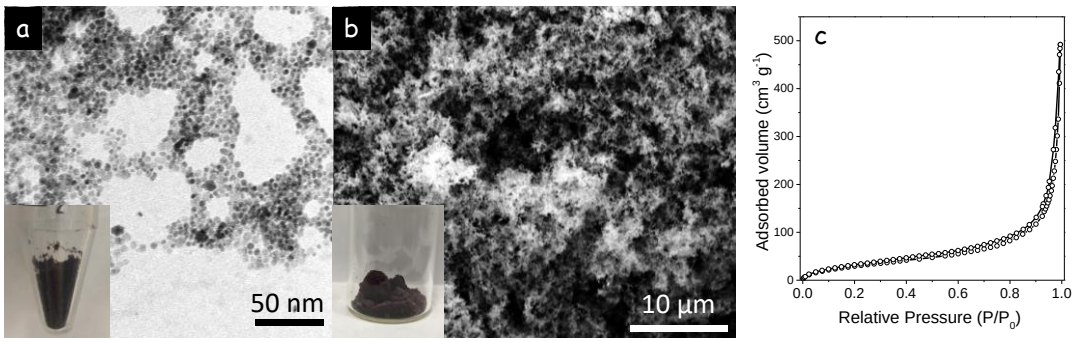

Fig. 3. a-b) TEM (a) and SEM (b) image of the Au-CeO_2 NCs gel and aerogel, respectively, obtained by mixing 4 ml of a 5 mg/mL MFA solution of Gln-CeO_2 NCs with 1 ml of a 5 mg/mL MFA solution of MUA-Au NCs. Optical photographs of the gel and the aerogel are shown as insets in a and b respectively. c) Adsorption–desorption isotherm measured from the Au-CeO_2 NCs aerogel.

NCs gelation was driven *via* electrostatic interaction of oppositely charged NCs (Fig. 5a). Gelation occurred within solutions containing a relatively wide range of CeO_2 and Au NC ratios and concentrations. To determine the CeO_2 and Au NC ratio required for gel formation, small amounts of a Au NC solution were stepwise added into a colloidal solution of CeO_2 NCs until gelation occurred. Following this procedure, we observed the gelation to take place already at a Au:CeO_2 NC mass ratio of 3:25 (Fig. 5b), equivalent to a ca. 6:25 NC ratio. When stepwise adding a CeO_2 NC solution into colloidal Au NCs, gelation started at a CeO_2:Au mass ratio of 10:25, equivalent to a NC ratio of ca. 5:25.

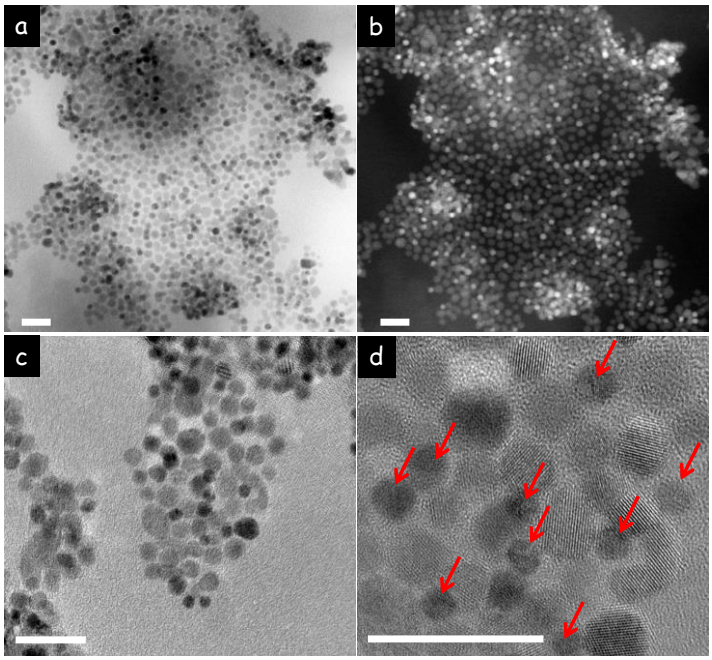

Fig. 4. Bright field (a), dark field (b) and high resolution (c,d) TEM micrographs of the 4:1 CeO_2:Au mass ratio gel. Gold NCs appear brighter in the dark field TEM micrograph. Gold NCs are pointed out with red arrows in the HRTEM micrograph in (d). All scale bars correspond to 20 nm.

In terms of total NC concentration (Fig, 5c), when using very high NC concentrations (50 mg/mL, on the limit of their colloidal stability) a very fast aggregation took place, resulting in a

NC precipitate rather than a gel. On the other extreme, when the concentration of the NCs was very low (0.005 mg/mL) we did not observe any NC aggregation for days due to an insufficient interaction of the NCs in solution (Figure 5). At moderate concentrations, 0.05-5 mg/mL, the solution started to gelate right after the oppositely charged NCs were combined. Within this range, we observed that the lower the NC concentration the larger the voluminosity of the formed gel (Fig. 5b). Note that in Figure 5b the gel obtained from combining 200 µL of a 0.05 mg/mL solution of Gln-CeO_2 and 50 µL of a 0.05 mg/mL solution of MUA-Au had approximately the same volume as that obtained from the same volumes of 0.5 mg/mL and 5 mg/mL NC solutions, which contained one and two orders of magnitude larger amounts of NCs, respectively.

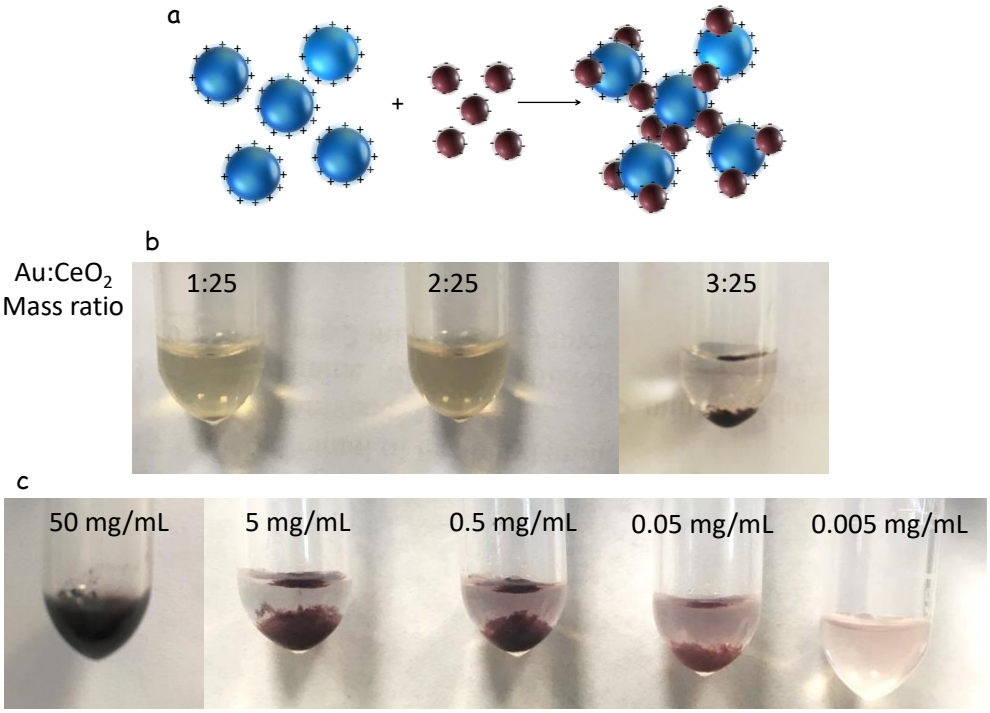

Fig. 5. a) Schematic representation of the gelation mechanism based on electrostatic interaction between oppositely charged NCs. b) Optical photographs of a colloidal solution of CeO_2 NCs where different amounts of Au NCs were stepwise added to reach Au:CeO_2 mass ratios of 1:25; 2:25; 3:25, as noted in each photograph. At a concentration of 3:25 gelation was observed. c) Optical photographs of Au-CeO_2 NCs gels obtained by combining 2 mL of a Gln-CeO_2 solution and 0.5 mL of a MUA-Au solution having increasingly higher (from right to left) concentrations (0.05, 0.5, 5, 50 mg/mL). Thus an order of magnitude in the amount of NCs exists between adjacent samples. Note that the CeO_2:Au mass ratio was fixed at 4:1. The Au-CeO_2 nanocomposite obtained from the 50 mg/mL solutions did not form a gel, but NCs rapidly precipitated upon mixing, forming relatively dense aggregates that stuck to the Eppendorf walls and its bottom.

We used CO oxidation as a model reaction to probe the effective formation of an interface between Au and CeO_2 NPs. Figure 6 shows the catalytic activity of the Au-CeO_2 aerogels toward CO oxidation. Results are compared with those obtained from a CeO_2 aerogel. The presence of Au catalytically activates the CO oxidation at much lower temperature than in pure CeO_2. The dramatic increase of activity observed for the Au-CeO_2 nanocomposite proves the formation a proper interface between gold and ceria.[40] The optimization of parameters of the catalysts NCs such as size, composition and facets using colloidal synthesis approaches already available will certainly allow maximizing the activity toward this and other reactions.

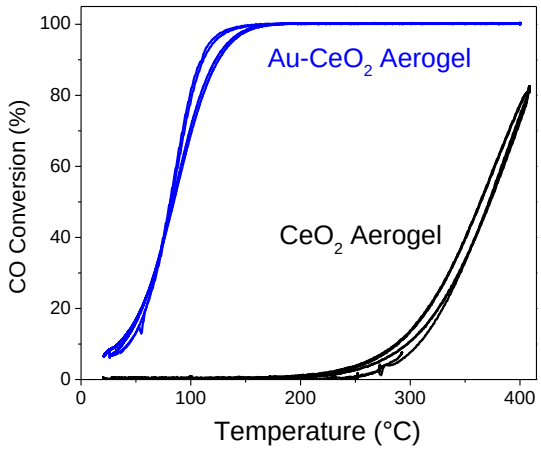

Fig. 6. Temperature dependence of the CO to CO_2 conversion on Au-CeO_2 and CeO_2 aerogels on two consecutive temperature ramps.

To prove the flexibility of the approach here reported, the same strategy was used to produce gels and aerogels from a combination of a metal chalcogenide and a metal oxide. In this case, the same positively charged NCs were used (Gln-CeO_2), while MUA-PbS NCs were selected as the negatively charged NCs. Upon mixing, gelation immediately started and it was completed within 30 min. Following the same procedure as for Au-CeO_2 gels, PbS-CeO_2 gels were dried into aerogels that also showed a highly porous structure. Fig. 7 displays a TEM micrograph of the initial CeO_2 and PbS NCs, their DLS size distribution and zeta potential curves, and TEM and SEM images of the gel and aerogel formed from their combination.

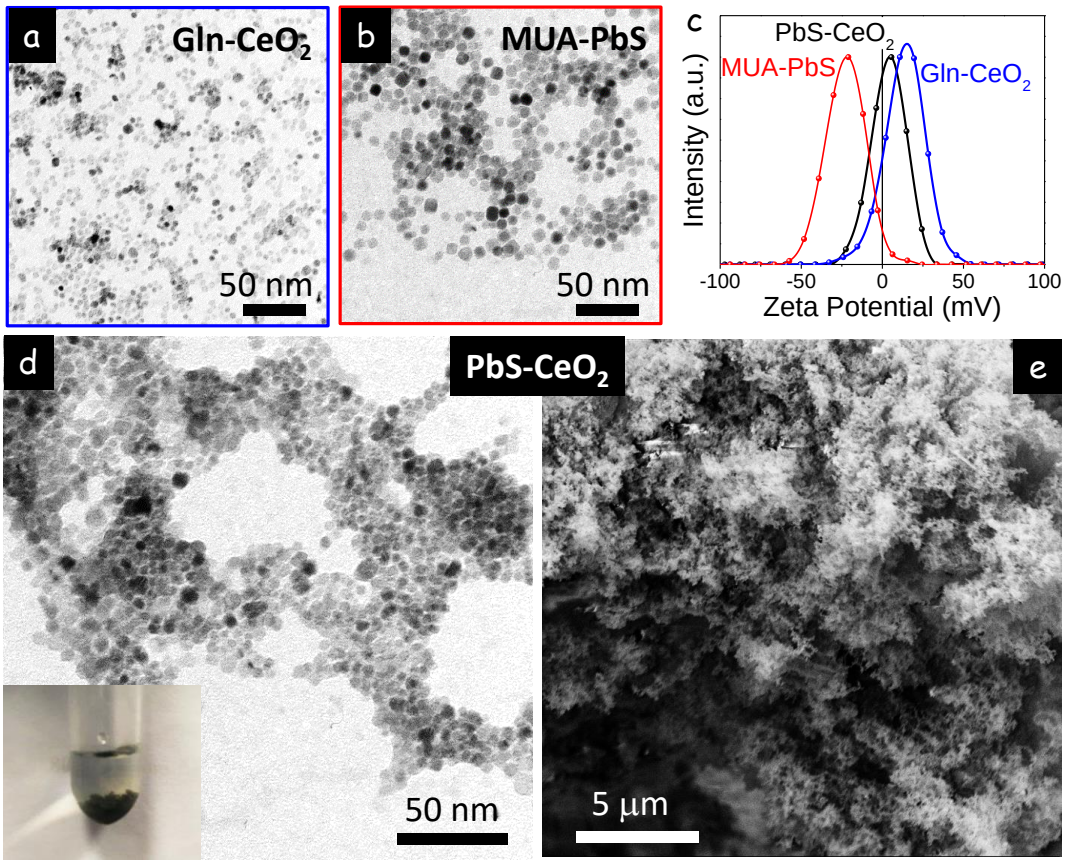

Fig. 7. a) TEM image of Gln-CeO_2 NCs. b) TEM image of MUA-PbS NCs. c) Zeta potential curves of MUA-PbS, Gln-CeO_2 and the gel obtained upon mixing Gln-CeO_2 and MUA-PbS NCs. d) TEM image of the PbS-CeO_2 NC-based gel obtained by mixing 4 ml of a 5 mg/mL MFA solution of Gln-CeO_2 NCs with 1 ml of a 5 mg/mL MFA solution of MUA-PbS NCs. e) SEM image of the corresponding PbS-CeO_2 NC-based aerogel.

7.4. Conclusions

A novel strategy to assemble NCs into multicomponent gels and aerogels based on electrostatic interactions between oppositely charged NCs was presented. Combining positively charged (Gln-capped) NCs with negatively charged (MUA-capped) NCs, metal-metal oxide (Au-CeO_2) and metal chalcogenide-metal oxide (PbS-CeO_2) nanocomposites with high specific surface areas were produced. The distribution of both NCs was rather homogeneous. We showed that the concentration of NCs in solution and the ratio between the amounts of NCs charged with each charge sign influenced the gel formation and voluminosity. We additionally demonstrated a proper interface between the two compounds, allowing a dramatic increase of the ceria catalytic activity toward CO oxidation. This new approach can be used to build-up porous nanocomposites with virtually any composition, and allows for a complete control over crystal domain size, facets, crystallographic structure and composition of the nanocomposite porous structures through control of these parameters at the NC level. This methodology can find numerous applications in fields such as catalysis, chemical sensing, filtering or energy storage among other.

7.5. References

1. Anderson, J. A., Supported metals in catalysis. *World Scientific*: **2012**; *11*.
2. Beloqui Redondo, A.; Ranocchiari, M.; van Bokhoven, J. A., Synthesis of sub-nanometer gold particles on modified silica. *Dalton Transactions* **2016**, *45 (7)*, 2983-2988.
3. Gutiérrez, L.-F.; Hamoudi, S.; Belkacemi, K., Synthesis of gold catalysts supported on mesoporous silica materials: recent developments. *Catalysts* **2011**, *1 (1)*, 97-154.
4. Li, B.; Hao, Y.; Shao, X.; Tang, H.; Wang, T.; Zhu, J.; Yan, S., Synthesis of hierarchically porous metal oxides and Au/TiO_2 nanohybrids for photodegradation of organic dye and catalytic reduction of 4-nitrophenol. *J. Catal.* **2015**, *329*, 368-378.
5. Rechberger, F.; Niederberger, M., Synthesis of aerogels: from molecular routes to 3-dimensional nanoparticle assembly. *Nanoscale Horizons* **2017**, *2 (1)*, 6-30.
6. Correa-Baena, J.-P.; Kriz, D. A.; Giotto, M.; Suib, S. L.; Agrios, A. G., Fluoride additive in epoxide-initiated sol-gel synthesis enables thin-film applications of SnO_2 aerogels. *RSC Advances* **2016**, *6 (26),* 21326-21331.
7. Laberty-Robert, C.; Long, J. W.; Lucas, E. M.; Pettigrew, K. A.; Stroud, R. M.; Doescher, M. S.; Rolison, D. R., Sol-Gel-Derived Ceria Nanoarchitectures: Synthesis, Characterization, and Electrical Properties. *Chem. Mater.* **2006**, *18 (1)*, 50-58.
8. Brinker, C. J.; Scherer, G. W., Sol-Gel Science: the physics and chemistry of sol-gel processing. Elsevier, 1 st ed., 2013.
9. Mohanan, J. L.; Arachchige, I. U.; Brock, S. L., Porous Semiconductor Chalcogenide Aerogels. *Science* **2005**, *307 (5708)*, 397-400.
10. Ziegler, C.; Wolf, A.; Liu, W.; Herrmann, A.-K.; Gaponik, N.; Eychmüller, A., Modern Inorganic Aerogels. *Angew. Chem. Int. Ed.* **2017**, *56 (43)*, 13200-13221.
11. Liu, J.; Meyns, M.; Zhang, T.; Arbiol, J.; Cabot, A.; Shavel, A., Triphenyl phosphite as phosphorous source for the scalable and cost-effective production of transition metal phosphides. *Chem. Mater.*, **2018**, *30* (5), 1799–1807.
12. Liu, Y.; García, G.; Ortega, S.; Cadavid, D.; Palacios, P.; Lu, J.; Ibáñez, M.; Xi, L.; De Roo, J.; López, A. M., Solution-based synthesis and processing of Sn- and Bi-doped Cu_3SbSe_4 nanocrystals, nanomaterials and ring-shaped thermoelectric generators. *J. Mater. Chem. A* **2017**, *5 (6)*, 2592-2602.
13. Meyns, M.; Iacono, F.; Palencia, C.; Geweke, J.; Coderch, M. D.; Fittschen, U. E.; Gallego, J. M.; Otero, R.; Juárez, B. H.; Klinke, C., Shape evolution of CdSe nanoparticles controlled by halogen compounds. *Chem. Mater.* **2014**, *26 (5)*, 1813-1821.
14. Luo, Z.; Lu, J.; Flox, C.; Nafria, R.; Genç, A.; Arbiol, J.; Llorca, J.; Ibáñez, M.; Morante, J. R.; Cabot, A., Pd 2 Sn [010] nanorods as a highly active and stable ethanol oxidation catalyst. *J. Mater. Chem. A* **2016**, *4 (42)*, 16706-16713.
15. Yin, Y.; Alivisatos, A. P., Colloidal nanocrystal synthesis and the organic–inorganic interface. *Nature* **2004**, *437 (7059)*, 664.
16. Boles, M. A.; Engel, M.; Talapin, D. V., Self-assembly of colloidal nanocrystals: From intricate structures to functional materials. *Chem. Rev.* **2016**, *116 (18)*, 11220-11289.
17. Nasilowski, M.; Mahler, B.; Lhuillier, E.; Ithurria, S.; Dubertret, B., Two-Dimensional Colloidal Nanocrystals. *Chem. Rev.* **2016**, *116 (18)*, 10934-10982.
18. Kovalenko, M. V.; Manna, L.; Cabot, A.; Hens, Z.; Talapin, D. V.; Kagan, C. R.; Klimov, V. I.; Rogach, A. L.; Reiss, P.; Milliron, D. J.; Guyot-Sionnnest, P.; Konstantatos, G.; Parak, W. J.;

Hyeon, T.; Korgel, B. A.; Murray, C. B.; Heiss, W., Prospects of Nanoscience with Nanocrystals. *ACS Nano* **2015**, *9 (2)*, 1012-1057.

19. Li, W.; Zamani, R.; Rivera Gil, P.; Pelaz, B.; Ibáñez, M.; Cadavid, D.; Shavel, A.; Alvarez-Puebla, R. A.; Parak, W. J.; Arbiol, J., CuTe nanocrystals: shape and size control, plasmonic properties, and use as SERS probes and photothermal agents. *J. Am. Chem. Soc.* **2013**, *135 (19)*, 7098-7101.

20. Berestok, T.; Guardia, P.; Blanco, J.; Nafria, R.; Torruella, P.; López-Conesa, L.; Estradé, S.; Ibáñez, M.; de Roo, J.; Luo, Z.; Cadavid, D.; Martins, J. C.; Kovalenko, M. V.; Peiró, F.; Cabot, A., Tuning Branching in Ceria Nanocrystals. *Chem. Mater.* **2017**, *29 (10)*, 4418-4424.

21. Wen, D.; Liu, W.; Haubold, D.; Zhu, C.; Oschatz, M.; Holzschuh, M.; Wolf, A.; Simon, F.; Kaskel, S.; Eychmüller, A., Gold Aerogels: Three-Dimensional Assembly of Nanoparticles and Their Use as Electrocatalytic Interfaces. *ACS Nano* **2016**, **10 (2)**, 2559-2567.

22. Liu, W.; Herrmann, A.-K.; Bigall, N. C.; Rodriguez, P.; Wen, D.; Oezaslan, M.; Schmidt, T. J.; Gaponik, N.; Eychmüller, A., Noble Metal Aerogels—Synthesis, Characterization, and Application as Electrocatalysts. *Acc. Chem. Res.* **2015**, *48 (2)*, 154-162.

23. Hendel, T.; Lesnyak, V.; Kühn, L.; Herrmann, A. K.; Bigall, N. C.; Borchardt, L.; Kaskel, S.; Gaponik, N.; Eychmüller, A., Mixed Aerogels from Au and CdTe Nanoparticles. *Adv. Funct. Mater.* **2013**, *23 (15)*, 1903-1911.

24. Voitekhovich, S. V.; Lesnyak, V.; Gaponik, N.; Eychmüller, A., Tetrazoles: Unique Capping Ligands and Precursors for Nanostructured Materials. *Small* **2015**, *11 (43)*, 5728-5739.

25. Heiligtag, F. J.; Rossell, M. D.; Suess, M. J.; Niederberger, M., Template-free co-assembly of preformed Au and TiO_2 nanoparticles into multicomponent 3D aerogels. *J. Mater. Chem*. **2011**, *21 (42)*, 16893-16899.

26. Da Silva, R. O.; Heiligtag, F. J.; Karnahl, M.; Junge, H.; Niederberger, M.; Wohlrab, S., Design of multicomponent aerogels and their performance in photocatalytic hydrogen production. *Catal. Today* **2015**, *246*, 101-107.

27. Peng, S.; Lee, Y.; Wang, C.; Yin, H.; Dai, S.; Sun, S., A facile synthesis of monodisperse Au nanoparticles and their catalysis of CO oxidation. *Nano Research* **2008**, *1 (3)*, 229-234.

28. Ibáñez, M.; Korkosz, R. J.; Luo, Z.; Riba, P.; Cadavid, D.; Ortega, S.; Cabot, A.; Kanatzidis, M. G., Electron Doping in Bottom-Up Engineered Thermoelectric Nanomaterials through HCl-Mediated Ligand Displacement. *J. Am. Chem. Soc.* **2015**, *137 (12),* 4046-4049.

29. De Roo, J.; Coucke, S.; Rijckaert, H.; De Keukeleere, K.; Sinnaeve, D.; Hens, Z.; Martins, J. C.; Van Driessche, I., Amino Acid-Based Stabilization of Oxide Nanocrystals in Polar Media: From Insight in Ligand Exchange to Solution ^{1}H NMR Probing of Short-Chained Adsorbates. *Langmuir* **2016**, *32 (8)*, 1962-1970.

30. Dragoman, R. M.; Grogg, M.; Bodnarchuk, M. I.; Tiefenboeck, P.; Hilvert, D.; Dirin, D. N.; Kovalenko, M. V., Surface-Engineered Cationic Nanocrystals Stable in Biological Buffers and High Ionic Strength Solutions. *Chem.Mater.* **2017,** *29* (21), 9416-9428.

31. Kalsin, A. M.; Fialkowski, M.; Paszewski, M.; Smoukov, S. K.; Bishop, K. J.; Grzybowski, B. A., Electrostatic self-assembly of binary nanoparticle crystals with a diamond-like lattice. *Science* **2006**, *312 (5772)*, 420-424.

32. Gittins, D. I.; Caruso, F., Spontaneous phase transfer of nanoparticulate metals from organic to aqueous media. *Angew. Chem. Int. Ed*. **2001**, *40 (16)*, 3001-3004.

33. Sapsford, K. E.; Algar, W. R.; Berti, L.; Gemmill, K. B.; Casey, B. J.; Oh, E.; Stewart, M. H.; Medintz, I. L., Functionalizing Nanoparticles with Biological Molecules: Developing Chemistries that Facilitate Nanotechnology. *Chem. Rev.* **2013**, *113 (3)*, 1904-2074.

34. Meador, M. A. B.; Fabrizio, E. F.; Ilhan, F.; Dass, A.; Zhang, G.; Vassilaras, P.; Johnston, J. C.; Leventis, N., Cross-linking Amine-Modified Silica Aerogels with Epoxies: Mechanically Strong Lightweight Porous Materials. *Chem. Mater.* **2005**, *17 (5)*, 1085-1098.

35. Leopold, L. F.; Tódor, I. S.; Diaconeasa, Z.; Rugină, D.; Ştefancu, A.; Leopold, N.; Coman, C., Assessment of PEG and BSA-PEG gold nanoparticles cellular interaction. *Colloids Surf. A* **2017**, *532*, 70-76.

36. Kimura, K.; Takashima, S.; Ohshima, H., Molecular Approach to the Surface Potential Estimate of Thiolate-Modified Gold Nanoparticles. *J. Phys. Chem. B* **2002**, *106 (29)*, 7260-7266.

37. Laaksonen, T.; Ahonen, P.; Johans, C.; Kontturi, K., Stability and Electrostatics of Mercaptoundecanoic Acid-Capped Gold Nanoparticles with Varying Counterion Size. *ChemPhysChem* **2006**, *7 (10)*, 2143-2149.

38. Amoli, B. M.; Gumfekar, S.; Hu, A.; Zhou, Y. N.; Zhao, B., Thiocarboxylate functionalization of silver nanoparticles: effect of chain length on the electrical conductivity of nanoparticles and their polymer composites. *J. Mater. Chem*. **2012**, *22 (37)*, 20048-20056.

39. Chen, S.; Kimura, K., Synthesis and Characterization of Carboxylate-Modified Gold Nanoparticle Powders Dispersible in Water. *Langmuir 1999*, *15(4),* 1075-1082.

40. Trovarelli, A.; Llorca, J., Ceria Catalysts at Nanoscale: How Do Crystal Shapes Shape Catalysis? *ACS Catalysis* **2017**, *7 (7)*, 4716-4735.

8. Conclusions

The work conducted in the thesis was focused on several topics: i) morphology controlled synthesis of colloidal NCs; ii) optimization NCs surface chemistry required for their further implementation/assembly; iii) production of porous structures from NCs. Particularly, two types of material were under investigation: metal oxides and metal chalcogenides.

The results obtained in the work allowed to make following conclusions:

- The conditions for the size- and shape-controlled synthetic procedure to grow ceria NCs as an example of metal oxides were established. Profound insight in the growth mechanism of the ceria NCs with the shapes evolving from spherical to branched-like in a wide range of sizes (from 7 nm to 50 nm) has been described. A great deal of attention was devoted to the NCs with branched morphology. The control of branching degree has been achieved by tuning the ratios of precursors used. Namely, addition of OAc along with cerium salt, OAm and ODE provoked NCs growth along [111] direction which was a key to commence the process of branching during the growth process. Presence of the alcohol molecules triggered the overbranching leading to the hyperbranched morphology of the NCs. Branched and hyperbranched NCs showed higher surface areas, porosities and OSC values compared to quasi-spherical NCs.

- The NCs morphology-controlled synthesis has been extended to quaternary $Cu_2ZnSnSe_4$ (CZTSe). The parameters for production of NCs with narrow size distribution and controlled composition have been found. The composition and stoichiometry control has been achieved by tuning the metal ratios. The non-stoichiometric CZTSe compositions had higher charge carrier concentrations and thus electrical conductivities, proving the control of the Fermi level by tuning the composition. A whole range of compositions (with very narrow size distributions) control enabled the possibility to tune the electronic properties.

- The strategy to functionalize the metal oxide NC surface composition by applying different ligands is proposed. The manipulation with the NCs surface ligands, namely ligand exchange with Gln allows rendering NCs soluble in non-polar and polar solvent which enables to develop a novel approach to assemble metal oxide NCs into porous gel and aerogel structures. PO has been found to trigger the gelation process of glutamine functionalized NCs. The detailed investigation of the gelation mechanism is demonstrated for the case of ceria. The method is applied for NCs with different morphologies. Eventually, the versatility of the concept is proved by using of the proposed approach for the iron oxide and titanium oxide nanocrystals. The catalytic properties of the produced porous architectures are discussed

- The assembly method has been extended to metal chalcogenides for the case of In_2S_3 NCs starting from the NCs synthesis, with further surface chemistry manipulation and eventually follows by the NC assembly into gels and aerogels. The optimization of NC surface chemistry was achieved by testing different ligand exchange approaches via

applying short-chain organic (MUA) and inorganic ligands (PTA, In-Cl complex). The assembly method based on ligand desorption from the NC surface and chalcogenide-chalcogenide bond formation has been established for In_2S_3. To trigger the ligand removal, the oxidation process was applied by introducing of the TNM. The comparison of the different ligands impact on the NC performance in colloidal form, when assembled into gels and when supported onto substrate is investigated towards photoelectrocatalysis.

- The oxidative ligand desorption assembly approach has been extended for multicomponent NCs for the case of $CuGaS_2$ and $CuGaS_2$-ZnS. Optimization of spin-coating process of the formed NCs inks followed by applying of sol-gel chemistry led to formation of highly porous layers from TGA-$CuGaS_2$ and TGA-ZnS. Applied results of $CuGaS_2$/ZnS nanocrystal-based bilayers and $CuGaS_2$–ZnS nanocrystal-based composite layers have been shown by testing their photoelectrochemical energy conversion capabilities.

- The approach to adjust NC surface chemistry has been proposed and tested for performing multicomponent NC assemblies. Applying of different ligands for NC surface functionalization endows their surface with different charges which usually provides colloidal NCs stabilization. It has been found that mixing of oppositely charged NCs with certain concentration enabled their assembly/gelation via electrostatic interaction. The proposed approach has been applied and optimized to produce multicomponent NC gels and aerogels. The detailed investigation of the gelation mechanism is shown for combination of metal-metal oxide and metal oxide-metal chalcogenide NCs (Au-CeO_2, CeO_2-PbS). Applied results of the Au-CeO_2 aerogels were demonstrated for CO-oxidation.

Future work and outlook

Variety of the available nanomaterials - nanoheterostructures, core-shell nanocrystals, dimers, etc, with a myriad of the different morphologies - has potential to be combined into even more sophisticated porous aerogel assemblies with outstanding functional properties. However, research on NC-based aerogels is still at the initial stage. Strategies on NCs implementation into aerogels have to be optimized and boost, as well as final properties and performance of aerogels built. The existent assembly strategies need to be extended for other multicomponent complex nanomaterial and their combination while adjusting their surface chemistry for maintaining and boosting their properties. Furthermore, the integration of NC-based aerogels is still a challenging task, first of all due to porous structure fragility. For efficient application, aerogel mechanical properties have to be improved without affecting the properties of the building blocks. Depending on the assembly process applied, the linkage between NCs can be week, which implies low mechanical performance of aerogel porous structure. Furthermore, large values of surface area entail large open pores and voids which do not necessarily lead to improved performance: often it contributes to enhanced fragility of the porous structure which can be an obstacle towards desirable application. Cost-effective application of aerogels requires simplification of the gel processing and elimination of high temperature and pressure gel drying processes. Considering all the aforementioned, particular future goals can be defined as:

- extending the assembly strategies for other NC compositions (phosphides, nitrides, etc) and nanoheterostructures for potential application in energy conversion systems, among other.
- improving of the mechanical properties of the obtained NC-based aerogels by using conductive polymers for instance.
- elimination of the super-critical drying process via applying room temperature sublimation solvents for instance.
- proving the applicability of the developed NC assembly approach for the implementation of this materials into real devices and systems.

Scientific output

Peer-reviewed articles in Journals

(ISI Indexed Journals with Impact Factor)

Ibáñez, M.; **Berestok, T.**; Dobrozhan, O.; Aaron LaLonde, O.A.; Izquierdo-Roca, V.; Shavel, A.; Pérez-Rodríguez, A.; Jeffrey Snyder, G.; Cabot, A. Phosphonic acids aid composition adjustment in the synthesis of $Cu_{2+x}Zn_{1-x}SnSe_{4-y}$ nanoparticles. *J. Nanopart. Res.* **2016**, *18,* 226.

Berestok, T.; Guardia, P.; Blanco, J.; Nafria, R.; Torruella, P.; López-Conesa, L.; Estradé, S.; Ibáñez, M.; de Roo, J.; Luo, Z.; Cadavid, D.; Martins, J. C.; Kovalenko, M. V.; Peiró, F.; Cabot, A., Tuning Branching in Ceria Nanocrystals. *Chemistry of Materials* **2017,** *29* (10), 4418-4424.

Blanco-Portals, J.; **Berestok, T.**; Torruella, P.; Coll, C.; López-Conesa, L.; Guardia, P.; Coy, L. E.; Cabot, A.; Estradé, S.; Peiró, F., Atomistic modelling and high resolution electron microscopy simulations of CeO_2 nanoparticles. *Applied Physics Letters* **2017,** *111* (22), 223107

Berestok, T.; Guardia, P.; Estradé, S.; Llorca, J.; Peiró, F.; Cabot, A., Brock, S.L. $CuGaS_2$ and $CuGaS_2$-ZnS porous layers from solution-processed nanocrystals. *Nanomaterials* **2018,** *8, 220.*

Berestok, T.; Guardia, P.; Du, R.; Blanco, J.; Estradé, S.; Peiró, F.; Brock, S.L.; Cabot, A., Metal oxide aerogels with controlled crystallinity and faceting from the epoxide-driven cross-linking of colloidal nanocrystals. *ACS Applied Materials and Interfaces* **2018,** *Article ASAP DOI: 10.1021/acsami.8b03754.*

Berestok, T.; Guardia, P.; Blanco, J.; Estradé, S.; Llorca, J.; Peiró, F.; Cabot, A., Brock, S.L. Surface chemistry and nano/microstructure engineering on photocatalytic In_2S_3 nanocrystals. *Langmuir* **2018.** *Accepted*

Berestok, T.; Guardia, P.; Ibáñez, M.; Meyns, M.; Colombo, M.; Kovalenko, M.; Peiró, F.; Cabot, A. Electrostatic-driven gelation of colloidal nanocrystals. **2018.** *Submitted*

Conference contributions

Authors: Taisiia Berestok, Pablo Guardia, Sonia Estrade, Francesca Peiró, Andreu Cabot

Title: **One-pot synthesis of CeO_2 NPs self-assembled onto Carbon Nanotubes**

Congress: E-MRS 2015 Fall Meeting, September 15-19 Warsaw University of Technology, Poland

Type: poster

Authors: Taisiia Berestok, Pablo Guardia, Raquel Nafria, Massimo Colombo, Sonia Estrade, Francesca Peiró, Andreu Cabot

Title: **Shape- and size-controlled synthesis of ligand free CeO_2 nanoparticles and their catalytic performances: From nanospheres to nanostars**

Congress: Applied Nanotechnology and Nanoscience International Conference, Barcelona, Spain, 2016, 11th November.

Type: oral

Authors: Taisiia Berestok, Pablo Guardia, Raquel Nafria, Sonia Estrade, Stephanie L. Brock Francesca Peiró, Andreu Cabot

Title: **Shape- and size-controlled synthesis of CeO_2 nanoparticles and their assembly into aerogels**

Congress: Bad Honnef Physics School on "Exciting Nanostructures: Probing and Tuning the Electronic Properties of Confined Systems" (21-31 July, 2017)

Type: poster

Authors: Taisiia Berestok, Pablo Guardia, Michaela Meyns, Javier Blanko, Lluis López-Conesa, Sonia Estrade, Stephanie L. Brock Francesca Peiró, Andreu Cabot

Title: **Assembly of sulfide-based nanoparticles into gels and aerogels**

Congress: Euromat 2017, Thessaloniki, Greece 2017, 17th September

Type: oral

CURRICULUM VITAE

Taisiia Berestok

Date birth: 09th December of 1989

Nationality: Ukrainian

Address: C. Felip II, 51-55, 1, 3, 08027 Barcelona, Spain

Phone number: 628812641

E-mail: taisiia.berestok@gmail.com, tberestok@irec-edu.cat

CURRENT POSITION

2015-recent	PhD student in Nanoscience	University of Barcelona, Barcelona, Spain

ACADEMIC TRAINING

2011-2012	Master in Physical and Biomedical Electronics	Sumy State University, Sumy, Ukraine
2007-2011	Bachelor in Micro- and Nanoelectronics	Sumy State University, Sumy, Ukraine

FELLOWSHIPS

05/2015-05/2018	PhD fellowship University of Barcelona	Catalan government
06/2016-09/2016	Mobility grant. Wayne State University	Catalan government
11/2013-01/2014	Mobility grant. Catalonia Institute for Energy Research	Ukrainian government

PROFESSIONAL EXPERIENCE

Period	Position/Place/Advisor	Research topic
05/2015-recent	PhD student. University of Barcelona and Catalonia Institute for Energy Research. Francesca Peiró, Andreu Cabot	Assembly of colloidal nanocrystals into porous nanomaterials

06/2016-09/2016	Visiting researcher. Chemistry Department. Wayne State University. Stephanie L. Brock	Assembly of quaternary chalcogenide nanoparticles into thin films and aerogels for photovoltaic and photocatalytic applications
11/2013-01/2014	Visiting researcher. Catalonia Institute for Energy Research. Andreu Cabot, Alexey Shavel	Synthesis and study of functional layers for sensitized solar cells based on perovskite absorbers

RESEARCH INTEREST

Synthesis of nanocrystals: shape- and size-controlled colloidal synthesis of metal, metal oxide and semiconductor nanocrystals. Structural and spectroscopic characterizations.

NC surface modification: general aspects of NC surface adjustment for morphology engineering; ligand-mediated NC' shape and size design; ligand exchange.

Assembly of nanocrystals: assembly of NCs into porous architectures. Assembly methods for producing NCs composites.

Application: application of NCs in catalytic systems (electrocatalysis, photocatalysis).

AWARDS:

05/2015 FI Agaur Fellowship

09/2017 Best oral presentation in the Functional Materials Section, EUROMAT Conference, 17-22 September, Thessaloniki, Greece. Title of the talk: Assembly of sulfide-based nanoparticles into gels and aerogels

06/2012 Master thesis dissertation best qualification.

PUBLICATIONS

In preparation:

1. **Berestok, T.**; Guardia, P.; Blanco, J.; Estradé, S.; Llorca, J.; Peiró, F.; Cabot, A., Brock, S.L. Surface chemistry and nano/microstructure engineering on photocatalytic In_2S_3 nanocrystals. *Langmuir* **2018.** *Submitted*

Published:

1. **Berestok, T.**; Guardia, P.; Estradé, S.; Llorca, J.; Peiró, F.; Cabot, A., Brock, S.L. $CuGaS_2$ and $CuGaS_2$-ZnS porous layers from solution-processed nanocrystals. *Nanomaterials* **2018,** *8, 220.*

2. **Berestok, T.**; Guardia, P.; Du, R.; Blanco, J.; Estradé, S.; Peiró, F.; Brock, S.L.; Cabot, A., Metal oxide aerogels with controlled crystallinity and faceting from the epoxide-driven cross-linking of colloidal nanocrystals. *ACS Applied Materials and Interfaces* **2018,** *Article ASAP DOI: 10.1021/acsami.8b03754.*

3. **Berestok, T.**; Guardia, P.; Blanco, J.; Estradé, S.; Llorca, J.; Peiró, F.; Cabot, A., Brock, S.L. Surface chemistry and nano/microstructure engineering on photocatalytic In_2S_3 nanocrystals. *Langmuir* **2018.** *Accepted*

4. Ibáñez, M.; **Berestok, T.**; Dobrozhan, O.; Aaron LaLonde, O.A.; Izquierdo-Roca, V.; Shavel, A.; Pérez-Rodríguez, A.; Jeffrey Snyder, G.; Cabot, A. Phosphonic acids aid composition adjustment in the synthesis of $Cu_{2+x}Zn_{1-x}SnSe_{4-y}$ nanoparticles. *J. Nanopart. Res.* **2016**, *18,* 226.

5. **Berestok, T.;** Guardia, P.; Blanco, J.; Nafria, R.; Torruella, P.; López-Conesa, L.; Estradé, S.; Ibáñez, M.; de Roo, J.; Luo, Z.; Cadavid, D.; Martins, J. C.; Kovalenko, M. V.; Peiró, F.; Cabot, A., Tuning Branching in Ceria Nanocrystals. *Chemistry of Materials* **2017,** *29* (10), 4418-4424.

6. Blanco-Portals, J.; **Berestok, T.**; Torruella, P.; Coll, C.; López-Conesa, L.; Guardia, P.; Coy, L. E.; Cabot, A.; Estradé, S.; Peiró, F., Atomistic modelling and high resolution electron microscopy simulations of CeO_2 nanoparticles. *Applied Physics Letters* **2017,** *111* (22), 223107

7. Mieshkov, M.; **Berestok**, **T.;** Sukhodub, L. F.; Opanasyuk, A. S.; Manzhos, O. P.; Danilchenko, S. M. Structural properties of zinc sulfide polymer nanocomposite with alginate. *J. Nano Electron. Phys.* **2015**, *7 (3)*, 03018.

8. **Berestok**, **T.;** Kurbatov, D. I.; Opanasyuk, N. M.; Opanasyuk, A. S. Influence of solution precursors on structure of ZnO films. *Functional Materials* **2015**, *22 (1)*, 93.

9. Pogrebnjak, A. D.; **Berestok**, **T.;** Opanasyuk, A. S.; Takeda, Y.; Oyoshi, K.; Komarov, F. F.; Kassi, J. Structural properties and elemental composition of Au^+ implanted ZnO films, obtained by sol-gel method. *J. Nano Electron. Phys.* **2014***, 6 (2)*, 02003.

10. **Berestok**, **T.;** Kurbatov, D. I.; Opanasyuk, N. M.; Manzhos, O. P.; Danilchenko, S. M. Structural properties of ZnO thin films obtained by chemical bath deposition technique. *J. Nano Electron. Phys.* **2013**, *3 (1)*, 01009.

ANNEX - PUBLICATIONS

CHEMISTRY OF MATERIALS

Article

pubs.acs.org/cm

Tuning Branching in Ceria Nanocrystals

Taisiia Berestok,[†,§] Pablo Guardia,[†,‡] Javier Blanco,[§] Raquel Nafria,[†] Pau Torruella,[§] Luis López-Conesa,[§] Sònia Estradé,[§] Maria Ibáñez,[∥,▽] Jonathan de Roo,[⊥] Zhishan Luo,[†] Doris Cadavid,[†] José C. Martins,[#] Maksym V. Kovalenko,[∥,▽] Francesca Peiró,[*,§] and Andreu Cabot[*,†,¶]

[†]Catalonia Institute for Energy Research − IREC, 08930 Sant Adrià de Besòs, Barcelona, Spain

[‡]Centre de Tecnologia Química de Catalunya and Universitat Rovira i Virgili, 43007 Tarragona, Spain

[§]LENS-MIND, Departament d'Enginyeries i Electrònica i Institut de Nanociència i Nanotecnologia (In2UB), Universitat de Barcelona, 08028, Barcelona, Spain

[∥]Institute of Inorganic Chemistry, Department of Chemistry and Applied Biosciences, ETH Zürich, Zürich, CH-8093, Switzerland

[⊥]Department of Inorganic and Physical Chemistry, Ghent University, B-9000 Ghent, Belgium

[#]Department of Organic and Macromolecular Chemistry, Ghent University, B-9000 Ghent, Belgium

[▽]EMPA-Swiss Federal Laboratories for Materials Science and Technology, Dübendorf, CH-8600, Switzerland

[¶]ICREA, Pg. Lluís Companys 23, 08010 Barcelona, Spain

Supporting Information

ABSTRACT: Branched nanocrystals (NCs) enable high atomic surface exposure within a crystalline network that provides avenues for charge transport. This combination of properties makes branched NCs particularly suitable for a range of applications where both interaction with the media and charge transport are involved. Herein we report on the colloidal synthesis of branched ceria NCs by means of a ligand-mediated overgrowth mechanism. In particular, the differential coverage of oleic acid as an X-type ligand at ceria facets with different atomic density, atomic coordination deficiency, and oxygen vacancy density resulted in a preferential growth in the [111] direction and thus in the formation of ceria octapods. Alcohols, through an esterification alcoholysis reaction, promoted faster growth rates that translated into nanostructures with higher geometrical complexity, increasing the branch aspect ratio and triggering the formation of side branches. On the other hand, the presence of water resulted in a significant reduction of the growth rate, decreasing the reaction yield and eliminating side branching, which we associate to a blocking of the surface reaction sites or a displacement of the alcoholysis reaction. Overall, adjusting the amounts of each chemical, well-defined branched ceria NCs with tuned number, thickness, and length of branches and with overall size ranging from 5 to 45 nm could be produced. We further demonstrate that such branched ceria NCs are able to provide higher surface areas and related oxygen storage capacities (OSC) than quasi-spherical NCs.

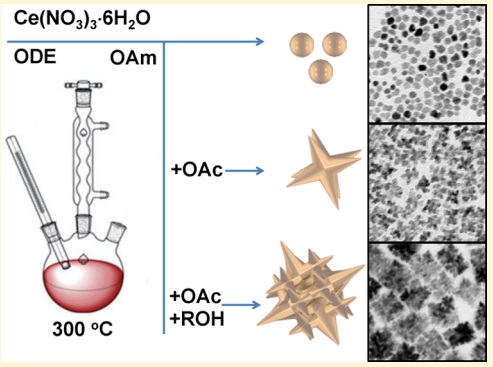

INTRODUCTION

Branching enables a significant increase of the surface-to-volume ratio of nanocrystals (NCs).[1,2] At the same time, compared with NCs having spherical or regular polyhedral geometries, the use of branched NCs as building blocks to produce macroscopic nanomaterials improves transport properties and provides higher levels of porosity by preventing close-packed aggregation.[1,3,4] Branching therefore allows a higher extent of interaction with the media while simultaneously facilitating charge carrier injection and extraction, characteristics that are particularly valuable in the fields of catalysis and sensing and in some biomedical applications. Besides, branched nanostructures may show additional advantages such as higher magnetic anisotropy in magnetic NCs[5,6] and improved surface enhanced Raman spectroscopy enhancement factors in plasmonic NCs.[7] Branched NCs are also easier to manipulate, purify, or recuperate than unbranched NCs with equivalent surface areas.

Branching is especially interesting in the field of catalysis, where it provides higher atomic surface exposure, potentially favorable facets, and very large densities of edges and corners with highly reactive sites.[8−10] A particularly interesting material in this field is ceria, which is one of the most technologically important rare earth oxides, being widely used in three way catalysts, gas sensors, and solid oxide fuel cells. Ceria is also used in biomedical applications to protect cells from radiation damages and oxidative stress.[11−13] As a result of its multivalence and the highly positive Ce^{4+}/Ce^{3+} reduction potential,

Received: March 3, 2017
Revised: April 18, 2017
Published: April 24, 2017

DOI: 10.1021/acs.chemmater.7b00896
Chem. Mater. 2017, 29, 4418−4424

ceria contains a mixture of Ce^{3+} and Ce^{4+} oxidation states which confers outstanding capabilities to store, release, and transport oxygen and oxygen vacancies, especially when nanostructured.[12−14] In all applications that involve interaction with the media, ceria performance depends not only on the crystal domain size but also on the facets exposed to the environment.[15−17] For instance, it has been established that (100) and (110) facets have lower activation energy for the formation of oxygen vacancies than (111) facets.[18] This translates into higher catalytic activities for a set of oxidation reactions of nanorods displaying (100) and (110) when compared with polyhedral NCs with (111) facets.[19−24] Several protocols to produce ceria NCs with controlled morphologies are already available.[25−30] However, a strategy or mechanism to control branching in such a technologically important material is yet to be reported.

Branching can be induced by several mechanisms, including template-directed growth, selective etching, twinning, crystal splitting, polymorphic or heterogeneous seeded growth, ligand-mediated overgrowth, and NC aggregation-based growth.[1,2,31−33] Among them, the overgrowth mechanism is the most versatile and simplest strategy to produce branched nanostructures as demonstrated for a number of systems.[1,9,34,35] Overgrowth mechanisms are generally considered as kinetically controlled. Thus, reactants and reaction conditions are selected so that ions add to the NC much faster than they can diffuse through the surface. In these conditions, the NC geometry is determined by the growth rate in each crystallographic direction, which depends on the accessibility and reactivity of each facet. These parameters, and thus the NC geometry, can be manipulated through the use of facet-selective surface ligands.

Here we describe a ligand-mediated overgrowth strategy to produce ceria NCs with tuned branching. By carefully adjusting the synthetic parameters and particularly the amount and type of ligands, branched NCs with different arm thicknesses and hyper-branched structures originated from side-branching can be produced. We also measure the surface area and oxygen storage capacity of the ceria NCs with different geometries.

METHODS

Chemicals. Cerium(III) nitrate hexahydrate ($Ce(NO_3)_3{\cdot}6H_2O$, 99%), oleic acid (OAc, $C_{18}H_{34}O_2$, 90%), 1-octadecene (ODE, $C_{18}H_{36}$, 90%), oleylamine (OAm, $C_{18}H_{37}N$, 70%), 1,2-decanediol (1,2-DDOL, $C_{10}H_{22}O_2$, 90%), 1,12-dodecanediol (1,12-DDDOL, $C_{12}H_{26}O_2$, 99%), 1,2-hexadecanediol (1,2-HDDOL, $C_{16}H_{34}O_2$, 90%), trifluoroacetic acid (TFA, $C_2HF_3O_2$, 99%), *N*,*N*-dimethylformamide (DMF, C_3H_7NO, 99.8%), decanoic acid (DAc, ≥98%), and propylene oxide (PO, C_3H_6O, ≥99.5%) were purchased from Sigma-Aldrich. 1-Dodecanol (1-DDOL, $C_{12}H_{26}O$, 98%) was purchased from Acros. Toluene, chloroform, and acetone were of analytical grade and were purchased from Panreac. OAm was purified by vacuum distillation. All other reagents were used as received without further purification. All experiments were carried out in 25 mL three-neck round-bottom flasks equipped with a condenser connected to a standard Schlenk line. Air- and moisture-sensitive chemicals were handled and stored under inert atmosphere.

Quasi-Spherical CeO_2 NCs. In a 25 mL three neck flask and under magnetic stirring, 0.434 g (1 mmol) of cerium(III) nitrate hexahydrate and 2 mL (6 mmol) of OAm were mixed in 4 mL of ODE. After degassing for 30 min at 80 °C, a brown colored solution was formed. The mixture was then heated under argon flow up to 300 °C at a rate of 15 °C/min. During heating up, at around 200 °C, the solution started to change color to dark brown. The mixture was allowed to react at 300 °C for 60 min before cooling to room temperature. During the cooling down, at around 160 °C, 2 mL of toluene were injected. NCs were finally collected by precipitation, adding 25 mL of acetone and centrifuging the solution at 6500 rpm for 6 min. The supernatant was discarded, and the black precipitate was dispersed in 5 mL of chloroform. This precipitation−redispersion procedure was repeated four times to remove excess of solvents and surfactants.

Branched CeO_2 NCs. To synthesize branched ceria NCs, the same protocol described above was used, but including OAc and eventually alcohols to the initial solution of cerium(III) nitrate hexahydrate, OAm and ODE. In particular, we added 2 mL of OAc (6 mmol) and selected amounts of alcohols (0, 2, and 2.5 mmol) to produced branched NCs with different geometries. Additional experimental details can be found in the Supporting Information. The specific syntheses parameters of each sample are provided in Table S1.

Structural and Chemical Characterization. Transmission electron microscopy (TEM) characterization was carried out using a ZEISS LIBRA 120, operating at 120 kV. High resolution TEM (HRTEM) studies were performed in a JEOL 2010F TEM operating at an accelerating voltage of 200 kV. Samples were prepared by drop casting a diluted solution of ceria NCs onto a carbon coated copper grid (200 mesh). Images were analyzed with the Gatan Digital Micrograph software. Scanning electron microscopy (SEM) analysis was carried out using a ZEISS Auriga microscope. For SEM characterization, NCs annealed at 400 °C for 4 h were dispersed in acetone and drop casted onto silicon substrates. X-ray power diffraction (XRD) analyses were carried out on a Bruker AXS D8 ADVANCE X-ray diffractometer with Ni-filtered (2 μm thickness) Cu Kα_1 radiation (λ = 1.5406 Å). Samples were drop casted (200−500 μL at a concentration of about 3 mg/mL) onto a zero-signal silicon wafer. UV−vis absorption spectra were recorded on a PerkinElmer LAMBDA 950 UV−vis spectrophotometer. Samples were prepared by diluting 100 μL in 3 mL of chloroform inside a 10 mm path length quartz cuvette. FTIR spectroscopy investigations were carried out using a PerkinElmer FT-IR 2000 spectrophotometer. Spectra were recorded from 500 cm^{-1} to 4000 cm^{-1}. Thermogravimetric analyses (TGA) were carried out on a PerkinElmer Diamond TG/DTA Instruments. For TGA analysis, samples were thoroughly dried, and 20 mg of the dried powder was loaded into a ceramic pan. Measurements were carried out in an air atmosphere from ambient temperature to 700 °C at a heating rate of 5 °C/min. Nuclear magnetic resonance (NMR) measurements were recorded on a Bruker Avance III Spectrometer operating at a ^1H frequency of 500.13 MHz and equipped with a BBI-Z probe. The sample temperature was set to 298.2 K.

Catalyst Preparation and Characterization. Once purified and dried, NCs, in the form of a nanopowder, were annealed at 400 °C for 4 h under air atmosphere using a heating ramp of 2 °C/min. The specific surface area and pore size of the materials was determined by N_2 adsorption at 77 K using a Tristar II 3020 Micromeritics system. Specific areas were calculated using the Brunauer−Emmet−Teller (BET) method, from the analysis of the adsorption at P/P_0 = 0.999. Hydrogen temperature-programmed reduction (TPR) was performed on annealed samples using a Micromeritics AutoChem HP 2950 chemisorption analyzer. Briefly, 50 mg of sample was pretreated at 90 °C for 15 min under flowing He (50 mL/min). After cooling to room temperature, the samples were reduced in a flow of 12 vol % H_2/Ar (50 mL/min), and temperature was linearly increased at a rate of 10 °C/min up to 930 °C. Oxygen storage capacities (OSC) were investigated by carrying out TGA experiments using a Sensys evo DSC instrument (Setaram) equipped with 3D thermal flow sensor. The sample was loaded into twin fixed-bed reactors, with one of the reactors serving as the reference. Each sample was treated in an Ar atmosphere for 1 h at 553 K to eliminate the adsorbed water, followed by heating at a constant rate (5 K/min) up to 673 K. At this temperature the materials were exposed to a flow of 12 vol % H_2/Ar (50 mL/min) and kept at this temperature for 1 h. The observed weight loss was associated with the removal of oxygen by H_2 to form water. Thus, from the weight loss an oxygen storage capacity at that temperature was calculated.

DOI: 10.1021/acs.chemmater.7b00896
Chem. Mater. 2017, 29, 4418−4424

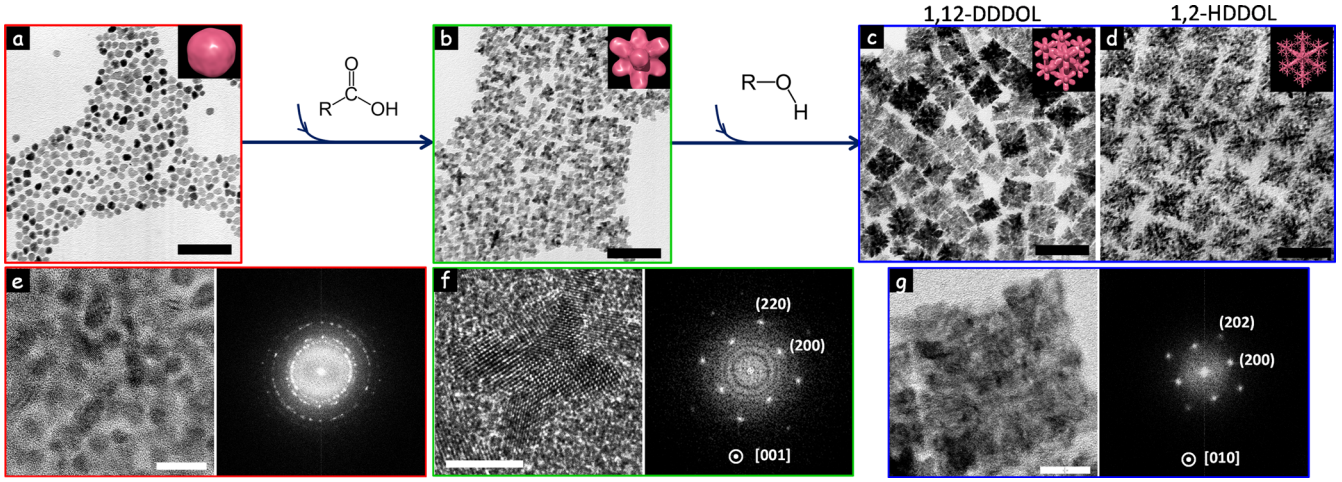

Figure 1. Representative TEM micrograph of ceria NCs obtained in the presence of different ligands: (a) Quasi-spherical NCs obtained in the presence of OAm; (b) branched ceria NCs produced with the additional incorporation of OAc; and (c, d) side-branched ceria NCs obtained in the presence of 1,12-DDDOL (c) and 1,2-HDDOL (d). Details for the syntheses are summarized in Table S1. (e–f) High-resolution TEM images and corresponding fast Fourier transform of quasi-spherical (e), branched (f), and hyperbranched (g) NCs. Scale bar of TEM images = 50 nm. Scale bar of HRTEM images = 5 nm.

RESULTS AND DISCUSSION

CeO_2 NCs were produced by the decomposition of cerium nitrate in the presence of OAm at temperatures up to 300 °C (see Methods and Supporting Information for details). Upon addition of the cerium salt to the ODE solution containing OAm and heating to 80 °C, a cerium–OAm complex was formed.[36] This complex started to decompose at around 200 °C to produce quasi-spherical CeO_2 NCs with an ca. 90% material yield (Figure 1a). Note that, in pure ODE, without OAm, cerium nitrate could not be dissolved, and when attempting to react it at high temperature (300 °C), no CeO_2 NCs could be recovered.

In the presence of OAc, cerium nitrate was soluble at moderate temperatures (~100 °C), probably forming cerium oleate.[37] However, in the sole presence OAc (without OAm), no CeO_2 NCs were produced, probably due to the stability of the cerium oleate complex and the chemical dissolution of ceria by OAc. The incorporation of equivalent amounts of OAc and OAm prevented NC dissolution and resulted in the growth of ceria NCs with branched geometries (Figure 1b). As calculated from the size of the obtained NCs and the total mass of material recovered, in the presence of OAc, a threefold decrease of the number of NCs and a twofold reduction of the final material yield of the reaction were obtained when compared with the growth in only OAm (Figure S6).

With respect to the reaction mixture containing OAm and OAc, the incorporation of alcohols accelerated the NC growth and strongly increased the material yield, to ca. 80%. In the presence of alcohols, systematically larger ceria NCs containing additional branches were produced (Figures 1c,d, and S6–S8). Relatively large concentrations of alcohols (e.g., 2.5 mmol of 1,2-HDDOL) resulted in hyperbranched NCs with an overall cubic shape.

HRTEM and electron diffraction analysis showed all branched NCs to be single crystal and branches to grow along the [111] crystallographic directions (Figures 1f,g and S9–S12). In contrast, aggregates of quasi-spherical NCs provided a polycrystalline SAED pattern (Figure 1e). XRD patterns (Figure S13) displayed the reflections of the CeO_2 fluorite structure (space group = $Fm3m$, JCPDS Card No. 34-0394) with lattice parameter a = 0.5412 nm. The crystal domain size calculated from the broadening of the XRD reflections using the Scherrer equation matched well with the NC size obtained from TEM, including clear differences in the crystal domain size in different crystallographic directions (Table S2).

High-angle annular dark-field scanning transmission electron microscope (HAADF-STEM) tomography analysis revealed the NCs produced in the presence of OAc, but no alcohols, to have an octapod-like geometry (Figure 2). A more detailed

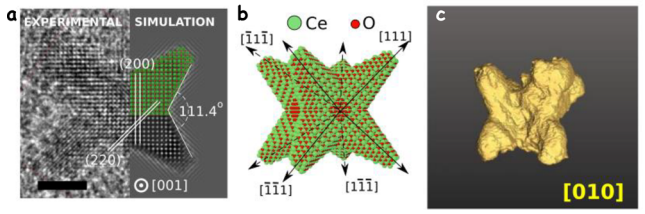

Figure 2. (a) Comparison between the HRTEM experimental (left) and simulated (right) images of a ceria octapod (scale bar = 2 nm). (b) 3D atomic model of a CeO_2 octapod. (c) HAADF tomographic reconstruction of a ceria octapod seen along the [010] direction.

view of the octapod morphology was obtained through atomic simulations (Figures 2 and S10). Modeling was conducted on NCs oriented along the [001] zone-axis, since HRTEM and FFT analyses showed this to be the most common for octapods. Simulations were carried out by dividing an octapod structure in a central body (spherical, zone-axis [001]) and a set of arms (hexagonal truncated pyramids) pointing in the [111] directions corresponding to the corners of a cube centered in the origin of the supercell. Simulation results were in good agreement with experimental HRTEM images, where the distribution of the NC atomic planes was well reproduced (Figures 2 and S10).

The formation of ceria octapods in the presence of OAc was consistent with previous reports demonstrating the synthesis of octapods of a range of metals and metal oxides.[5,6,36,38–40] Octapod formation has been associated either with a selective

DOI: 10.1021/acs.chemmater.7b00896
Chem. Mater. 2017, 29, 4418–4424

etching of [100] facets or the selective overgrowth in the [111] crystallographic direction. The latter case has been hypothesized to be triggered either by the preferential interaction of OAc with [100] facets blocking monomer delivery and thus hindering their growth or quite the opposite by its preferential interaction with the [111] facets, providing monomer (oleate) and thus accelerating growth in this direction.[41,42] However, scarce evidence to support these hypotheses have been given.

Some previous works also reported the formation of complex CeO_2 nanostructures through the oriented attachment of cubic NCs mediated by the preferential binding of OAc at [100] facets.[43] While it is not always straightforward to discern the mechanism involved in the formation of particular branched NCs, a main differential characteristic of aggregation growth when compared with atomic addition is that aggregation growth takes place within a solution containing a population of small NCs which decreases as being added to larger structures. Eventually, when all small NCs have been consumed, growth stops. To elucidate the growth mechanism of the ceria branched structures here described, aliquots at different reaction times were withdrew and analyzed (Figures 3 and S14). Interesting, NCs produced at low reaction times already showed a branched geometry, and no population of smaller NCs was observed. As reaction time increased, the size of all NCs in the ensemble simultaneously augmented while their geometry was preserved (Figures 3 and S14). This observation clearly pointed toward the formation of branched NCs through atomic addition and not through a selective etching or NC aggregation mechanism.

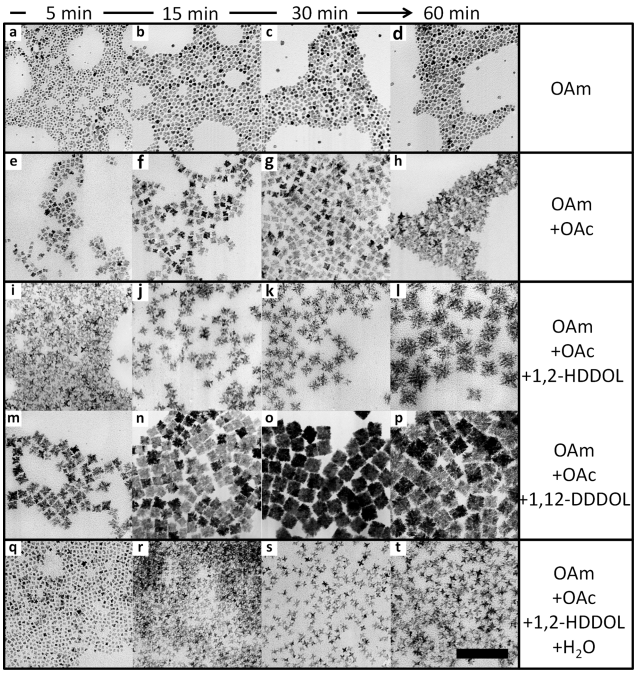

Figure 3. Representative TEM micrographs of the ceria NCs obtained at different reaction times (5, 15, 30, and 60 min): (a–d) in the presence of only OAm; (e–h) adding OAc; (i–l) adding OAc and 1,2-HDDOL; (m–p) adding OAc and 1,12-DDDOL; and (q–t) adding OAc, 1,2-HDDOL, and MQ-water. Experimental details for each image are summarized in Table S1. All images were taken at the same magnification. Scale bar = 50 nm.

To determine the specific OAc effect, either to block monomer delivery to the (100) facets favoring in this way the preferential growth of the [111] direction or to preferentially deliver monomer to the (111) facets in an OAm-passivated crystal, the NC surface chemistry was examined. In the ^{1}H NMR spectrum of purified hyperbranched NCs (obtained in the presence of OAm, OAc, and an alcohol), the ligand resonances were broadened, which is in line with the large size and the many chemical environments of such nanostructures (Figure S19). This broadening impeded the unequivocally direct determination of the ligand's identity. Therefore, we added TFA, which is known to be able to strip all kind of ligands from the NC surface.[44,45] Upon trifluoroacetic acid addition, the NC precipitate was separated by centrifugation from the supernatant (containing the stripped ligands). Figure S16 shows the FTIR spectra of NCs before and after ligand removal with TFA. As is clear from the absence of C–H stretching vibrations in the stripped samples, all the original ligands with aliphatic chains were removed. The only residual signals were attributed to bound TFA molecules, as is expected in an X-for-X type exchange and considering the charge neutrality conditions. Figure 4 shows the ^{1}H NMR spectrum of

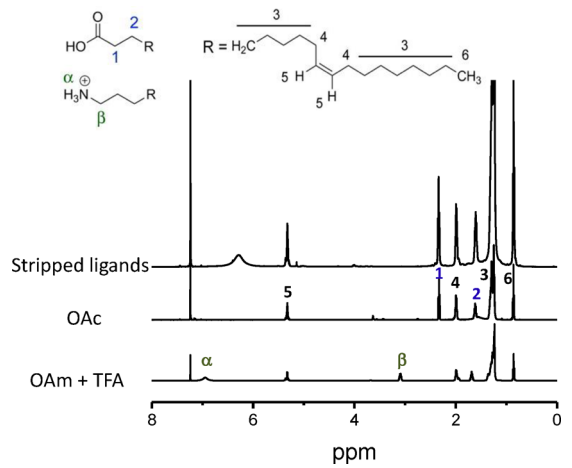

Figure 4. ^{1}H NMR spectrum of stripped ligands from hyperbranched ceria NCs and reference spectra of OAc and OAm in $CDCl_3$.

the cleaved ligands. A set of resonances that agrees with the fingerprint of OAc was clearly observed, while no sign of OAm and alcohols was visible. To further exclude the presence of OAm in the NC surface, we replaced OAc by decanoic acid in the synthesis, stripped the ligands from the NC surface, and studied their composition (Figures S17 and S18). The ^{1}H NMR spectrum of the ligands stripped from hyperbranched NCs produced in the presence of decanoic acid did not display the peak at around 5.33 ppm characteristic of the double bond present both in OAc and OAm, conclusively proving the absence of OAm at the NC surface.

To further determine the type of binding of OAc to the NC surface,[46,47] we added increasing amounts of 10-undecenoic acid to a dispersion of hyperbranched NCs and we measured the ^{1}H NMR spectra of the NCs. When raising the amount of added 10-undecenoic acid, an increasing contribution of its broadened resonances and a concomitant sharpening of the OAc features were observed in the ^{1}H NMR spectra (Figure S19). These features indicated a progressive replacement of OAc by 10-undecenoic acid, i.e., an X-for-X ligand exchange, that proved OAc to bind as an X-type ligand at the CeO_2 surface.[47]

DOI: 10.1021/acs.chemmater.7b00896
Chem. Mater. 2017, 29, 4418–4424

With OAc being the surfactant covering the NC surface, stabilizing it in solution and controlling its growth, as deduced from ^{1}H NMR analysis, the formation of branches triggered by its presence must be related to its differential coverage of particular facets, underprotecting them, instead of to its preferential decomposition in specific growth directions. With branches being grown in the [111] crystallographic directions, we conclude the (111) facets to have a lower coverage of OAc and thus are less protected from monomer delivery. Three intrinsic properties of the ceria crystal structure may explain the lower coverage of the (111) facets by OAc. First, the (111) is the most compact surface, which may prevent a close packed assembly of relatively bulky OAc. Additionally, (111) facets have surface atoms with the lowest coordination deficiency, thus limited ligand bonding. Moreover, this facet is characterized by the highest oxygen vacancy formation energies and thus has the lowest density of such a defect which is required to compensate charge when OAc coordinates as an X-type ligand.

The absence of the alcohol fingerprint in the NMR spectrum and the increased growth rates observed with their presence in the reaction mixture indicated that alcohols took a role as reactant. We hypothesize alcohols accelerated the reaction by participating in an esterification alcoholysis reaction of the oleate monomer.[48−50] In parallel, alcohols may consume part of the free acid via the esterification reaction, reducing the ceria dissolution rate. This overall modification of the growth kinetics directed the formation of sharper branches and triggered the creation of higher amounts of defects which acted as nucleation sites for new side branches, thus resulting in hyperbranched structures. At high concentrations of alcohol groups, very fast growth rates and high side nucleation rates were obtained, resembling a dendritic growth. The UV−vis spectra of hyperbranched CeO_2 NCs (Figure S20) shows a sign of their large density of defects in the form of a 20 nm shift of the wavelength of the absorption edge.

Testing different alcohols (1-DDOL, 1,2-DDOL, 1,2-HDDOL, and 1,12-DDDOL) showed that the aliphatic chain length did not have evident influence on the NC growth, while the number of alcohol groups and their position just slightly modified the branch thickness and density (Figures 1c,d, S7, and S21). For instance, 1,12-DDDOL promoted more densely packed branched structures when compared with 1-DDOL or 1,2- HDDOL.

Water is a byproduct of the esterification reaction that could influence the reaction kinetics. To elucidate this influence, controlled amounts of MQ-water were injected to the reaction mixture. The presence of MQ-water had a contrary effect to that of alcohols, reducing the growth rate and yield and preventing side branching. As shown in Figure 5, at a set amount of an alcohol (e.g., 2.5 mmol of 1,2-HDDOL), increasing the amount of added MQ-water (0, 1, and 1.5 mL) induced a morphology transformation from hyperbranched to octapod structures. Additionally, NCs obtained in the presence of water were systematically smaller than those produced under the same conditions but in its absence. We believe that the presence of water slowed down the reaction of alcohols and fatty acids and thus the formation of an ester by a displacement of the esterification reaction. An alternative explanation is the more effective protection of NC facets by filling the gaps between/left by OAc and increasing the overall ligand surface coverage.[51]

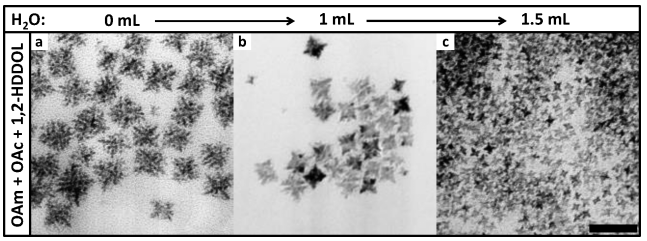

Figure 5. Representative TEM micrograph of ceria NCs produced in the presence of different amounts of water while maintaining constant all other conditions. Notice with the increase of the water content, NCs become smaller and side branching is prevented. Scale bar = 50 nm.

Before characterizing their functional properties, ceria NCs were annealed at 400 °C for 4 h under oxygen atmosphere to completely remove surface ligands. This temperature was selected on the basis that it permitted to remove residual organics while conserving the NC morphologies (Figures S16, S22, and S23). Adsorption−desorption isotherm N_2 cycles were performed on the annealed samples showing physisorption isotherms characteristic of microporous materials for the quasi-spherical NCs and a distinctive IV type isotherm characteristic of mesoporous materials for all branched nanostructures (Figure 6a, Table 1).[52] The specific surface areas of the annealed samples were calculated using the Brunauer−Emmett−Teller (BET) model.

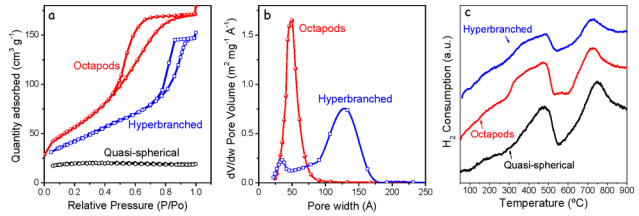

Figure 6. (a) Adsorption/desorption isotherm cycles performed on quasi-spherical, octapods, and hyperbranched ceria NCs. (b) BJH pore size distributions. (c) H_2 temperature-programmed reduction profiles. Samples were preheated at 90 °C for 15 min under a He flow (50 mL/min) before reducing them in a 12% vol H_2/Ar (50 mL/min) flow while increasing the temperature from room temperature up to 930 °C at a rate of 10 °C/min.

As expected, branched structures, particularly octapods, were characterized by much higher surface areas, up to 212 m^2/g against 63 m^2/g for quasi-spheres. We associated these differences mainly to the different packing of each type of NC. This packing difference was also manifested in the much higher porosity obtained from the branched structures (Figure

Table 1. Summary of the Characterization Performed on Ceria Spherical NCs, Octapods, and Hyperbranched NCs[a]

CeO_2 NCs	BET surface area (m^2/g)	pore volume (cm^3/g)	reduction at 823 K (x in CeO_x)[b]	OSC (μmol O/g)[c]
quasi-spherical	63	0.03	1.81	490
octapods	212	0.28	1.56	720
hyperbranched	157	0.24	1.53	630

[a]Description of experiments is summarized in the Methods section. [b]Value of x in CeO_x as measured at 823 K from hydrogen consumption. [c]Calculated from TGA in H_2 flow at 673 K.

DOI: 10.1021/acs.chemmater.7b00896
Chem. Mater. 2017, 29, 4418−4424

6b). We believe octapods showed larger surface areas than hyperbranched NCs because of the smaller size and arm thickness of the former. Also, part of the surface (interface) area of the hyperbranched structures could be not accessible due to a too close NC packing within such highly branched nanostructures.

TPR profiles of the annealed samples showed two major features (Figure 6c): In the range between 300 and 500 °C the reduction from Ce^{4+} to Ce^{3+} took place. This reduction occurred at lower temperatures at the NC surface compared with the bulk counterpart. The relative intensity between these two peaks in all the samples revealed a higher surface to volume ratio for the branched structures compared with the quasi-spherical, consistent with BET surface area results.[16,17] In the same direction, higher OSC values were also obtained for branched materials, reaching values up to 720 mmol O_2/g (Table 1).

CONCLUSION

Branched ceria NCs were synthesized by reacting cerium nitrate in the presence of OAm, OAc, and alcohols. OAc was found to bond to the NC surface as an X-type ligand hindering NC growth in all crystallographic directions but less efficiently in the [111]. This effect was attributed to the lower OAc coverage of the (111) facets due to their higher atomic compactness, lower coordination deficiency, and reduced oxygen vacancy density. The preferential growth in the [111] direction resulted in the formation of ceria octapods. The presence of alcohols strongly accelerated the NC growth through an esterification alcoholysis reaction, which resulted in larger NCs with side branching. The concentration of water in the reaction mixture was found to play an import role in controlling this alcoholysis reaction and possibly in better protecting the NC surface. It was further demonstrated that branched NCs provided higher surface areas, porosities, and OSC values when compared with quasi-spherical NCs.

ASSOCIATED CONTENT

Supporting Information

The Supporting Information is available free of charge on the ACS Publications website at DOI: 10.1021/acs.chemmater.7b00896.

Extended synthesis details; size distribution; XRD, UV−vis, HRTEM, and SEM characterization; details of the annealing treatment procedure; and additional details on surface characterization by NMR (PDF)

AUTHOR INFORMATION

Corresponding Authors

*(F.P.) E-mail: francesca.peiro@ub.edu.
*(A.C.) E-mail: acabot@irec.cat.

ORCID

Taisiia Berestok: 0000-0002-3066-9691
Jonathan de Roo: 0000-0002-1264-9312
Maksym V. Kovalenko: 0000-0002-6396-8938
Andreu Cabot: 0000-0002-7533-3251

Notes

The authors declare no competing financial interest.

ACKNOWLEDGMENTS

This work was supported by the European Regional Development Funds and the Spanish MINECO project BOOSTER. T.B. is grateful for the FI-AGAUR Research Fellowship Program, Generalitat de Catalunya (2015 FI_B 00744). P.G. acknowledges the People Programme (Marie Curie Actions) of the FP7/2007-2013 European Union Program (TECNIOspring Grant Agreement No. 600388) and the Agency for Business Competitiveness of the Government of Catalonia, ACCIÓ. M.I. thanks AGAUR for Beatriu de Pinós postdoctoral grant (2013 BP-A00344). Z.L. thanks the China Scholarship Council for scholarship support.

REFERENCES

(1) Li, H.; Kanaras, A. G.; Manna, L. Colloidal Branched Semiconductor Nanocrystals: State of the Art and Perspectives. *Acc. Chem. Res.* **2013**, *46*, 1387−1396.

(2) Ye, E.; Regulacio, M. D.; Zhang, S.-Y.; Loh, X. J.; Han, M.-Y. Anisotropically branched metal nanostructures. *Chem. Soc. Rev.* **2015**, *44*, 6001−6017.

(3) Miszta, K.; de Graaf, J.; Bertoni, G.; Dorfs, D.; Brescia, R.; Marras, S.; Ceseracciu, L.; Cingolani, R.; van Roij, R.; Dijkstra, M.; Manna, L. Hierarchical self-assembly of suspended branched colloidal nanocrystals into superlattice structures. *Nat. Mater.* **2011**, *10*, 872−876.

(4) Arciniegas, M. P.; Kim, M. R.; De Graaf, J.; Brescia, R.; Marras, S.; Miszta, K.; Dijkstra, M.; van Roij, R.; Manna, L. Self-Assembly of Octapod-Shaped Colloidal Nanocrystals into a Hexagonal Ballerina Network Embedded in a Thin Polymer Film. *Nano Lett.* **2014**, *14*, 1056−1063.

(5) Zhao, Z.; Zhou, Z.; Bao, J.; Wang, Z.; Hu, J.; Chi, X.; Ni, K.; Wang, R.; Chen, X.; Chen, Z.; Gao, J. Octapod iron oxide nanoparticles as high-performance T2 contrast agents for magnetic resonance imaging. *Nat. Commun.* **2013**, *4*, 2266.

(6) Douglas, F. J.; MacLaren, D. A.; Tuna, F.; Holmes, W. M.; Berry, C. C.; Murrie, M. Formation of octapod MnO nanoparticles with enhanced magnetic properties through kinetically-controlled thermal decomposition of polynuclear manganese complexes. *Nanoscale* **2014**, *6*, 172−176.

(7) Rodríguez-Lorenzo, L.; de la Rica, R.; Álvarez-Puebla, R. A.; Liz-Marzán, L. M.; Stevens, M. M. Plasmonic nanosensors with inverse sensitivity by means of enzyme-guided crystal growth. *Nat. Mater.* **2012**, *11*, 604−607.

(8) Yang, H.; Zhang, Y.; Hu, F.; Wang, Q. Urchin-like CoP Nanocrystals as Hydrogen Evolution Reaction and Oxygen Reduction Reaction Dual-Electrocatalyst with Superior Stability. *Nano Lett.* **2015**, *15*, 7616−7620.

(9) Zhao, R.; Fu, G.; Zhou, T.; Chen, Y.; Zhu, X.; Tang, Y.; Lu, T. Multi-generation overgrowth induced synthesis of three-dimensional highly branched palladium tetrapods and their electrocatalytic activity for formic acid oxidation. *Nanoscale* **2014**, *6*, 2776−2781.

(10) Tsai, Y.-H.; Chanda, K.; Chu, Y.-T.; Chiu, C.-Y.; Huang, M. H. Direct formation of small Cu_2O nanocubes, octahedra, and octapods for efficient synthesis of triazoles. *Nanoscale* **2014**, *6*, 8704−8709.

(11) Sun, C.; Li, H.; Chen, L. Nanostructured ceria-based materials: synthesis, properties, and applications. *Energy Environ. Sci.* **2012**, *5*, 8475−8505.

(12) Walkey, C.; Das, S.; Seal, S.; Erlichman, J.; Heckman, K.; Ghibelli, L.; Traversa, E.; McGinnis, J. F.; Self, W. T. Catalytic properties and biomedical applications of cerium oxide nanoparticles. *Environ. Sci.: Nano* **2015**, *2*, 33−53.

(13) Trovarelli, A. Catalytic Properties of Ceria and CeO2-Containing Materials. *Catal. Rev.: Sci. Eng.* **1996**, *38*, 439−520.

(14) Esch, F.; Fabris, S.; Zhou, L.; Montini, T.; Africh, C.; Fornasiero, P.; Comelli, G.; Rosei, R. Electron Localization Determines Defect Formation on Ceria Substrates. *Science* **2005**, *309*, 752−755.

(15) Sun, C.; Xue, D. Size-dependent oxygen storage ability of nanosized ceria. *Phys. Chem. Chem. Phys.* **2013**, *15*, 14414−14419.

DOI: 10.1021/acs.chemmater.7b00896
Chem. Mater. 2017, 29, 4418−4424

(16) Aneggi, E.; Wiater, D.; de Leitenburg, C.; Llorca, J.; Trovarelli, A. Shape-Dependent Activity of Ceria in Soot Combustion. *ACS Catal.* **2014**, *4*, 172−181.
(17) Vilé, G.; Colussi, S.; Krumeich, F.; Trovarelli, A.; Pérez-Ramírez, J. Opposite Face Sensitivity of CeO_2 in Hydrogenation and Oxidation Catalysis. *Angew. Chem., Int. Ed.* **2014**, *53*, 12069−12072.
(18) Conesa, J. Computer modeling of surfaces and defects on cerium dioxide. *Surf. Sci.* **1995**, *339*, 337−352.
(19) Lei, W.; Zhang, T.; Gu, L.; Liu, P.; Rodriguez, J. A.; Liu, G.; Liu, M. Surface-Structure Sensitivity of CeO_2 Nanocrystals in Photocatalysis and Enhancing the Reactivity with Nanogold. *ACS Catal.* **2015**, *5*, 4385−4393.
(20) Jiang, D.; Wang, W.; Zhang, L.; Zheng, Y.; Wang, Z. Insights into the Surface-Defect Dependence of Photoreactivity over CeO_2 Nanocrystals with Well-Defined Crystal Facets. *ACS Catal.* **2015**, *5*, 4851−4858.
(21) Mann, A. K. P.; Wu, Z.; Calaza, F. C.; Overbury, S. H. Adsorption and Reaction of Acetaldehyde on Shape-Controlled CeO_2 Nanocrystals: Elucidation of Structure−Function Relationships. *ACS Catal.* **2014**, *4*, 2437−2448.
(22) Sayle, D. C.; Maicaneanu, S. A.; Watson, G. W. Atomistic Models for CeO_2(111), (110), and (100) Nanoparticles, Supported on Yttrium-Stabilized Zirconia. *J. Am. Chem. Soc.* **2002**, *124*, 11429−11439.
(23) Si, R.; Flytzani-Stephanopoulos, M. Shape and Crystal-Plane Effects of Nanoscale Ceria on the Activity of Au-CeO_2 Catalysts for the Water−Gas Shift Reaction. *Angew. Chem., Int. Ed.* **2008**, *47*, 2884−2887.
(24) Carrettin, S.; Concepción, P.; Corma, A.; López Nieto, J. M.; Puntes, V. F. Nanocrystalline CeO_2 Increases the Activity of Au for CO Oxidation by Two Orders of Magnitude. *Angew. Chem., Int. Ed.* **2004**, *43*, 2538−2540.
(25) Mai, H.-X.; Sun, L.-D.; Zhang, Y.-W.; Si, R.; Feng, W.; Zhang, H.-P.; Liu, H.-C.; Yan, C.-H. Shape-Selective Synthesis and Oxygen Storage Behavior of Ceria Nanopolyhedra, Nanorods, and Nanocubes. *J. Phys. Chem. B* **2005**, *109*, 24380−24385.
(26) Yang, S.; Gao, L. Controlled Synthesis and Self-Assembly of CeO_2 Nanocubes. *J. Am. Chem. Soc.* **2006**, *128*, 9330−9331.
(27) Wang, D.; Kang, Y.; Doan-Nguyen, V.; Chen, J.; Küngas, R.; Wieder, N. L.; Bakhmutsky, K.; Gorte, R. J.; Murray, C. B. Synthesis and Oxygen Storage Capacity of Two-Dimensional Ceria Nanocrystals. *Angew. Chem., Int. Ed.* **2011**, *50*, 4378−4381.
(28) Li, P.; Zhou, Y.; Zhao, Z.; Xu, Q.; Wang, X.; Xiao, M.; Zou, Z. Hexahedron Prism-Anchored Octahedronal CeO_2: Crystal Facet-Based Homojunction Promoting Efficient Solar Fuel Synthesis. *J. Am. Chem. Soc.* **2015**, *137*, 9547−9550.
(29) Lee, S. S.; Song, W.; Cho, M.; Puppala, H. L.; Nguyen, P.; Zhu, H.; Segatori, L.; Colvin, V. L. Antioxidant Properties of Cerium Oxide Nanocrystals as a Function of Nanocrystal Diameter and Surface Coating. *ACS Nano* **2013**, *7*, 9693−9703.
(30) Yu, T.; Joo, J.; Park, Y. I.; Hyeon, T. Large-Scale Nonhydrolytic Sol−Gel Synthesis of Uniform-Sized Ceria Nanocrystals with Spherical, Wire, and Tadpole Shapes. *Angew. Chem., Int. Ed.* **2005**, *44*, 7411−7414.
(31) Lim, B.; Xia, Y. Metal Nanocrystals with Highly Branched Morphologies. *Angew. Chem., Int. Ed.* **2011**, *50*, 76−85.
(32) Milliron, D. J.; Hughes, S. M.; Cui, Y.; Manna, L.; Li, J.; Wang, L.-W.; Paul Alivisatos, A. Colloidal nanocrystal heterostructures with linear and branched topology. *Nature* **2004**, *430*, 190−195.
(33) Weiner, R. G.; Skrabalak, S. E. Metal Dendrimers: Synthesis of Hierarchically Stellated Nanocrystals by Sequential Seed-Directed Overgrowth. *Angew. Chem.* **2015**, *127*, 1197−1200.
(34) Li, Y.; Ding, W.; Li, M.; Xia, H.; Wang, D.; Tao, X. Synthesis of core-shell Au-Pt nanodendrites with high catalytic performance via overgrowth of platinum on in situ gold nanoparticles. *J. Mater. Chem. A* **2015**, *3*, 368−376.
(35) Lim, B.; Lu, X.; Jiang, M.; Camargo, P. H. C.; Cho, E. C.; Lee, E. P.; Xia, Y. Facile Synthesis of Highly Faceted Multioctahedral Pt Nanocrystals through Controlled Overgrowth. *Nano Lett.* **2008**, *8*, 4043−4047.
(36) Lee, S. S.; Zhu, H.; Contreras, E. Q.; Prakash, A.; Puppala, H. L.; Colvin, V. L. High Temperature Decomposition of Cerium Precursors To Form Ceria Nanocrystal Libraries for Biological Applications. *Chem. Mater.* **2012**, *24*, 424−432.
(37) Gu, H.; Soucek, M. D. Preparation and Characterization of Monodisperse Cerium Oxide Nanoparticles in Hydrocarbon Solvents. *Chem. Mater.* **2007**, *19*, 1103−1110.
(38) Cheong, S.; Watt, J.; Ingham, B.; Toney, M. F.; Tilley, R. D. In Situ and Ex Situ Studies of Platinum Nanocrystals: Growth and Evolution in Solution. *J. Am. Chem. Soc.* **2009**, *131*, 14590−14595.
(39) Yin, Z.; Zheng, H.; Ma, D.; Bao, X. Porous Palladium Nanoflowers that Have Enhanced Methanol Electro-Oxidation Activity. *J. Phys. Chem. C* **2009**, *113*, 1001−1005.
(40) Zhou, H.-P.; Zhang, Y.-W.; Mai, H.-X.; Sun, X.; Liu, Q.; Song, W.-G.; Yan, C.-H. Spontaneous Organization of Uniform CeO_2 Nanoflowers by 3D Oriented Attachment in Hot Surfactant Solutions Monitored with an In Situ Electrical Conductance Technique. *Chem. - Eur. J.* **2008**, *14*, 3380−3390.
(41) Jun, Y.-w.; Choi, J.-s.; Cheon, J. Shape Control of Semiconductor and Metal Oxide Nanocrystals through Nonhydrolytic Colloidal Routes. *Angew. Chem., Int. Ed.* **2006**, *45*, 3414−3439.
(42) Zhang, J.; Ohara, S.; Umetsu, M.; Naka, T.; Hatakeyama, Y.; Adschiri, T. Colloidal Ceria Nanocrystals: A Tailor-Made Crystal Morphology in Supercritical Water. *Adv. Mater.* **2007**, *19*, 203−206.
(43) Deori, K.; Gupta, D.; Saha, B.; Deka, S. Design of 3-Dimensionally Self-Assembled CeO_2 Nanocube as a Breakthrough Catalyst for Efficient Alkylarene Oxidation in Water. *ACS Catal.* **2014**, *4*, 3169−3179.
(44) Mastria, R.; Rizzo, A.; Nobile, C.; Kumar, S.; Maruccio, G.; Gigli, G. Improved photovoltaic performances by post-deposition acidic treatments on tetrapod shaped colloidal nanocrystal solids. *Nanotechnology* **2012**, *23*, 305403.
(45) Liu, Y.; Cadavid, D.; Ibáñez, M.; De Roo, J.; Ortega, S.; Dobrozhan, O.; Kovalenko, M. V.; Cabot, A. Colloidal $AgSbSe_2$ nanocrystals: surface analysis, electronic doping and processing into thermoelectric nanomaterials. *J. Mater. Chem. C* **2016**, *4*, 4756−4762.
(46) Green, M. L. H.; Parkin, G. Application of the Covalent Bond Classification Method for the Teaching of Inorganic Chemistry. *J. Chem. Educ.* **2014**, *91*, 807−816.
(47) De Roo, J.; De Keukeleere, K.; Hens, Z.; Van Driessche, I. From ligands to binding motifs and beyond; the enhanced versatility of nanocrystal surfaces. *Dalton Trans.* **2016**, *45*, 13277−13283.
(48) Buonsanti, R.; Llordes, A.; Aloni, S.; Helms, B. A.; Milliron, D. J. Tunable Infrared Absorption and Visible Transparency of Colloidal Aluminum-Doped Zinc Oxide Nanocrystals. *Nano Lett.* **2011**, *11*, 4706−4710.
(49) Zhong, X.; Feng, Y.; Zhang, Y.; Lieberwirth, I.; Knoll, W. Nonhydrolytic Alcoholysis Route to Morphology-Controlled ZnO Nanocrystals. *Small* **2007**, *3*, 1194−1199.
(50) Chen, Y.; Kim, M.; Lian, G.; Johnson, M. B.; Peng, X. Side Reactions in Controlling the Quality, Yield, and Stability of High Quality Colloidal Nanocrystals. *J. Am. Chem. Soc.* **2005**, *127*, 13331−13337.
(51) Zherebetskyy, D.; Scheele, M.; Zhang, Y.; Bronstein, N.; Thompson, C.; Britt, D.; Salmeron, M.; Alivisatos, P.; Wang, L.-W. Hydroxylation of the surface of PbS nanocrystals passivated with oleic acid. *Science* **2014**, *344*, 1380−1384.
(52) Sing, K. S. W.; Eerett, D. H.; Haul, R. A. W.; Moscou, L.; Pierotti, R. A.; Rouquerol, J.; Siemieniewska, T. Reporting physisorption data for gas/solid systems with special reference to the determination of surface area and porosity. *Pure Appl. Chem.* **1985**, *57*, 603.

DOI: 10.1021/acs.chemmater.7b00896
Chem. Mater. 2017, 29, 4418−4424

J Nanopart Res (2016) 18:226
DOI 10.1007/s11051-016-3545-4

RESEARCH PAPER

Phosphonic acids aid composition adjustment in the synthesis of $Cu_{2+x}Zn_{1-x}SnSe_{4-y}$ nanoparticles

Maria Ibáñez · Taisiia Berestok · Oleksandr Dobrozhan · Aaron LaLonde · Victor Izquierdo-Roca · Alexey Shavel · Alejandro Pérez-Rodríguez · G. Jeffrey Snyder · Andreu Cabot

Received: 3 April 2016 / Accepted: 30 July 2016 / Published online: 11 August 2016

Abstract The functional properties of quaternary I_2–II–IV–VI_4 nanomaterials, with potential interest in various technological fields, are highly sensitive to compositional variations, which is a challenging parameter to adjust. Here we demonstrate the presence of phosphonic acids to aid controlling the reactivity of the II element monomer to be incorporated in quaternary $Cu_2ZnSnSe_4$ nanoparticles and thus to provide a more reliable way to adjust the final nanoparticle metal ratios. Furthermore, we demonstrate the composition control in such multivalence nanoparticles to allow modifying charge carrier concentrations in nanomaterials produced from the assembly of these building blocks.

Keywords CZTSe · Nanostructured materials · Colloidal synthesis · Composition control · Electrical transport · Thermoelectric

M. Ibáñez · T. Berestok · O. Dobrozhan · V. Izquierdo-Roca · A. Shavel · A. Pérez-Rodríguez · A. Cabot
Catalonia Institute for Energy Research (IREC), Sant Adrià de Besós, 08930 Barcelona, Spain

A. LaLonde · G. J. Snyder
Materials Science, California Institute of Technology, 1200 East California Boulevard, Pasadena, CA 91125, USA

A. Pérez-Rodríguez
Departament d'Electrònica, IN2UB, Universitat de Barcelona, C. Martí i Franquès 1, 08028 Barcelona, Spain

G. J. Snyder
Materials Science and Engineering, Northwestern University, Evanston, USA

A. Cabot (✉)
Institució Catalana de Recerca i Estudis Avançats (ICREA), Pg. Lluís Companys 23, 08010 Barcelona, Spain
e-mail: acabot@irec.cat

Introduction

Quaternary copper-based chalcogenides have been proposed as low-cost and nontoxic alternative materials in numerous applications (Aldakov et al. 2013; Berger and Prochukhan 1969). In particular, I_2–II–IV–VI_4 compounds, such as Cu_2ZnSnS_4 (CZTS) and $Cu_2ZnSnSe_4$ (CZTSe) are highly suitable as photovoltaic (Carrete et al. 2013; Fella et al. 2013; Mitzi et al. 2011; Todorov et al. 2012) and photocatalytic (Aldakov et al. 2013; Ikeda et al. 2010; Miyauchi et al. 2012; Yu et al. 2014, 2015a, b) light absorbers. Besides, some of these I_2–II–IV–VI_4 compounds have been proposed as potential *p*-type thermoelectric materials due to a convenient band structure and low thermal conductivity (Heinrich et al. 2013; Ibáñez et al. 2012a, b. 2013; Li et al. 2013, 2014; Liu et al. 2009a; Zeier et al. 2012). In any of these applications, adjusting the cation ratios is fundamental to optimize functional properties. CZTSe materials with [Cu]/([Sn] + [Zn]) <1 and [Zn]/[Sn] >1 have provided

solar cells with the highest efficiencies (Chen et al. 2010; Tanaka et al. 2011; Xiao et al. 2015). In contrast, higher photocatalytic activities have been obtained with Cu-rich materials (Sevik and Cagin 2009; Yu et al. 2014). Besides, off-stoichiometric compositions allow to adjust charge carrier concentration, which is a critical parameter in the thermoelectric energy conversion field (Liu et al. 2009b).

While several protocols to produce quaternary chalcogenide nanoparticles (NPs) already exist (Fan et al. 2012; Ibáñez et al. 2012a, b, c; Khare et al. 2011; Riha et al. 2011; Singh et al. 2012, 2013), the control of the nanocrystal size, shape, and composition of such complex materials still remains a challenge, especially for selenide compounds. Generally, relatively large size and shape dispersions have been obtained. While size and shape may play an irrelevant role in several applications, especially on those requiring a posterior crystallization treatment, broad distributions denote a poor control of the reaction mechanism and thus also of the composition. Indeed, broad size and shape distributions may be indicative of a large compositional dispersion within each sample, which may difficult the optimization of the compositional-dependent functional properties of the final nanomaterials (Fan et al. 2012; Guo et al. 2009; Haas et al. 2011; Riha et al. 2009).

The formation of quaternary copper-based selenides is generally assumed not to proceed through the simultaneous reaction of the four elements in the stoichiometric amounts, but through the initial formation of Cu_xSe nuclei and the subsequent incorporation of the II and IV cations (Ibáñez et al. 2012a, b, c; Shavel et al. 2010). Within this reaction mechanism, the reactivity of the II and IV precursors, or the related monomers formed, is essential. In this regard, conventional procedures based on the reaction of metal chlorides with trioctylphosphine selenide in the presence of amines have demonstrated the introduction of the II element to be particularly challenging (Shavel et al. 2010).

We demonstrate here the addition of phosphonic acids during NP synthesis to aid introducing controlled amounts of Zn in CZTSe NPs. Furthermore, we also present here the compositional dependence of the electronic properties of CZTSe nanomaterials obtained from the consolidation of CZTSe NPs into pellets.

Methodology

Chemicals

Copper (I) chloride (97 %), zinc oxide (99.9 %), 1-octadecene (ODE, 90 %), oleic acid (OA, ≥99 %), hexadecylamine (HDA, tech. 90 %) were purchased from Aldrich. Tin (IV) chloride pentahydrate (98 %) and selenium (IV) oxide (99.8 %) were purchased from Strem. Phosphonic acids were purchased from PCI Synthesis. Chloroform, isopropanol, and ethanol were of analytical grade and obtained from various sources. All chemicals were used as received without further purification.

Synthesis of $Cu_2ZnSnSe_4$ NPs

CZTSe NPs were prepared following a similar procedure as the ones used to prepare other copper-based quaternary NPs (Ibáñez et al. 2012c). Copper (I) chloride (50 mg, 0.50 mmol), zinc oxide (41 mg, 0.50 mmol), tin (IV) chloride pentahydrate (88 mg, 0.25 mmol), hexadecylamine (1234 mg, 5 mM), and *n*-phosphonic acid (0.1 mmol, hexylphosphonic acid, HPA, tetradecylphosphonic acid, TDPA, or octadecylphosphonic acid, ODPA) were dissolved in 10 mL ODE within a 50 ml three-neck flask connected to a Schlenk line through a Liebig condenser. The solution was heated under argon flow to 200 °C and maintained at this temperature for 1 h to get rid of low-boiling point impurities, including water. Then, the solution was heated to 295 °C. At this temperature, 4 mL of a 3 mM selenium solution prepared by dissolving selenium (IV) oxide in ODE (5 h stirring at 180 °C under argon atmosphere) and pre-heated to 180 °C to reduce the temperature drop, was injected through a septum. The mixture was allowed to react for 5 min before cooling down to ambient temperature. The formation of CZTSe NPs was qualitatively followed by the color change of the mixture from an initial light yellow to green and eventually black. 3 mL of oleic acid was added to the mixture during the cooling at ~70 °C to replace the weakly bound HDA. The final solution containing the CZTSe NPs was mixed with 10 mL of chloroform and sonicate for 5 min. Finally CZTSe NPs were separated by centrifugation at 4000 rpm during 5 min. The yield of this synthetic procedure is between 80–90 % with respect to Cu. It must be pointed out that the content of Zn is twice the

needed stoichiometric amount, thereof while the [Cu]/[Zn] in the reaction pot is 1, the maximum we obtained in the CZTSe NPs is [Cu]/[Zn] = 2.

Preparation of pellets

To characterize CZTSe transport properties, NPs were thoroughly purified by multiple re-dispersion (chloroform) and precipitation (isopropanol) cycles until they could not be re-dispersed in organic solvents. Dried NPs were heated to 500 °C for 1 h under an Ar flow inside a tube furnace. The obtained nanopowder was hot pressed into 12 mm pellets at 40 MPa and 500 °C for 5 min using a rapid hot press (RHP) system (LaLonde et al. 2011). In this system, the heat is provided by an induction coil operated in the RF range applied directly to a graphite die acting as a susceptor. This set up configuration allows increasing temperature at a similar rate than spark plasma sintering (SPS). However, during RHP only the die body is heated inside the induction coil enabling faster cooling of the die and chamber. The density of the pressed pellets was in the range 92–95 % of theoretical value, measured by weight/volume.

Structural characterization

X-ray diffraction (XRD) analyses were collected directly on the as-synthesized NPs and on the final pellets using a Bruker AXS D8 Advance X-ray diffractometer with Ni-filtered (2 μm thickness) Cu K_λ radiation ($\lambda = 1.5406$ Å) operating at 40 kV and 40 mA. A LynxEye linear position-sensitive detector was used in reflection geometry. Inductively coupled plasma (ICP) atomic emission spectrometry measurements were carried out using a Perkin–Elmer Optima instrument, model 3200RL, under standard operating conditions. Scanning electron microscopy (SEM) is a Carl ZEISS Auriga microscope with an energy dispersive X-ray spectroscopy (EDX) detector. The EDX Oxford detector allows to do quantitative analysis with a resolution of 1278 eV at 5.9 keV. High-resolution transmission electron microscopy (HRTEM) was performed on a JEOL JEM 2100 with accessories for EDX analysis, STEM annular dark field, precession, and tomographic detectors. Raman scattering measurements were made using a Raman probe developed at IREC coupled with optical fiber to an iHR320 Horiba Jovin Yvon spectrometer. The measurements were performed in backscattering configuration focusing the excitation laser spot directly on the surface of the sample with an excitation wavelength of 532 nm, and a spot diameter of around 70 μm. To avoid thermal effects, the density power was kept below 0.5 kW cm^{-2}. All measurements were calibrated spectrally using a silicon monocrystalline reference setting the position of the main band at 520 cm^{-1}.

Electrical conductivity and thermopower measurements

Seebeck coefficients were measured using a static DC method. Electrical resistivities were obtained by four-probe method. Both Seebeck coefficient and electrical resistivity were simultaneously measured on a Linseis LSR-3 system under helium atmosphere at ambient temperature. Hall coefficients were measured using the Van der Pauw technique under a reversible magnetic field of 2 T.

Results and Discussion

CZTSe NPs with narrow size distributions, having size dispersions below 10 %, were systematically obtained by the above detailed procedure as shown in the representative transmission electron microscopy (TEM) micrographs of Fig. 1. The average NP size could be controlled by the reaction time and temperature in the range from 10 to 25 nm. The particular reaction kinetics of the different elements with selenium impeded the preparation of stoichiometric CZTSe NPs with sizes below 10 nm as relatively long reaction times, few minutes, were needed for all the elements to be introduced in the appropriate amount. CZTSe NPs typically showed tetrahedral geometries, but the exact morphology after 5 min of reaction strongly depended on the phosphonic acid used. The length of the alkyl chain of the phosphonic acid ligands has been already demonstrated to be crucial in controlling the morphology of CdSe NPs (Wang et al. 2007). However, in CZTSe NPs we could not identify a clear trend which we associated to the complexity of the system and the different reactivity of each elements. Further explanation on the role of the phosphonic acid will be addressed further on.

The overall composition of the initially formed NPs was rich in Cu and Se thus poor in Zn and Sn as

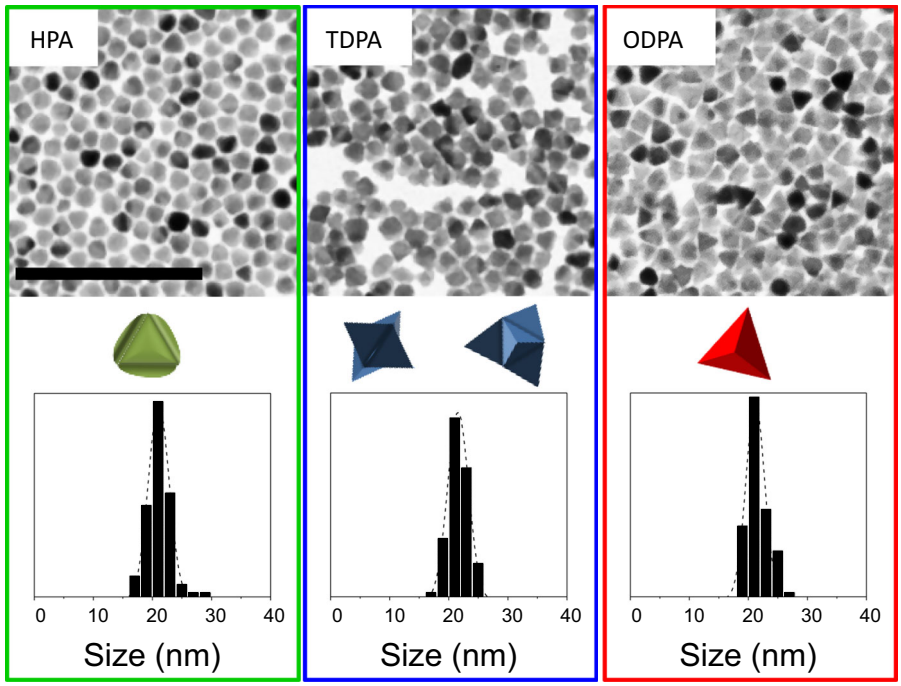

Fig. 1 TEM micrographs and size distribution histograms of the CZTSe particles obtained after 5 min of reaction using different phosphonic acids: HPA, TDPA, and ODPA as indicated

determined by energy dispersive EDX and verified by ICP analysis. With the reaction time, Sn first and Zn afterward were introduced within the NPs. In the absence of any phosphonic acid, zinc content introduced into the NPs was $\leq$10 % of the stoichiometric amount even with an excess of Zn precursor and after long reaction times. On the contrary, the addition of phosphonic acids allowed systematically obtaining >50 % of the stoichiometric Zn amount. However, just with TDPA acid, stoichiometric compositions could be properly obtained after 5 min reaction. Alkylphosphonic acids have been extensibly used to control nucleation and growth of II–VI semiconductors due to their stronger affinity with Cd^{2+} and Zn^{2+} ions to form complexes than fatty amines (García-Rodríguez et al. 2013; Ji et al. 2008; Peng and Peng 2002; Pradhan et al. 2007). As previously reported, we believe phosphonic acids to complexate with Zn^{2+} via dissolution of ZnO in the mixture of surfactants during decomposition of the alkylphosphonic acid (Liu et al. 2007). Such Zn-phosphonate complexes facilitate the introduction of Zn ions in preformed Cu–Se and Cu–Sn–Se NPs. This experimental evidence could be associated with the fact that usually a phosphonate group can coordinate with three or more cation centers, instead of one or two for the amine group (Cao et al. 1993; Fredoueil et al. 2002). This higher coordination could facilitate the incorporation of Zn^{2+} in the partially formed NPs and hence determine the NP shape as well.

Figure 2a shows a ternary diagram with the reaction time evolution of the NP composition when TDPA is used. After 10 s reaction $Cu_{2-x}Se$ NPs were obtained and the content of Zn and Sn slowly increased with reaction time until stoichiometric composition is obtained at 300 s. In view of these results, the different reaction kinetics of Cu, Zn, and Sn with Se offers a simple strategy to control the composition of such quaternary particles by just tuning the reaction time. Another obvious strategy to control composition is to adjust the ratio of the different elements in the precursor solution and give enough time for all the components to incorporate within the NP. In Fig. 2b, the average composition of CZTSe NP ensembles obtained from precursor solutions with tuned Zn composition is displayed. With this approach we could go from Cu_2SnSe_3 to $Cu_2ZnSnSe_4$, by simply adding increasing amounts of Zn. Stoichiometric composition was obtained for a [Cu]/[Zn] ratio of 1 (notice that we ha a large nominal excess of Zn).

XRD patterns of the obtained NPs, resembled that of a tetragonal symmetry structure with the $I\overline{4}2m$

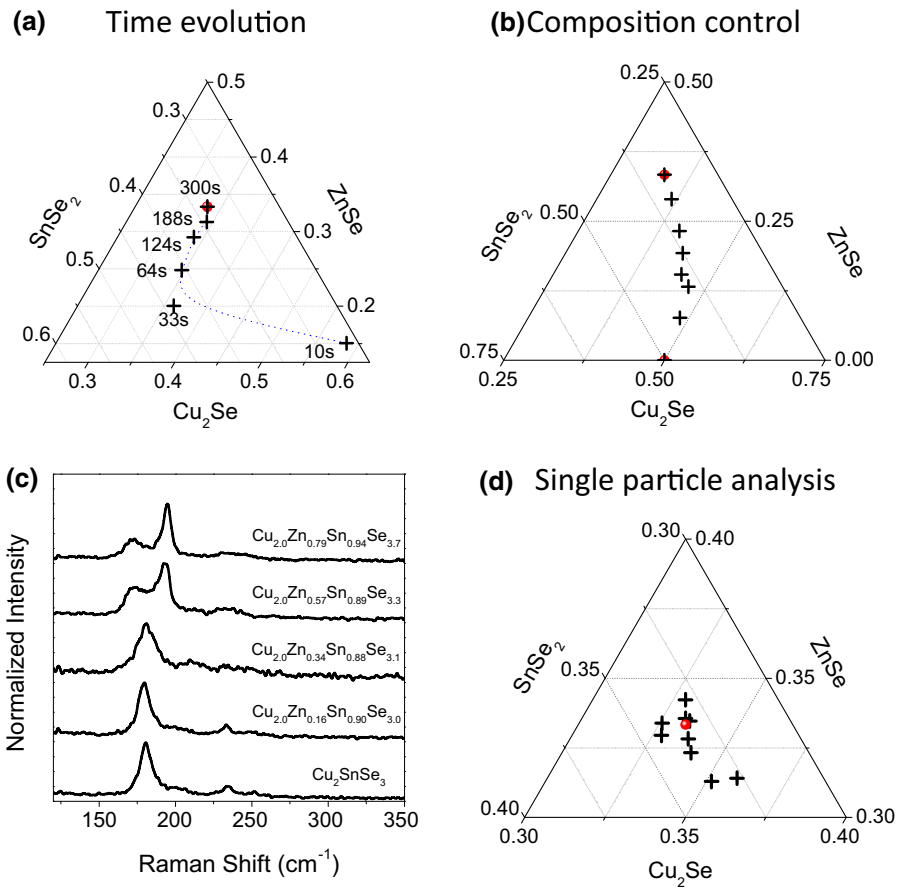

Fig. 2 **a** Composition evolution of CZTSe NPs obtained at 295 °C in the presence of TDPA and using stoichiometric metal ratios in the precursor solution. **b** Composition of NP ensembles obtained after 5 min reaction time at 295 °C in the presence of TDPA but using different initial precursor ratios. **c** Raman spectra of the materials obtained after 5 min reaction time at 295 °C in the presence of TDPA using different initial precursor ratios. **d** Composition distribution as obtained by single-particle HRTEM-EDX within a stoichiometric NP ensemble

space group (JCPDS No. 01-070-7623). The similar crystal structures of compounds having different amounts of Zn did not allow us to follow the NP structural evolution with the reaction time by means of XRD. Conveniently, phonon resonance modes are much more sensitive to atomic dissimilarities within the structure. Figure 2c shows the Raman spectra of the CZTSe NPs having different amounts of Zn. A clear evolution of the spectra from Cu_2SnSe_3 to CZTSe could be observed when incorporating different amounts of Zn. No additional XRD or Raman peak was observed, pointing at the absence of secondary phases and to the possibility to produce NPs with a much broader compositional range than what can be obtained for bulk materials (Dudchak and Piskach 2003; Nakamura et al. 2010; Tsuyoshi et al. 2011). To confirm NP composition, single-particle analysis using HRTEM-EDX was also performed. On Fig. 2d a ternary diagram with the composition distribution of a stoichiometric CZTSe sample is displayed. Each cross corresponds to the composition of a single particle. In accordance with their narrow size and shape distribution, slim NP composition distributions also were measured. On the same graph, the average value of the single-particle analysis is also indicated (red point). This is in good agreement with the results of the SEM−EDX, HRTEM–EDX, and ICP analyses performed.

The high yield of the detailed synthetic route (close to 90 % with respect to Cu precursor) allowed the production of grams of CZTSe NPs with narrow size distributions and controlled compositions and thus to measure their electronic properties as a function of composition. With this goal in mind, NPs were purified by multiple precipitation and re-dispersion treatments until they were not further soluble in chloroform. The final dried nanopowder was thermal treated at 500 °C for 1 h under argon atmosphere. Finally, 12 mm in diameter and 1 mm thick pellets with relative densities 92–95 % of the theoretical

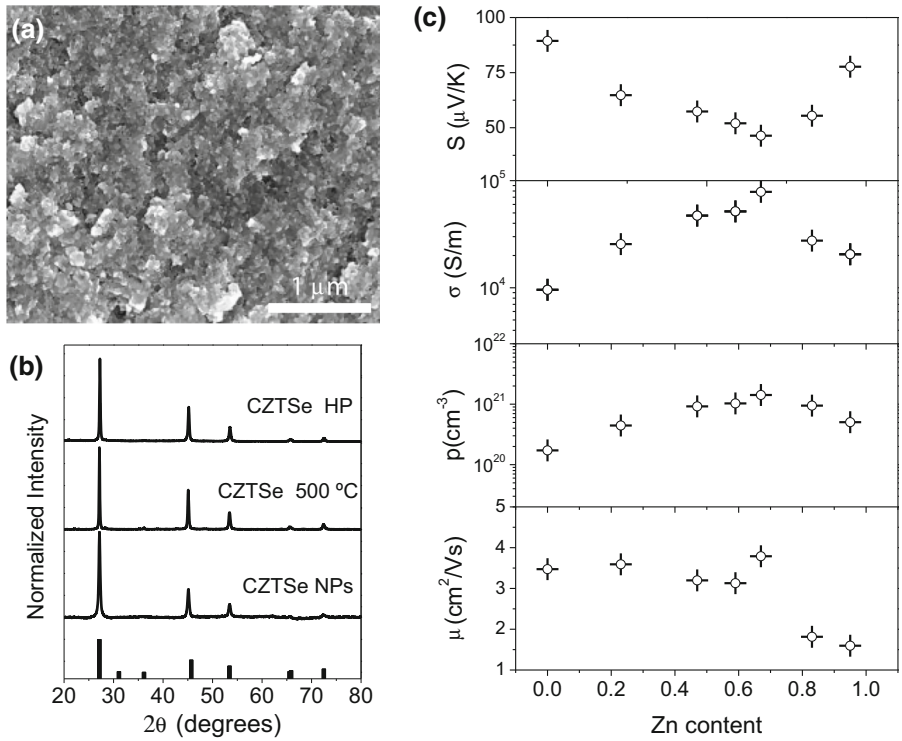

Fig. 3 **a** SEM image of the hot-pressed CZTSe material. **b** XRD patterns of the initial NP and the nanomaterials annealed at 500 °C and hot pressed at 500 °C and 40 MPa. **c** Ambient temperature seebeck coefficient (S), electrical conductivity (σ), hole carrier concentration (p), and mobility (μ) of the hot-pressed nanomaterials with different Zn composition

value were prepared by rapid hot pressing (LaLonde et al. 2011) (40 MPa and 500 °C for 5 min) 1 g of the annealed nanopowder. Figure 3a, b show an SEM image and the XRD patterns of the final CZTSe nanomaterial produced. With the annealing and hot press treatments, the CZTSe crystal domain size increased by a factor 2, from an average size of 22 nm of the initial particles to an average size of 45 nm as estimated from the fitting of the XRD pattern of the final pellets. No measurable composition variations were observed with the thermal treatments.

The Seebeck coefficient and electrical conductivity of the CZTSe nanomaterials with different Zn composition was measured at ambient temperature and are displayed in Fig. 3c. Notice how the electrical conductivity increased for the off-stoichiometric nanomaterials containing growing amounts of Zn, but decreases once approaching to the stoichiometric CZTSe composition. Hall measurements at ambient temperature showed very high carrier concentrations for all the nanomaterials, which we associate with a large interface area of the material which has associated with a large density of defects. Charge carrier concentrations increased with the initial introduction of Zn and decreased as the samples approximate the stoichiometric compositions. On the other hand, the mobility decrease with the Zn concentration in the whole composition range characterized.

Conclusions and outlook

A new synthetic strategy to produce CZTSe NPs with narrow size distribution and controlled composition involving the use of phosphonic acids was detailed. This procedure allowed controlling the composition of the final NPs in a wide range. We further demonstrated that, compositional control in these bottom-up processed multinary nanomaterials offered an accessible method to tune their charge carrier concentration within a relatively wide range.

Acknowledgments At IREC, work was supported by European Regional Development Funds and the Framework 7 program under project UNION (FP7-NMP 310250). M.I. Thanks AGAUR for her Beatriu i Pinós post-doctoral Grant.

References

Aldakov D, Lefrancois A, Reiss P (2013) Ternary and quaternary metal chalcogenide nanocrystals: synthesis properties and applications. J Mater Chem C 1:3756–3776

Berger LI, Prochukhan VD (1969) Ternary diamond-like semiconductors. Consultants Bureau, New York

Cao G, Lynch VM, Yacullo LN (1993) Synthesis, structural characterization, and intercalation chemistry of two layered cadmium organophosphonates. Chem Mater 5:1000–1006. doi:10.1021/cm00031a021

Carrete A et al (2013) Antimony-based ligand exchange to promote crystallization in spray-deposited Cu2ZnSnSe4 solar cells. J Am Chem Soc 135:15982–15985. doi:10.1021/ja4068639

Chen S, Gong XG, Walsh A, Wei S-H (2010) Defect physics of the kesterite thin-film solar cell absorber Cu2ZnSnS4. App Phys Lett 96:02. doi:10.1063/1.3275796

Dudchak IV, Piskach LV (2003) Phase equilibria in the Cu2SnSe3–SnSe2–ZnSe system. J Alloys Compd 351:145–150. doi:10.1016/S0925-8388

Fan F-J, Wang Y-X, Liu X-J, Wu L, Yu S-H (2012) Large-scale colloidal synthesis of Non-stoichiometric $Cu_2ZnSnSe_4$ nanocrystals for thermoelectric applications. Adv Mater 24:6158–6163. doi:10.1002/adma.201202860

Fella CM, Romanyuk YE, Tiwari AN (2013) Technological status of Cu2ZnSn(S, Se)4 thin film solar cells. Sol Energy Mater Sol Cells 119:276–277. doi:10.1016/j.solmat.2013.08.027

Fredoueil F, Evain M, Massiot D, Bujoli-Doeuff M, Janvier P, Clearfield A, Bujoli B (2002) Synthesis and characterization of two new cadmium phosphonocarboxylates Cd2(O-H)(O3PC2H4CO2) and Cd3(O3PC2H4CO2)22H2O. J Chem Soc Dalton Trans 7:1508–1512. doi:10.1039/B110275N

García-Rodríguez R, Hendricks MP, Cossairt BM, Liu H, Owen JS (2013) Conversion reactions of cadmium chalcogenide nanocrystal precursors. Chem Mater 25:1233–1249. doi:10.1021/cm3035642

Guo Q, Hillhouse HW, Agrawal R (2009) Synthesis of Cu2ZnSnS4 nanocrystal ink and its use for solar cells. J Am Chem Soc 131:11672–11673

Haas W, Rath T, Pein A, Rattenberger J, Trimmel G, Hofer F (2011) The stoichiometry of single nanoparticles of copper zinc tin selenide. Chem Commun 47:2050–2052

Heinrich CP, Day TW, Zeier WG, Snyder GJ, Tremel W (2013) Effect of isovalent substitution on the thermoelectric properties of the $Cu_2ZnGeSe_{4-x}S_x$ series of solid solutions. J Am Chem Soc 136:442–448. doi:10.1021/ja410753k

Ibáñez M et al (2012a) Composition control and thermoelectric properties of quaternary chalcogenide nanocrystals: the case of stannite $Cu_2CdSnSe_4$. Chem Mater 24:562–570

Ibáñez M et al (2012b) $Cu_2ZnGeSe_4$ nanocrystals: synthesis and thermoelectric properties. J Am Chem Soc 134:4060–4063

Ibáñez M, Zamani R, Li W, Shavel A, Arbiol J, Morante JR, Cabot A (2012c) Extending the nanocrystal synthesis control to quaternary compositions. Cryst Growth Des 12:1085–1090

Ibáñez M et al (2013) Colloidal synthesis and thermoelectric properties of Cu_2SnSe_3 nanocrystals. J Mater Chem A 1:1421

Ikeda S, Nakamura T, Harada T, Matsumura M (2010) Multicomponent sulfides as narrow gap hydrogen evolution photocatalysts. Phys Chem Chem Phys 12:13943–13949. doi:10.1039/c0cp00267d

Ji X, Copenhaver D, Sichmeller C, Peng X (2008) Ligand bonding and dynamics on colloidal nanocrystals at room temperature: the case of alkylamines on CdSe nanocrystals. J Am Chem Soc 130:5726–5735. doi:10.1021/ja710909f

Khare A, Wills AW, Ammerman LM, Norris DJ, Aydil ES (2011) Size control and quantum confinement in Cu_2ZnSnS_4 nanocrystals. Chem Commun 47:11721–11723

LaLonde AD, Ikeda T, Snyder GJ (2011) Rapid consolidation of powdered materials by induction hot pressing. Rev Sci Instrum 82:025104. doi:10.1063/1.3534080

Li W et al (2013) $Cu_2HgSnSe_4$ nanoparticles: synthesis and thermoelectric properties. Cryst Eng Comm 15:8966–8971. doi:10.1039/c3ce41583j

Li W et al (2014) Colloidal synthesis and functional properties of quaternary Cu-Based semiconductors: $Cu_2HgGeSe_4$. J Nanopart Res 16:1–6. doi:10.1007/s11051-014-2297-2

Liu H, Owen JS, Alivisatos AP (2007) Mechanistic study of precursor evolution in colloidal Group II–VI semiconductor nanocrystal synthesis. J Am Chem Soc 129:305–312. doi:10.1021/ja0656696

Liu M-L, Chen IW, Huang F-Q, Chen L-D (2009a) Improved thermoelectric properties of Cu-doped quaternary chalcogenides of $Cu_2CdSnSe_4$. Adv Mater 21:3808–3812

Liu M-L, Huang F-Q, Chen L-D, Chen I-W (2009b) A wide-band-gap p-type thermoelectric material based on quaternary chalcogenides of Cu2ZnSnQ4 (Q=S, Se). Appl Phys Lett 94:202103

Mitzi DB, Gunawan O, Todorov TK, Wang K, Guha S (2011) The path towards a high-performance solution-processed kesterite solar cell. Sol Energ Mat Sol C 95:1421–1436

Miyauchi M, Hanayama T, Atarashi D, Sakai E (2012) Photoenergy conversion in p-Type Cu_2ZnSnS_4 nanorods and n-Type metal oxide composites. J Phys Chem C 116:23945–23950. doi:10.1021/jp307949n

Nakamura S, Maeda T, Wada T (2010) Phase stability and electronic structure of In-free photovoltaic materials: $Cu_2ZnSiSe_4$, $Cu_2ZnGeSe_4$, and $Cu_2ZnSnSe_4$. Jpn J Appl Phys 49:121203

Peng ZA, Peng X (2002) Nearly monodisperse and shape-controlled CdSe nanocrystals via alternative routes: nucleation and growth. J Am Chem Soc 124:3343–3353. doi:10.1021/ja0173167

Pradhan N, Reifsnyder D, Xie R, Aldana J, Peng X (2007) Surface ligand dynamics in growth of nanocrystals. J Am Soc Chem 129:9500–9509. doi:10.1021/ja0725089

Riha SC, Parkinson BA, Prieto AL (2009) Solution-based synthesis and characterization of Cu_2ZnSnS_4 nanocrystals. J Am Chem Soc 131:12054–12055

Riha SC, Parkinson BA, Prieto AL (2011) Compositionally tunable $Cu_2ZnSn(S_{(1-x)}Se_{(x)})_4$ Nanocrystals: probing the effect of Se-inclusion in mixed chalcogenide thin films. J Am Chem Soc 133:15272–15275

Sevik C, Cagin T (2009) Assessment of thermoelectric performance of Cu2ZnSnX4, X=S, Se, and Te. Appl Phys Lett 95:112105

Shavel A, Arbiol J, Cabot A (2010) Synthesis of quaternary chalcogenide nanocrystals: stannite $Cu_2Zn_xSn_ySe_{1+x+2y}$. J Am Chem Soc 132:4514–4515

Singh A, Geaney H, Laffir F, Ryan KM (2012) Colloidal synthesis of wurtzite Cu_2ZnSnS_4 nanorods and their perpendicular assembly. J Am Chem Soc 134:2910–2913

Singh A, Singh S, Levcenko S, Unold T, Laffir F, Ryan KM (2013) Compositionally tunable photoluminescence emission in $Cu_2ZnSn(S_{1-x}Se_x)_4$ nanocrystals. Angew Chem Int Ed 52:9120–9124. doi:10.1002/anie.201302867

Tanaka K, Fukui Y, Moritake N, Uchiki H (2011) Chemical composition dependence of morphological and optical properties of Cu2ZnSnS4 thin films deposited by solâ€“gel sulfurization and Cu2ZnSnS4 thin film solar cell efficiency. Sol Energ Mat Sol C 95:838–842

Todorov TK, Tang J, Bag S, Gunawan O, Gokmen T, Zhu Y, Mitzi DB (2012) Beyond 11 % efficiency: characteristics of state-of-the-art Cu2ZnSn(S, Se)4. Solar Cells Adv Energy Mater 3(1):34–38. doi:10.1002/aenm.201200348

Tsuyoshi M, Satoshi N, Takahiro W (2011) First principles calculations of defect formation in In-free photovoltaic semiconductors Cu 2 ZnSnS 4 and Cu 2 ZnSnSe4. Jpn J Appl Phys 50(4S):04DP07

Wang W, Banerjee S, Jia S, Steigerwald ML, Herman IP (2007) Ligand control of growth morphology and capping structure of colloidal CdSe nanorods. Chem Mater 19:2573–2580. doi:10.1021/cm0705791

Xiao W et al (2015) Intrinsic defects and Na doping in Cu2ZnSnS4: a density-functional theory study. Sol Energy 116:125–132. doi:10.1016/j.solener.2015.04.005

Yu X, Shavel A, An X, Luo Z, Ibáñez M, Cabot A (2014) Cu_2ZnSnS_4–Pt and Cu_2ZnSnS_4–Au heterostructured nanoparticles for photocatalytic water splitting and pollutant degradation. J Am Chem Soc 136:9236–9239. doi:10.1021/ja502076b

Yu X, An X, Genç A, Ibáñez M, Arbiol J, Zhang Y, Cabot A (2015a) Cu_2ZnSnS_4–PtM (M=Co, Ni) nanoheterostructures for photocatalytic hydrogen evolution. J Phys Chem C 119:21882–21888. doi:10.1021/acs.jpcc.5b06199

Yu X et al (2015b) Cu2ZnSnS4–Ag2S nanoscale p–n Heterostructures as sensitizers for photoelectrochemical water splitting. Langmuir 31:10555–10561. doi:10.1021/acs.langmuir.5b02490

Zeier WG, LaLonde A, Gibbs ZM, Heinrich CP, Panthöfer M, Snyder GJ, Tremel W (2012) Influence of a nano phase segregation on the thermoelectric properties of the p-Type doped stannite compound $Cu_{2+x}Zn_{1-x}GeSe_4$. J Am Chem Soc 134:7147–7154. doi:10.1021/ja301452j

ACS APPLIED MATERIALS & INTERFACES

Research Article

Cite This: ACS Appl. Mater. Interfaces XXXX, XXX, XXX−XXX

www.acsami.org

Metal Oxide Aerogels with Controlled Crystallinity and Faceting from the Epoxide-Driven Cross-Linking of Colloidal Nanocrystals

Taisiia Berestok,[†,‡] Pablo Guardia,[†] Ruifeng Du,[†] Javier Blanco Portals,[‡,§] Massimo Colombo,[∥] Sònia Estradé,[‡,§] Francesca Peiró,[‡,§] Stephanie L. Brock,[⊥] and Andreu Cabot*[,†,#]

[†]Catalonia Institute for Energy Research−IREC, 08930 Sant Adrià de Besòs, Barcelona, Spain

[‡]LENS-MIND, Departament d'Enginyeria Electrònica I Biomèdica, Universitat de Barcelona, 08028 Barcelona, Spain

[§]Institute of Nanoscience and Nanotechnology (In2UB), Universitat de Barcelona, 08028 Barcelona, Spain

[∥]Nanochemistry Department, Istituto Italiano di Tecnologia, via Morego 30, 16130 Genova, Italy

[⊥]Department of Chemistry, Wayne State University, Detroit, Michigan 48202, United States

[#]ICREA, Pg. Lluís Companys 23, 08010 Barcelona, Spain

Supporting Information

ABSTRACT: We present a novel method to produce crystalline oxide aerogels which is based on the cross-linking of preformed colloidal nanocrystals (NCs) triggered by propylene oxide (PO). Ceria and titania were used to illustrate this new approach. Ceria and titania colloidal NCs with tuned geometry and crystal facets were produced in solution from the decomposition of a suitable salt in the presence of oleylamine (OAm). The native surface ligands were replaced by amino acids, rendering the NCs colloidally stable in polar solvents. The NC colloidal solution was then gelled by adding PO, which gradually stripped the ligands from the NC surface, triggering a slow NC aggregation. NC-based metal oxide aerogels displayed both high surface areas and excellent crystallinity associated with the crystalline nature of the constituent building blocks, even without any annealing step. Such NC-based metal oxide aerogels showed higher thermal stability compared with aerogels directly produced from ionic precursors using conventional sol−gel chemistry strategies.

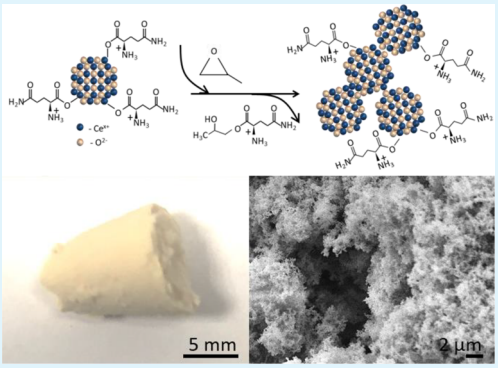

KEYWORDS: *aerogel, ceria, nanocrystal, sol−gel, ligand exchange*

INTRODUCTION

Mesoporous materials with high surface to bulk ratios are essential components in applications involving interactions with the surrounding media, including catalysis, sensing, filtering, and adsorption.[1,2] Among them, the highly porous disordered networks found in gels and aerogels are particularly appealing owing to the high accessibility they provide to fluids and reactants.

Such highly porous materials are commonly produced from ionic or molecular precursors following sol−gel chemistry approaches. Common protocols involve the use of metal alkoxide precursors that undergo hydrolysis and condensation.[3,4] Alternative metal salts are also used with the aid of an epoxide as gelation promoter.[5−8] Because of the moderate temperature of the gelation processes, the gels produced in this way are characterized by low crystallinities, thus generally requiring thermal annealing to achieve long-range atomic order. This thermal process usually results in a reduction of the surface area and prevents accurate control over crystallographic domain size, facets, and phase.

An alternative strategy to produce mesoporous materials with full versatility in terms of crystal domain parameters and composition is the cross-linking of presynthesized colloidal NCs.[9−12] This approach allows one to exploit the huge palette of colloidal NCs with precisely controlled properties currently available. It thus offers evident advantages in terms of producing porous nanomaterials with improved crystallinity, controlled composition, structure and surface facets, and porous nanocomposites with tuned phase distributions.

Colloidal NCs are generally produced using long chain surface organic ligands that control their growth and sterically stabilize them in nonpolar solvents.[13,14] To optimize the NCs' performance, such ligands are generally replaced by smaller molecules that maximize or tune interaction with the surrounding media. In this vein, the use of short amino acids as surface ligands provides NCs with a high versatility and thus an ample range of potential applications, from biomedical,

Received: March 6, 2018
Accepted: April 19, 2018
Published: April 19, 2018

DOI: 10.1021/acsami.8b03754
ACS Appl. Mater. Interfaces XXXX, XXX, XXX−XXX

taking advantage of the biocompatibility of amino acids,[15] to technological, taking advantage, for instance, of the efficient CO_2 adsorption provided by the amino group.[16−19] Additionally, the presence of both a carboxyl and an amino group provides amino acids with a very appealing surface chemistry versatility since depending on pH, the terminal amino or carboxyl group can bind to the surface.[20−22] Thus, the surface can be charged positively or negatively, which controls the capability of the NC to interact with different species in the media.

Among metal oxides, ceria is a particularly appealing material, especially in the form of a highly porous gel/aerogel. Cerium presents relatively stable Ce^{3+} and a Ce^{4+} oxidation states which can be exploited for redox chemistry.[23] This particularity and its high photo, thermal, and chemical stability makes ceria an excellent candidate material for a number of application fields that involve interaction with the surrounding media, e.g., heterogeneous catalysis,[24−28] solid oxide fuel cells,[29] gas sensors,[30] and environmental remediation.[31] While having no biological role, its low toxicity and its particular characteristics also make ceria an interesting material for biomedical applications, e.g., as a scavenger of reactive oxidation species through shuttling between Ce^{3+} and Ce^{4+} oxidation states.[32]

Titanium dioxide is one of the most used metal oxides in the field of heterogeneous catalysis and particularly in photocatalysis. Its advantages include the high abundance of its constituent elements, low toxicity, its use in paints, sunscreen, and even food coloring, outstanding stability, direct bandgap, low density of recombination centers, sufficiently positive valence band edge to oxidize water to oxygen, and overall suitability of the surface for a range of applications involving interaction with the media.[33,34]

Recent advances in the synthesis of colloidal ceria and titania NCs with tuned size and shape make such building blocks particularly appropriate to produce NC-based mesoporous nanomaterials.[35,36] Here, we use preformed ceria and titania NCs functionalized with amino acids to exemplify a novel strategy to produce metal oxide gels and aerogels. The process is based on the ligand displacement from the NC surface by the introduction of an epoxide, which triggers the cross-linking of NCs into a porous network.

EXPERIMENTAL SECTION

Materials. Cerium(III) nitrate hexahydrate ($Ce(NO_3)_3{\cdot}6H_2O$, 99%), 1-octadecene (ODE, $C_{18}H_{36}$, 90%), oleylamine (OAm, $C_{18}H_{37}N$, 70%), L-glutamine (Gln, $C_5H_{10}N_2O_3$, ≥ 99%), trifluoroacetic acid (TFA, $C_2HF_3O_2$, 99%), *N*-methylformamide (MFA, C_3H_7NO, 99.8%), propylene oxide (PO, C_3H_6O, ≥ 99.5%), neopentyl glycol diglycidyl ether (NGDE, $C_{11}H_{20}O_4$, ≥ 95%), dopamine hydrochloride (DA, $C_8H_{12}ClNO_2$, 98%), glutamic acid (Glu, $C_5H_9NO_4$, ≥ 99%), titanium(IV) fluoride (TiF_4, 99%), and tetramethylammonium hydroxide pentahydrate (TMAOH, $C_4H_{23}NO_6$, ≥ 99%) were purchased from Sigma-Aldrich. Hexane, 2-propanol, acetone, and methanol were of analytical grade and were purchased from Panreac. OAm was purified by vacuum distillation. All other reagents were used as received without further purification. All NC syntheses were carried out in three-neck round-bottomed flasks equipped with a condenser connected to a standard Schlenk line. Air- and moisture-sensitive chemicals were handled and stored under inert atmosphere.

Synthesis of Ceria Spherical NCs. Ceria NCs were synthesized though the thermal decomposition of cerium(III) nitrate within ODE in the presence of OAm, according to a procedure we previously reported.[35] Briefly, 0.434 g (1 mmol) of cerium(III) nitrate hexahydrate was mixed with 2 mL (6 mmol) of OAm in 4 mL of ODE in a 25 mL three-neck flask under magnetic stirring. After degassing the mixture for 30 min at 80 °C, the obtained brown color solution was heated under argon flow up to 300 °C at a rate of 15 °C/min. The mixture was allowed to react at this temperature for 60 min before cooling it down. NCs were washed with acetone at least four times and finally dispersed in a suitable solvent (hexane, chloroform, or toluene) with a concentration of 10 mg/mL for later use. Such NCs were labeled as ceria OAm-NCs.

Synthesis of Titania Nanoplates. Titanium dioxide NCs with plate morphology were synthesized via seeded growth following the procedure reported by Gordon et al.[36] The synthesis started from the preparation of a 0.2 M Ti precursor stock solution by dissolving the proper amount of TiF_4 within a 1 M OAc solution in ODE. This solution was maintained at 80 °C for 30 min under stirring within an Ar-filled glovebox. Meanwhile, 30 mmol of OAm, 1.5 mmol of OAc, and 10 mL of ODE were loaded into a 100 mL flask and degassed under vacuum and magnetic stirring at 120 °C for 60 min. After degassing, the flask was cooled down to 60 °C, and 1.5 mL of the TiF_4 stock solution was injected. Then, the temperature was increased up to 290 °C and maintained at this point for 10 min to allow seed formation. Subsequently, 8 mL of the TiF_4 stock solution was continuously added to the flask at a rate of 0.3 mL/min using a syringe pump. Afterward, the reaction was stopped by removing the heating mantle. Finally, NCs were isolated by adding a mixture of 2-propanol and methanol followed by centrifuging at 6000 rpm. These NCs were labeled as TiO_2 OAm-NCs.

Surface Modification with Amino Acids. The procedure used to replace native organic ligands with amino acids was inspired by previous work by J. de Roo et al.[19] Ligand exchange processes were carried out in air atmosphere. In a typical procedure, 1 mL of NCs dispersed in hexane (typically, 10 mg/mL) was added to a solution (prepared using mild sonication) of 7 mg of Gln in 1 mL of MFA, followed by the addition of TFA (0.2 mM). The two phase mixture obtained was stirred until NCs were transferred from the upper to the bottom phase. Then, the hexane phase was discarded, and a hexane/acetone mixture was added to the remaining MFA solution containing the NCs. Then, NCs were precipitated and subsequently washed at least two more times by the addition of MFA as a solvent and a mixture of hexane/acetone and acetonitrile as an antisolvent. Finally, NCs were redispersed in a polar solvent such as water, methanol, or MFA for later use. NCs obtained after surface modification with Gln were labeled as Gln-NCs.

Preparation of NC-Based Gels. The gelation procedure was carried out in air. In a typical experiment, 2 mL of MQ-water was added to 2 mL of a MFA solution of amino acid functionalized NCs (20 mg/mL). The mixture was sonicated for approximately 15 min. Then gelation was induced by adding 4 mL of PO and leaving the solution undisturbed. Gelation started after 1 h of undisturbed storage of the solution, and it was completed within 24 h. However, the gels were aged for several days. Then, MFA was carefully replaced by acetone using 5 mL of acetone each time. It must be noted that the solvent exchange should be conducted with special care to avoid destroying the NC network structure. The solvent exchange was repeated at least 6 times to ensure the complete removal of MFA.

Preparation of Ceria Gel from a Cerium Salt. Gelation of a cerium chloride sol was performed under ambient conditions following a previously reported procedure.[8] Briefly, 1 mmol of $CeCl_3{\cdot}6H_2O$ was dissolved in 3 mL of methanol. To the obtained mixture, 10 mL of PO was added. The formed solution was shaken vigorously for approximately 10 s and left undisturbed. Gelation occurred in 30 min and was followed by a change of the sol color from transparent to milky white and light brown when the gel was formed. The obtained gel was aged undisturbed for 12 h. Afterward, the solvent was exchanged by fresh acetone and isopropanol in order to get rid of unreacted products.

Gel Drying into Aerogel. In order to prevent collapsing its porous structure, gels were dried from supercritical CO_2. Briefly, the gel in acetone was loaded into a supercritical point dryer (SCD) chamber. Then, the chamber was sealed, and it was slowly filled with liquid CO_2 until the pressure reached 73 bar. To ensure that the CO_2 was in liquid state, the temperature of the system was maintained at

DOI: 10.1021/acsami.8b03754
ACS Appl. Mater. Interfaces XXXX, XXX, XXX−XXX

17−18 °C using a Peltier element. After overnight undisturbed storage, the liquid CO_2 inside of the chamber was half-drained, and fresh CO_2 was introduced. This procedure was repeated at least 6 times in 1 h intervals in order to fully replace acetone with liquid CO_2. Then, the Peltier element was switched off, and the chamber was heated up to 39 °C resulting in a pressure increase up to 80−90 bar and the transition of the CO_2 from liquid to a supercritical phase. The sample was kept under these conditions for 1 h followed by slowly releasing the pressure while keeping the temperature constant.

Structural and Chemical Characterization. Transmission electron microscopy (TEM) characterization was carried out using a ZEISS LIBRA 120, operating at 120 kV. High resolution TEM (HRTEM) analyses were performed in a JEOL 2010F TEM operating at an accelerating voltage of 200 kV. Samples were prepared by drop casting a diluted solution of NCs onto a carbon coated copper grid (200 mesh). Images were analyzed with Gatan Digital Micrograph software. X-ray power diffraction (XRD) analyses were carried out on a Bruker AXS D8 ADVANCE X-ray diffractometer with Ni-filtered (2 μm thickness) Cu Kα1 radiation (λ = 1.5406 Å). Samples were drop casted (200−500 μL at a concentration of about 3 mg/mL) onto a zero-background silicon wafer. UV−vis absorption spectra were recorded on a PerkinElmer LAMBDA 950 UV−vis spectrophotometer. Samples were prepared by diluting 100 μL in 3 mL of chloroform inside a 10 mm path length quartz cuvette. FTIR spectroscopy investigations were carried out using a PerkinElmer FT-IR 2000 spectrophotometer. Spectra were recorded from 500 to 4000 cm^{-1}. Thermogravimetric analyses (TGA) were carried out on PerkinElmer Diamond TG/DTA instruments. For TGA analysis, samples were thoroughly dried, and 20 mg of the dried powder was loaded into a ceramic pan. Measurements were carried out in an air atmosphere from ambient temperature to 700 °C at a heating rate of 5 °C/min. Dynamic light scattering (DLS) measurements were performed using Zeta Sizer (Malvern Instruments) equipped with a 4.0 mW HeNe laser operating at 633 nm and an avalanche photodiode detector. The specific surface area and pore size of the materials were determined by N_2 adsorption at 77 K using a Tristar II 3020 Micromeritics system. Specific areas were calculated using the Brunauer−Emmet−Teller (BET) method, considering equally spaced points in the P/P_o range from 0.05 to 0.30. The pore size distribution was evaluated from the desorption branches of isotherms according to the Barrett-Joyner-Halenda (BJH) method. Specific surface areas and pore size distributions were obtained from the materials annealed at 400 °C for 2 h under air atmosphere using a heating ramp of 2 °C/min.

RESULTS AND DISCUSSION

Quasi-spherical ceria NCs with an average size of 7 ± 1 nm were produced following our previously reported procedure.[35] In brief, NCs were obtained through the decomposition at 300 °C of cerium nitrate hexahydrate in an ODE solution containing OAm (Figure 1a). The presence of OAm at the surface of the ceria NCs limited their growth and rendered them soluble in nonpolar organic solvents.

OAm was replaced by amino acids using a two-phase procedure involving the mixing of the selected amino acid dissolved in MFA and TFA with a hexane solution containing the NCs. This mixture was mixed and sonicated for several minutes, resulting in the transfer of the NCs from hexane to MFA (see Experimental Section for details). The final NCs could be redispersed in polar solvents such as MFA, isopropanol, methanol, or water. Figure 1 displays TEM micrographs of ceria NCs before (OAm-NCs) and after ligand exchange with Gln (Gln-NCs). Similar hydrodynamic radii were measured by DLS from OAm-NCs dispersed in hexane and Gln-NCs in different polar solvents (Figure 1e). Additionally, positive zeta potentials (+26 mV) were measured for Gln-NCs, which were consistent with the passivation of these NCs with a ligand containing protonated amino group (Figure 1f).

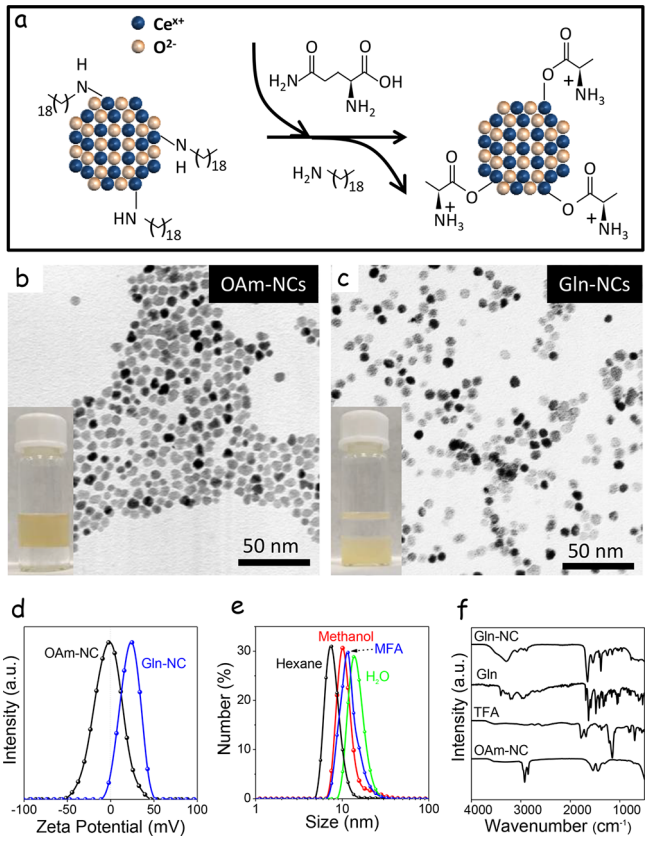

Figure 1. (a) Scheme of the OAm-to-Gln ligand exchange procedure. (b) TEM micrograph of ceria NCs with native organic ligands (OAm-NC). The inset shows a photograph of the two-phase mixture used for ligand exchange purposes before mixing. The top phase corresponds to the nonpolar solvent (hexane) containing the NCs and the bottom phase to the polar solvent (MFA) containing the amino acid and TFA. (c) TEM micrograph of ceria NCs after ligand exchange with Gln (Gln-NC). The inset shows the two-phase mixture after ligand exchange, with the NCs in the polar phase. (d) Zeta potential measurement of OAm-NCs and Gln-NCs. (e) DLS curves of OAm-NCs in hexane and Gln-NC in H_2O, methanol, and MFA. (f) FTIR spectra of OAm-NCs, TFA, Gln, and Gln-NCs.

FTIR analysis confirmed the displacement of OAm from the NCs surface upon ligand exchange with Gln (Figure 1f). The FTIR spectrum of the NCs after ligand exchange showed a strong suppression of the organic ligand fingerprint, i.e., the peaks in the region of 2820−2946 cm^{-1} attributed to the C−H stretching vibration. Besides, the similarity of the Gln and Gln-NC FTIR spectra and in particular the peaks at around 1538 and 1650 cm^{-1} ascribed to N−C = O and NH_2 stretching from the Gln molecule confirmed the presence of this amino acid on the surface of ceria NCs after the ligand exchange process.

Amino acid-functionalized NCs were highly stable in solution, but they could be destabilized through the addition of a base. We triggered the gelation of MFA solutions of ceria NCs by the addition of PO. Gelation became visually evident 4 h after the addition of the epoxide, and it evolved for the following 20 h. Twenty-four hours after the addition of PO, the solvent was exchanged several times to eliminate residual reaction products, and it was finally replaced by acetone. Then, the gel was loaded into a SCD chamber where acetone was replaced by liquid CO_2. Finally, the gel was dried from supercritical CO_2 to obtain a self-standing monolithic aerogel (see details in the Experimental Section and Figures 2 and S1).

DOI: 10.1021/acsami.8b03754
ACS Appl. Mater. Interfaces XXXX, XXX, XXX−XXX

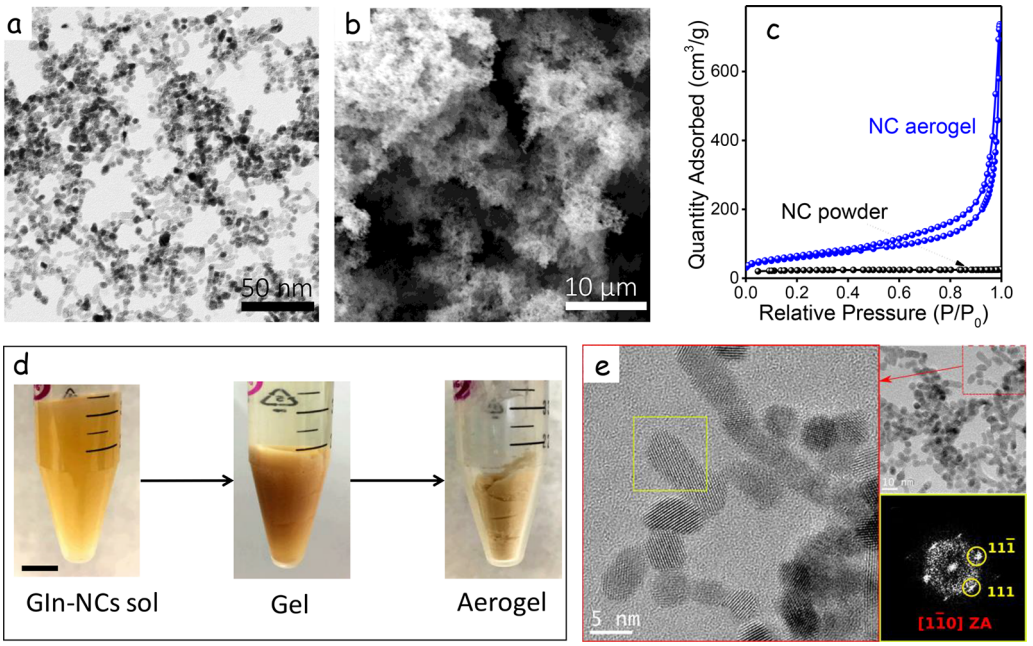

Figure 2. (a) TEM micrograph of the NC-based ceria gel obtained by the cross-linking of ceria NCs triggered by the addition of PO. (b) SEM micrograph of the NC-based ceria aerogel obtained from drying the gel from supercritical CO_2. (c) Adsorption−desorption isotherm obtained from a NC-based ceria aerogel and from a NC powder obtained by precipitation of the colloidal NCs using an antisolvent and posterior centrifugation. Both materials were annealed at 400 °C for 2 h. (d) Optical photographs of the colloidal ceria NCs, the gel, and the aerogel. (e) HRTEM micrograph of a NC-based CeO_2 aerogel including a zoomed micrograph of the highlighted area in red and the FFT of the highlighted area in yellow.

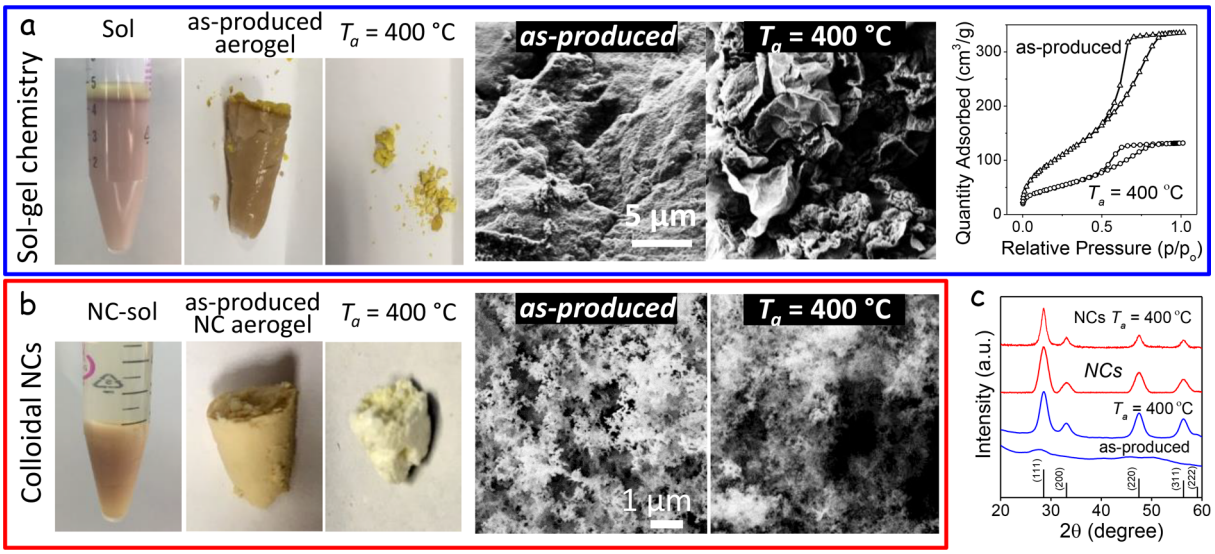

Figure 3. (a) Gel and aerogel produced following a sol−gel chemistry approach:[8] Optical photographs of the sol, the as-produced aerogel and the aerogel annealed at 400 °C; SEM micrographs of the as-produced aerogel and the aerogel annealed at 400 °C; and adsorption−desorption isotherms of the as-produced aerogel and the aerogel annealed at 400 °C. (b) Gel and aerogel produced from the cross-linking of colloidal NCs: Optical photographs of the sol, the as-produced aerogel and the aerogel annealed at 400 °C; and SEM micrographs of the as-produced aerogel and the aerogel annealed at 400 °C. (c) XRD patterns of (from bottom to top) the ceria aerogel produced following a sol−gel chemistry approach, as-produced and after annealing at 400 °C; the ceria NCs and the ceria NC-based aerogel annealed at 400 °C.

Upon the supercritical drying process, the gel lost ca. 20% of its volume (Figures 2d and S1).

TEM and SEM micrographs (Figure 2a and b, respectively) displayed the ceria aerogels to have highly porous structures made of randomly interconnected ceria NCs. HRTEM analysis revealed that most ceria NCs were interconnected with no crystallographic alignment (Figure 2e).

Figure 2c shows an adsorption−desorption isotherm obtained from a NC-based ceria aerogel annealed at 400 °C for 2 h. A specific surface area of 200 ± 20 m^2/g was calculated using the BET method. This value was over 3-fold larger than that measured from the same ceria NCs directly precipitated in the form of a nanopowder through the use of an antisolvent and centrifugation: 63 m^2/g.[35] NC-based ceria aerogels displayed a type IV adsorption−desorption isotherm with a hysteresis associated with capillary condensation (Figure 2c). Barrett−Joynes−Halenda (BJH) plots of the pore-size distribution of the aerogel sample revealed broad pore-size

DOI: 10.1021/acsami.8b03754
ACS Appl. Mater. Interfaces XXXX, XXX, XXX−XXX

distributions, consistent with the porous but random nature of the aerogel (Figure S2).

XRD analysis demonstrated that, unlike aerogels conventionally produced from sol−gel chemistry methods, as-prepared NC-based aerogels were highly crystalline, retaining the crystallinity of the precursor NCs (Figure 3). XRD patterns displayed the reflections of the CeO_2 fluorite structure (space group = *Fm*3*m*, JCPDS card no. 34-0394) with lattice parameter a = 0.5412 nm.

To further compare the two methodologies, we produced ceria aerogels from the gelation of a ceria chloride solution, also using PO as gelator promoter, as described by C. Laberty-Robert et al.[8] Figure 3a displays optical photographs and SEM micrographs of the aerogel produced by this strategy before and after annealing at 400 °C. Using this approach, the BET specific surface areas of the as-produced aerogel were larger, up to 380 m^2/g, than that of the NC-based aerogel. However, this initial ceria aerogel was mostly amorphous, and a thermal treatment at 400 °C was required to crystallize it (Figure 3c). During this thermal annealing process, notable shrinkage of the aerogel took place, and the monolithic structure was lost (Figure 3a). Additionally, the specific surface area obtained decreased down to 180 m^2/g, below that obtained from the initial NC-based aerogel already displaying a proper crystallinity (Figure 3b). Additionally, NC-based aerogels did not collapse during the thermal treatment at 400 °C, and their structure was mostly maintained.

Introducing PO into a Gln-NC sol resulted in a slow cross-linking of the NCs into a disordered network, i.e., a gel. We hypothesize that the NC cross-linking was triggered by a gradual stripping of Gln from the NC surface through interaction with PO. PO interacted with the acid group bond at the cerium sites, resulting in an opening of the PO ring and the stripping of the amino acid.[37] A scheme of the proposed gelation mechanism is shown in Figure 4.

FTIR spectra of the gel supernatant showed the presence of peaks at around 1538 and 1650 cm^{-1} ascribed to N−C═O and NH_2 stretching confirming stripping of Gln during the gelation process. FTIR spectra of the aerogel also displayed that part of the Gln remained on the NC surface as required to prevent the full collapse of the structure in solution. Additionally, TGA analysis confirmed the amount of organics in the final aerogel to be ca. 25% lower than that in the precursor Gln-NCs, confirming partial ligand removal.

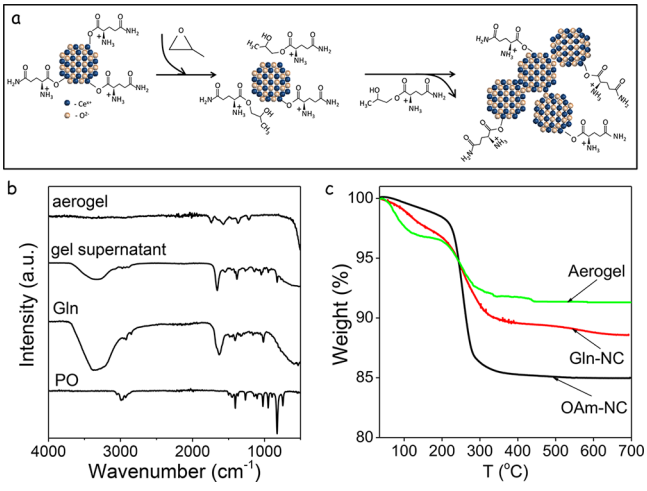

Figure 4. (a) Schematic representation of the gelation of the Gln-NC solution triggered by the introduction of PO. (b) FTIR spectra of PO, Gln, the gel supernatant, and the aerogel. (c) TGA profiles of the OAm-NCs, Gln-NCs, and the Gln-NC-based aerogel.

PO, a soft base, triggers a slow cross-linking of the NCs, which favors the formation of a voluminous gel. On the contrary, when a strong base such as TMAOH was added, a rapid aggregation of the NCs occurred with no gel formation (Figure 5a and Figure S6). Actually, the amount of epoxide

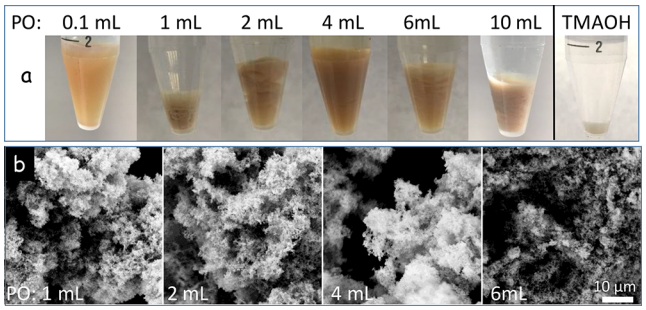

Figure 5. (a) Optical photographs of the ceria NC-based gels obtained 24 h after the introduction of different amounts of PO: 0.1 mL (no gel formed), 1 mL, 2 mL, 4 mL, 6 mL, 8 mL, and 10 mL or 500 μL of TMAOH (no gel formed, fast NC aggregation into powder), as indicated on top of each photograph. (b) SEM images of the aerogels produced from the gels obtained from 1 mL, 2 mL, 4 mL, and 6 mL of PO.

controlled the ligand stripping rate and thus the rate of NC cross-linking, which translated in gels with different voluminosity (Figure 5). In this regard, an excessive amount of PO led to higher NC aggregation and gel shrinkage, while insufficient amounts were not able to cross-link all the particles, resulting in no or partial gelation (Figure 5a).

The use of molecules with multiple epoxy groups had a similar effect as PO. As an example, the addition of NGDE, with 2 epoxy groups instead of PO, also triggered NC gelation but with a lower voluminosity when added in the same amount as PO. Injection of 11 mL (0.057 mol) of NGDE, the molar equivalent to 4 mL of PO, resulted in gels with dense aggregates of NCs, which we associate with the double number of epoxy groups introduced (Figure 6a). When reducing the amount of NGDE by half, thus introducing the same amount of epoxy groups, less dense aerogels, similar to those produced with PO, were obtained (Figure 6b).

While the addition of H_2O to the MFA resulted in gels with higher voluminosity, the presence of H_2O was not essential for NC gelation to occur. Attempts using MFA as the only solvent also led to NC gelation, but the obtained gels were significantly less voluminous (Figure S3). When replacing MFA + H_2O with alcohols as the only solvent for NC gelation, no gel was formed. Upon PO addition to an alcohol solution of NCs, all NCs precipitated. Nevertheless, the addition of small amounts of water to the alcohol also allowed NC gelation, although with a moderate voluminosity compared with that of MFA + H_2O (Figure S3). Note that the poor miscibility of PO with H_2O barred the use of H_2O as the only solvent for NC gelation. Attempts to gelate NCs in the two-phase mixture created from the addition of PO to a NC solution in water resulted in NC precipitation.

The same methodology allowed the formation of NC-based ceria gels using ceria NCs functionalized with other amino

DOI: 10.1021/acsami.8b03754
ACS Appl. Mater. Interfaces XXXX, XXX, XXX−XXX

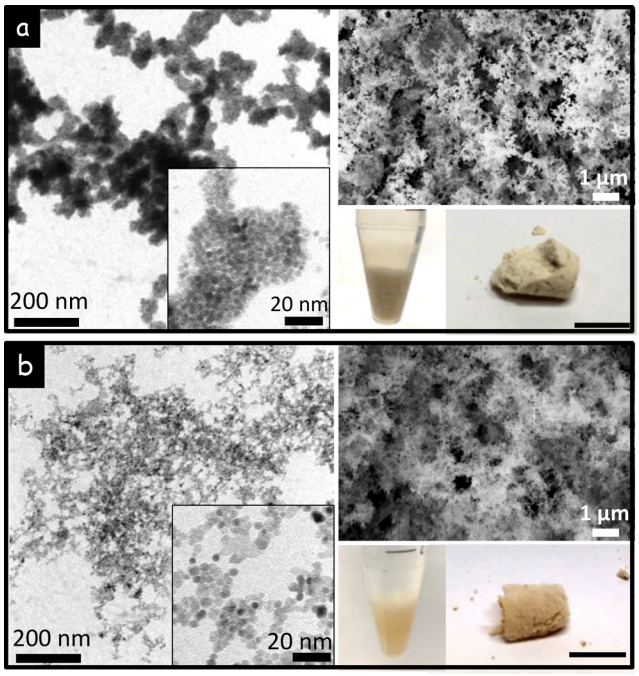

Figure 6. (a) TEM, SEM, and optical photographs of the ceria NC-based gel and aerogel formed from the addition of 10 mL of NGDE. (b) TEM, SEM, and optical photographs of the ceria NC-based gel and aerogel formed from the addition of 5 mL of NGDE. Scale-bars in the optical photographs of the aerogels correspond to 1 cm.

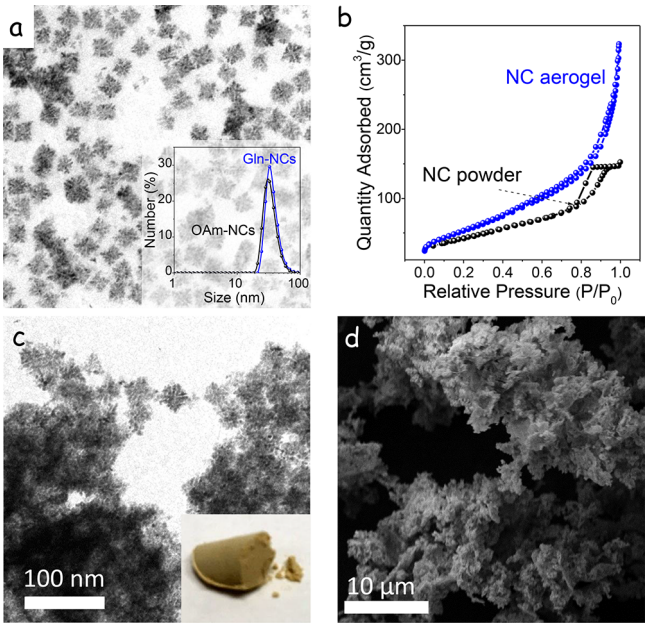

Figure 7. (a) TEM micrograph of hyperbranched ceria NCs. The inset displays DLS curves of hyperbranched OAm-NCs and Gln-NCs. (b) Adsorption−desorption isotherm obtained from a hyperbranched NC-based ceria aerogel and from a NC powder obtained by precipitation of the colloidal NCs using an antisolvent and posterior centrifugation. Both materials were annealed at 400 °C for 2 h. (c) TEM micrograph of the hyperbranched NC-based aerogel and optical photograph of the monolith aerogel (inset). (d) SEM micrograph of the hyperbranched NC-based aerogel.

acids, such as Glu and DA (Figures S4 and S5). However, the gels produced from Glu-NCs and DA-NCs were slightly less voluminous than those produced from Gln-NCs (Figure S5). We hypothesize the different gel voluminosity to be related to variations in the ligand displacement kinetics that would be in part associated with the fact that DA and Glu have just one amino group while Gln has two. Identical amounts of PO may result in a faster ligand displacement in DA- and Glu-NCs than in Gln-NCs and thus in less voluminous gels.

The gelation approach here proposed was also used to produce NC-based ceria aerogels employing NCs with other sizes and geometries, and particularly hyperbranched ceria NCs (Figure 7).[35] Hyperbranched ceria NCs were characterized by an intrinsic porous structure that provides them with specific surface areas up to 157 m^2/g.[35] As for spherical ceria NCs, the surface of ceria hyperbranched NCs was in a first step functionalized with Gln to render the NCs soluble in polar solvents. In a second step, PO was added to trigger gelation. The gel obtained after 24 h from the injection of PO was dried from supercritical CO_2. Figure 7 displays representative TEM and SEM micrographs of the aerogels produced following this procedure. N_2 adsorption/desorption isotherm curves of hyperbranched NCs aerogels displayed a type IV character with a H1 hysteresis loop that evidenced mesoporosity (Figure 7c). BET calculations demonstrated large specific surface areas of 200 m^2/g, similar to those measured from aerogels produced from quasi-spherical NCs and above those of the precipitated hyperbranched NCs.

The general approach to produce metal oxide aerogels detailed here was demonstrated for a second oxide besides ceria. As a second example, we targeted the production of NC-based aerogels of titanium dioxide, a key industrial nanomaterial in a range of applications. For this purpose, we produced TiO_2 NCs with controlled geometry and facets. In particular, for the present work, we produced anatase TiO_2 nanoplates with ample {001} facets following the procedure by Gordon et al. (Figure 8).[36] Using the same procedure as that for ceria NCs, we replaced the native organic ligands from the TiO_2 NC surface by Gln. Subsequently, the addition of PO to a solution containing TiO_2 Gln-NCs resulted in their random aggregation into a network, i.e., its gelation (Figure 8). TiO_2 NCs gelation occurred slightly faster than that for CeO_2, and it was completed after 60 min of reaction. Supercritical drying of the NC-based TiO_2 gels resulted in blue colored monolithic aerogels (Figure 8d). The blue color, characteristic of the initial TiO_2 NCs, evidenced the presence of a high concentration of oxygen vacancies and the overall nonstoichiometric composition of the TiO_2 NCs obtained from the used colloidal synthesis protocol.[36]

Despite the fact that plate-like NCs were prone to stick together to form compact aggregates, SEM imaging evidenced NC-based TiO_2 aerogels to be characterized by highly porous structures. NC-based TiO_2 aerogels displayed type IV adsorption/desorption isotherms (Figure 8b) and BET specific surface area up to 70 m^2/g.

CONCLUSIONS

A novel strategy to produce crystalline oxide aerogels was detailed. The described approach was based on the cross-linking of colloidal NCs by the addition of an epoxide to the colloidal NC dispersion. We hypothesize the epoxide gradually displaced amino acid ligands from the NC surface, thus triggering their slow cross-linking into randomly interconnected networks, i.e., their gelation. NC-based ceria aerogels displayed both high surface areas and highly crystalline structures that were associated with the high crystallinity of the precursor NC

DOI: 10.1021/acsami.8b03754
ACS Appl. Mater. Interfaces XXXX, XXX, XXX−XXX

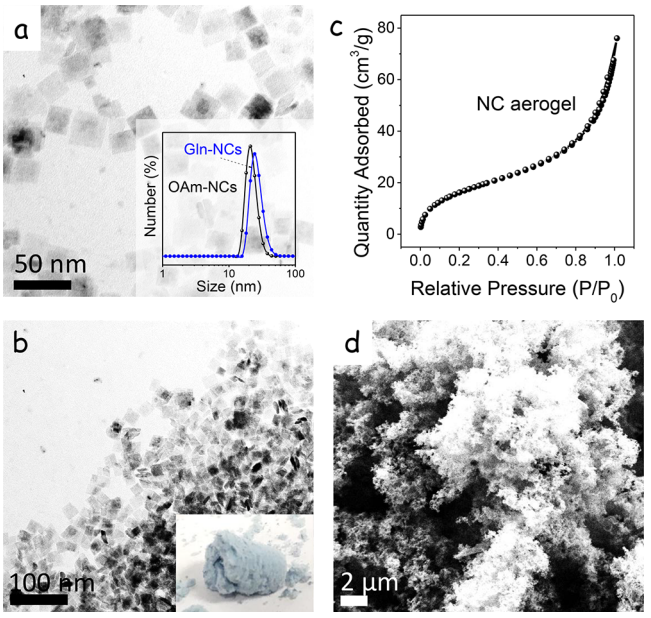

Figure 8. (a) TEM micrograph of TiO_2 NCs. The inset shows the DLS curves of TiO_2 OAm-NCs and Gln-NCs. (b) Adsorption–desorption isotherms obtained from a NC-based TiO_2 aerogel. The material was measured after annealing at 400 °C for 2 h. (c) TEM micrograph of the NC-based TiO_2 aerogel and optical photograph of the monolith aerogel (inset). (d) SEM micrograph of the NC-based TiO_2 aerogel.

building blocks. Additionally, the versatility of the proposed strategy was proved by using the same procedure to produce NC-based titanium dioxide aerogels using NC building blocks with controlled geometry and facets.

■ ASSOCIATED CONTENT

Supporting Information

The Supporting Information is available free of charge on the ACS Publications website at DOI: 10.1021/acsami.8b03754.

Optical photographs of the gelation process; pore size distribution of the NC-based aerogel; study of the solvent influence on the gelation process; study of the influence of different amino acids on the gelation process; study of the NC precipitate after the addition of a strong base (PDF)

■ AUTHOR INFORMATION

Corresponding Author

*E-mail: acabot@irec.cat.

ORCID

Taisiia Berestok: 0000-0002-3066-9691
Javier Blanco Portals: 0000-0002-7037-269X
Massimo Colombo: 0000-0002-0817-0229
Stephanie L. Brock: 0000-0002-0439-302X
Andreu Cabot: 0000-0002-7533-3251

Notes

The authors declare no competing financial interest.

■ ACKNOWLEDGMENTS

This work was supported by the European Regional Development Funds and the Spanish MINECO project SEHTOP (ENE2016-77798-C4-3-R) and TEMPTATION (MAT2016-79455-P). T.B. thanks FI-AGAUR Research Fellowship Program, Generalitat de Catalunya (2015 FI_B 00744). P.G. acknowledges the People Programme (Marie Curie Actions) of the FP7/2007-2013 European Union Program (TECNIOspring grant agreement no. 600388) and the Agency for Business Competitiveness of the Government of Catalonia, ACCIÓ. S.B. acknowledges the U.S. National Science Foundation, CHE-1361741.

■ ABBREVIATIONS

NC, nanocrystal
OAm, oleylamine
ODE, 1-octadecene
TMOH, tetramethylammonium hydroxide pentahydrate
MFA, *n*-methylformamide
TFA, trifluoroacetic acid
NGDE, neopentyl glycol diglycidyl ether
Gln, L-glutamine
PO, propylene oxide
DA, dopamine hydrochloride
Glu, glutamic acid
TEM, transmission electron microscopy
HRTEM, high-resolution TEM
SEM, scanning electron microscopy
UV–vis, ultraviolet–visible spectroscopy;
XRD, X-ray power diffraction
DLS, dynamic light scattering
FTIR, Fourier-transform infrared spectroscopy
TGA, thermogravimetric analysis
BET, Brunauer–Emmet–Teller method
OAm-NC, OAm-capped NCs
Gln-NC, Gln-capped NCs

■ REFERENCES

(1) Zhang, J.; Li, C. M. Nanoporous metals: fabrication strategies and advanced electrochemical applications in catalysis, sensing and energy systems. *Chem. Soc. Rev.* **2012**, *41* (21), 7016–7031.
(2) Rolison, D. R. Catalytic Nanoarchitectures–the Importance of Nothing and the Unimportance of Periodicity. *Science* **2003**, *299* (5613), 1698–1701.
(3) Brinker, C. J.; Scherer, G. W. Hydrolysis and Condensation I: Nonsilicates. In *Sol-Gel Science*; Academic Press: San Diego, CA, 1990; pp 20–95.
(4) Gash, A. E.; Tillotson, T. M.; Satcher, J. H., Jr.; Hrubesh, L. W.; Simpson, R. L. New sol–gel synthetic route to transition and main-group metal oxide aerogels using inorganic salt precursors. *J. Non-Cryst. Solids* **2001**, *285* (1), 22–28.
(5) Ziegler, C.; Wolf, A.; Liu, W.; Herrmann, A.-K.; Gaponik, N.; Eychmüller, A. Modern Inorganic Aerogels. *Angew. Chem., Int. Ed.* **2017**, *56* (43), 13200–13221.
(6) Katti, A.; Shimpi, N.; Roy, S.; Lu, H.; Fabrizio, E. F.; Dass, A.; Capadona, L. A.; Leventis, N. Chemical, Physical, and Mechanical Characterization of Isocyanate Cross-linked Amine-Modified Silica Aerogels. *Chem. Mater.* **2006**, *18* (2), 285–296.
(7) Gash, A. E.; Tillotson, T. M.; Satcher, J. H.; Poco, J. F.; Hrubesh, L. W.; Simpson, R. L. Use of Epoxides in the Sol–Gel Synthesis of Porous Iron(III) Oxide Monoliths from Fe(III) Salts. *Chem. Mater.* **2001**, *13* (3), 999–1007.
(8) Laberty-Robert, C.; Long, J. W.; Lucas, E. M.; Pettigrew, K. A.; Stroud, R. M.; Doescher, M. S.; Rolison, D. R. Sol–Gel-Derived Ceria Nanoarchitectures: Synthesis, Characterization, and Electrical Properties. *Chem. Mater.* **2006**, *18* (1), 50–58.
(9) Rechberger, F.; Niederberger, M. Synthesis of aerogels: from molecular routes to 3-dimensional nanoparticle assembly. *Nanoscale Horizons* **2017**, *2* (1), 6–30.

DOI: 10.1021/acsami.8b03754
ACS Appl. Mater. Interfaces XXXX, XXX, XXX–XXX

(10) Rechberger, F.; Niederberger, M. Translucent nanoparticle-based aerogel monoliths as 3-dimensional photocatalysts for the selective photoreduction of CO_2 to methanol in a continuous flow reactor. *Mater. Horiz.* **2017**, *4* (6), 1115−1121.
(11) Heiligtag, F. J.; Rossell, M. D.; Suess, M. J.; Niederberger, M. Template-free co-assembly of preformed Au and TiO_2 nanoparticles into multicomponent 3D aerogels. *J. Mater. Chem.* **2011**, *21* (42), 16893−16899.
(12) Heiligtag, F. J.; Kränzlin, N.; Süess, M. J.; Niederberger, M. Anatase−silica composite aerogels: a nanoparticle-based approach. *J. Sol-Gel Sci. Technol.* **2014**, *70* (2), 300−306.
(13) Kovalenko, M. V.; Manna, L.; Cabot, A.; Hens, Z.; Talapin, D. V.; Kagan, C. R.; Klimov, V. I.; Rogach, A. L.; Reiss, P.; Milliron, D. J.; Guyot-Sionnnest, P.; Konstantatos, G.; Parak, W. J.; Hyeon, T.; Korgel, B. A.; Murray, C. B.; Heiss, W. Prospects of Nanoscience with Nanocrystals. *ACS Nano* **2015**, *9* (2), 1012−1057.
(14) Coughlan, C.; Ibáñez, M.; Dobrozhan, O.; Singh, A.; Cabot, A.; Ryan, K. M. Compound Copper Chalcogenide Nanocrystals. *Chem. Rev.* **2017**, *117* (9), 5865−6109.
(15) Sapsford, K. E.; Algar, W. R.; Berti, L.; Gemmill, K. B.; Casey, B. J.; Oh, E.; Stewart, M. H.; Medintz, I. L. Functionalizing Nanoparticles with Biological Molecules: Developing Chemistries that Facilitate Nanotechnology. *Chem. Rev.* **2013**, *113* (3), 1904−2074.
(16) Zhang, C. Carbon dioxide capture: Multiple site absorption. *Nat. Energy* **2016**, *1*, 16084.
(17) Ciftja, A. F.; Hartono, A.; Svendsen, H. F. Selection of Amine Amino Acids Salt Systems for CO_2 Capture. *Energy Procedia* **2013**, *37*, 1597−1604.
(18) Sanz, R.; Calleja, G.; Arencibia, A.; Sanz-Pérez, E. S. CO_2 capture with pore-expanded MCM-41 silica modified with amino groups by double functionalization. *Microporous Mesoporous Mater.* **2015**, *209*, 165−171.
(19) De Roo, J.; Coucke, S.; Rijckaert, H.; De Keukeleere, K.; Sinnaeve, D.; Hens, Z.; Martins, J. C.; Van Driessche, I. Amino Acid-Based Stabilization of Oxide Nanocrystals in Polar Media: From Insight in Ligand Exchange to Solution 1H NMR Probing of Short-Chained Adsorbates. *Langmuir* **2016**, *32* (8), 1962−1970.
(20) Sousa, M. H.; Rubim, J. C.; Sobrinho, P. G.; Tourinho, F. A. Biocompatible magnetic fluid precursors based on aspartic and glutamic acid modified maghemite nanostructures. *J. Magn. Magn. Mater.* **2001**, *225* (1), 67−72.
(21) Shultz, M. D.; Reveles, J. U.; Khanna, S. N.; Carpenter, E. E. Reactive Nature of Dopamine as a Surface Functionalization Agent in Iron Oxide Nanoparticles. *J. Am. Chem. Soc.* **2007**, *129* (9), 2482−2487.
(22) Stamplecoskie, K. G.; Kamat, P. V. Size-Dependent Excited State Behavior of Glutathione-Capped Gold Clusters and Their Light-Harvesting Capacity. *J. Am. Chem. Soc.* **2014**, *136* (31), 11093−11099.
(23) Alessandro, T. Catalysis by Ceria and Related Materials; World Scientific: Singapore, 2002; Vol. *2*.
(24) Bell, A. T. The Impact of Nanoscience on Heterogeneous Catalysis. *Science* **2003**, *299* (5613), 1688−1691.
(25) Xu, H.; Wang, A.-L.; Tong, Y.-X.; Li, G.-R. Enhanced catalytic activity and stability of Pt/CeO_2/PANI hybrid hollow nanorod arrays for methanol electro-oxidation. *ACS Catal.* **2016**, *6* (8), 5198−5206.
(26) Zhou, H.-P.; Wu, H.-S.; Shen, J.; Yin, A.-X.; Sun, L.-D.; Yan, C.-H. Thermally Stable Pt/CeO2 Hetero-Nanocomposites with High Catalytic Activity. *J. Am. Chem. Soc.* **2010**, *132* (14), 4998−4999.
(27) Wang, D.; Kang, Y.; Doan-Nguyen, V.; Chen, J.; Küngas, R.; Wieder, N. L.; Bakhmutsky, K.; Gorte, R. J.; Murray, C. B. Synthesis and Oxygen Storage Capacity of Two-Dimensional Ceria Nanocrystals. *Angew. Chem., Int. Ed.* **2011**, *50* (19), 4378−4381.
(28) Zhou, L.; Li, X.; Yao, Z.; Chen, Z.; Hong, M.; Zhu, R.; Liang, Y.; Zhao, J. Transition-Metal Doped Ceria Microspheres with Nanoporous Structures for CO Oxidation. *Sci. Rep.* **2016**, *6*, 23900.
(29) Kharton, V. V.; Figueiredo, F. M.; Navarro, L.; Naumovich, E. N.; Kovalevsky, A. V.; Yaremchenko, A. A.; Viskup, A. P.; Carneiro, A.; Marques, F. M. B.; Frade, J. R. Ceria-based materials for solid oxide fuel cells. *J. Mater. Sci.* **2001**, *36* (5), 1105−1117.
(30) Liao, L.; Mai, H. X.; Yuan, Q.; Lu, H. B.; Li, J. C.; Liu, C.; Yan, C. H.; Shen, Z. X.; Yu, T. Single CeO_2 Nanowire Gas Sensor Supported with Pt Nanocrystals: Gas Sensitivity, Surface Bond States, and Chemical Mechanism. *J. Phys. Chem. C* **2008**, *112* (24), 9061−9065.
(31) Channei, D.; Inceesungvorn, B.; Wetchakun, N.; Ukritnukun, S.; Nattestad, A.; Chen, J.; Phanichphant, S. Photocatalytic degradation of methyl orange by CeO_2 and Fe−doped CeO_2 films under visible light irradiation. *Sci. Rep.* **2015**, *4*, 5757.
(32) Kwon, H. J.; Cha, M.-Y.; Kim, D.; Kim, D. K.; Soh, M.; Shin, K.; Hyeon, T.; Mook-Jung, I. Mitochondria-Targeting Ceria Nanoparticles as Antioxidants for Alzheimer's Disease. *ACS Nano* **2016**, *10* (2), 2860−2870.
(33) Fujishima, A.; Rao, T. N.; Tryk, D. A. Titanium dioxide photocatalysis. *J. Photochem. Photobiol., C* **2000**, *1* (1), 1−21.
(34) Zhao, Z.; Tian, J.; Sang, Y.; Cabot, A.; Liu, H. Structure, synthesis, and applications of TiO_2 nanobelts. *Adv. Mater.* **2015**, *27* (16), 2557−2582.
(35) Berestok, T.; Guardia, P.; Blanco, J.; Nafria, R.; Torruella, P.; López-Conesa, L.; Estradé, S.; Ibáñez, M.; de Roo, J.; Luo, Z.; Cadavid, D.; Martins, J. C.; Kovalenko, M. V.; Peiró, F.; Cabot, A. Tuning Branching in Ceria Nanocrystals. *Chem. Mater.* **2017**, *29* (10), 4418−4424.
(36) Gordon, T. R.; Cargnello, M.; Paik, T.; Mangolini, F.; Weber, R. T.; Fornasiero, P.; Murray, C. B. Nonaqueous Synthesis of TiO_2 Nanocrystals Using TiF_4 to Engineer Morphology, Oxygen Vacancy Concentration, and Photocatalytic Activity. *J. Am. Chem. Soc.* **2012**, *134* (15), 6751−6761.
(37) Kakiuchi, H.; Iijima, T. The ring-opening reactions of propylene oxide with chloroacetic acids. *Tetrahedron* **1980**, *36* (8), 1011−1016.

DOI: 10.1021/acsami.8b03754
ACS Appl. Mater. Interfaces XXXX, XXX, XXX−XXX

Surface chemistry and nano/microstructure engineering on photocatalytic In_2S_3 nanocrystals

Taisiia Berestok,[†,‡] *Pablo Guardia,*[†] *Javier Blanco Portals,*[‡] *Sònia Estradé,*[‡] *Jordi Llorca,*[⊥] *Francesca Peiró,*[‡] *Andreu Cabot*[†,ǁ,*] *Stephanie L. Brock,*[§,*]

[†]Catalonia Institute for Energy Research – IREC, 08930 Sant Adrià de Besòs, Barcelona, Spain

[‡] LENS-MIND, Departament d'Enginyeries i Electrònica i Institut de Nanociència i Nanotecnologia (In2UB), Universitat de Barcelona, 08028, Barcelona, Spain

[⊥] Institute of Energy Technologies, Department of Chemical Engineering and Barcelona Research Center in Multiscale Science and Engineering, Universitat Politècnica de Catalunya, EEBE, 08019 Barcelona, Spain

[ǁ] ICREA, Pg. Lluís Companys 23, 08010 Barcelona, Spain

[§] Department of Chemistry, Wayne State University, Detroit, Michigan 48202, United States

KEYWORDS. Aerogel, gel, In_2S_3, dye degradation, photocatalysis, colloid, nanocrystal, nanomaterial.

ABSTRACT: Colloidal nanocrystals (NCs) compete with molecular catalysts in the field of homogenous catalysis, offering an easier recyclability and a number of potentially advantageous functionalities, such as tunable band gaps, plasmonic properties or a magnetic moment. Using

high throughput printing technologies, colloidal NCs can be also supported onto substrates to produce cost-effective electronic, optoelectronic, electrocatalytic and sensing devices. For both catalytic and technological application, NCs surface chemistry and supracrystal organization are key parameters determining final performance. Here, we study the influence of the surface ligands and the NC organization on the catalytic properties of In_2S_3, both in colloidal form and as a supported layer. In colloidal form, NCs stabilized in solution by inorganic ligands show the highest photocatalytic activities, which we associate with their large and more accessible surfaces. On the other hand, when NCs are supported on a substrate, their organization becomes an essential parameter determining performance. For instance, NC-based films produced through a gelation process provided five-fold higher photocurrent densities than those obtained from dense films produced by the direct printing of NCs.

INTRODUCTION

Semiconductor nanocrystals (NCs) combine huge surface areas with a solid state platform for charge carrier photogeneration and transport.[1] This combination of properties makes them particularly appealing for applications involving interaction with the surrounding media, such as catalysis,[2,3,4] environmental remediation,[5,6] and sensing.[7] Colloidal NCs are especially suited for quasi-homogenous catalysis because relative to molecular catalysts they offer easier recyclability and added functionalities such as a magnetic moment for remote location or recovery, tunable band gaps for photocatalysis, and modulability to produce multisite systems by combining multiple co-catalysts.[8,9] However, the ability of colloidal NCs to interact with the surrounding media is controlled by their surface chemistry, which also determines several other fundamental properties, including colloidal and chemical stabilities and charge carrier and surface trap

densities.[10] To find surface chemistries that simultaneously optimize all these parameters is extremely challenging and at the same time critical to exploit their full potential.

Colloidal NCs can be also assembled or supported within macroscopic structures and devices as required in electrocatalysis or sensing, for instance.[11-13] Beyond their huge surface area, solution processability, associated with high throughput and cost-effectiveness, is the main advantage of colloidal NCs in technological applications, especially when compared with thin films produced by vacuum-based technologies. When supported, a proper NC organization becomes essential to maintain their inherent large surface areas, while ensuring at the same time proper electrical conductivities for effective charge injection/extraction.[14-15] To face this key challenge, a plethora of approaches to engineer NC solids with controlled NC arrangement have been developed. A highly used approach involves slow NC assembly driven by an oversaturation of the NC concentration during solvent removal.[16,17] While yielding in some cases astonishing NC assemblies, this strategy does not generally provide materials with large surface areas and is strongly limited in terms of reproducibility, production throughput and scale up potential. To produce highly porous structures in a cost-effective manner, faster assembly strategies, based on destabilizing the NC dispersion in solution, are more suitable. This destabilization can be induced by externally triggering the ligand desorption or stimulating its binding.[11,18] The ultimate goal is to produce an interconnected NC network, i.e. a gel, with a proper surface chemistry to interact with the media.[19] In this direction, an effective approach to produce highly porous NC superstructures with good transport properties is the oxidative removal of thiolate ligands to link chalcogenide NCs through chalcogen-chalcogen bonds.[20] Following this approach, gels of different metal chalcogenides have been produced.[21-23]

In_2S_3 is an n-type semiconductor (2.6 eV band gap) with large exciton Bohr radius of 33.8 nm[24] used in lithium-ion batteries,[25] in light emission devices,[26] as photodetector,[27] for solar energy conversion through photocatalysis,[28-30] and particularly as a host material for two-photon absorption processes through an intermediate band.[31-32] While its chemical stability, low defect density, simple synthesis, and proper band gap makes it an excellent candidate for photocatalytic applications, this material is yet underexplored in this area. A number of synthetic procedures to produce In_2S_3 NCs with different morphologies have been reported.[27,30,33,34] Ultrathin In_2S_3 nanobelts showed promise for phosphorous displays due to the blue emission in photoluminescence spectra.[27] Doping of In_2S_3 by Mn or Cu demonstrated tunable dual color emission at blue and orange depending on the excitation wavelength.[35] Moreover, depending on the morphology of the NCs and facets enclosed, In_2S_3 can serve as an efficient catalysts for dye degradation under either UV, visible or NIR light irradiation.[36] Several previous works have detailed the photocatalytic degradation of methylene blue,[30] methylene orange[28] and rhodamine B[37] over In_2S_3 NCs. Furthermore, several works have demonstrated an improvement of photocatalytic performance in In_2S_3-based composites. In_2O_3/In_2S_3/Ag nanoheterostructures have demonstrated improved activity toward photoelectrochemical water splitting.[29] However, to the best of our knowledge, the study on the influence of the In_2S_3 NC surface chemistry and supracrystal organization has not been shown.

In this work, we evaluate the photocatalytic activity of colloidal In_2S_3 NCs both in solution and when supported. We analyze the effect of different surface chemistries and NC organizations to determine the conditions resulting in best performances for quasi-homogeneous catalysis and photoelectrocatalysis.

EXPERIMENTAL DETAILS

Materials. Indium trichloride ($InCl_3$, 98%), oleylamine (OAm, 70%), oleic acid (OAc, 90%), sulfur powder (99.998 %), 11-mercaptoundecanoic acid (MUA, 95%), tetramethylammonium hydroxide pentahydrate (TMAOH, ≥97%), dodecanethiol (DDT, ≥98%), tert-dodecanethiol (tDDT, 98.5 %), N-methylformamide (MFA, 99 %), phosphotungstic acid hydrate ($H_3[PW_{12}O_{40}]\cdot xH_2O$, PTA, 95 %), trifluoroacetic acid (TFA, 99 %), tetranitromethane (TNM, 95 %), rhodamine B (RhB, 97 %), sodium hydroxide (NaOH, ≥98 %), sodium sulfide (Na_2S), indium sulfide (In_2S_3, 99.99%) and potassium chloride (KCl, ≥99 %) were purchased from Sigma-Aldrich. Titanium dioxide (TiO_2, Degussa, P25) was purchased from Alfa Aesar, NanoTek. Hexane, methanol and acetone were of analytical grade and were purchased from Panreac. Glass substrates coated with indium tin oxide (ITO, ~8 Ω/sq) were acquired from VWR. Milli-Q water (MQ-Water): 18.2 MΩ, filtered with filter pore size 0.22 μM, Millipore. All syntheses were carried out using standard air-free Schlenk-line techniques.

Synthesis of In_2S_3 NCs: Among the several established synthetic protocols to produce In_2S_3 NCs with different shapes and sizes,[23-24,27,29] we followed a slight variation of the procedure reported by K. H. Park et al.,[30] to obtain In_2S_3 NCs with a two-dimensional disk-like morphology. The difference between the synthesis procedure reported by K. H. Park et al. and ours is that we used an injection step instead of a heating up procedure, since the latter led to a broader size-distribution in our hands (Figure S1 b). Briefly, in a 25 mL three-neck flask, 1 mmol of $InCl_3$ and 10 mL of OAm were mixed and degassed (~100 mTorr) for 60 minutes at 80 °C under magnetic stirring. During this time, a clear solution formed. Then, the temperature was raised up to 220 °C (5 °C/min) and a previously degassed (15 minutes) solution containing 1.5 mmol of sulphur powder in 5 mL of OAm was swiftly injected. Upon injection of the sulphur

precursor solution, the color of the solution gradually changed from transparent to orange, indicating the NC formation. After 10 minutes, the reaction was quenched by removing the heating mantle and placing the flask in a water bath. During the cooling step, the color of the solution changed from orange to yellow. NCs were precipitated by adding 30 mL of acetone to the crude solution and centrifuging the mixture at 5700 rpm for 5 min. The supernatant was discarded and the precipitate was redispersed in 5 mL of hexane. A second purification step was performed following the same procedure. Finally, NCs were dispersed in 5 mL of hexane (~ 10 mg/mL solution) and stored for later use.

Surface modification with PTA: The procedure used to replace native organic ligands with PTA was based on previous work by J. Huang et al.[38] Briefly, 1 mL of a 10 mg/mL dispersion of In_2S_3 NCs in hexane was mixed with 1 mL of a MFA solution that contained 20 mL of TFA and 50 mg (0.0173 mmols) of PTA. The formed biphasic solution was shook vigorously for 10 seconds and then stirred for 30-60 minutes. After stirring, the mixture was allowed to separate into the two phases. The migration of NCs from the upper hexane phase to the lower MFA phase indicated the ligand exchange and transfer of particles into a polar solvent. The upper liquid phase was discarded and then 2 mL of a hexane: acetone (1:1) mixture was added to the vial. The solution was then shook and centrifuged at 3000 rpm for 5 min. This step was repeated 3 times for the purpose of removing as much of the residual ligands as possible. Finally, the precipitated NCs were redispersed in MQ-Water for dye degradation measurements and in methanol for film preparation.

Surface modification with $InCl_3$: The procedure used to replace native organic ligands with an In-Cl complex was based on previous work by V. Sayevich et al.[39] Basically, the same steps followed above to modify the In_2S_3 NCs surface with PTA were used to modify them with $InCl_3$,

with two small differences: i) the 1 mL MFA solution contained 30 mg of $InCl_3$ (0.135 mmols); ii) to facilitate the phase transfer / ligand exchange, instead of TFA, 1 mL of acetone was additionally introduced in the initial biphasic solution before shaking. Finally, NCs were redispersed in MQ-Water or in methanol depending on whether they were to be used for dye degradation measurements or film preparation, respectively.

Surface modification with MUA: The procedure used to replace native organic ligands with MUA was based on a previous work by S. F Wuister et al.[40] Briefly, 5 mL of a 20 mg/mL dispersion of In_2S_3 NCs were mixed with 5 mL of a MUA solution (2 mM in methanol). The resulting biphasic solution was stirred under inert atmosphere for 30 min. During this time, NCs moved from the upper hexane phase to the bottom methanol phase. The upper part was removed and NCs were precipitated by addition of 30 mL of acetone and centrifuging at 4000 rpm for 5 min. The obtained precipitate was redispersed in methanol and precipitated one more time with acetone. NCs were finally dispersed in MQ-Water or methanol. It should be noted that repeating the washing procedure several more times led to NCs aggregation, but addition of few mL of the MUA solution (2 mM in methanol) permitted redispersion NCs back in solution.

Direct NC deposition: 1 mL of the hexane or methanol solution containing In_2S_3 NCs (20 mg/mL) with the selected surface ligand (OAm, PTA, $InCl_3$, MUA) was spin-coated on previously washed ITO substrates at a rotation speed of 2000 rpm for 20 seconds. The obtained films were annealed at 250 °C for 60 min under argon flow.

NC deposition through xerogel formation: 1 mL of MUA-caped In_2S_3 NCs (20 mg/mL) in methanol was spin-coated on ITO substrates at a rotation speed of 2000 rpm for 20 seconds. Immediately after preparation, the film was dipped in a TNM solution (50 µL of 3% TNM in 5

mL of acetone) for 1 min. Subsequently, the film was rinsed with fresh methanol to remove by-products and then annealed at 250 °C for 60 min under argon flow.

Gel and aerogel preparation: The procedure used to produce In_2S_3 NC gels and aerogels was based on our previous work.[19] To produce In_2S_3 NC gels, 50 µL of a TNM solution (3% in acetone) were added into 2 mL of a methanol solution containing MUA-capped In_2S_3 NCs (10 mg/mL). The mixture was shaken vigorously for 30 seconds and then kept undisturbed for the whole gelation process. The gelation process visually evolved during 2 h, but the solution was left undisturbed for two days to ensure its completion. After two days, the solvent mixture (methanol and acetone) was exchanged to pure acetone, removing all the methanol and TNM residues. This process must be carried out with special care in order to not damage the porous network of the gel. At the same time, the solvent cannot be completely removed at any step. Thus, we partially replaced the solvent every 1-2 h for 2 days. While not optimized, relatively long time intervals between solvent replacements were used to ensure complete penetration of the fresh solvent into the porous structure of the gel. After the solvent exchange, the gel immersed in acetone was loaded into a supercritical point dryer chamber and soaked with liquid CO_2 overnight. After 12 h, the chamber was half drained and filled with fresh liquid CO_2. This procedure was repeated at least 6 times in one-hour intervals in order to replace acetone by liquid CO_2. Finally, the chamber was completely filled with liquid CO_2 and heated to 39 °C. Upon heating, the pressure increased up to 75-80 bars, thus surpassing the supercritical point of CO_2. The sample was kept under these conditions for 1 h. Afterward, the pressure was released while keeping the temperature constant.

Dye degradation experiments: The photocatalytic activity of In_2S_3 NCs was evaluated by photodegradation of RhB. RhB was chosen as a conventional example of dye that is both a

potential environmental pollutant and at the same time an easy molecule to optically follow during its catalytic degradation in the laboratory. In a typical experiment, 1 mL of an aqueous RhB solution (100 ppm) was added to 9 mL of an aqueous solution containing In_2S_3 NCs (1.1 mg/mL). Before reaction, the mixture was kept in the dark for 30 min under magnetic stirring. Then, the glass reaction vessel was exposed through its open top to a 300 W xenon lamp for 2 h providing ca. 100 mW/cm^2 irradiance at the sample.

Photoelectrochemical measurements: The photoelectrocatalytic activity of In_2S_3 NCs was evaluated through the photoelectrochemical oxidation of a polysulfide electrolyte:[41]

$S^{2-} + 2h^+ \rightarrow S$

$S + S_{x-1}^{2-} \rightarrow S_x^{2-}$ (x = 2–5)

the oxidized species, S_x^{2-}, is converted back (reduced) to S^{2-} on the counter electrode:

$S_x^{2-} + 2e^- \rightarrow S_{x-1}^{2-} + S^{2-}$

Photocurrent measurements were performed using a three-electrode cell configuration with a Pt-coiled wire having a surface area of 2 cm^2 as a counter electrode and an Ag/AgCl reference electrode filled with 3M KCl solution. A 1M aqueous solution of S, NaOH and Na_2S at pH7 was used as electrolyte. A bias voltage to the working electrode was applied through an electrical contact to the uncoated part of the ITO-glass substrate. A surface area of 1 cm^2 of the deposited film was in contact with the electrolyte. Illumination was provided by 8 xenon lamps (35 W each) radially distributed with a total power of 280 W and irradiance on the sample of ca. 100 mW/cm^2. Electrochemical impedance spectroscopy (EIS) was performed using versaSTAT3. Measurements were conducted in the frequency range from 100 kHz to 1 mHz with a 5 mV AC amplitude using the three-electrode cell configuration with the same conditions used for photocurrent measurements.

Characterization techniques: Transmission electron microscopy (TEM) characterization was carried out using a ZEISS LIBRA 120, operating at 120 kV. Samples were prepared by drop casting a diluted NC solution onto a carbon coated copper grid (200 mesh). Scanning electron microscopy (SEM) analysis was carried out using a ZEISS Auriga microscope. For SEM characterization, NCs were dispersed in appropriate solvent and drop casted onto silicon substrates. X-ray power diffraction (XRD) analyses were carried out on a Bruker AXS D8 ADVANCE X-ray diffractometer with Ni-filtered (2 μm thickness) Cu Kα1 radiation (λ = 1.5406 Å). For XRD analysis, NCs in solution were drop casted (200-500 μL at a concentration of about 3 mg/mL) onto a zero-signal silicon wafer. UV-vis diffuse reflectance spectra were acquired with a PerkinElmer LAMBDA 950 UV−vis spectrophotometer equipped with an integrating sphere. The solid sample was placed on the sample holder and measured from 1000 to 300 nm and the baseline was corrected using a $BaSO_4$ reflectance standard. The Kubelka-Munk equation was employed to convert reflectance to absorption.[42] FTIR spectra were recorded form 500 cm^{-1} to 4000 cm^{-1} using a PerkinElmer FT-IR 2000 spectrophotometer. Dynamic light scattering (DLS) measurements were performed using a Zeta Sizer (Malvern Instruments) equipped with a 4.0 mW HeNe laser operating at 633 nm and an avalanche photodiode detector. For DLS analysis, samples were diluted in 2 mL of appropriate solvent inside a 10 mm path length glass cuvette. X-ray photoelectron spectroscopy (XPS) measurements were carried out on a SPECS system equipped with an Al anode XR50 source operating at 150 mW and a Phoibos 150 MCD-9 detector. The pressure in the analysis chamber was kept below 10^{-7} Pa. The area analyzed was about 2 mm x 2 mm. The pass energy of the hemispherical analyzer was set at 25 eV and the energy step was maintained at 1.0 eV. Data processing was performed with the Casa XPS program (Casa Software Ltd., UK). Binding energies were shifted according to the

reference C 1s peak that was located at 284.8 eV. The fitting of each component was performed taking into account the characteristic width of each peak (taking into account the particular element and electronic state) and the separation of each doublet, as reported in the Handbook of X-ray photoelectron spectroscopy.[43] Thermogravimetric analyses (TGA) were carried out using PerkinElmer Diamond TG/DTA instrument. For TGA, samples were dried and 20 mg of the dried powder was loaded into a ceramic pan. Measurements were carried out in an Ar atmosphere from ambient temperature to 500 °C at a heating rate of 2 °C/min.

RESULTS AND DISCUSSIONS

Figure 1 a displays a representative TEM micrograph of the 18 ± 2 nm In_2S_3 NCs produced through the injection of a OAm-sulfur solution into a hot (220 °C) OAm solution containing $InCl_3$, as described in the experimental section. Using this synthetic protocol, a slight variation of that reported by K. H. Park et al.,[34] β-In_2S_3 NCs with disk-like morphology were produced. The thickness of the In_2S_3 nanodisks was previously reported at 0.76 nm,[34] which corresponds to a single unit cell, and their diameter could be adjusted in the range from 18 nm to 90 nm by using different sulfur precursors and/or reaction times (see details in the supporting information, SI, Figure S1).

XRD patterns of the as-synthesized NCs displayed the reflections of the β-In_2S_3 crystallographic phase with a tetragonal crystal structure (Figure 2). Two particularly intense peaks were observed on the diffraction patterns, suggesting a preferential growth of the material in these directions, which is consistent with the very asymmetric disk-shape of the NCs as observed by TEM. Similar patterns were reported by Park et al for In_2S_3 nanoplates.[34]

The presence of OAm in the reaction mixture was fundamental to produce In_2S_3 crystals with sizes in the nanometer size regime and with narrow size and shape distributions. OAm binds indium ions at the NCs surface, limiting the access/reaction of additional monomer and thus confining the NC growth. At the same time, OAm molecules bound at the NC surface colloidally stabilized them during synthesis, enabling their homogeneous growth. The presence of OAm was indicated by FTIR analysis (Figure 3 c), and was expected to modulate the NC catalytic activity.

To determine the effect of surface ligands on the photocatalytic properties of In_2S_3 NCs and to direct their assembly, OAm was replaced from as-produced NCs (OAm-NCs) with three different ligands: a composition-matched inorganic ligand, In-Cl complex (InCl-NCs); a non-matching inorganic ligand, $(PW_{12}O_{40})^{3-}$ ($(PW_{12}O_{40})^{3}$-NCs); and a shorter organic ligand, MUA (MUA-NCs). In all cases, new ligands were introduced using previously reported two-phase methods adapted to our system.[38,39] In brief, OAm was replaced with MUA by mixing In_2S_3 NCs in hexane with a MUA solution in methanol.[18] On the other hand, MFA was used as a solvent to replace the native OAm with inorganic ligands. Briefly, a hexane solution containing the In_2S_3 NCs was mixed with a PTA/TFA solution in MFA or with an $InCl_3$ solution in MFA.

This process rendered the NCs soluble in polar media such as methanol or H_2O, as confirmed by TEM and DLS measurements (Figure 1 b, c, d). The surface of In_2S_3 NCs capped with MUA, InCl and $(PW_{12}O_{40})^{3-}$ ligands was characterized by the presence of negatively charged species, which resulted in negative ζ-potential values of -19 mV, -26 mV and -28 mV, respectively (Figure 1 e).

FTIR spectra of In_2S_3 NCs stabilized with MUA (MUA-NCs) showed the presence of peaks at 2924 cm^{-1} and 2830 cm^{-1} that correspond to C-H stretching (Figure 3 c). However, due to the shorter chain length of MUA compared with OAm, the intensity of these peaks was lower than in

the initial OAm-stabilized In_2S_3 NCs (OAm-NCs). The disappearance of the weak peak at 2547 cm^{-1} present in the spectrum of pure MUA, and which was attributed to the S-H stretching, indicated the binding of the ligand to the metal atom through the thiolate group. Finally, the peaks at 1547 cm^{-1} and 1406 cm^{-1} observed in the FTIR spectrum of the MUA-NCs were attributed to the asymmetric and symmetric vibrational bands of the carboxylate, again consistent with the presence of the MUA functional group.

FTIR spectra from the NCs stabilized with inorganic ligands demonstrated a strong but not total reduction of the peaks at 2800-2900 cm^{-1} assigned to the C-H vibration band from OAm (Figure S4). TGA analysis further confirmed OAm displacement. $(PW_{12}O_{40})^{3-}$ -NCs showed 9% weight loss, much lower than the 50% loss measured for OAm-NCs, (Figure 1 f). MUA-NCs contained a lower amount of organics than OAm-NCs, 18%, which was related to the lower molecular weight MUA compared with OAm.

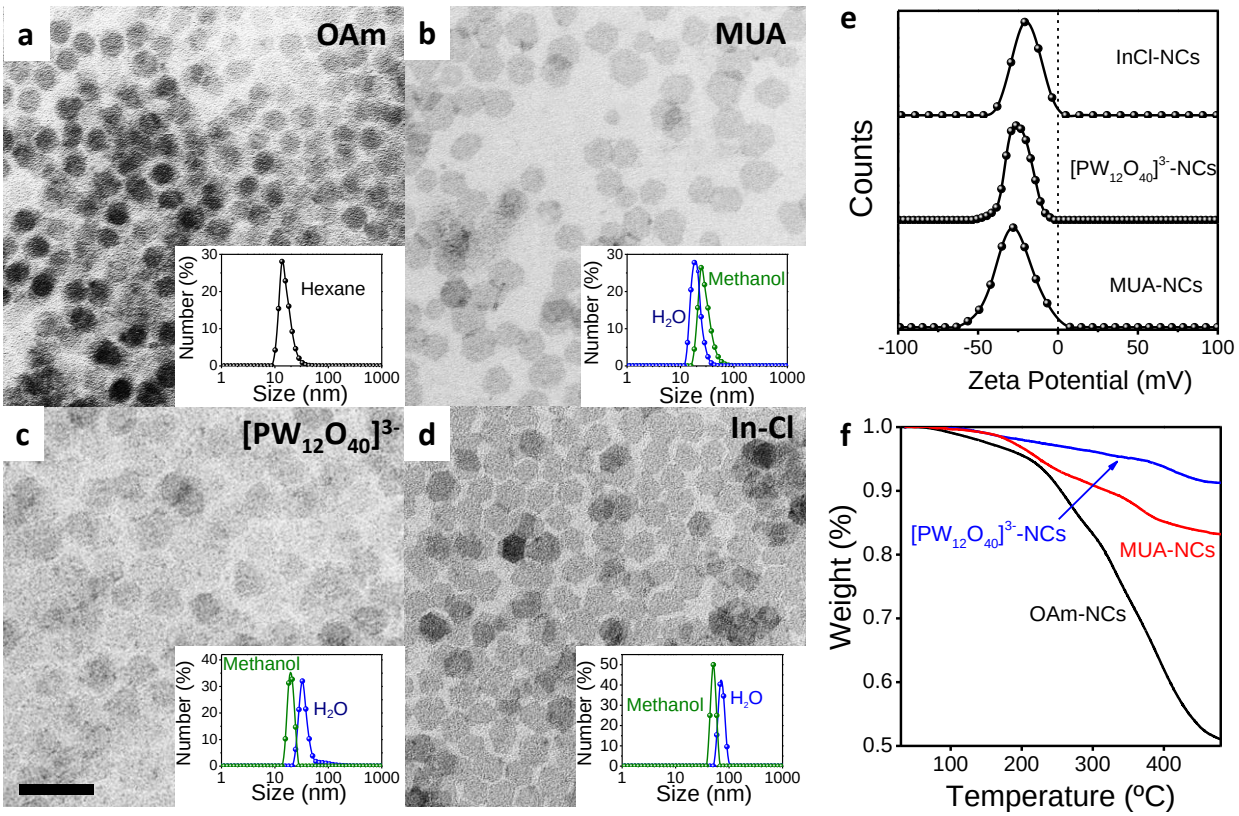

Figure 1. a-d) Representative TEM micrographs and corresponding DLS spectra of the initial In_2S_3 NCs (a) and of the In_2S_3 NCs capped with MUA (b), $(PW_{12}O_{40})^{3-}$ (c), and an In-Cl complex (d). All micrographs have the same scale bar = 50 nm. e) ζ-potential measurements of the In_2S_3 NCs capped with MUA, $(PW_{12}O_{40})^{3-}$, and the In-Cl complex. e) TGA profiles of the initial In_2S_3 NCs (OAm-NCs) and of the In_2S_3 NCs capped with MUA and $(PW_{12}O_{40})^{3-}$.

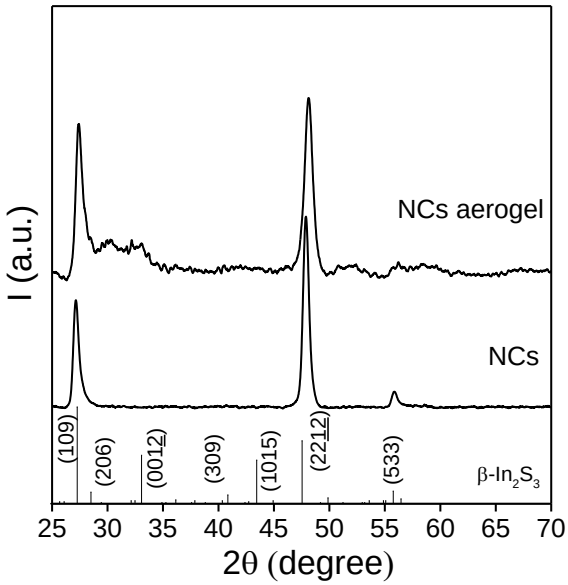

Figure 2. XRD patterns of the In_2S_3 NCs and aerogel. The bars in the bottom correspond to the bulk β- In_2S_3 (JCPDS N 25-0390).

XPS measurements corroborated the presence of $(PW_{12}O_{40})^{3-}$ and Cl on the surface of In_2S_3 NCs (Figure 3). The XPS spectrum of $(PW_{12}O_{40})^{3-}$-NCs displayed the presence of tungsten at the In_2S_3 NC surface (~ 1 %), with a main oxidation state compatible with that of a tungstate (W 4f7/2 binding energy = 35.8 eV, Figure 3 a).[35] The ratio In/S in $(PW_{12}O_{40})^{3-}$-NCs was slightly above that of stoichiometric In_2S_3: In/S = 0.87, and the main contribution to the In $3d_{5/2}$ electronic states (77 %) displayed a relatively high binding energy (In $3d_{5/2}$ binding energy =446.1 eV) compared to that of In_2S_3, which would be compatible with a higher electronegativity of $(PW_{12}O_{40})^{3-}$ anions. The second contribution to In $3d_{5/2}$ (In $3d_{5/2}$ binding energy =444.7 eV) was assigned to lattice In^{3+} in a In_2S_3 chemical environment. Two sulfur chemical states were also identified in this sample. Both components were found at lower binding energies than elemental sulfur, thus proving their less electronegative environment. The component at a higher binding energy (S $2p_{3/2}$ binding energy =162.9 eV) was assigned to surface sulfur exposed to the

more electronegative $(PW_{12}O_{40})^{3-}$ anions, while the component at a lower binding energy (S $2p_{3/2}$ binding energy =161.6 eV) was assigned to S^{2-} within the In_2S_3 lattice.

The XPS spectrum of In_2S_3 NCs stabilized with $InCl_3$ (InCl-NCs) displayed the presence of Cl (~ 3%) in a metal chloride environment (Cl $2p_{3/2}$ binding energy = 198.9 eV, Figure 3 b). Additionally, the surface of InCl-NCs contained an even larger excess of In: In/S = 1.0. The main contribution to In electronic states (70 %) was compatible with both an In_2S_3 and an InCl chemical environment (In $3d_{5/2}$ binding energy = 445.2 eV, Figure 3 b), and a minor component at (In $3d_{5/2}$ binding energy =445.8 eV) could be assigned to $InCl_3$.[43] The S 2p region displayed a unique sulfur contribution (S $2p_{3/2}$ binding energy =161.7 eV) approximately coinciding with the lowest energy component in $(PW_{12}O_{40})^{3-}$-NCs and assigned to S^{2-} within the In_2S_3 chemical environment.

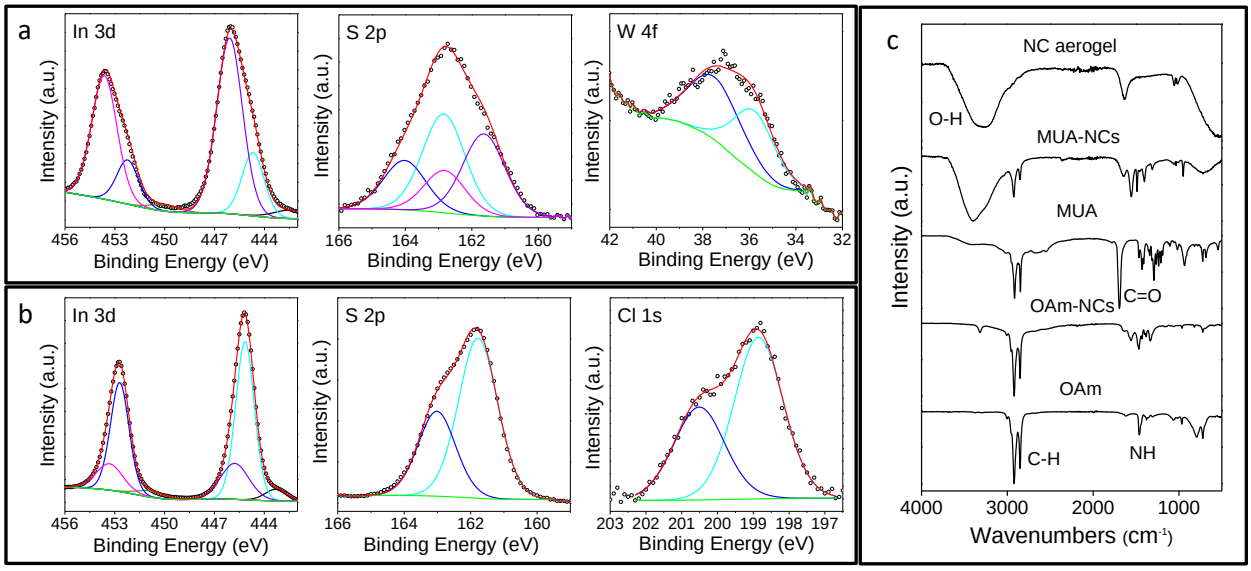

Figure 3. a) XPS spectrum of the In 3d, S 2p and Cl 1s regions obtained from $(PW_{12}O_{40})^{3-}$-NCs. b) XPS spectrum of the In 3d, S 2p and Cl 1s regions obtained from InCl-NCs. c) FTIR spectra

of OAm, MUA, MUA-NCs, OAm-NCs and a NC aerogel. Note that MUA-NCs and OAm-NCs were dispersed in methanol and hexane respectively.

MUA-NCs were used as building blocks to produce In_2S_3 gels (Figure 4). The assembly of MUA-NCs was triggered by exposing them to a non-oxygen-transferring oxidant, TNM (3% TNM solution in methanol).[44] As previously described,[20] TNM oxidized the thiolate ligands bound to In^{3+} ions at the NC surface producing disulfides. Upon thiolate displacement from the NC surface, In^{3+} ions at the NC surface can be easily solvated by the carboxylate species or methanol, leaving a chalcogen-rich NC surface. In such chalcogen-rich NCs, and in the presence of sufficient oxidizer, chalcogen catenation takes place, resulting in the aggregation of the NCs into a network held together by interparticle chalcogen–chalcogen bonding.[19] This ligand-free gelation mechanism allows for direct connection of NCs without any intermediary ligand that could hinder, for instance, inter-particle charge transfer.

The formed gel was subsequently dried under super-critical CO_2 to retain the porous structure. TEM characterization of the resulting aerogel (Figures 4a and S2) revealed the random aggregation of the NCs. However, HRTEM micrographs showed some of the attached NCs to have coincident crystallographic orientations (Figure S2). The assembly of the In_2S_3 NCs into a gel did not substantially affect the material crystallinity as observed from the XRD pattern (Figure 2), however additional peaks raised which could be related to the oriented attachment of the NCs and their growth in the direction normal to the disk plane.

Figure 5 displays the absorption spectra of the as-synthesized OAm-NCs and a NC-based aerogel. UV-vis measurements showed a slight blue shift of the absorption edge for the NC aerogel compared with OAm-NCs suggesting a change in the NCs sizes upon gelation. Indeed

calculation of the NCs sizes using Scherrer equation demonstrated a slight decrease from $L_{(311)}$ = 18 nm for precursor NCs to $L_{(311)}$ = 15 nm for NC aerogel. These results are consistent with those obtained from CdSe NC aerogels and might be related to the etching of the NCs surface during the gelation process.[20] A shift of the absorption edge related to the aerogel interconnected structure was also observed for CdSe NC-based aerogels.[45] However, this effect had associated a red shift of the spectra, which was not observed here.

SEM characterization of aerogels suggested a highly porous three dimensional structure with large voids (Figure 4 b). FTIR analysis of the final aerogel evidenced that the gelation process was accompanied by the removal of MUA as proven by the suppression of the 2800-2900 cm^{-1} peak corresponding to the C-H vibration band (Figure 3 c). The peak with low intensity at 2400 cm^{-1} could be ascribed to a residual amount of CO_2 in the measurement atmosphere or to the vibration of C=O ketone group originated from carboxylate group of MUA.

The amount of oxidizing agent introduced was a key parameter controlling the gelation process. On one hand, low amounts of TNM resulted in partial NC aggregation and precipitation but without the formation of a proper NC network. On the other hand, an excess of the oxidizing agent resulted in much denser gels by strongly accelerated the NC aggregation through efficiently removing all the MUA molecules and leading to extensive chalcogen-chalcogen bond formation (Figure S3).

Type IV nitrogen adsorption/desorption isotherms, characteristic of mesoporous structures, were observed for the NC aerogels (Figure 4 d). From the fitting of the data to a Brunauer-Emmett-Teller (BET) model,[46] the surface area of In_2S_3 NC aerogels was determined to be ca. 134 m^2/g, while that of precipitated MUA-NCs was just 40 m^2/g (Figure 4 d). For comparison,

the calculated surface area for colloidal In_2S_3 NCs with a disk-like geometry, a thickness of 1 nm and a diameter of 18 nm was 225 m^2/g.

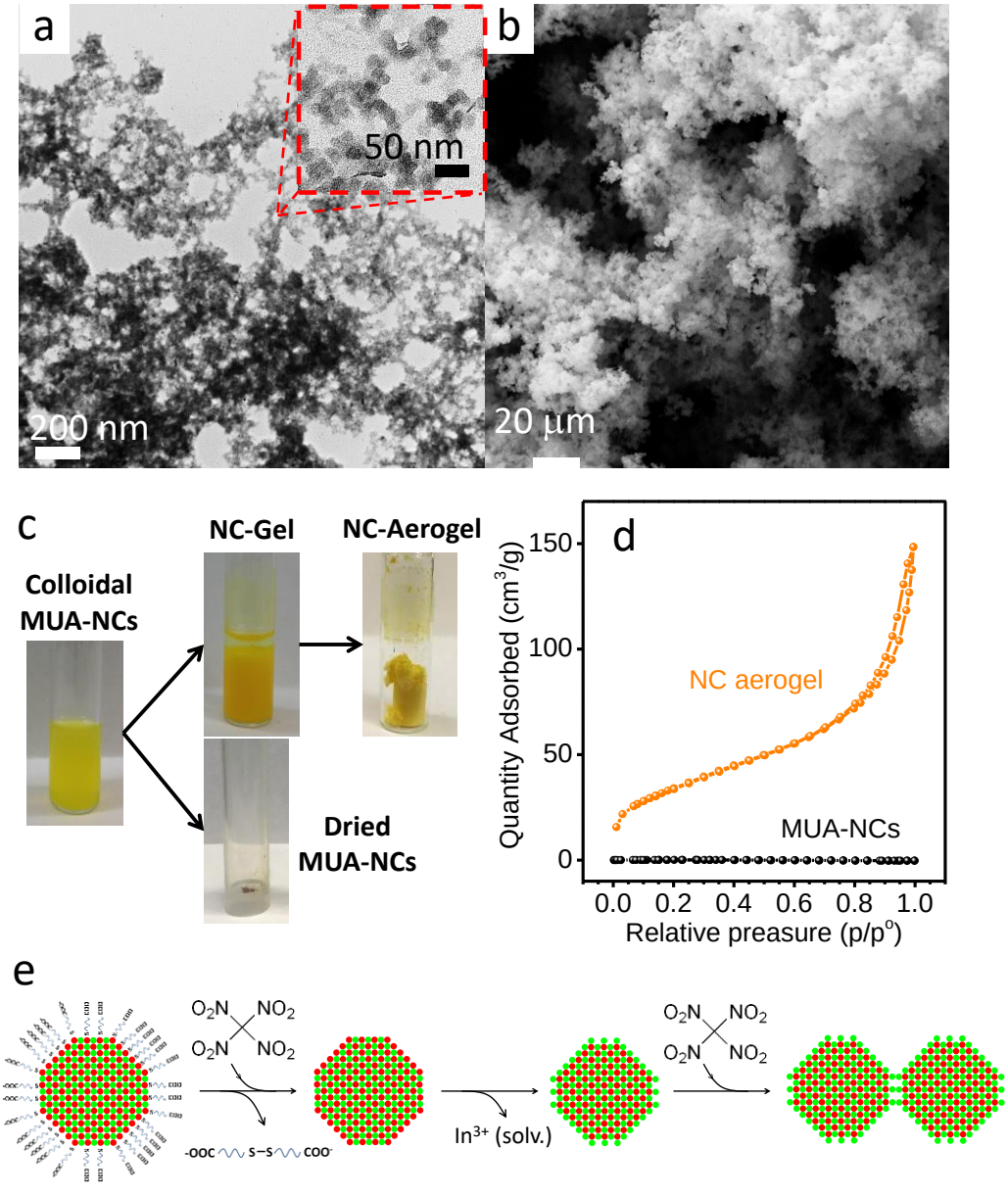

Figure 4. a) TEM and b) SEM micrographs of an In_2S_3 NC aerogel. c) Vials containing the MUA-NC solution in methanol, a NC wet gel, the super-critically dried NCs aerogel and the precipitated and dried MUA-NCs. d) Nitrogen adsorption/desorption isotherms of an In_2S_3 NC

aerogel and of dried MUA-NCs. e) Scheme of the gel formation by TNM oxidation of MUA and sulphur ions at the NC surface.

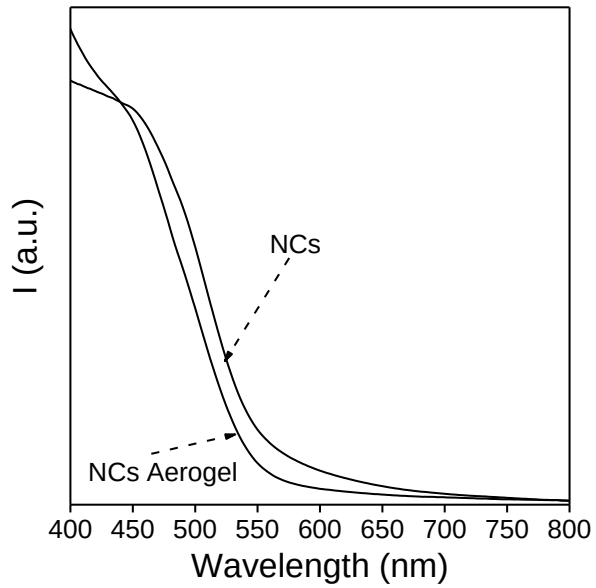

Figure 5. Absorption spectra from OAm-NC and a NC aerogel.

The photocatalytic performance of In_2S_3 NCs in suspension was evaluated through the degradation of RhB under xenon lamp irradiation (300 W). In a typical measurement, 20 mg of NCs were suspended in 10 mL of MQ-water containing 10 ppm of RhB. Before irradiation, the solution was stirred in the dark for 30 min to achieve adsorption equilibrium. Note that OAm-NCs were not stable in MQ-water and thus were not tested for RhB degradation. MUA-NCs showed a poor activity toward photodegradation of RhB, reaching just 50% of RhB degradation after 2 h illumination (Figure 6). We associated this poor performance to the limited access of RhB to the MUA-covered NC surface. Under illumination, photogenerated electrons are transferred to adsorbed dye molecules to decompose them. If not properly extracted, photogenerated holes accumulate at the In_2S_3 NC and result in the oxidation of the NC surface.[11]

In MUA-NCs, this photooxidation results in the detachment of MUA ligands as disulphides and, hence, induce irreversible NCs aggregation and consequent surface loss.[47-49]

$(PW_{12}O_{40})^{3-}$- and InCl-NCs provided the highest RhB degradation rates, which we attributed to the superior surface accessibility on these NCs due to the absence of organic ligands and their fair stability in solution during the whole experiment (Figure 6). No photooxidation-induced aggregation was observed for $(PW_{12}O_{40})^{3-}$-NCs and InCl-NCs proving the presence of these ligands to provide a better stability. Noteworthy, the In_2S_3 NC-gel showed intermediate activity for RhB degradation (65 %) under the same experimental conditions. This intermediate efficiency of NC-gels corresponded to a partially organic-free surface compared to MUA-NCs but associated with a lower total active area if compared with colloidal $(PW_{12}O_{40})^{3-}$-NCs and InCl-NCs.

Additionally, we compared the catalytic performance of the In_2S_3 nanocrystalline material with that of bulk In_2S_3 and of a conventional TiO_2 catalyst. As expected, bulk In_2S_3 exhibited moderate catalytic activity compared to the nanocrystalline materials here analyzed. The TiO_2 nanopowder also showed a lower catalytic activity under the xenon light irradiation compared to In_2S_3 NCs stabilized with inorganic ligands. A comparison of the performance of the In_2S_3 NCs measured here with those obtained in previous works is given in the SI (Table S1)

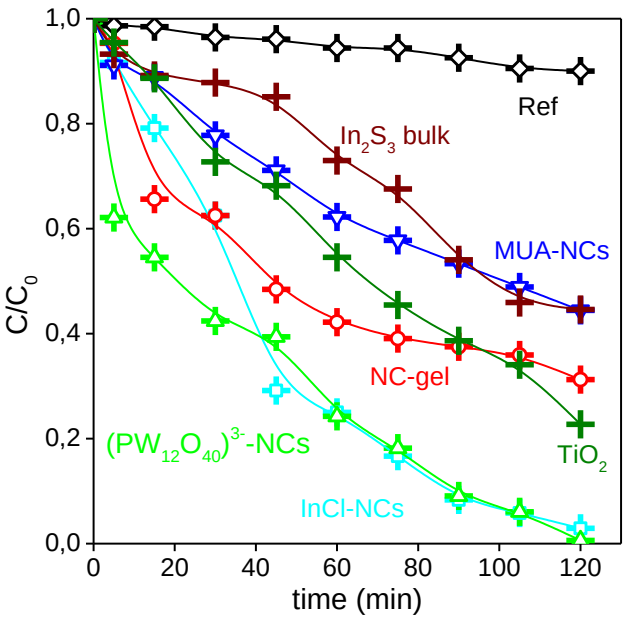

Figure 6. Photocatalytic degradation curves of RhB on MUA-NCs, $(PW_{12}O_{40})^{3-}$-NCs, InCl-NCs and a NC-gel compare to commercial TiO_2 photocatalyst (Degussa P25) powder and In_2S_3 bulk. Experiments were carried out by irradiating a 10 ppm RhB mixture containing 20 mg of sample in MQ-water with a xenon lamp (300 W) for 2 hours.

To investigate their photoelectrocatalytic properties, In_2S_3 NCs were supported on ITO-covered glass substrates. NC layers were prepared by spin coating a methanol solution of the NCs (Figure 7). To produce porous films, the MUA-NC layer was dipped into a TNM solution immediately after spin coating, interconnecting in this way the In_2S_3 NCs into a porous network.[20] The substrate was afterwards rinsed with methanol to remove excess of TNM and reaction by-products. All layers were annealed at 250 °C for 60 min under argon flow before photoelectrocatalytic characterization.

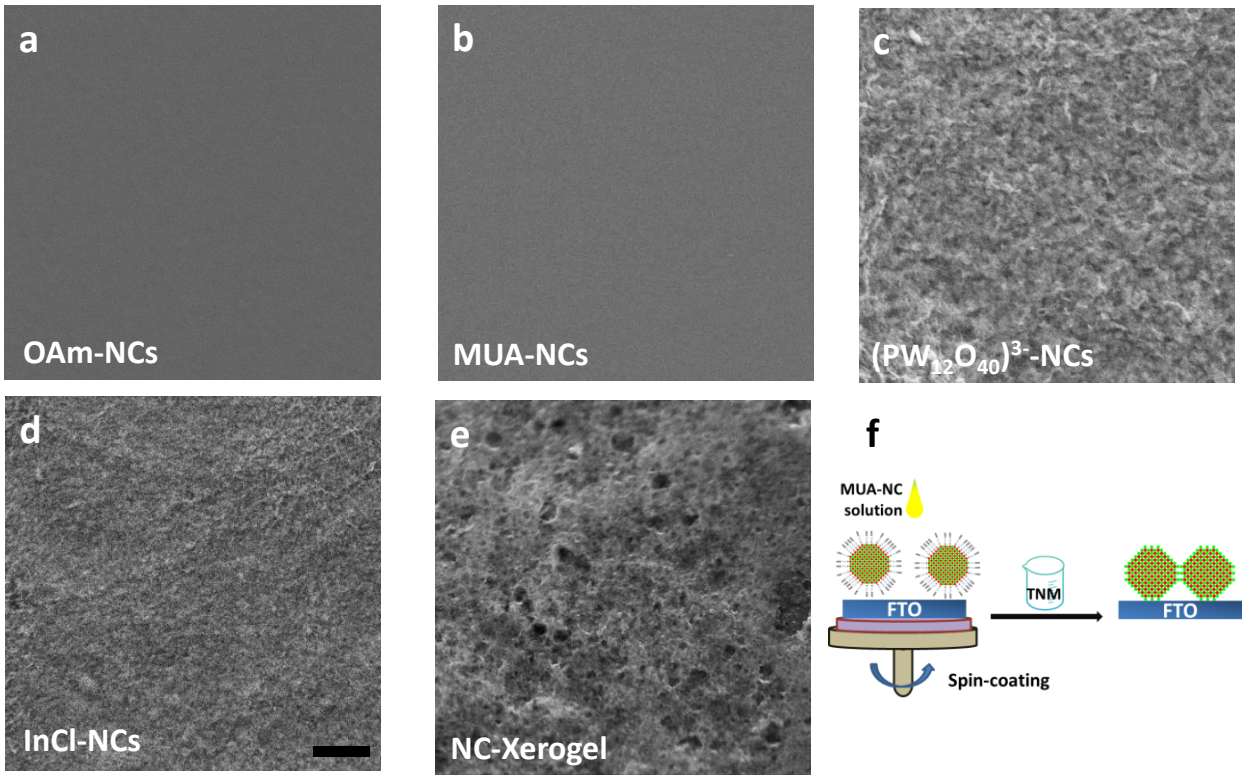

Figure 7. a-e) SEM images of films obtained by spin-coating OAm-NCs (a), MUA-NCs (b), $(PW_{12}O_{40})^{3-}$-NCs (c), InCl-NCs (d), and MUA-NCs that were subsequently linked together by oxidation with TNM to produce a xerogel layer (e). Scale bar = 2 µm. f) Scheme of the process of formation of a gel layer.

The photoelectrocatalytic performance of In_2S_3 NCs was evaluated using a three-electrode cell with a Pt-coiled counter electrode, an Ag/AgCl reference electrode and the NCs film as working electrode. A polysulfide solution, consisting of a 1 M aqueous solution of Na_2S, NaOH and S, was used as electrolyte. Figure 8 shows the results obtained from linear sweep voltammograms and time-dependent photocurrent measurements of the different samples analysed.

Films obtained by spin coating OAm- and MUA-NCs showed the lowest performance. We attribute this poor performance to a limited access of the sulphide species to the NC's surface and to the low electrical conductivity of the film due to the presence of the insulating organic

ligands. The lower performance of OAm-NCs if compared to MUA-NCs could result from the hydrophobic nature of OAm-NCs which may reduce the interaction with the reaction solution hence reducing the current density. The hydrophilic nature of MUA-NC films provided a better contact between the NCs and the electrolyte and hence slightly higher photocurrent densities. Layers produced from $(PW_{12}O_{40})^{3-}$-NCs and InCl-NCs showed improved photocurrents compared with OAm-NCs, which we attributed to a more efficient charge transfer with the media and a faster charge transport between the NCs. Surprisingly, gel layers provided the highest photocurrent densities, reaching 150 µA/cm^2 at 1.0 V vs Ag/AgCl which represent a five-fold increase compared to the $(PW_{12}O_{40})^{3-}$-NCs and InCl-NCs films (Figure 8 a). We attributed such enhanced performance of the gel layers to: i) an organic-free NC interconnection, resulting in improved interaction and charge transfer, ii) a high degree of porosity offering large active surface areas for interaction with the media. EIS measurements confirmed the lower charge transfer resistance of the gel layers compared with $(PW_{12}O_{40})^{3-}$-NCs and InCl-NCs films, associated again to the higher surface area and the NC interconnection within the gel layers (Figure 8 c).

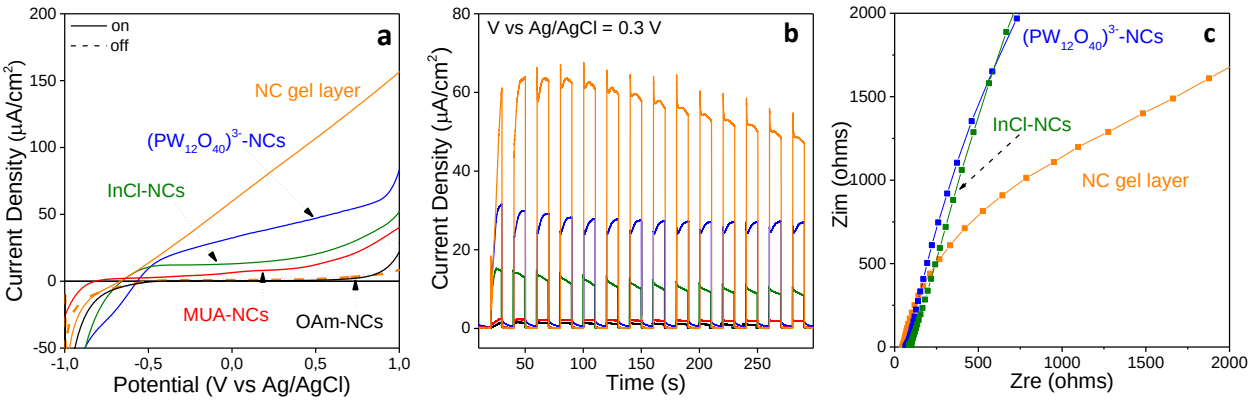

Figure 8. Linear sweep voltammogram curves (a) and chronoamperometric characteristics normalized by the amount of photoactive material at 0.3 V vs. Ag/AgCl (b) of gel layers and

layers produced from OAm-, MUA-, $(PW_{12}O_{40})^{3-}$- and InCl-NCs. Nyquist plots for $(PW_{12}O_{40})^{3-}$ NCs, InCl-NCs and gel layer (c).

CONCLUSIONS

We compared the photocatalytic and photoelectrocatalytic performance of 18 nm disk-shaped In_2S_3 NCs with different surface chemistries and supra-crystalline organization. Dispersions of In_2S_3 NCs, colloidally stabilized with inorganic ligands such as polyoxometallates or chlorides, showed the highest photocatalytic performance toward dye degradation in solution. We attributed this experimental fact to the higher accessibility of the NC surface provided by the inorganic ligands compared with the organic ones and to the colloidal stability of the materials, which provided maximized surface areas to interact with the media. On the other hand, organized NC assemblies provided higher photoelectrocatalytic performances than organic- and inorganic-capped NCs. The organization of the NCs into networks held together through chalcogen-chalcogen bonds simultaneously provided larger surface areas for interaction with the media compared with layers of precipitated NCs, and effective avenues for charge transport through the layer.

ASSOCIATED CONTENT

Supporting Information

The Supporting Information is available free of charge at DOI:

Additional experimental details. TEM images of In_2S_3 NCs with different sizes and shapes, optical photographs of In_2S_3 NC-gel obtained using different amount of TNM, HRTEM

analysis, complementary FTIR data, comparison of dye degradation performance.

AUTHOR INFORMATION

Corresponding Authors

*E-mail: acabot@irec.cat

*E-mail: sbrock@chem.wayne.edu

ACKNOWLEDGMENT

This work was supported by the European Regional Development Funds and the Spanish MINECO project BOOSTER. TB thanks FI-AGAUR Research Fellowship Program, Generalitat de Catalunya (2015 FI_B 00744). PG acknowledges the People Programme (Marie Curie Actions) of the FP7/2007-2013 European Union Program (TECNIOspring grant agreement no. 600388) and the Agency for Business Competitiveness of the Government of Catalonia, ACCIÓ. SB acknowledges the U.S. National Science Foundation, CHE-1361741. JL is a Serra Hunter Fellow and is grateful to ICREA Academia program and grants MINECO/FEDER ENE2015-63969-R and GC 2017 SGR 128.

ABBREVIATIONS

NC, nanocrystal; OAm, oleylamine; OAc, oleic acid; MUA, 11-mercaptoundecanoic acid; TMOH, tetramethylammonium hydroxide pentahydrate; DDT, dodecanethiol; tDDT, tert-dodecanethiol; MFA, n-methylformamide; PTA, phosphotungstic acid hydrate; TFA, trifluoroacetic acid; TNM, tetranitromethane; RhB, rhodamine B; ITO, indium tin oxide; TEM, transmission electron microscopy; HRTEM, high-resolution TEM; SEM, scanning electron

microscopy; UV-vis, ultraviolet-visible spectroscopy; UV/vis/NIR, ultraviolet-visible near infrared spectroscopy; X-ray power diffraction (XRD); DLS, dynamic light scattering; FTIR, Fourier-transform infrared spectroscopy; XPS, X-ray photoelectron spectroscopy; ICP, inductively coupled plasma mass spectroscopy; OAm-NCs, OAm-capped NCs; $(PW_{12}O_{40})^{3-}$-NCs, $(PW_{12}O_{40})^{3-}$-capped NCs; InCl-NCs, InCl-capped NCs; MUA-NCs, MUA-capped NCs.

REFERENCES

(1) Talapin, D. V.; Lee, J.-S.; Kovalenko, M. V.; Shevchenko, E. V., Prospects of colloidal nanocrystals for electronic and optoelectronic applications. *Chem. Rev.* **2010,** *110*, 389-458.

(2) Popczun, E. J.; McKone, J. R.; Read, C. G.; Biacchi, A. J.; Wiltrout, A. M.; Lewis, N. S.; Schaak, R. E., Nanostructured nickel phosphide as an electrocatalyst for the hydrogen evolution reaction. *J. Am. Chem. Soc.* **2013,** *135*, 9267-9270.

(3) Li, D.; Baydoun, H.; Kulikowski, B.; Brock, S. L., Boosting the catalytic performance of iron phosphide nanorods for the oxygen evolution reaction by incorporation of manganese. *Chem. Mat.* **2017,** *29*, 3048-3054.

(4) Lim, W. Y.; Hong, M.; Ho, G. W., In situ photo-assisted deposition and photocatalysis of $ZnIn_2S_4$/transition metal chalcogenides for enhanced degradation and hydrogen evolution under visible light. *Dalton Transactions* **2016,** *45* (2), 552-560.

(5) Thatai, S.; Khurana, P.; Boken, J.; Prasad, S.; Kumar, D., Nanoparticles and core–shell nanocomposite based new generation water remediation materials and analytical techniques: A review. *Microchem. J.* **2014,** *116*, 62-76.

(6) Yu, X.; Shavel, A.; An, X.; Luo, Z.; Ibáñez, M.; Cabot, A., Cu_2ZnSnS_4-Pt and Cu_2ZnSnS_4-Au heterostructured nanoparticles for photocatalytic water splitting and pollutant degradation. *J. Am. Chem. Soc.* **2014,** *136*, 9236-9239.

(7) Mahmoud, M. A.; O'Neil, D.; El-Sayed, M. A., Hollow and solid metallic nanoparticles in sensing and in nanocatalysis. *Chem. Mat.* **2014,** *26* (1), 44-58.

(8) Zhang, Q.; Su, H.; Luo, J.; Wei, Y., A magnetic nanoparticle supported dual acidic ionic liquid: a "quasi-homogeneous" catalyst for the one-pot synthesis of benzoxanthenes. *Green Chem.* **2012,** *14*, 201-208.

(9) Xiang, Q.; Yu, J.; Jaroniec, M., Synergetic effect of MoS_2 and graphene as cocatalysts for enhanced photocatalytic h_2 production activity of TiO_2 nanoparticles. *J. Am. Chem. Soc.* **2012,** *134*, 6575-6578.

(10) Talapin, D. V., Nanocrystal solids: A modular approach to materials design. *MRS Bull.* **2012,** *37*, 63-71.

(11) Stolarczyk, J. K.; Deak, A.; Brougham, D. F., Nanoparticle clusters: assembly and control over internal order, current capabilities, and future potential. *Adv. Mater.* **2016,** *28*, 5400-5424.

(12) Korala, L.; Germain, J. R.; Chen, E.; Pala, I. R.; Li, D.; Brock, S. L., CdS aerogels as efficient photocatalysts for degradation of organic dyes under visible light irradiation. *Inorg. Chem. Front.* **2017,** *4*, 1451-1457.

(13) Wu, Z.-S.; Yang, S.; Sun, Y.; Parvez, K.; Feng, X.; Müllen, K., 3D nitrogen-doped graphene aerogel-supported Fe_3O_4 nanoparticles as efficient electrocatalysts for the oxygen reduction reaction. *J. Am. Chem. Soc.* **2012,** *134*, 9082-9085.

(14) Kagan, C. R.; Lifshitz, E.; Sargent, E. H.; Talapin, D. V., Building devices from colloidal quantum dots. *Science* **2016,** *353,* 6302.

(15) Yang, M.-Q.; Xu, Y.-J.; Lu, W.; Zeng, K.; Zhu, H.; Xu, Q.-H.; Ho, G. W., Self-surface charge exfoliation and electrostatically coordinated 2D hetero-layered hybrids. *Nature Communications* **2017,** *8*, 14224

(16) Shevchenko, E. V.; Talapin, D. V.; Kotov, N. A.; O'Brien, S.; Murray, C. B., Structural diversity in binary nanoparticle superlattices. *Nature* **2006,** *439*, 55.

(17) Redl, F. X.; Cho, K. S.; Murray, C. B.; O'Brien, S., Three-dimensional binary superlattices of magnetic nanocrystals and semiconductor quantum dots. *Nature* **2003,** *423*, 968.

(18) Gaponic, N.; Herrmann, A.-K.; Eychmuller, A., Colloidal Nanocrystal-Based Gels and Aerogels: Material Aspects and Application Perspectives. *J. Phys. Chem. Lett.* **2012**, *3*, 8-17.

(19) Mohanan, J. L.; Arachchige, I. U.; Brock, S. L., Porous semiconductor chalcogenide aerogels. *Science* **2005,** *307*, 397-400.

(20) Pala, I. R.; Arachchige, I. U.; Georgiev, D. G.; Brock, S. L., Reversible gelation of II–VI nanocrystals: the nature of interparticle bonding and the origin of nanocrystal photochemical instability. *Angew. Chem. Int. Edit.* **2010,** *49*, 3661-3665.

(21) Arachchige, I. U.; Brock, S. L., Sol–gel methods for the assembly of metal chalcogenide quantum dots. *Accounts Chem. Res.* **2007,** *40*, 801-809.

(22) Korala, L.; Wang, Z.; Liu, Y.; Maldonado, S.; Brock, S. L., Uniform thin films of CdSe and CdSe(ZnS) Core(Shell) quantum dots by sol–gel assembly: enabling photoelectrochemical characterization and electronic applications. *ACS Nano* **2013,** *7*, 1215-1223.

(23) Korala, L.; Li, L.; Brock, S. L., Transparent conducting films of CdSe(ZnS) core(shell) quantum dot xerogels. *Chem. Commun.* **2012,** *48*, 8523-8525.

(24) Gschneidner, K.A.; Eyring, Jr. and L. *Handbook on the Physics and Chemistry of Rare Earths*; Gschneidner, K.A.; Eyring, Jr. and L., Eds.; Elsevier, 1999; Vol. 11, p.148.

(25) Peng, S.; Li, L.; Wu, Y.; Jia, L.; Tian, L.; Srinivasan, M.; Ramakrishna, S.; Yan, Q.; Mhaisalkar, S. G., Size- and shape-controlled synthesis of $ZnIn_2S_4$ nanocrystals with high photocatalytic performance. *CrystEngComm* **2013,** *15*, 1922-1930.

(26) Chen, W.; Bovin, J.-O.; Joly, A. G.; Wang, S.; Su, F.; Li, G., Full-color emission from In_2S_3 and In_2S_3: Eu^{3+} nanoparticles. *J. Phys. Chem. B* **2004,** *108* (32), 11927-11934.

(27) Xie, X.; Shen, G., Single-crystalline In_2S_3 nanowire-based flexible visible-light photodetectors with an ultra-high photoresponse. *Nanoscale* **2015,** *7*, 5046-5052.

(28) He, Y.; Li, D.; Xiao, G.; Chen, W.; Chen, Y.; Sun, M.; Huang, H.; Fu, X., A New application of nanocrystal In_2S_3 in efficient degradation of organic pollutants under visible light irradiation. *J. Phys. Chem. C* **2009,** *113*, 5254-5262.

(29) Xu, R.; Li, H.; Zhang, W.; Yang, Z.; Liu, G.; Xu, Z.; Shao, H.; Qiao, G., The fabrication of In_2O_3/In_2S_3/Ag nanocubes for efficient photoelectrochemical water splitting. *Phys. Chem. Chem. Phys.* **2016,** *18*, 2710-2717.

(30) Du, W.; Zhu, J.; Li, S.; Qian, X., Ultrathin β-In_2S_3 Nanobelts: Shape-Controlled Synthesis and Optical and Photocatalytic Properties. *Cryst. Growth Des.* **2008,** *8*, 2130-2136.

(31) Lucena, R.; Aguilera, I.; Palacios, P.; Wahnón, P.; Conesa, J. C., Synthesis and spectral properties of nanocrystalline V-substituted In_2S_3, a novel material for more efficient use of solar radiation. *Chem. Mat.* **2008,** *20*, 5125-5127.

(32) Tapia, C.; Berglund, S. P.; Friedrich, D.; Dittrich, T.; Bogdanoff, P.; Liu, Y.; Levcenko, S.; Unold, T.; Conesa, J. C.; De Lacey, A. L.; Pita, M.; Fiechter, S., Synthesis and

characterization of V-doped β-In_2S_3 thin films on FTO substrates. *J. Phys. Chem. C* **2016,** *120*, 28753-28761.

(33) Xue, B.; Xu, F.; Wang, B.; Dong, A., Shape-controlled synthesis of β-In_2S_3 nanocrystals and their lithium storage properties. *CrystEngComm* **2016,** *18* (2), 250-256.

(34) Park, K. H.; Jang, K.; Son, S. U., Synthesis, Optical properties, and self-assembly of ultrathin hexagonal In_2S_3 nanoplates. *Angew. Chem. Int. Edit.* **2006,** *45*, 4608-4612.

(35) Ghosh, S.; Saha, M.; Ashok, V. D.; Chatterjee, A.; De, S., Excitation dependent multicolor emission and photoconductivity of Mn, Cu doped In_2S_3 monodisperse quantum dots. *Nanotechnology* **2016,** *27* (15), 155708.

(36) Chen, J.; Liu, W.; Gao, W., Tuning photocatalytic activity of In2S3 broadband spectrum photocatalyst based on morphology. *Appl. Surf. Sci.* **2016,** *368*, 288-297.

(37) Liu, G.; Jiao, X.; Qin, Z.; Chen, D., Solvothermal preparation and visible photocatalytic activity of polycrystalline β-In_2S_3 nanotubes. *CrystEngComm* **2011,** *13* (1), 182-187.

(38) Huang, J.; Liu, W.; Dolzhnikov, D. S.; Protesescu, L.; Kovalenko, M. V.; Koo, B.; Chattopadhyay, S.; Shenchenko, E. V.; Talapin, D. V., Surface functionalization of semiconductor and oxide nanocrystals with small inorganic oxoanions (PO_4^{3-}, MoO_4^{2-}) and polyoxometalate ligands. *ACS Nano* **2014,** *8*, 9388-9402.

(39) Sayevich, V.; Guhrenz, C.; Sin, M.; Dzhagan, V. M.; Weiz, A.; Kasemann, D.; Brunner, E.; Ruck, M.; Zahn, D. R. T.; Leo, K.; Gaponik, N.; Eychmüller, A., Chloride and indium-chloride-complex inorganic ligands for efficient stabilization of nanocrystals in solution and doping of nanocrystal solids. *Adv. Funct. Mat.* **2016,** *26*, 2163-2175.

(40) Wuister, S. F.; de Mello Donegá, C.; Meijerink, A., Influence of thiol capping on the exciton luminescence and decay kinetics of CdTe and CdSe quantum dots. *J. Phys. Chem. B* **2004,** *108*, 17393-17397.

(41) Yang, Z.; Chen, C.-Y.; Roy, P.; Chang, H.-T., Quantum dot-sensitized solar cells incorporating nanomaterials. *Chem. Commun.* **2011,** *47*, 9561-9571.

(42) Tauc, J.; Grigorovici, R.; Vancu, A., Optical properties and electronic structure of amorphous germanium. *Phys. Status Solidi B* **1966,** *15*, 627-637.

(43) Moulder, J. F.; Stickle, W. F.; Sobol, P. E.; Bomben, K. D. Handbook of X-Ray Photoelectron Spectroscopy; Perkin-Elmer: Eden Prairie, MN, 1992.

(44) Evans, B. J.; Takahashi Doi, J.; Kenneth Musker W., ^{19}F NMR study of the reaction of p-fluorobenzenethiol and disulfide with periodate and other selected oxidizing agents. *J. Org. Chem*. **1990**, *55*, 2337.

(45) Yu, H.; Liu, Y.; Brock, S. L., Tuning the Optical Band Gap of Quantum Dot Assemblies by Varying Network Density. *ACS Nano* **2009,** *3* (7), 2000-2006.

(46) Sing K. S. W., Reporting physisorption data for gas/solid systems with special reference to the determination of surface area and porosity*, Pure Appl. Chem.* **1982***,* 54, 2201.

(47) Simon, T.; Bouchonville, N.; Berr, M. J.; Vaneski, A.; Adrović, A.; Volbers, D.; Wyrwich, R.; Döblinger, M.; Susha, A. S.; Rogach, A. L.; Jäckel, F.; Stolarczyk, J. K.; Feldmann, J., Redox shuttle mechanism enhances photocatalytic H_2 generation on Ni-decorated CdS nanorods. *Nat. Mater.* **2014,** *13*, 1013.

(48) Aldana, J.; Wang, Y. A.; Peng, X., Photochemical Instability of CdSe Nanocrystals Coated by Hydrophilic Thiols. *J. Am. Chem. Soc.* **2001,** *123*, 8844-8850.

(49) Rogach, A. L.; Kornowski, A.; Gao, M.; Eychmüller, A.; Weller, H., Synthesis and characterization of a size series of extremely small thiol-stabilized CdSe nanocrystals. *J. Phys. Chem. B* **1999,** *103*, 3065-3069.

TOC Graphic

nanomaterials

MDPI

Article

$CuGaS_2$ and $CuGaS_2$–ZnS Porous Layers from Solution-Processed Nanocrystals

Taisiia Berestok [1,2], Pablo Guardia [1], Sònia Estradé [2], Jordi Llorca [3], Francesca Peiró [2], Andreu Cabot [1,4,*] and Stephanie L. Brock [5,*]

1 Catalonia Institute for Energy Research—IREC, Sant Adrià de Besòs, 08930 Barcelona, Spain; taisiia.berestok@gmail.com (T.B.); pavyel1980@gmail.com (P.G.)
2 LENS-MIND, Departament d'Enginyeries i Electrònica i Institut de Nanociència i Nanotecnologia (In2UB), Universitat de Barcelona, 08028 Barcelona, Spain; sestrade@ub.edu (S.E.); francesca.peiro@ub.edu (F.P.)
3 Institute of Energy Technologies, Department of Chemical Engineering and Barcelona Research Center in Multiscale Science and Engineering. Universitat Politècnica de Catalunya, EEBE, Eduard Maristany 16, 08019 Barcelona, Spain; jordi.llorca@upc.edu
4 ICREA, 08010 Barcelona, Spain
5 Department of Chemistry, Wayne State University, Detroit, MI 48202, USA
* Correspondence: acabot@irec.cat (A.C.); sbrock@chem.wayne.edu (S.L.B.); Tel.: +34 625615115 (A.C.) & +313 5773102 (S.L.B.)

Received: 12 February 2018; Accepted: 4 April 2018; Published: 5 April 2018

Abstract: The manufacturing of semiconducting films using solution-based approaches is considered a low cost alternative to vacuum-based thin film deposition strategies. An additional advantage of solution processing methods is the possibility to control the layer nano/microstructure. Here, we detail the production of mesoporous $CuGaS_2$ (CGS) and ZnS layers from spin-coating and subsequent cross-linking through chalcogen-chalcogen bonds of properly functionalized nanocrystals (NCs). We further produce NC-based porous CGS/ZnS bilayers and NC-based CGS–ZnS composite layers using the same strategy. Photoelectrochemical measurements are used to demonstrate the efficacy of porous layers, and particularly the CGS/ZnS bilayers, for improved current densities and photoresponses relative to denser films deposited from as-produced NCs.

Keywords: aerogel; xerogel; porous layer; $CuGaS_2$/ZnS; photoresponse; nanomaterial

1. Introduction

The solution-based processing of semiconductor films has a number of advantages over the use of vacuum-based technologies. Solution-based processes require lower capital investments, have associated lower maintenance costs, and provide higher production throughput and material yields. These characteristics make them highly appropriate for large scale industrial production. Among the different solution-processing technologies, the deposition of inks formulated from nanocrystals (NCs) is particularly interesting as it allows unparalleled control over material properties and layer nano/microstructure, and it provides crystalline layers without mediating a thermal annealing step, thus reducing processing costs. However, in the absence of a sintering step, ink-based processes generally result in layers characterized by poor electrical conductivities, which is a drawback in most applications. While a thermal annealing is frequently used to improve performance, such treatment spoils the main advantages of NC-based solution processes, such as the precise composition control and the cost reduction associated with the production of crystalline layers without the need of a sintering process. Additionally, even annealed NC-based layers contain significant amounts of carbon coming from added binders and from the surface ligands used to control NC growth and

render NCs soluble in the ink media [1]. To fully remove carbon, heat treatments in an oxygen atmosphere are needed, but this is not compatible with materials that are susceptible to oxidation, such as chalcogenides. An alternative strategy to remove organics is the use of solution-based treatments, but these processes often involve toxic compounds such as hydrazine [2,3]. Besides toxicity, if not properly controlled, such solution-based ligand-stripping strategies can result in large concentrations of surface traps that may strongly limit the material performance [4]. An alternative strategy to remove organic ligands from NC-based layers and cross-link the NCs to facilitate charge transport involves using a non-oxygen-transferring oxidant [5–7]. This oxidizing agent produces chalcogen-chalcogen bonds between the NCs, potentially reducing surface recombination sites and facilitating charge transfer between NCs [8,9]. The concentration of this oxidizing agent also allows the porosity of the final material to be controlled. In this regard, in the particular case of photocatalysis and photoelectrocatalytic applications, the formation of porous layers may be advantageous since porous materials allow penetration of reactive species and expose huge surface areas for interaction with the media [10].

Relative to metal oxides, metal sulfide NCs are of great importance because of their covalent bonding, which results in higher charge carrier mobilities, broader bands and narrower energy gaps [1]. Relative to other selenides and tellurides, sulfides present an obvious advantage in terms of abundance and cost. Among metal sulfides, $CuGaS_2$ (CGS), a p-type semiconductor, has gained special attention due to its relatively good stability, moderate cost and toxicity and its direct band gap in the visible (2.4 eV) [11]. CGS is employed in green-light emitting LEDs as well as in visible-light-induced photocatalysis. Furthermore, its relatively large band gap makes it promising as host material for the introduction of intermediate band states to widen its absorption spectra [12,13].

In the present work, we use the oxidative assembly strategy [14] to produce porous CGS NC-based layers. We further extend this strategy to the production of porous multilayers of CGS and ZnS, and of porous composite layers combining CGS and ZnS NCs. We additionally characterize their photoelectrochemical performance toward hydrogen evolution from a Na_2SO_4-containing water solution.

2. Materials and Methods

2.1. Materials

Copper(II) acetylacetonate ($Cu(acac)_2$, 98%), gallium(III) acetylacetonate ($Ga(acac)_3$, 99.99%), trioctylphosphine oxide (TOPO, 99%), zinc chloride ($ZnCl_2$, ≥98%), oleylamine (OAm, 70%), sulfur powder (99.998%), thioglycolic acid (TGA, ≥98%), 11-mercaptoundecanoic acid (MUA, 95%), tetramethylammonium hydroxide pentahydrate (TMAOH, ≥97%), dodecanethiol (DDT, ≥98%), tert-dodecanethiol (t-DDT, 98.5%), tetranitromethane (TNM, 95%), sodium sulfate (Na_2SO_4, ≥99%) and potassium chloride (KCl, ≥99%) were purchased from Sigma-Aldrich (Madrid, Spain). Hexane, methanol and acetone were of analytical grade and were purchased from Panreac (Barcelona, Spain). Glass substrates coated with fluorine doped tin oxide (FTO, ~8 Ω/sq) were acquired from VWR (Leuven, Belgium). All the syntheses were carried out using standard air-free Schlenk-line techniques.

2.2. Synthesis of CGS NCs

For the experiment, 1 mmol of $Cu(acac)_2$ and 1 mmol of $Ga(acac)_3$ together with 3.5 mmol of TOPO were mixed with 10 mL of OAm upon magnetic stirring. After degassing at 90 °C for 60 min under vacuum, an argon atmosphere was introduced and the reaction mixture was heated to 270 °C. At 150 °C, 1.12 mmol (0.25 mL) of DDT and 7.4 mmol (1.75 mL) of t-DDT were injected, which changed the color of the solution from dark blue to clear yellow. While increasing temperature, the solution color further changed to clear brown, indicating the NC nucleation, and dark-brown at 250 °C. The mixture was allowed to react at 270 °C for 30 min and afterwards the heating mantle was removed to allow the solution to cool down naturally. NCs were isolated by adding 5 mL of acetone and centrifuging at

5700 rpm for 5 min. The supernatant was discarded and the precipitate was redispersed in 5 mL of hexane. Additional purification steps were performed following the same procedure. Finally, NCs were redispersed in 5 mL of hexane for later use.

2.3. Synthesis of ZnS NCs

The experiment also involved 2 mmol of $ZnCl_2$ and 6.5 mmol of TOPO being dissolved in 10 mL of OAm under Ar atmosphere at 170 °C for 60 min. The clear transparent solution formed was allowed to cool down to room temperature. At this point, a degassed mixture of 2.5 mmol of sulfur in 5 mL of OAm was injected. Then, the reaction mixture was heated to 320 °C and allowed to react at this temperature for 60 min. Afterwards, the heating mantle was removed to allow the solution to cool down naturally and NCs were collected and washed by adding 5 mL of ethanol followed by centrifugation. The washing procedure was repeated at least 2 more times and NCs were finally dispersed in 5 mL of hexane for later use.

2.4. TGA Ligand Exchange

In addition, 20 mg of CGS NCs were dispersed through 15 min of sonication and shaking in 10 mL of methanol containing 4 mmol of TGA and the proper amount of TMAOH to adjust the pH to 10. Afterwards, NCs were washed by adding 10 mL of acetone and centrifugation at 5700 rpm for 5 min. The purification step was repeated twice, followed by redispersion of NCs in 1 mL of methanol.

2.5. MUA Ligand Exchange

1 mL of a ZnS NCs solution (20 mg/mL in hexane) was mixed with 1 mL of a MUA solution (4 mmol in 10 mL of methanol) at pH 10 (adjusted using TMAOH). The resulting bi-phase solution was shaken and sonicated for 15 min. Afterwards, the upper part was removed and 5 mL of fresh acetone was added. This step was followed by centrifugation for 5 min at 5000 rpm. The obtained precipitate was redispersed in 1 mL of methanol for later use.

2.6. NCs Films

1 mL of a hexane or methanol solution of NCs (20 mg/mL) was spin-coated on FTO-coated glass substrates at a rotation speed of 1500 rpm for 20 s. Afterwards, the NC layer was annealed at 250 °C for 60 min under argon flow.

2.7. Porous Xerogel Films

For the experiment, 1 mL of a methanol solution of TGA-capped CGS NCs or MUA-capped ZnS NCs (20 mg/mL) were spin-coated on FTO-coated glass substrates at a rotation speed of 1500 rpm for 20 s. Immediately afterwards, the NC layer was dipped for 1 min into an acetone solution containing 3 vol % of TNM. Films were rinsed with fresh methanol to remove by-products and afterwards annealed at 250 °C for 60 min under argon flow.

2.8. Gel Preparation

Fifty microliters of a TNM solution (3 vol % in acetone) was added into a 2 mL methanol solution containing TGA-capped CGS NCs (10 mg/mL). The mixture was shaken vigorously for 30 s and kept undisturbed for the whole gelation process. The gelation process visually evolved for 15 min after the addition of the TNM solution, but it was left to react for two days to ensure completion. Then, the solvent was exchanged with fresh methanol or acetone to remove TNM-residues and by-products, in 1–2 h steps over 2 days. This process must be carried out with special care in order to not damage the porous network of the wet-gel. The wet-gel could be dried into a xerogel at room temperature and ambient pressure, resulting in a significant shrinkage.

2.9. Aerogel Preparation

The wet-gel (in acetone) was loaded in a supercritical point drier chamber, which was filled with liquid CO_2 and kept filled overnight. Then, the chamber was half drained and filled with fresh liquid CO_2. This procedure was repeated at least 6 times in one-hour intervals in order to completely replace acetone by liquid CO_2. Then, the chamber was completely filled with liquid CO_2 and heated above 39 °C. Upon heating, pressure increased up to 75–80 bars, thus surpassing the supercritical point of CO_2. The sample was kept under these conditions for 1 h followed by releasing the pressure at constant temperature.

2.10. Photoelectrochemical Measurements

Photocurrent measurements were performed using a three-electrode cell configuration with a Pt-mesh as a counter electrode (2 cm^2 surface area) and a Ag/AgCl reference electrode filled with 3 M KCl solution. A 0.1 M aqueous solution of Na_2SO_4 at pH = 7 was used as electrolyte. The bias voltage was applied to the working electrode through an electrical contact to the uncoated part of the FTO layer. 1 cm^2 of the tested semiconductor layer was in contact with the electrolyte. Illumination was provided by 8 xenon lamps (35 W each, Osram, Madrid, Spain) radially distributed with a total power of 280 W and irradiance on the sample of ca. 100 mW/cm^2.

2.11. Characterization

Transmission electron microscopy (TEM) characterization was carried out using a ZEISS LIBRA 120 (Carl Zeiss, Jena, Germany), operating at 120 kV. Samples were prepared by drop casting a diluted NC solution onto a carbon-coated copper grid (200 mesh). Scanning electron microscopy (SEM) analysis was carried out using a ZEISS Auriga microscope (Carl Zeiss, Jena, Germany). For SEM characterization, NCs dispersed in proper solvent were drop casted onto silicon substrates. X-ray power diffraction (XRD) analyses were carried out on a Bruker AXS D8 ADVANCE X-ray diffractometer (Bruker, Karlsruhe, Germany) with Ni-filtered (2 μm thickness) Cu Kα1 radiation (λ = 1.5406 Å). Samples were drop casted (200–500 μL at a concentration of about 3 mg/mL) onto a zero-signal silicon wafer. UV-Vis absorption spectra were recorded on a PerkinElmer LAMBDA 950 UV-Vis spectrophotometer (PerkinElmer, Walthham, MA, USA). Samples were prepared by diluting 100 μL in 2 mL of hexane inside a quartz cuvette with a 10 mm path length. Fourier Transform Infrared (FTIR) spectroscopy investigations were carried out using a PerkinElmer FT-IR 2000 spectrophotometer (PerkinElmer, Walthham, MA, USA). Spectra were recorded from 500 to 4000 cm^{-1}. Samples were characterized by electrochemical impedance spectroscopy (EIS) using a versaSTAT3 (Ametek, Madrid, Spain). Measurements were conducted in the frequency range from 100 kHz to 1 mHz with a 5 mV AcCamplitude using the three-electrode cell configuration with the same conditions used for photocurrent measurements. To perform thickness measurements, the FTO substrate was partially masked prior to the spin-coating of the NC inks. The thickness profiles were taken at the edge of the film sample and bare FTO using a Sensofar Plu Neox laser scanning confocal microscope (Sensofar, Terrassa, Spain) with a Nikon TU Plan Fluor objective at a magnification of 100×. X-ray photoelectron spectroscopy (XPS) was done on a SPECS system (SPECS GmbH, Berlin, Germany) equipped with an Al anode XR50 source operating at 150 mW and a Phoibos 150 MCD-9 detector (SPECS GmbH, Berlin, Germany). The pressure in the analysis chamber was kept below 10^{-7} Pa. The area analyzed was about 2 mm × 2 mm. The pass energy of the hemispherical analyzer was set at 25 eV and the energy step was maintained at 1.0 eV. Data processing was performed with the Casa XPS program (version, Casa Software Ltd., Teignmouth, UK). Binding energies were shifted according to the reference C 1s peak that was located at 284.8 eV. Thermogravimetric (TG) analyses were carried out using a PerkinElmer Diamond TG/DTA instrument (PerkinElmer, Walthham, MA, USA). For TG analysis, samples were dried and 20 mg of the dried powder was loaded into a ceramic pan. Measurements were carried out in an Ar atmosphere from ambient temperature to 500 °C at a heating rate of 2 °C/min.

3. Results

CGS NCs were synthesized using a previously reported procedure with some modifications (see experimental section for details) [15]. Briefly, NCs were produced through the reaction of DDT and t-DDT with $Cu(acac)_2$ and $Ga(acac)_3$ dissolved in OAm and in the presence of TOPO. The reaction mixture was heated up to 270 °C and maintained at this temperature for 30 min. From this procedure, CGS NCs with the wurtzite crystal phase, tadpole geometry and an average length of ca. 50 nm were produced (Figure 1).

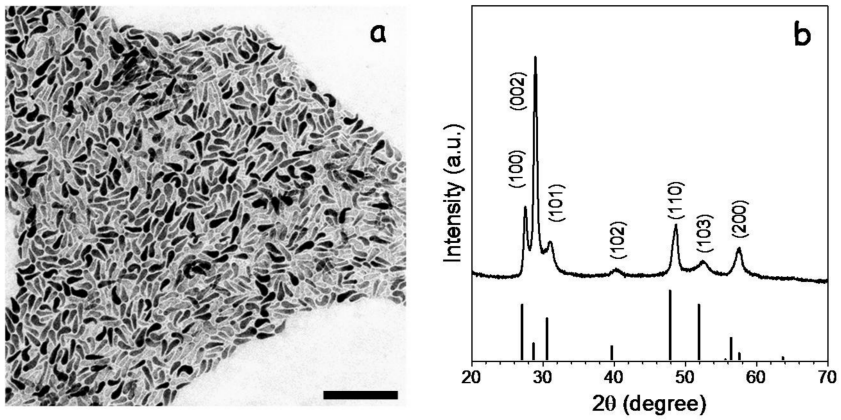

Figure 1. Representative TEM micrograph (**a**) and XRD pattern (**b**) of CGS NCs with wurtzite crystal phase. TEM scale bar = 200 nm. The JCPDS (Joint Committee on Powder Diffraction Standards) 001-1280 phase standard card, corresponding to wurtzite CGS, is included as a reference [16].

FTIR characterization showed the as-prepared CGS NCs to contain significant amounts of organic ligands, as revealed by the presence of peaks at 2924 and 2830 cm^{-1} that correspond to C–H stretching (Figure 2a). This native surface organic ligand, most probably DDT according to previous reports [17], was displaced using TGA. For this purpose, as-prepared CGS NCs (DDT-CGS) were dispersed through sonication and shaking in a methanol solution of TGA and the proper amount of TMAOH to adjust the pH to 10. After purification, FTIR spectra showed a drastic reduction of the C–H peak intensity consistent with the shorter organic chain of TGA. Thermogravimetric analysis also showed a significantly lower decrease of the weight loss from the TGA-CGS NCs compared with the DDT-CGS NCs, consistent with the lower organic content of the former (Figure 2b).

After ligand exchange, TGA-CGS NCs in methanol were spin-coated onto FTO substrates to form CGS layers. Subsequently, TGA was removed using a TNM solution in acetone. For this purpose, immediately after spin coating, CGS layers were dipped into an acetone solution containing 3 vol % TNM for 1 min. Layers were washed afterwards with methanol and allowed to dry naturally. Finally, they were annealed at 250 °C in Ar for 60 min. For comparison, we also produced CGS layers using DDT-CGS and TGA-CGS but with no ligand displacement/oxidation step. Figure 3 shows top-view SEM images of the different layers. The films produced after the displacement of TGA showed a much rougher surface than those obtained from DDT-CGS and from TGA-CGS (without TGA displacement/oxidation) suggesting greater porosity. As schematized in Figure 3d, exposure of TGA-CGS to the non-oxygen transferring oxidizer (TNM) resulted in partial removal of TGA. Unprotected surface metal ions were then solvated to result in a chalcogen rich NC surface that underwent NC-NC cross-linking through oxidation-induced chalcogen-chalcogen bonding. This mode of NCs cross-linking resulted in the formation of a porous network of interconnected NCs in solution—an NC-based gel [18]. The final material still contains TGA on the surface of particles. The ligand-oxidation process is competitive with ZnS sulfide oxidation; as portions of the particle are de-protected, they undergo assembly to form a linked network, but a portion of the particles still

remains ligand-capped. To fully remove the ligand-related carbon from the final film, an additional chemical or thermal treatment of the layer is required.

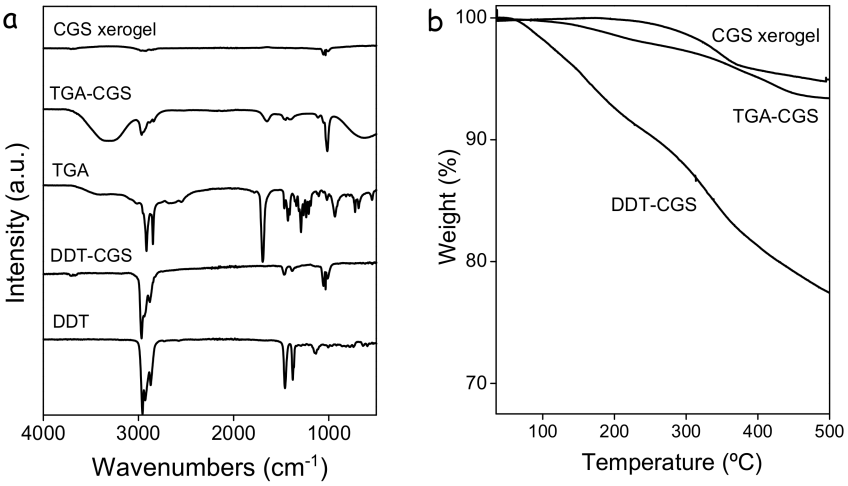

Figure 2. (**a**) from bottom to top: FTIR spectra of DDT; as-prepared CGS NCs (DDT-CGS); TGA; NCs functionalized with TGA (TGA-CGS); and the NC xerogel obtained by exposing TGA-NCs to the oxidant solution and naturally drying them; (**b**) thermogravimetric profile of the DDT-CGS NCs, TGA-CGS NCs and CGS xerogel.

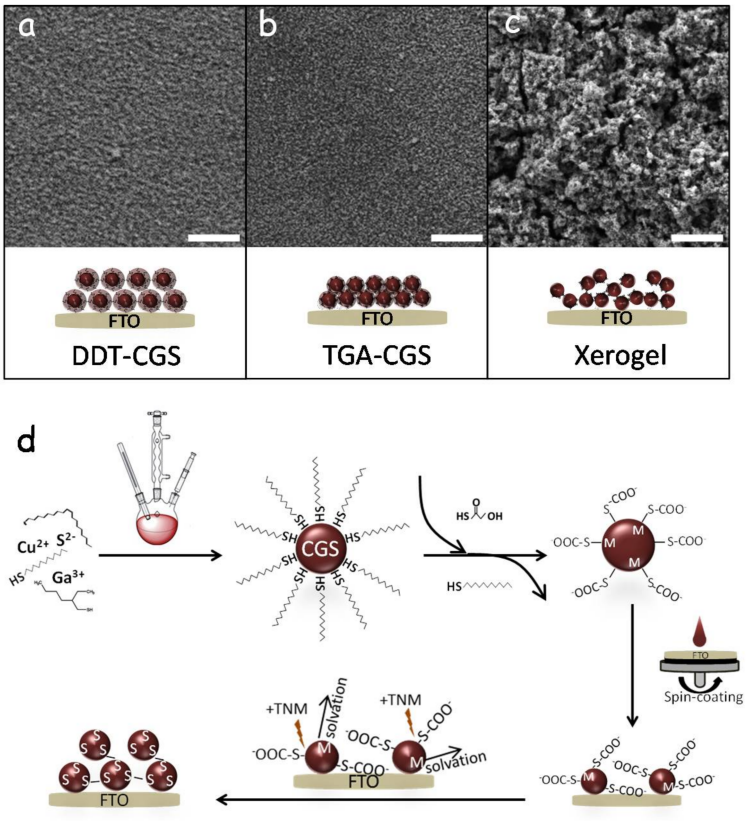

Figure 3. (**a**–**c**) representative SEM micrographs and schematic representations of the CGS layers produced via spin-coating of DDT-CGS (**a**), TGA-CGS (**b**), and TGA-CGS after undergoing oxidative assembly with TNM to form a xerogel film (**c**). Scale bars = 1 μm; (**d**) schematic representation of the procedure to produce porous xerogel NC films by removal of the thiol ligand through a non-oxygen transferring oxidant, TNM.

The layer thickness could be controlled through the NC concentration in solution and the number of spin coated layers. Figure 4a shows the UV-Vis spectra of a TGA-CGS NC film and three xerogel films with different thicknesses produced by the successive deposition of one, two or three CGS layers followed by their gelation. Notice how the transmittance of the layers decreases with the film thickness. Transmittance is slightly lower for the single xerogel film compared with the TGA-CGS film, which we associate with the higher scattering of the former. Figure 4b,c display the thickness profiles of the films and their optical photographs.

To gain insight into the mechanism of displacement of the TGA ligand in TGA-CGS NCs and the NC network formation, the same treatment was applied to unsupported NCs. In this case, the TNM solution in acetone was injected into a colloidal solution of TGA-CGS NCs in methanol. Upon injection, a gel started to form. Gelation visually evolved for 15 min but was allowed to carry on for 48 h. Afterwards, the CGS NC gel was rinsed with fresh methanol and allowed to dry naturally into a xerogel (Figure 5). FTIR characterization (Figure 2a) of the CGS xerogels revealed a significant decrease of the intensity of the C–H stretching peaks when compared with TGA-CGS NCs, providing evidence of a strong, but not complete, reduction of the amount of organics at the CGS NC surface. Thermogravimetric analysis (Figure 2b) further demonstrated the reduction of the organic content.

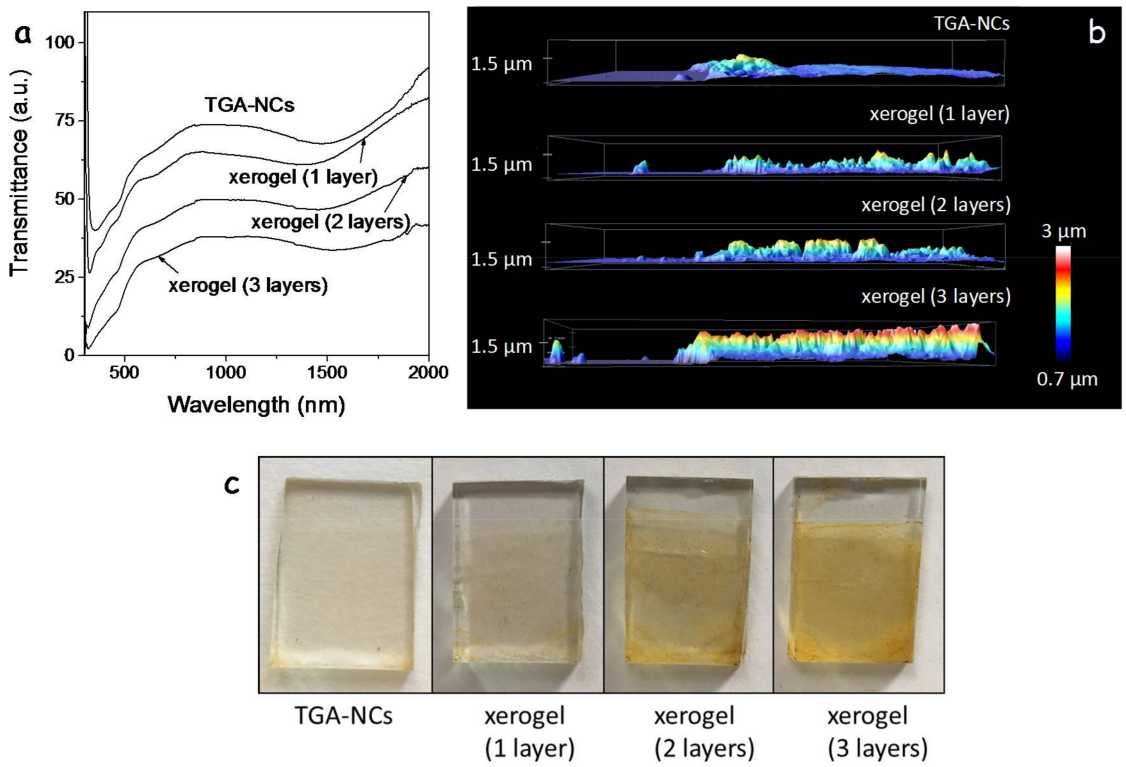

Figure 4. (**a**) transmittance spectra of films produced from as-synthesized NCs, TGA-NCs, and xerogel films with different numbers of layers (1 layer, 2 layers; 3 layers); (**b**) thickness profiles of the produced films; (**c**) optical photographs of the films.

SEM micrographs of the obtained CGS xerogels displayed a porous structure of interconnected NCs (Figure 5b,c). When drying the CGS gel from supercritical CO_2 (see experimental section for details), highly porous aerogels, characterized with Brauner-Emmett-Teller (BET) surface areas of 46 $m^2 \cdot g^{-1}$, were obtained. Approximating the CGS NC geometry as cylindrical and considering an average cylinder length of 50 nm and an average diameter of 15 nm, their total surface area would be 64 $m^2 \cdot g^{-1}$. Thus, within this approximation, the produced aerogels were able to keep over 70% of the surface area of the colloidal NCs. CGS aerogels showed type IV adsorption-desorption isotherms with

a combination of H1- and H3-type hysteresis loops, consistent with a mesoporous structure (Figure 5d). Barrett–Joynes–Halenda (BJH) plots displayed a broad pore size distribution, characteristic of their aerogel nature (Figure 5e).

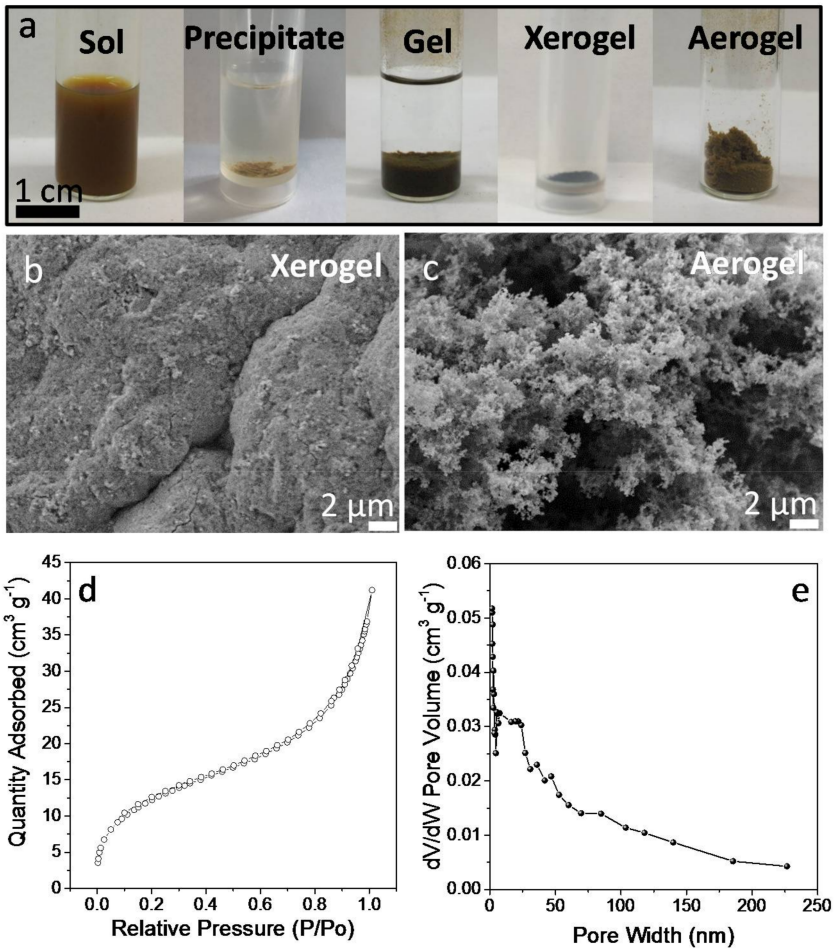

Figure 5. (**a**) optical images of the CGS NC-based sol, precipitate, gel, aerogel and xerogel; (**b**) SEM micrograph of a CGS xerogel; (**c**) SEM micrograph of a CGS aerogel; (**d**) adsorption/desorption isotherm cycle from a CGS NC-aerogel, and (**e**) its corresponding BJH pore size distribution.

XPS analysis confirmed the formation of chalcogen-chalcogen bonds between the particles (Figure 6). XPS spectra of TGA-NCs exposed to air displayed two contributions to the S 2p regions, one associated with the lattice S^{2-} (S $2p_{3/2}$ binding energy = 161.8 eV) and the second one associated with a sulphate (S $2p_{3/2}$ binding energy = 168.6 eV) [19]. In the XPS spectra of the TNM-treated sample, a third component became evident. This third chemical state (S $2p_{3/2}$ binding energy = 163.2 eV) had a slightly lower binding energy than elemental sulfur (S $2p_{3/2}$ binding energy = 163.7 eV) [19]. Thus, we associated it to sulfur with a chemical environment compatible with that of disulphides, which is consistent with formation of S_2^{2-} type linkages. Additionally, the sulphate component was strongly decreased in the gelated sample, and the treatment with TNM eliminated both suface thiolates and surface oxidation layers.

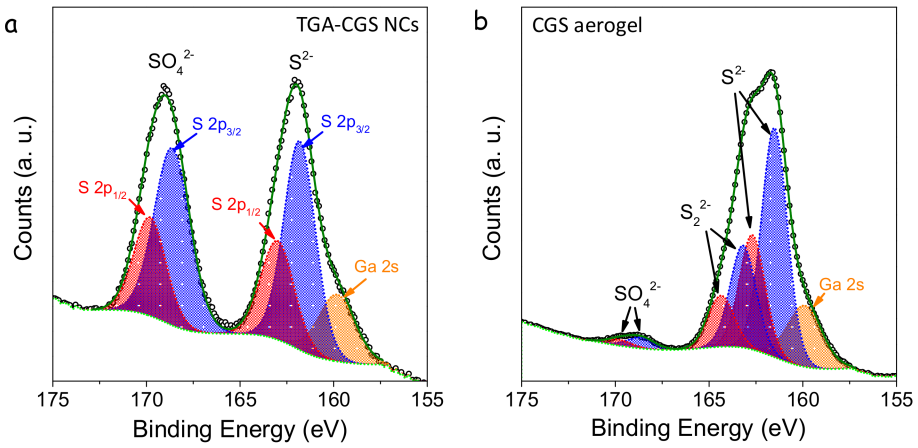

Figure 6. S 2p region of the XPS spectra of the TGA-CGS NCs (**a)** and the CGS NC-based aerogel (**b**). S 2p3/2 states are plotted in blue and S 2p1/2 states in red. In the same region, the Ga 2s state is observed.

ZnS NCs were produced following the procedure reported by Hyeon et al. [19], reacting $ZnCl_2$ with elemental sulfur in OAm at 320 °C (see details in the experimental section). ZnS NCs produced following this procedure displayed the sphalerite crystal structure and quasi-spherical geometry with an average size of 10 nm (Figure 7a,b). The growth of ZnS NCs and their colloidal stability were controlled by the presence of OAm at their surface as observed by FTIR characterization (Figure 7c) and reported previously [20]. We replaced OAm with MUA by shaking and sonicating a bi-phase solution of OAm-ZnS NCs in hexane and MUA in methanol. Through this process, ZnS NCs moved from the hexane to the methanol phase, where they were stabilized by MUA (MUA-ZnS). Then, the upper hexane solution containing the displaced OAm was discarded and the MUA-ZnS NCs in the methanol solution were collected and further purified as described in the experimental section.

Porous layers of interconnected ZnS NCs were produced following the same procedure as for CGS NCs, using TNM as a non-oxygen transferring agent. Bulk ZnS gels and xerogels were also produced by adding TNM to a colloidal solution of MUA-ZnS NCs in methanol. Figure 7d shows a representative TEM micrograph and an optical image of the interconnected ZnS NC network produced upon addition of TNM to the colloidal solution of MUA-ZnS NCs. FTIR spectra from these gels showed a reduction of the intensity of the peaks at 2924 and 2830 cm^{-1} attributed to organic ligands, consistent with their partial removal (Figure 7c). Notice that, due to the larger size of MUA compared with TGA, the intensity of the peaks associated with C–H vibrations in the FTIR spectrum of the ZnS-based gel is stronger than in the CGS-based one.

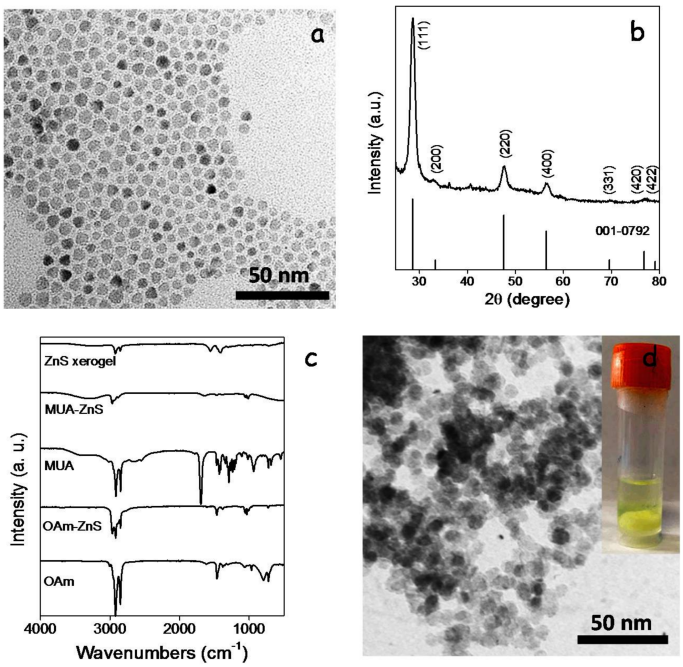

Figure 7. (**a**) TEM micrograph of ZnS NCs; (**b**) XRD pattern of ZnS NCs including the JCPDS 001-0792 phase standard card corresponding to sphalerite ZnS as reference; [21] (**c**) from bottom to top, FTIR spectra of: OAm, as-produced ZnS NCs (OAm-ZnS), MUA, ZnS NCs obtained after ligand exchange with MUA (MUA-ZnS) and ZnS NC-based xerogel; (**d**) TEM micrographs of the ZnS xerogel obtained from MUA-NCs treated with TNM. Inset shows an optical image of the formed ZnS gel.

Combining p-type CGS with n-type ZnS in bilayer structures or blended layers should allow a more effective separation of photogenerated charge carriers, reducing charge recombination and promoting photocatalytic performance. Additionally, a faster charge carrier separation should promote the material chemical stability, since metal sulfides suffer from significant photocorrosion during photocatalytic reactions associated with the surface accumulation of photogenerated holes that induce rapid oxidation of lattice S^{2-} ions to S^0 or soluble sulfates [22,23]. Therefore, beyond single component films, we produced CGS/ZnS bilayers and CGS-ZnS mixed layers. Figure 8a,b show top-view SEM micrographs of CGS/ZnS bilayers produced from the sequential spin-coating of DDT-CGS and OAm-ZnS NCs (Figure 8a) and from the sequential spin coating and gelation of TGA-CGS and MUA-ZnS NCs (Figure 8b). Figure 8c shows a top-view SEM micrograph of the layer produced from the spin coating and subsequent gelation of a solution containing a blend of TGA-CGS and MUA-ZnS NCs. Note that a thermal treatment (250 °C for 60 min under Ar atmosphere) was required to stabilize the DDT-CGS layer before deposition of the OAm-ZnS NCs layer, in order to prevent dissolution of the former. However, such thermal treatment was not necessary for layer deposition on top of gelated materials. This represents a clear advantage over multiple layer deposition procedures that require an annealing step in between each process.

The performance of CGS NC-based layers was evaluated against the photoelectrocatalytic hydrogen evolution reaction in a 0.1 M aqueous solution of Na_2SO_4 at neutral pH. Photoelectrocatalytic measurements were carried out with a three-electrode electrochemical cell using the NC-based layers annealed at 250 °C for 60 min as working electrodes.

Note that no catalyst was used in these experiments, thus overall layer performances were relatively low, but still qualitatively significant to probe dissimilarities between the differently treated samples. Compared with the layers produced from DDT-CGS, higher current densities were obtained from the layers prepared with a shorter organic ligand (TGA-CGS) and particularly from the gelated layer (CGS xerogel) (Figure 9a). This experimental evidence is associated with two properties: (i) the

higher surface area of the CGS xerogel, which provided enhanced interaction with the media; and (ii) the enhanced charge carrier transport within the TGA-CGS layer and particularly the CGS xerogel layer compared with DDT-CGS. EIS measurements confirmed the lower impedance of the gelated layers compared with DDT-CGS and TGA-CGS films, associated again with the lower organic content and the higher surface area of the xerogel films (Figure 9b). Similar results were obtained from ZnS layers, demonstrating significantly larger current densities for ZnS xerogels than for OAm-ZnS-based layers (Figure 9c).

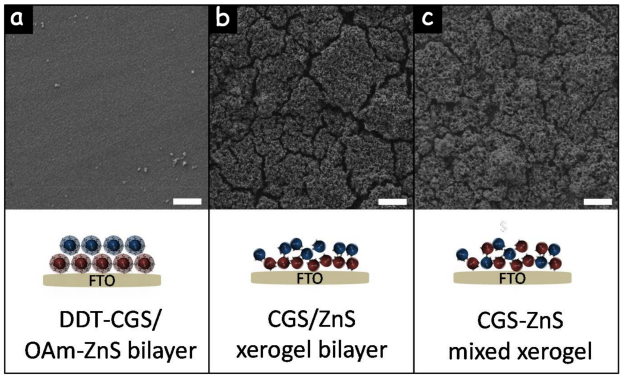

Figure 8. SEM micrographs and schematic representations of the following structures: (**a**) a bilayer obtained from the sequential spin coating of DDT-CGS NCs and OAm-ZnS NCs; (**b**) a bilayer produced from the spin coating and gelation of TGA-CGS NCs and the subsequent deposition and gelation of MUA-ZnS NCs; (**c**) a blended CGS-ZnS NC layer obtained from the spin coating of a solution containing both TGA-CGS NCs and MUA-ZnS NCs followed by treating it with TNM. Scale-bars = 1 μm.

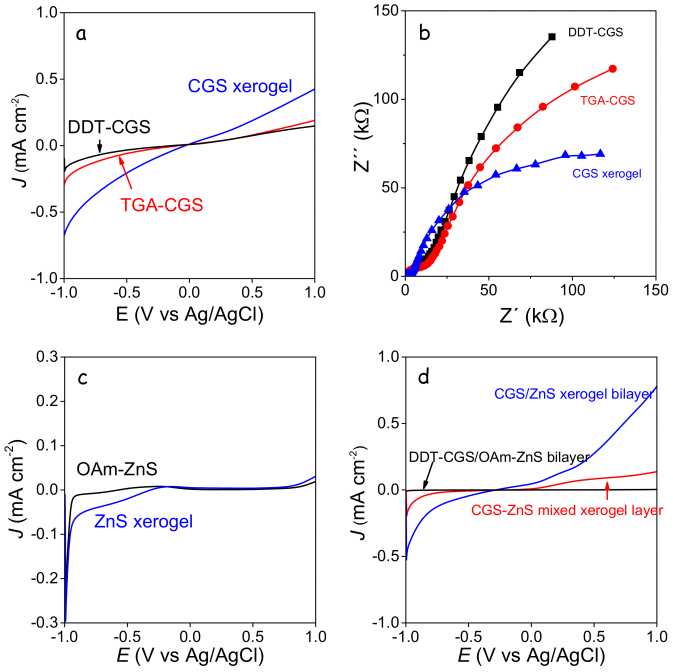

Figure 9. (**a**) linear sweep voltammogram curves at a scan rate of 0.1 $V \cdot s^{-1}$ of DDT-CGS, TGA-CGS and gelated TGA-CGS NC-based layers; (**b**) Nyquist plots for DDT-CGS, TGA-CGS and CGS xerogel films; (**c**) linear sweep voltammogram curves at a scan rate of 0.1 $V \cdot s^{-1}$ of OAm-ZnS and gelated MUA-ZnS NC-based layers; (**d**) linear sweep voltammogram curves at a scan rate of 0.1 $V \cdot s^{-1}$ of DDT-CGS/OAm-ZnS NC-based bilayer, a gelated TGA-CGS/MUA-ZnS NC-based bilayer and a gelated layer produced from a blend of TGA-CGS and MUA-CGS.

Current densities were increased when combining CGS and ZnS xerogels into a bilayer structure, which we associated with a favorable surface energy band arrangement. On the other hand, blended xerogel layers were characterized by lower current densities probably associated to the reduced charge carrier mobility in a nanocrystalline network containing a large density of energy barriers introduced by the random distribution of the p-type and n-type semiconductors.

The highest photocurrents were obtained from CGS xerogel monolayers and CGS/ZnS xerogel bilayers (Figure 10). Improved photocatalytic performance with respect to DDT-CGS, TGA-CGS and DDT-CGS/MUA-ZnS layers was related to the enhanced charge transport within the interconnected NC network and the larger surface area of the porous xerogel films. CGS/ZnS xerogel bilayers provided even higher photocurrents than CGS xerogel layers, which we attributed to the more efficient charge separation at the p-n junctions, reducing recombination, and possibly to a more efficient injection of charge to the solution species through a proper band adjustment.

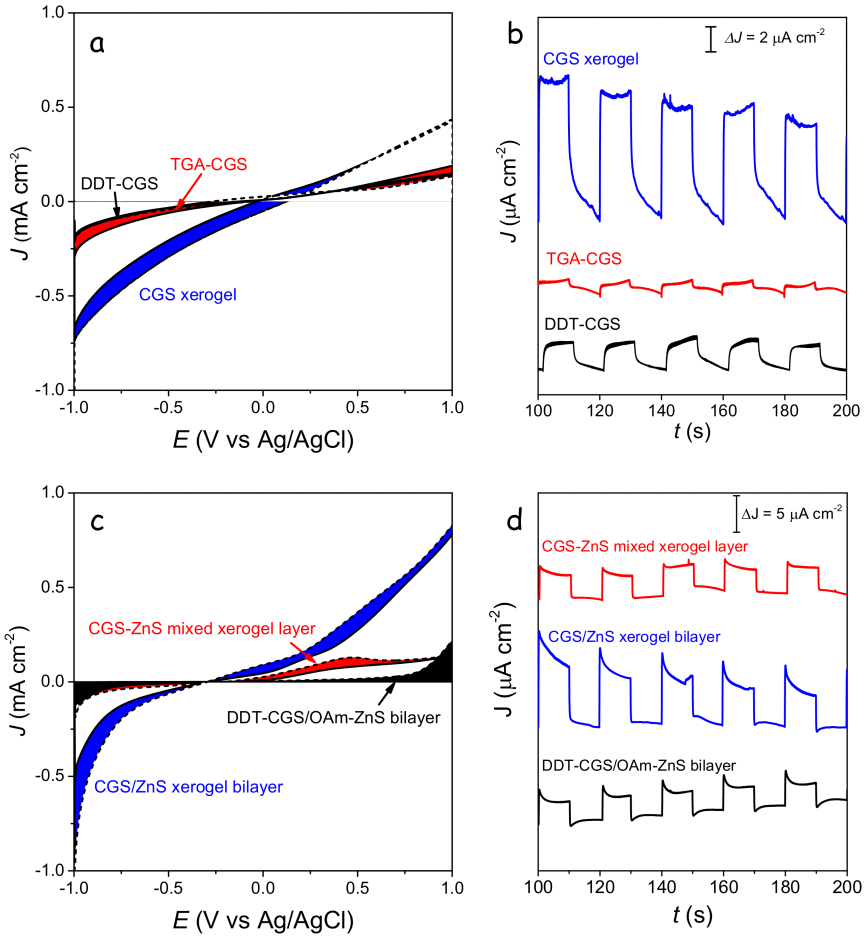

Figure 10. (**a**,**b**) linear sweep voltammogram curves at a scan rate of 0.1 V·s^{-1} (**a**) and time-dependent characteristics (**b**) of the photocurrent response of CGS layers having different surface chemistries. (**c**,**d**) linear sweep voltammogram curves at a scan rate of 0.1 V·s^{-1} (**c**) and time-dependent characteristics (**d**) of the photocurrent response of CGS/ZnS bilayers and a CGS-ZnS mixed layer. Time-dependent characteristics were obtained by applying −0.6 V with respect to an Ag/AgCl reference electrode.

4. Conclusions

We demonstrated the formation of porous layers of CGS and ZnS from the treatment of TGA-capped CGS NCs and MUA-capped ZnS NCs with a non-oxygen transferring agent, TNM. This oxidizing agent indirectly created chalcogen-chalcogen bonds between the NCs, anchoring them together. Compared to organic-capped layers, CGS xerogel films were characterized with higher current densities and photoresponses due to improved interparticle coupling and the porous structure. We further produced CGS/ZnS NC-based bilayers and CGS–ZnS NC-based composite layers that exhibited higher current densities and photoresponses than layers deposited from as-produced NCs. In particular, porous CGS/ZnS bilayers showed the highest current densities and photocurrents, associated with improved charge transport due to chalcogen-chalcogen cross-linking between NCs, enhanced interaction with the media due to its high surface area, and more efficient charge separation in the p-n bilayer structure.

Acknowledgments: This work was supported by the European Regional Development Funds and the Spanish MINECO project SEHTOP (ENE2016-77798-C4-3-R). T.B. thanks the FI-AGAUR Research Fellowship Program, Generalitat de Catalunya (2015 FI_B 00744). P.G. acknowledges the People Programme (Marie Curie Actions) of the FP7/2007-2013 European Union Program (TECNIOspring grant agreement No. 600388) and the Agency for Business Competitiveness of the Government of Catalonia, ACCIÓ. S.B. acknowledges the U.S. National Science Foundation, CHE-1361741. J.L. is a Serra Hunter Fellow and is grateful to the ICREA Academia program and grants MINECO/FEDER ENE2015-63969-R and GC 2017 SGR 128 for support.

Author Contributions: Taisiia Berestok and Pablo Guardia conceived, designed and performed the experiments; Jordi Llorca, Sònia Estradé and Francesca Peiró contributed analysis tools; Andreu Cabot and Stephanie L. Brock wrote the paper.

Conflicts of Interest: The authors declare no conflict of interest.

References

1. Coughlan, C.; Ibáñez, M.; Dobrozhan, O.; Singh, A.; Cabot, A.; Ryan, K.M. Compound Copper Chalcogenide Nanocrystals. *Chem. Rev.* **2017**, *117*, 5865–6109. [CrossRef] [PubMed]
2. Lee, J.-S.; Kovalenko, M.V.; Huang, J.; Chung, D.S.; Talapin, D.V. Band-like transport, high electron mobility and high photoconductivity in all-inorganic nanocrystal arrays. *Nat. Nanotechnol.* **2011**, *6*, 348–352. [CrossRef] [PubMed]
3. Kovalenko, M.V.; Scheele, M.; Talapin, D.V. Colloidal Nanocrystals with Molecular Metal Chalcogenide Surface Ligands. *Science* **2009**, *324*, 1417–1420. [CrossRef] [PubMed]
4. Engel, J.H.; Alivisatos, A.P. Postsynthetic Doping Control of Nanocrystal Thin Films: Balancing Space Charge to Improve Photovoltaic Efficiency. *Chem. Mater.* **2014**, *26*, 153–162. [CrossRef]
5. Brock, S.L.; Arachchige, I.U.; Kalebaila, K.K. Metal chalcogenide gels, xerogels and aerogels. *Comments Inorg. Chem.* **2006**, *27*, 103–126. [CrossRef]
6. Muthuswamy, E.; Brock, S.L. Oxidation Does Not (Always) Kill Reactivity of Transition Metals: Solution-Phase Conversion of Nanoscale Transition Metal Oxides to Phosphides and Sulfides. *J. Am. Chem. Soc.* **2010**, *132*, 15849–15851. [CrossRef] [PubMed]
7. Davis, J.L.; Chalifoux, A.M.; Brock, S.L. Role of Crystal Structure and Chalcogenide Redox Properties on the Oxidative Assembly of Cadmium Chalcogenide Nanocrystals. *Langmuir* **2017**, *33*, 9434–9443. [CrossRef] [PubMed]
8. Pala, I.R.; Arachchige, I.U.; Georgiev, D.G.; Brock, S.L. Reversible Gelation of II–VI Nanocrystals: The Nature of Interparticle Bonding and the Origin of Nanocrystal Photochemical Instability. *Angew. Chem. Int. Ed.* **2010**, *49*, 3661–3665. [CrossRef] [PubMed]
9. Evans, B.J.; Doi, J.T.; Musker, W.K. Fluorine-19 NMR study of the reaction of p-fluorobenzenethiol and disulfide with periodate and other selected oxidizing agents. *J. Org. Chem.* **1990**, *55*, 2337–2344. [CrossRef]
10. Hagfeldt, A.; Grätzel, M. Molecular Photovoltaics. *Acc. Chem. Res.* **2000**, *33*, 269–277. [CrossRef] [PubMed]
11. Ghosh, A.; Thangavel, R.; Rajagopalan, M. Electronic and optical modeling of solar cell compound Cu_XY_2 (X = In, Ga, Al; Y = S, Se, Te): first-principles study via Tran–Blaha-modified Becke–Johnson exchange potential approach. *J. Mater. Sci.* **2015**, *50*, 1710–1717. [CrossRef]

12. Hashemi, J.; Akbari, A.; Huotari, S.; Hakala, M. Multi-intermediate-band character of Ti-substituted $CuGaS_2$: Implications for photovoltaic applications. *Phys. Rev. B* **2014**, *90*, 075154. [CrossRef]
13. Han, M.; Zhang, X.; Zeng, Z. The investigation of transition metal doped $CuGaS_2$ for promising intermediate band materials. *RSC Adv.* **2014**, *4*, 62380–62386. [CrossRef]
14. Korala, L.; Wang, Z.; Liu, Y.; Maldonado, S.; Brock, S.L. Uniform Thin Films of CdSe and CdSe(ZnS) Core(Shell) Quantum Dots by Sol–Gel Assembly: Enabling Photoelectrochemical Characterization and Electronic Applications. *ACS Nano* **2013**, *7*, 1215–1223. [CrossRef] [PubMed]
15. Yu, X.; An, X.; Shavel, A.; Ibanez, M.; Cabot, A. The effect of the Ga content on the photocatalytic hydrogen evolution of $CuIn_{1-x}Ga_xS_2$ nanocrystals. *J. Mater. Chem. A* **2014**, *2*, 12317–12322. [CrossRef]
16. Fuller, M.L. LXX. The crystal structure of wurtzite. *Philos. Mag.* **1929**, *8*, 658–664. [CrossRef]
17. Xia, C.; Cao, L.; Liu, W.; Su, G.; Gao, R.; Qu, H.; Shi, L.; He, G. One-step synthesis of near-infrared emitting and size tunable $CuInS_2$ semiconductor nanocrystals by adjusting kinetic variables. *CrystEngComm* **2014**, *16*, 7469–7477. [CrossRef]
18. Mohanan, J.L.; Arachchige, I.U.; Brock, S.L. Porous Semiconductor Chalcogenide Aerogels. *Science* **2005**, *307*, 397–400. [CrossRef] [PubMed]
19. Moulder, J.F.; Stickle, W.F.; Sobol, P.E.; Bomben, K.D. *Handbook of X-ray Photoelectron Spectroscopy*; Perkin-Elmer: Eden Prairie, MN, USA, 1992. [CrossRef]
20. Joo, J.; Na, H.B.; Yu, T.; Yu, J.H.; Kim, Y.W.; Wu, F.; Zhang, J.Z.; Hyeon, T. Generalized and Facile Synthesis of Semiconducting Metal Sulfide Nanocrystals. *J. Am. Chem. Soc.* **2003**, *125*, 11100–11105. [CrossRef] [PubMed]
21. Hanawalt, J.D.; Rinn, H.W.; Frevel, L.K. Chemical Analysis by X-Ray Diffraction. *Ind. Eng. Chem. Anal. Ed.* **1938**, *10*, 457. [CrossRef]
22. Iwase, A.; Ng, Y.H.; Amal, R.; Kudo, A. Solar hydrogen evolution using a $CuGaS_2$ photocathode improved by incorporating reduced graphene oxide. *J. Mater. Chem. A* **2015**, *3*, 8566–8570. [CrossRef]
23. Shen, Q.; Kobayashi, J.; Diguna, L.J.; Toyoda, T. Effect of ZnS coating on the photovoltaic properties of CdSe quantum dot-sensitized solar cells. *J. Appl. Phys.* **2008**, *103*, 084304. [CrossRef]